

**Construction and operation of the EXO-100
cryogenic facility for R & D in liquid xenon:
advances in barium ion tagging**

Inauguraldissertation

der Philosophisch-naturwissenschaftlichen Fakultät
der Universität Bern

vorgelegt von

Sébastien Claude Delaquis

von Rechthalten FR

Leiter der Arbeit:

Prof. Dr. R. S. Gornea

Physikalisches Institut

Albert Einstein Center for Fundamental Physics

Laboratorium für Hochenergiephysik

Originaldokument gespeichert auf dem Webserver der Universitätsbibliothek Bern



Dieses Werk ist unter einem
Creative Commons Namensnennung-Keine kommerzielle Nutzung-Keine Bearbeitung 2.5
Schweiz Lizenzvertrag lizenziert. Um die Lizenz anzusehen, gehen Sie bitte zu
<http://creativecommons.org/licenses/by-nc-nd/2.5/ch/> oder schicken Sie einen Brief an
Creative Commons, 171 Second Street, Suite 300, San Francisco, California 94105, USA.

Urheberrechtlicher Hinweis

Dieses Dokument steht unter einer Lizenz der Creative Commons
Namensnennung-Keine kommerzielle Nutzung-Keine Bearbeitung 2.5 Schweiz.
<http://creativecommons.org/licenses/by-nc-nd/2.5/ch/>

Sie dürfen:



dieses Werk vervielfältigen, verbreiten und öffentlich zugänglich machen

Zu den folgenden Bedingungen:



Namensnennung. Sie müssen den Namen des Autors/Rechteinhabers in der von ihm festgelegten Weise nennen (wodurch aber nicht der Eindruck entstehen darf, Sie oder die Nutzung des Werkes durch Sie würden entlohnt).



Keine kommerzielle Nutzung. Dieses Werk darf nicht für kommerzielle Zwecke verwendet werden.



Keine Bearbeitung. Dieses Werk darf nicht bearbeitet oder in anderer Weise verändert werden.

Im Falle einer Verbreitung müssen Sie anderen die Lizenzbedingungen, unter welche dieses Werk fällt, mitteilen.

Jede der vorgenannten Bedingungen kann aufgehoben werden, sofern Sie die Einwilligung des Rechteinhabers dazu erhalten.

Diese Lizenz lässt die Urheberpersönlichkeitsrechte nach Schweizer Recht unberührt.

Eine ausführliche Fassung des Lizenzvertrags befindet sich unter
<http://creativecommons.org/licenses/by-nc-nd/2.5/ch/legalcode.de>

**Construction and operation of the EXO-100
cryogenic facility for R & D in liquid xenon:
advances in barium ion tagging**

Inauguraldissertation

der Philosophisch-naturwissenschaftlichen Fakultät
der Universität Bern

vorgelegt von

Sébastien Claude Delaquis

von Rechthalten FR

Leiter der Arbeit:

Prof. Dr. R. S. Gornea

Physikalisches Institut
Albert Einstein Center for Fundamental Physics
Laboratorium für Hochenergiephysik

Von der Philosophisch-naturwissenschaftlichen Fakultät angenommen.

Bern, 29. Oktober 2015

Der Dekan:
Prof. Dr. Gilberto Colangelo

*To my parents Gäse u Fränze,
my brother Dölu Dölux,
and my friends
without whom my life would be nothing but agony.*

Abstract

Neutrinoless double-beta decay is a hypothetical process which, if observed, implies that neutrinos are Majorana particles. Moreover, it is a lepton-number-violating process and thus forbidden in the Standard Model of particle physics. Measuring its half-life would allow the determination of the effective Majorana neutrino mass and shed light on the neutrino mass hierarchy. For decades, experiments have been carried out to search for this process, so far without success. The Enriched Xenon Observatory, EXO, is an ongoing multi-stage project searching for neutrinoless double-beta decay in the isotope ^{136}Xe . As detectors, EXO uses time projection chambers (TPC's) filled with liquid xenon. In the current stage of the project, EXO-200, the two-neutrino double-beta decay of ^{136}Xe allowed in the Standard Model has been discovered; its half-life was found to be $T_{1/2}^{\beta\beta(2\nu)} = 2.165(16) \times 10^{21}$ yr [1]. Furthermore, EXO-200 set a lower limit on the half-life of the neutrinoless double-beta decay $T_{1/2}^{\beta\beta(0\nu)} > 1.1 \times 10^{25}$ yr at 90% C.L. [2]. The next stage of the project, nEXO, is currently being developed. In its first phase, nEXO aims for a sensitivity sufficiently high to survey the complete parameter range of the inverted-neutrino-mass-hierarchy scheme. To further increase sensitivity in the second phase of nEXO, barium ion tagging, a novel background rejection technique, is being developed. The principle of this technique is to identify in real-time the decay product of ^{136}Xe double-beta decay, a single barium ion. This technique would reject all backgrounds not related to double-beta decay, and it is thus considered the ultimate background rejection technique.

The framework of this dissertation achieved both advances in barium ion tagging and R&D for nEXO. This paper presents the construction and operation of the EXO-100 cryogenic facility and a study of ion properties in liquid xenon. EXO-100 is a very versatile facility and was operated with liquid argon, liquid xenon, and liquid tetrafluoromethane (CF_4). To study barium ion tagging, a TPC was constructed and successfully tested in liquid argon. Moreover, high voltage breakdowns in liquid xenon were studied with miniEXO, a miniaturised mock-up of the EXO-200 TPC. The results show a qualitative agreement with finite element simulations and help to understand high voltage problems in EXO-200. During these tests, EXO-100 was equipped with cryo-cameras, which were specifically developed for operation in EXO-100 [3]. Furthermore, the ion properties relevant for barium ion tagging were studied for polonium. To study these properties, EXO-200 data were analysed and the delayed coincidence between ^{222}Rn and ^{218}Po , which is part of the naturally occurring ^{238}U -series, was sought. Clean fully reconstructed events were studied. The ion fraction was measured to be 52(10) %, and no indication was observed of ion neutralisation during drift. This suggests that the ion life-time is large compared to the drift time. The ion drift speed was measured to be $1.4(4) \text{ mm s}^{-1}$ (for a drift field of $380(5) \text{ kV cm}^{-1}$). This confirms results from an analysis of partially reconstructed events, with more statistics, which revealed a behaviour of the ions [4] never observed before. It was shown that the ions have two drift speeds, between which they change with a transition time τ . It was found that τ depends on the purity of the xenon. The present analysis is consistent with these findings.

Contents

Contents	iii
List of tables	vii
List of figures	ix
1 Introduction	1
2 Search for neutrinoless double-beta decay	3
2.1 The neutrino in the Standard Model	3
2.2 Neutrino flavour oscillations	5
2.3 Three ways to determine the absolute neutrino mass	7
2.4 Neutrinoless double-beta decay	11
2.4.1 Double-beta candidate isotopes	14
2.4.2 Detection techniques	15
2.4.3 The time projection chamber	16
3 The Enriched Xenon Observatory	19
3.1 EXO-200	19
3.2 nEXO	23
3.3 Ba-tagging: the ultimate background rejection technique	25
3.3.1 The Ba-tagging techniques	27
3.3.2 Ba ion properties relevant for Ba-tagging	27
3.3.3 The uranium series and the concept of Po-tagging	28
4 The EXO-100 cryogenic R&D facility	31
4.1 The EXO-100 cryostat	33
4.2 The gas handling system	41
4.3 The EXO-100 slow control system	44
4.4 The safety systems and the emergency handling	48
5 The EXO-100 detector	53
5.1 The EXO-100 time projection chamber	53
5.1.1 The detection volume	55
5.1.2 The charge-collection system	58

5.1.3	The light-collection system	62
5.2	Muon veto and muon trigger	64
5.3	DAQ and trigger logic	67
6	The cryo-camera	75
6.1	The design of the cryo-camera	76
6.2	Tests of the cryo-camera	80
6.3	An investigation of high voltage discharges in EXO-200	83
6.3.1	The miniEXO mock-up	83
6.3.2	High voltage tests	84
6.3.3	Simulation of the electric field in the miniEXO	87
6.3.4	Conclusions of the tests with miniEXO	89
7	Ion tracking with EXO-200 data	91
7.1	The fully reconstructed data set	92
7.1.1	The populations in the light-charge map	93
7.2	Fiducial cuts	95
7.2.1	Cut in z	95
7.2.2	Cut in x - y	98
7.2.3	Combined fiducial cuts	103
7.3	Identifying alphas	103
7.4	Event linking	107
7.4.1	Verification of the linking algorithm	109
7.5	Radon-222—polonium-218 pairs	111
7.6	Conclusion of the data analysis	117
8	Conclusions and outlook	119
A	Indium seals	121
B	Cryogenic level meters	127
C	Development of a displacement device	131
D	TPB coating technique	135
E	The performance of EXO-100's muon veto	141
F	EXO-100 event gallery	145
G	The multivariate normal distribution	151
	Bibliography	153
	Acknowledgement	159
	Declaration of consent	161

Curriculum vitae	163
List of publications	165

List of Tables

2.1	Summary of neutrino oscillation parameters.	7
2.2	Best present results on $\beta\beta(0\nu)$ decay.	10
2.3	Summary of the most relevant characteristics of the nine candidates of interest. . .	15
4.1	Overview of the emergency levels of the EXO-100 gas handling system	50
6.1	Specifications of the Logitech HD Webcam C525.	76
6.2	Results of the vacuum tightness test.	80
6.3	Heating power required to maintain the inner unit at a certain target temperature. .	82
6.4	Maximal electric fields in the miniEXO simulations.	89
7.1	The fiducial cut fz applied on the full data set.	97
7.2	The fiducial cut fz applied on the 3σ ^{222}Rn - ^{218}Po region.	98
7.3	The fiducial cut fh applied to the full data set.	102
7.4	The fiducial cut fh applied to the 3σ ^{222}Rn - ^{218}Po region.	102
7.5	The combined cuts applied to the full data set.	103
7.6	The combined cuts applied to the 3σ ^{222}Rn - ^{218}Po region.	103
7.7	The four regions around ^{222}Rn	106
7.8	The four regions around ^{218}Po	106
B.1	Comparison of the two level meter types.	130
D.1	Solutions used for the TPB coatings.	135
E.1	Accidental coincident rate of muon veto.	142
E.2	Accidental coincident rate of muon trigger.	143

List of Figures

2.1	The Standard Model of particle physics.	4
2.2	Feynman diagrams of the neutral current and the charge current.	5
2.3	The three possible mass hierarchy schemes.	8
2.4	The electron energy spectrum of tritium β decay.	9
2.5	Relation between m_{min} and $m_{\beta\beta}$	10
2.6	The two mass parabolas for isobars with $A = 136$	11
2.7	Feynman diagram of the double-beta decay.	12
2.8	Illustration of the spectra of the sum of the electron kinetic energies K_e	13
2.9	Feynman diagrams of the double-beta plus decay modes.	13
2.10	The Q-values of the 35 double-beta candidates.	14
2.11	Basic components and the working principle of a TPC.	16
3.1	The EXO-200 TPC.	20
3.2	Artistic view of the EXO-200 detector.	20
3.3	Location of the EXO-200 detector at WIPP.	21
3.4	EXO-200 energy spectra.	22
3.5	Sensitivity of EXO-200.	23
3.6	Artistic view of a nEXO detector concept.	23
3.7	Location of nEXO in SNOLAB and the muon flux at this depth.	24
3.8	Sensitivity of nEXO.	24
3.9	Sensitivity of nEXO with Ba-tagging.	25
3.10	Excitation levels of singly ionized barium.	26
3.11	The fluorescence power of Ba^+ in arbitrary units versus time.	26
3.12	Extract from the uranium series.	28
4.1	Photograph of the EXO-100 set-up.	32
4.2	Schematic view of the EXO-100 cryostat.	33
4.3	Photograph and CAD render of the inner cryostat.	34
4.4	Photographs of the different lids.	35
4.5	Heat transfer simulation of the EXO-100 cryostat.	36
4.6	Photographs of the upper section of the inner chamber.	37
4.7	Photographs of the interface box.	38
4.8	Photograph and CAD render of the liquid nitrogen tank.	39
4.9	Photograph of the outer vacuum vessel.	39

4.10	Photograph made during the closing of the cryostat.	40
4.11	Photographs of the super insulation coat.	41
4.12	Scheme of the gas handling system with the gas flow for tasks.	42
4.13	Photograph of the gas handling system.	43
4.14	Scheme of the argon handling system.	44
4.15	Photograph of the EXO-100 control centre.	44
4.16	The "Temperature" window of the EXO-100 slow control program.	45
4.17	The "LN2 Level" window of the EXO-100 slow control program.	46
4.18	The "Valve Control" window of the EXO-100 slow control program.	47
4.19	The "Power Output" window of the EXO-100 slow control program.	47
4.20	The main window of the EXO-100 slow control program.	48
4.21	Scheme of the gas handling system with the gas flow for emergency levels.	49
4.22	Photograph of the safety system control.	50
4.23	Balloon installation.	51
5.1	Cutaway CAD render of the EXO-100 cryostat.	54
5.2	The EXO-100 TPC.	55
5.3	Sketch of the field cage and the charge-collecting system.	56
5.4	Simulation of electro-statics in the EXO-100 TPC.	57
5.5	The high voltage circuit of the EXO-100 detector.	57
5.6	The resistive voltage divider.	58
5.7	Typical signals after amplification.	59
5.8	A muon event in EXO-100.	60
5.9	The wire planes of the charge-collecting system.	61
5.10	Photographs of the cabling of the TPC.	61
5.11	The emission spectra of TPB and the sensitivity curve of the R6237-01 MOD PMT.	62
5.12	The reflectors and wave length shifter of the light-collecting system.	63
5.13	The light-collecting system without the reflectors and the field cage.	63
5.14	CAD render and photographs of the muon veto.	64
5.15	Photograph of the muon veto's electronic crates.	65
5.16	Diagram of the muon veto scheme.	66
5.17	The electronics of the data acquisition system and the trigger scheme.	68
5.18	Diagram of the trigger logic.	69
5.19	Two events triggered by the internal alpha event trigger.	70
5.20	Two events triggered by the muon trigger.	71
5.21	Two events triggered by the source trigger.	72
6.1	Photograph of the cryo-camera.	76
6.2	CAD render and photograph of the inner unit.	77
6.3	Photograph of the inner unit wrapped super insulation.	77
6.4	Cutaway view of the cryo-camera	78
6.5	Exploded view of the vacuum tight camera body	78
6.6	Photograph of the gas purifying system.	79
6.7	Photograph of the EXO-100 detector with the mounted cryo-camera.	80
6.8	Temperature of the inner unit and the required heating power.	81
6.9	Picture taken with the cryo-camera while immersed in liquid nitrogen.	82

6.10	Picture taken with the cryo-camera while installed in the EXO-100 cryostat.	83
6.11	Photographs of miniEXO and of EXO-200.	84
6.12	Photographs of the cryo-cameras and miniEXO.	85
6.13	Electrical diagram of the high voltage tests.	86
6.14	Photographs of discharges in miniEXO.	86
6.15	Renders of miniEXO.	87
6.16	Simulation of the electric field in miniEXO.	88
7.1	Charge-light maps of EXO-200 data.	92
7.2	Charge-light maps of EXO-200 data.	93
7.3	Charge-light maps of sliced EXO-200 data.	94
7.4	EXO-200 data: position of all charge clusters.	94
7.5	Histogram of the z -coordinate of all CC's.	95
7.6	Histogram of the z -coordinate of the CC's close to the cathode.	96
7.7	Histogram of the z -coordinate of the CC's close to an anode.	96
7.8	The cathode is not located exactly at $z = 0$	97
7.9	The radioactivity at the cathode.	98
7.10	Histogram of the x coordinates.	98
7.11	The coordinate systems in EXO-200.	99
7.12	Artefact in the position reconstruction.	99
7.13	Chess board like pattern originating from the wire triplets.	100
7.14	Reconstructed position of CC's detected with only one U and one V wire.	100
7.15	Reconstructed position of CC's detected with 3 and 4 wires.	101
7.16	Hexagonal cut in the x - y plane.	101
7.17	Irregular hexagonal cut in the x - y plane.	102
7.18	Charge-light maps of EXO-200 data after applying cuts.	104
7.19	The ^{222}Rn and ^{218}Po populations with fit.	104
7.20	The theoretical distributions in the α region.	105
7.21	The theoretical distributions in the 3σ ^{218}Po region.	105
7.22	The four regions around ^{222}Rn	106
7.23	The four regions around ^{218}Po	106
7.24	The charge-light relation for α events.	107
7.25	The one dimensional linking probability function.	109
7.26	Test of the linking algorithm in the charge light map.	110
7.27	Test of the linking algorithm with the decay time.	110
7.28	The position of the mother and daughter decays.	111
7.29	Arrows showing the displacement of the polonium.	112
7.30	Arrows showing the drift speed of the polonium.	113
7.31	Histogram of the z -component of polonium's drift speed.	114
7.32	Histogram of the z -component of polonium's drift speed with applied 'fair cut'.	114
7.33	Dependence of the drift speed on the drift time.	115
7.34	Dependence of the drift speed on the drift time (full data set).	116
7.35	Dependence of the reaction time on the xenon purity.	116
7.36	Arrows showing the displacement between the ^{218}Po and ^{214}Po decay.	117
A.1	Cross section view of the groove of an indium seal.	121

A.2	Schematic view of pressure cones in a flange connection.	122
A.3	Simulation of mechanical stress and pressure on a sealing surface.	123
A.4	Simulation of mechanical stress and strain of a bolt assembly.	124
A.5	An example of an indium seal.	125
B.1	The design of the capacitive level meter probe.	128
B.2	Two designs of a RLM probe.	129
B.3	The read-out circuit of the RLM.	129
C.1	Two displacement devices made with different rail designs.	131
C.2	Photographs of the mono-rail mock-up.	132
C.3	Photographs of the current version of the displacement device.	132
C.4	Measurement of the power required to drive the displacement device.	133
D.1	Photographs of the TPB coating on glass.	136
D.2	Photographs of the TPB coating on acrylic glass.	137
D.3	Photographs of a TPB coating on Teflon before and after a cryogenic test.	137
D.4	Photographs of the UVO surface treatment.	138
D.5	Photograph of a Teflon sample coated with the pure solution.	139
F.1	Muon tracks recorded with EXO-100.	145
F.2	Moun events recorded with EXO-100.	146
F.3	Muon events recorded with EXO-100.	147
F.4	Electro magnetic showers recorded with EXO-100.	148
F.5	Electro magnetic showers recorded with EXO-100.	149
F.6	Electro magnetic showers recorded with EXO-100.	150

Introduction

The Standard Model of particle physics (SM) was developed in the second half of the 20th century. Since its early days, the SM has had to be extended several times (e.g. to include the third generation of leptons). Nevertheless, the SM has proven a great success. It unifies three of the four known forces, the electromagnetic force, the weak force, and the strong force, and it incorporates all of the known sub-atomic particles. In 2012, the last particle predicted by the SM, the Higgs boson, was found with the LHC at CERN by the ATLAS [5] and the CMS [6] experiments.

Despite the great success of the SM, several questions remain unanswered. The SM does not incorporate the gravitational force, nor does it offer any particle suited as candidate for dark matter. Baryon asymmetry is not explained by the SM, and the coupling constant of all particles to the Higgs field — determining their masses — are free parameters. Furthermore, the neutrino sector is not fully explored in the SM. The study of neutrinos could reveal CP violation in the lepton sector and thus give us information on the origin of baryon asymmetry or even lead to physics beyond the SM. For these reasons, the neutrino sector is particularly interesting, and thus, a world-wide effort has been devoted to the study of neutrino physics.

Initially, neutrinos were introduced into the SM as massless particles. Our understanding of neutrinos has since evolved. From neutrino oscillation experiments, we learned that neutrinos oscillate between their flavours and thus violate lepton flavour number. Neutrino oscillations are only possible if their flavour eigenstates are super-positions of their mass eigenstates and if all mass eigenstates have unequal masses. Therefore, neutrino oscillation experiments show that neutrinos are massive. However, these experiments are only sensitive to differences in squared masses and not to the absolute masses themselves nor to the mass hierarchy, the question how the mass eigenstates are ordered by mass.

There are three complementary approaches to the measurement of the absolute neutrino mass. Currently, the most stringent limit on the neutrino mass is given by cosmology — based on measurements of the anisotropies of the primordial microwave background. However, these results are highly model dependent. The direct approach includes the study of the kinematics of weak decays and time-of-flight measurements from neutrinos emitted in supernovae. The third approach is the search for neutrinoless double-beta decay. Neutrinoless double-beta decay is a hypothetical

nuclear reaction. If observable, measuring its half-life would allow the determination of the effective neutrino mass and provide hints on the mass hierarchy. Moreover, in the neutrinoless double-beta decay the total lepton number, as well as the lepton flavour number, is violated by $\Delta L = \pm 2$. Thus, detection of this reaction would show that the lepton number is not conserved in nature. Neutrinoless double-beta decay can only occur if neutrinos are Majorana particles (i.e. they are their own antiparticles).

Since the first theoretical formulation of *neutrinoless double-beta decay* $\beta\beta(0\nu)$ by Furry in 1939 [7], numerous experiments have been conducted to search for this nuclear process. So far, these experiments have only yielded limits on the half-life of this process for various isotopes. The *Enriched Xenon Observatory EXO* is an ongoing experiment searching for the neutrinoless double-beta decay of ^{136}Xe . The *two-neutrino double-beta decay* $\beta\beta(2\nu)$ of ^{136}Xe was measured for the first time with the current set-up, EXO-200. This measurement is currently the most precise measured half-life of any $\beta\beta(2\nu)$ decay [1]; it is also the slowest process ever observed directly. This discovery settled a long-standing discrepancy between limits and theory predictions. Moreover, using EXO-200 pushed the limit on the $\beta\beta(0\nu)$ in ^{136}Xe up to $T_{1/2}^{0\nu} > 1.1 \times 10^{25}$ yr at 90% C.L [2]. While in future some improved results can be expected from EXO-200, a next phase set-up, the *next Enriched Xenon Observatory nEXO*, is under development. With nEXO, the sensitivity can be increased by more than two orders of magnitude in terms of half-life. To increase the sensitivity yet further, barium ion tagging, a novel background rejection technique, is being developed. The principle of this technique is to identify in real-time the decay product of ^{136}Xe double-beta decay, a single barium ion. This technique would reject all backgrounds not related to double-beta decay, and it is thus considered the ultimate background rejection technique.

The framework of this dissertation achieved both advances in barium ion tagging and R&D for nEXO. This paper presents the construction and operation of the EXO-100 cryogenic facility and a study of ion properties in liquid xenon. EXO-100 is a very versatile facility and was operated with liquid argon, liquid xenon, and liquid tetrafluoromethane (CF_4). To study barium ion tagging, a TPC was constructed and successfully tested in liquid argon. Moreover, high voltage breakdowns in liquid xenon were studied with miniEXO, a miniaturised mock-up of the EXO-200 TPC. The results show a qualitative agreement with finite element simulations and help to understand high voltage problems in EXO-200. During these tests, EXO-100 was equipped with cryo-cameras, which were specifically developed for operation in EXO-100 [3]. Furthermore, the ion properties relevant for barium ion tagging were studied for polonium. To study these properties, EXO-200 data were analysed and the delayed coincidence between ^{222}Rn and ^{218}Po , which is part of the naturally occurring ^{238}U -series, was sought. Clean fully reconstructed events were studied. The ion fraction was measured to be 52(10) %, and no indication was observed of ion neutralisation during drift. This suggests that the ion life-time is large compared to the drift time. The ion drift speed was measured to be 1.4(4) mm s⁻¹ (for a drift field of 380(5) kV cm⁻¹). This confirms results from an analysis of partially reconstructed events, with more statistics, which revealed a behaviour of the ions [4] never observed before. It was shown that the ions have two drift speeds, between which they change with a transition time τ . It was found that τ depends on the purity of the xenon. The present analysis is consistent with these findings.

Search for neutrinoless double-beta decay

This Chapter provides a brief theoretical motivation for the search for neutrinoless double-beta decay. A detailed dealing with the theory of particle physics [8, 9], massive neutrinos [10, 11, 12, 13], and double-beta decay [14, 15] can be found elsewhere.

2.1	The neutrino in the Standard Model	3
2.2	Neutrino flavour oscillations	5
2.3	Three ways to determine the absolute neutrino mass	7
2.4	Neutrinoless double-beta decay	11
2.4.1	Double-beta candidate isotopes	14
2.4.2	Detection techniques	15
2.4.3	The time projection chamber	16

2.1 The neutrino in the Standard Model

In 1927, Ellis and Wooster used a calorimeter to measure the energy released by a radium-E source — ^{210}Bi , a beta emitter [16]. They correctly concluded that the average energy of the electron released in this process is below the Q-value —the difference in energy between the mother nuclei and the daughter nuclei. However, this result was not in agreement with the laws of energy and angular momentum conservation. In 1930, Pauli predicted a neutral particle with spin 1/2 — which was later found to be the neutrino — to re-establish conservation of energy and angular momentum. This particle would have left the calorimeter of Ellis and Wooster undetected; carrying away the missing energy and angular momentum. In 1956, the neutrino — in fact the electron anti-neutrino — was discovered by Reines and Cowan [17].

Since the discovery of the first neutrino, our understanding of these particles has improved. Nowadays, we know that three lepton generations exist — electron (e^- , e^+ , ν_e , and $\bar{\nu}_e$), muon

$(\mu^-, \mu^+, \nu_\mu, \text{ and } \bar{\nu}_\mu)$, and tau $(\tau^-, \tau^+, \nu_\tau, \text{ and } \bar{\nu}_\tau)$ — each with its neutrino and anti-neutrino (see Figure 2.1). Neutrinos are neutral and do not participate in the electromagnetic nor in the strong interaction. They have tiny masses and interact gravitationally, although in particle physics (in particular in the SM) gravity is neglected due to its weakness and complexity. Consequently, neutrinos effectively interact only via the weak interaction.

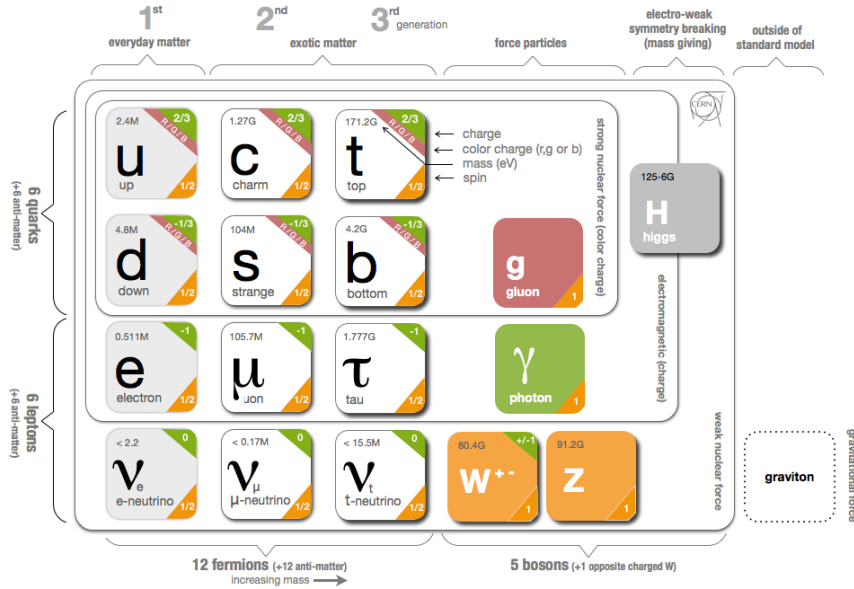


Figure 2.1: A schematic view of all matter particles and force mediators in the Standard Model of particle physics (graphic from [18]).

The experiment by Wu in 1956 [19] — following the proposal by Lee and Yang [20] — proved that the weak interaction violates parity. Parity violation in the weak interaction turned out to be maximal — i.e. in the ultra relativistic limit, as well as for massless particles, the weak interaction couples only to left handed particles and right handed anti-particles. Therefore, in the SM the leptons with left chirality are grouped in weak isospin doublets and those with right chirality in weak isospin singlets

$$\begin{pmatrix} e \\ \nu_e \end{pmatrix}_L, \begin{pmatrix} \mu \\ \nu_\mu \end{pmatrix}_L, \begin{pmatrix} \tau \\ \nu_\tau \end{pmatrix}_L, e_R, \mu_R, \tau_R. \quad (2.1)$$

The electromagnetic force couples equally to the left and right electrically charged chirality states — in the electromagnetic interaction parity is conserved. However, the weak interaction only couples to the left chirality doublets — parity is maximally violated. In the SM the neutrinos are massless and the right chirality states of the neutrino do not need to exist. In the SM, neutrinos couple only to the W^\pm bosons — *Charged Current CC* interactions — and Z boson — *Neutral Current NC* interactions. Hence, all neutrino interactions are described by two terms of the Lagrangian (2.2 & 2.3) and the corresponding Feynman diagrams (see Figure 2.2).

$$-\mathcal{L}_{CC} = \frac{g}{\sqrt{2}} \sum_l \bar{\nu}_{Ll} \gamma^\mu l_L^- W_\mu^+ + h.c. \quad (2.2)$$

$$-\mathcal{L}_{NC} = \frac{g}{2 \cos(\theta_W)} \sum_l \bar{\nu}_{Ll} \gamma^\mu \nu_{Ll} Z_\mu^0 \quad (2.3)$$

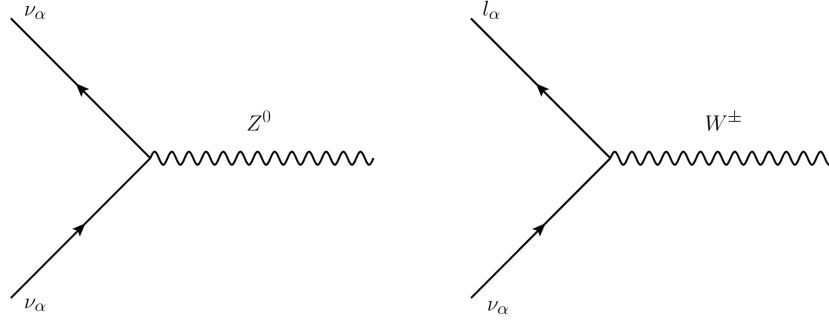


Figure 2.2: Feynman diagrams of the two neutrino interactions. Left, the neutral current and right the charge current.

In the SM the neutrinos are strictly massless particles. However, from neutrino oscillation experiments we know that neutrinos are massive. Therefore, the SM needs to be extended.

2.2 Neutrino flavour oscillations

Neutrino oscillations is the process in which a neutrino is emitted in flavour state α and later detected in a different flavour state β . This process violates the lepton flavour number, however, the total lepton number remains conserved. In order for neutrino oscillations to occur, the neutrino flavour eigenstates need to be super-positions of their mass eigenstates — and vice versa:

$$|\nu_\alpha\rangle = \sum_i U_{\alpha i}^* |\nu_i\rangle \quad (2.4)$$

$$|\nu_i\rangle = \sum_\alpha U_{\alpha i} |\nu_\alpha\rangle \quad (2.5)$$

where $|\nu_\alpha\rangle$ are the flavour eigenstates ($\alpha \in \{e, \mu, \tau\}$), $|\nu_i\rangle$ are the mass eigenstates ($i \in \{1, 2, 3\}$) with the mass m_i , and $U_{\alpha i}$ are elements of the *Pontecorvo-Maki-Nakagawa-Sakata PMNS* mixing matrix. U is a 3 dimensional unitary matrix

$$U = \begin{bmatrix} c_{12}c_{13} & s_{12}c_{13} & s_{13}e^{-i\delta} \\ -s_{12}c_{23} - c_{12}s_{23}s_{13}e^{i\delta} & c_{12}c_{23} - s_{12}s_{23}s_{13}e^{i\delta} & s_{23}c_{13} \\ s_{12}s_{23} - c_{12}c_{23}s_{13}e^{i\delta} & -c_{12}s_{23} - s_{12}c_{23}s_{13}e^{i\delta} & c_{13}c_{23} \end{bmatrix} \begin{bmatrix} 1 & 0 & 0 \\ 0 & e^{i\alpha_1/2} & 0 \\ 0 & 0 & e^{i\alpha_2/2} \end{bmatrix}. \quad (2.6)$$

where s_{ij} , c_{ij} , δ , α_1 , and α_2 denote $\sin(\theta_{ij})$, $\cos(\theta_{ij})$, CP-violating phase, and two Majorana phases, respectively. Hence, U is parametrised by 3 angles (θ_{12} , θ_{13} , and θ_{23}) and 3 phases (δ , α_1 , and α_2). For clarity, U can be decomposed into sub-matrices

$$U = \begin{bmatrix} 1 & 0 & 0 \\ 0 & c_{23} & s_{23} \\ 0 & -s_{23} & c_{23} \end{bmatrix} \begin{bmatrix} c_{13} & 0 & s_{13}e^{-i\delta} \\ 0 & 1 & 0 \\ -s_{13}e^{i\delta} & 0 & c_{13} \end{bmatrix} \begin{bmatrix} c_{12} & s_{12} & 0 \\ -s_{12} & c_{12} & 0 \\ 0 & 0 & 1 \end{bmatrix} \begin{bmatrix} 1 & 0 & 0 \\ 0 & e^{i\alpha_1/2} & 0 \\ 0 & 0 & e^{i\alpha_2/2} \end{bmatrix}. \quad (2.7)$$

The probability to detect a neutrino as flavour β when created as flavour α (the so-called oscillation probability) depends on its energy E and the distance travelled L [21]

$$P(\nu_\alpha \rightarrow \nu_\beta) = \left| \sum_i U_{\alpha i} U_{\beta i}^* e^{-i\frac{m_i^2}{2E}L} \right|^2 \quad (2.8)$$

$$= \sum_i |U_{\alpha i} U_{\beta i}^*|^2 + \Re \sum_i \sum_{j \neq i} U_{\alpha i} U_{\beta i}^* U_{\alpha j}^* U_{\beta j} e^{i\frac{|\Delta m_{ij}^2|L}{2E}} \quad (2.9)$$

where $\Delta m_{ij}^2 = m_i^2 - m_j^2$. In Eq. 2.8 one can see that the oscillation probability — which is what neutrino oscillation experiments measure — depends on $\frac{L}{E}$ and on $|\Delta m_{ij}^2|$. For oscillations to occur, at least two masses must be different. If all three masses are different, the phase δ could lead to an observable CP violation. However, the oscillation probability is independent of the two Majorana phases $\alpha_{1,2}$ and the absolute mass of the neutrinos. Hence, these parameters cannot be determined from neutrino oscillation experiments.

Neutrino oscillations have been initially suggested by several experiments. In 1964, Davis measured with his Cl experiment [22] a deficit in the solar ν_e neutrino flux predicted by the *standard solar model SSM* —substantiating the so-called solar neutrino puzzle. This deficit was confirmed for solar neutrinos at lower energies by the *Gallium Experiment GALLEX* [23] and the *Soviet-American Gallium Experiment SAGE* [24].

In 1996, the Super-Kamiokande experiment measured an unexpected dependence of the atmospheric ν_μ neutrino flux on the zenith angle [25, 26], and thus, the distance. This was explained in terms of oscillations, namely, ν_μ disappearance. This observation explained the deficit in the solar neutrino flux — the solar neutrino puzzle was solved.

In 2001, the *Sudbury Neutrino Observatory SNO* experiment published its results on the study of ^8B solar neutrinos [27]. SNO was capable of measuring the total neutrino flux and the flux of electron neutrinos. The results showed that the total ^8B solar neutrino flux is in agreement with the SSM and that indeed a large fraction of the neutrinos must have changed their flavour from ν_e to another flavour due to oscillation. Thereafter this was confirmed by the *Kamioka Liquid Scintillator Antineutrino Detector KamLAND* experiment which measured a reduced $\bar{\nu}_e$ neutrino flux at a large distance from several nuclear reactors.

Parameter	Best fit	2σ range (90% C.L.)
Δm_{21}^2 [$10^{-5}eV^2$]	7.62	7.27 – 8.01
$ \Delta m_{31}^2 $ [$10^{-3}eV^2$]	2.55	2.38 – 2.68
	2.43	2.29 – 2.58
$\sin^2\theta_{12}$	0.320	0.29 – 0.35
$\sin^2\theta_{23}$	0.613	0.38 – 0.66
	0.600	0.39 – 0.65
$\sin^2\theta_{13}$	0.0246	0.019 – 0.030
	0.0250	0.020 – 0.030
δ	0.8π	$0 - 2\pi$
	-0.03π	

Table 2.1: Summary of neutrino oscillation parameters. The upper (lower) row corresponds to normal (inverted) neutrino mass hierarchy (extract from [28]). Solar neutrino oscillation experiments measure Δm_{21}^2 , while, atmospheric neutrino oscillation experiments measure $|\Delta m_{32}^2|$ ($\approx |\Delta m_{31}^2|$).

Experiments with intense accelerator neutrino beams — such as *KEK To Kamioka K2K*, *Tokat To Kamioka T2K*, and *Oscillation Project with Emulsion tRacking Apparatus OPERA* — allowed for improved measurements of the oscillation parameters. The current best fit results of these parameters is given in Table 2.1. Moreover, OPERA showed that muon neutrinos oscillate predominantly to tau neutrinos.

The $|\Delta m_{ij}^2|$ determined by oscillation experiments do not allow to identify which mass eigenstate ν_i is the lightest nor how massive it is. Therefore, three mass hierarchy schemes are possible (see Figure 2.3). In case of the normal-hierarchy, the lightest mass eigenstate is ν_1 . In case of the inverted-hierarchy, ν_3 is the lightest state. In the third scheme, the lightest neutrino’s mass squared is large compared with the mass squared differences — $m_i^2 \gg 10^{-3} eV^2$. Consequently, all neutrinos have a similar mass. This scheme is called quasi-degenerate hierarchy.

2.3 Three ways to determine the absolute neutrino mass

To determine the absolute neutrino mass scale, as well as the mass hierarchy, input from different types of experiments is required. They can be categorised into three groups. Experiments of the first type derive the neutrino masses indirectly from measurements of the cosmic microwave background — e.g. COBE, WMAP, and PLANCK — in conjunction with redshift survey’s — e.g. SDSS [29, 30]. These experiments are sensitive to matter density in the universe, and thus,

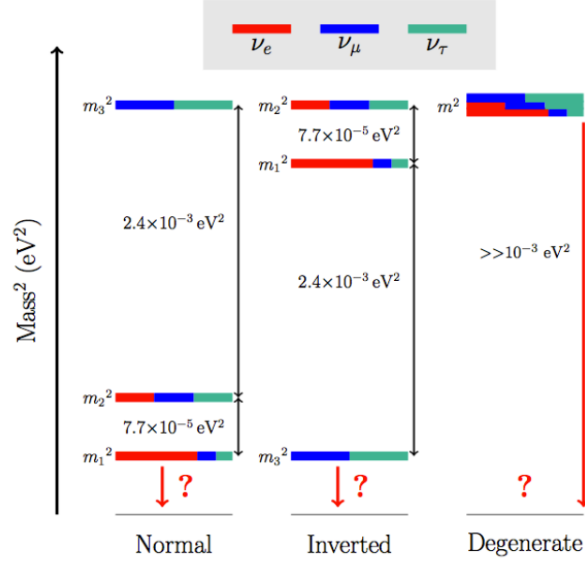


Figure 2.3: The three possible mass hierarchy schemes. The mass of the lightest neutrino is unknown.

to the sum of the neutrino masses

$$M = \sum_i m_{\nu_i}. \quad (2.10)$$

Combined, these experiments give presently the strongest limit on the sum of the neutrino masses [31]

$$\sum m_\nu < 0.23 \text{ eV (95\% C.L.)}. \quad (2.11)$$

Experiments of the second type measure the neutrino mass directly by studying neutrinos from supernovae or studying low energy beta decays [32]. These experiments are sensitive to the effective electron neutrino mass

$$m_{\nu_e}^{2(\text{eff})} = \sum_i |U_{ei}|^2 m_i^2. \quad (2.12)$$

However, current experiments are only sensitive to the degenerated mass region, where all three masses are nearly equal.

Various experiments measured the energy versus time of arrival of neutrinos from the supernova SN1987A [33]. They were able to measure the electron neutrino mass squared

$$m_{\nu_e}^2 = 4_{-63}^{+28} \text{ eV}^2. \quad (2.13)$$

Due to low statistics and the systematic uncertainties, this result is compatible with vanishing neutrino masses.

Experiments studying low energy beta decays — such as ${}^3\text{H} \rightarrow {}^3\text{He} + e^- + \bar{\nu}_e$ — measure the energy spectrum of the emitted electron. The spectrum close to the endpoint depends on neutrino mass (see Figure 2.4). The two favourable candidates are ${}^3\text{H}$ (tritium) and ${}^{187}\text{Re}$ with Q -values of 18.6 keV and 2.6 keV, respectively. Current experiments are *KATRIN* and *Project 8* using ${}^3\text{H}$ and *MARE* using ${}^{187}\text{Re}$.

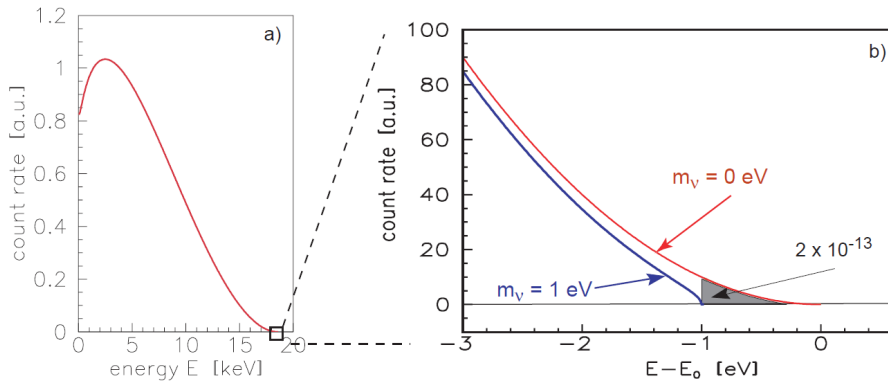


Figure 2.4: The electron energy spectrum of tritium β decay: (a) complete and (b) narrow region around endpoint E_0 . The β spectrum is shown for neutrino masses of 0eV and 1eV (graph and caption from [34]).

The best results on the effective electron neutrino mass are given by the Troitsk Nu-Mass [35] and the Mainz [36] experiments

$$m_{\nu_e} < 2.05 \text{ eV (95\% C.L.)}. \quad (2.14)$$

Experiments of the third type searches for the hypothetical neutrinoless double-beta decay. This approach is discussed in details in Section 2.4. These experiments are sensitive to the effective Majorana neutrino mass given by

$$\langle m_{\beta\beta} \rangle^2 = \left| \sum_i^N U_{ei}^2 m_i \right|^2 = \left| \sum_i^N |U_{ei}|^2 e^{\alpha_i} m_i \right|^2. \quad (2.15)$$

This quantity vanishes for Dirac neutrinos, but can take a finite value if neutrinos are Majorana particles. Moreover, neutrinoless double-beta decay is the only process sensitive to the Majorana phases α_i , and, to the nature of the neutrinos. The other processes yield the same result independently of the neutrino nature – Dirac or Majorana. In this sense, the search for neutrinoless double-beta decay is complementary to the other approaches. Presently, the best limits on the effective Majorana neutrino mass are given in Table 2.2.

Isotope	$T_{1/2}$ [yr]	$\langle m_{\beta\beta} \rangle$ [eV]	Experiment
^{76}Ge	$> 2.1 \cdot 10^{25}$	$< 0.25 - 0.62$	GERDA-I
^{100}Mo	$> 1.1 \cdot 10^{24}$	$< 0.34 - 0.87$	NEMO-3
^{130}Te	$> 2.8 \cdot 10^{24}$	$< 0.31 - 0.76$	CUORICINO
^{136}Xe	$> 1.9 \cdot 10^{25}$	$< 0.14 - 0.34$	KamLAND-Zen

Table 2.2: Best present results on $\beta\beta(0\nu)$ decay (limits at 90% C.L.). Table and caption from [37]. A range is presented due to the uncertainties in the nuclear matrix elements.

In combination with data from other experiments, the discovery of neutrinoless double-beta decay could clarify the mass hierarchy (see Figure 2.5). If $m_{\beta\beta} > 5 \cdot 10^{-2}$ eV, the quasi degenerate-hierarchy is realised in nature. In case $5 \cdot 10^{-2}$ eV $> m_{\beta\beta} > 1 \cdot 10^{-2}$ eV, additional information from e.g. cosmology is required. If these experiments are able to exclude $m_{\min} > 1 \cdot 10^{-2}$ eV, the inverted-hierarchy is realised. And, in case $m_{\beta\beta} < 1 \cdot 10^{-2}$ eV, the normal-hierarchy is realised. However, due to the Majorana phases, the summands in 2.15 could cancel each other and lead to $m_{\beta\beta} = 0$ — only for the normal-hierarchy — hence, $\beta\beta(0\nu)$ would not occur.

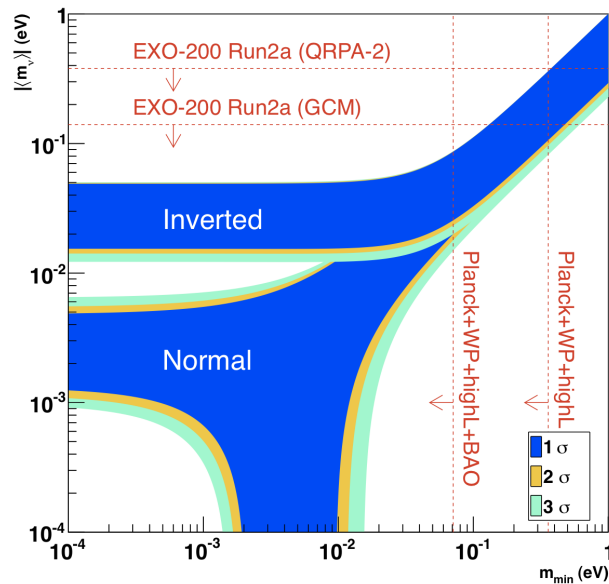


Figure 2.5: The effective Majorana neutrino mass $m_{\beta\beta}$ as a function of the lightest neutrino mass m_{\min} . The current bounds from $\beta\beta(0\nu)$ experiments limits the parameter space from top to bottom while the bound from cosmology, beta decay, and time-of-flight experiments limit the parameter space from right to left. IS denotes the inverted-hierarchy and NS the normal-hierarchy.

2.4 Neutrinoless double-beta decay

Double-beta decay is a rare nuclear process first described by M. Goeppert-Mayer [38]. In the *two-neutrino decay mode* $\beta\beta(2\nu)$ two neutrons of a nucleus decay into two protons with the emission of two electrons and two electron anti-neutrinos (see Figure 2.7),

$${}^A_Z X \rightarrow {}^A_{Z+2} Y + 2e^- + 2\bar{\nu}_e \quad (2.16)$$

where A is the number of nucleons and Z the number of protons in the parent nucleus X . Double-beta decay is a second order weak process, and thus, its decay rate is extremely small — measured half-lives range from 7.1×10^{18} yr to 7.2×10^{24} yr for the isotopes ^{100}Mo and ^{128}Te , respectively.

In the SM, $\beta\beta(2\nu)$ is an allowed process and many isotopes are predicted to undergo it. However, double-beta decay can only be observed in isotopes for which single beta decay is energetically forbidden or — for the two special cases ^{48}Ca and ^{96}Zr — spin suppressed.

For even-even nuclei — nuclei with an even number of protons and an even number of neutrons — the nuclear pairing interaction naturally filters these two transitions. The pairing interaction splits the mass parabola in two (see Figure 2.6). One parabola for the stronger bound even-even nuclei and one for the less bound odd-odd nuclei. In some cases this leads to the circumstance that a nuclei would be less bound after single beta decay, hence this process is forbidden. This is the case for ^{136}Xe . It is stronger bound than ^{136}Cs . The daughter nucleus for double-beta decay however — ^{136}Ba — is bound more strongly, and double beta decay is energetically possible.

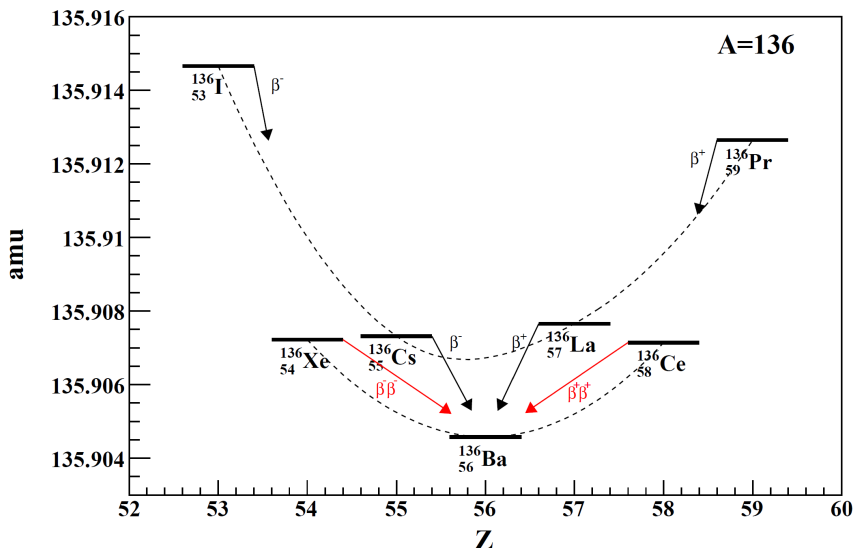


Figure 2.6: The two mass parabolas for isobars with $A = 136$. For ^{136}Xe the beta transition to ^{136}Cs is energetically forbidden, however, it can double-beta decay to ^{136}Ba (figure from [39]).

A different, however hypothetical, decay mode is the *neutrinoless double-beta decay* $\beta\beta(0\nu)$ (see Figure 2.7)

$${}^A_Z\text{X} \rightarrow {}^A_{Z+2}\text{Y} + 2e^-. \quad (2.17)$$

In contrast to the $\beta\beta(2\nu)$, this decay mode is not allowed in the SM. It violates the total lepton number by $\Delta L = \pm 2$ and can only occur if the neutrino is a Majorana particle. Its decay rate is given as

$$\frac{1}{T_{1/2}^{0\nu}} = G^{0\nu} \cdot |M^{0\nu}|^2 \cdot \langle m_\nu \rangle^2 \quad (2.18)$$

where $T_{1/2}^{0\nu}$ is the half live, $G^{0\nu}$ the phase space factor, $M^{0\nu}$ the nuclear matrix element, and $\langle m_\nu \rangle$ the effective Majorana neutrino mass. The phase space factor can be calculated exactly, knowing the energy released in the decay (Q value).

However, the nuclear matrix element is model dependent and can only be calculated approximately. Hence, if $T_{1/2}^{0\nu}$ is measured, one can derive the effective Majorana neutrino mass within the uncertainties of the nuclear matrix element.

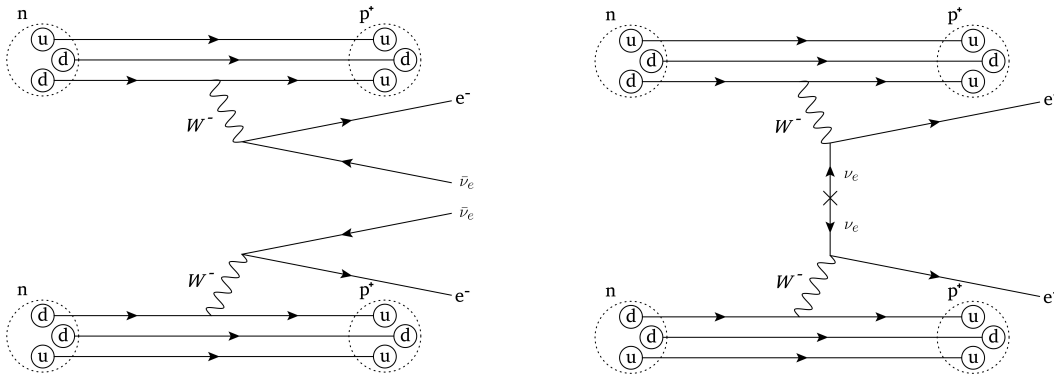


Figure 2.7: Feynman diagram of the double-beta decay. Left, the in the SM allowed $\beta\beta(2\nu)$ decay mode. Right, the hypothetical $\beta\beta(0\nu)$ decay mode.

Experimentally, $\beta\beta(0\nu)$ can be distinguished using $\beta\beta(2\nu)$ only by the energy spectrum of the emitted electrons (see Figure 2.8). In the $\beta\beta(2\nu)$ decay mode, some energy is given to the two neutrinos, and hence — like in the beta decay — the electron energy spectrum is continuous. In contrast, in the $\beta\beta(0\nu)$ decay mode the full energy is given to the two electrons. The sum of the kinetic energy of these electrons corresponds to the Q-value.

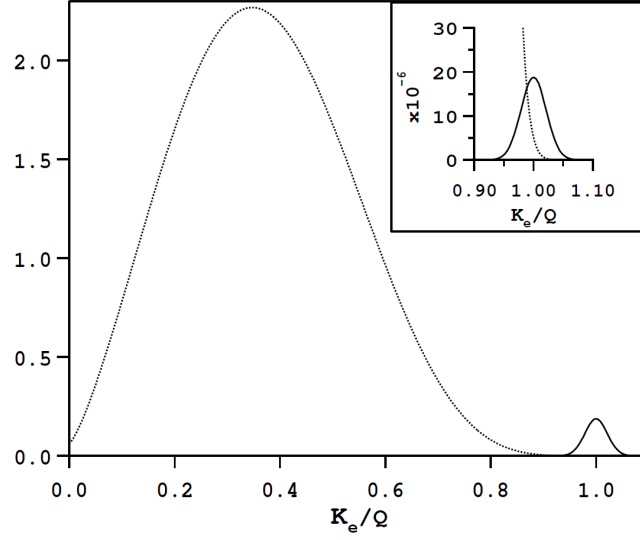


Figure 2.8: Illustration of the spectra of the sum of the electron kinetic energies K_e (Q is the endpoint) for the $\beta\beta(2\nu)$ normalised to 1 (dotted curve) and $\beta\beta(0\nu)$ decays (solid curve). The $\beta\beta(0\nu)$ spectrum is normalised to 10^2 (10^6 in the figure inset). All spectra are convoluted with an energy resolution of 5%, representative of several experiments. Graph and caption from [15].

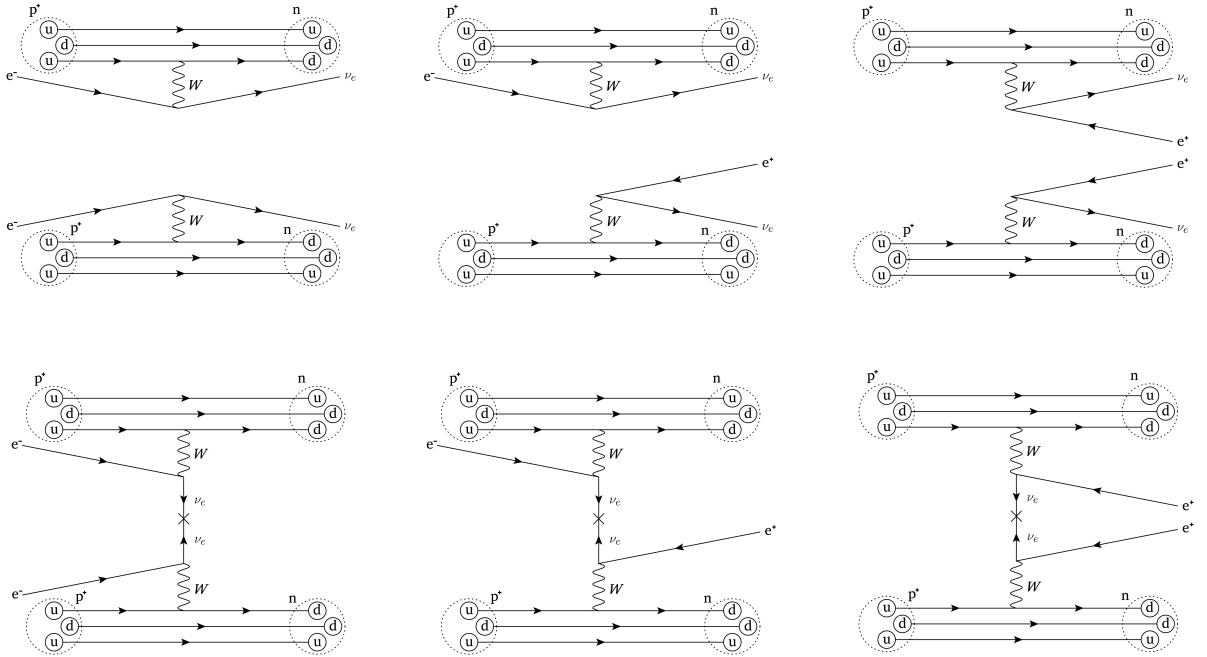


Figure 2.9: Feynman diagrams of the double-beta plus decay modes. Top, the in the SM allowed two neutrino modes. Bottom, the corresponding hypothetical neutrinoless modes. From left to right, double-electron capture $\epsilon\epsilon$, electron capture positron emission $\epsilon\beta^+$, and double-beta plus decay $\beta^+\beta^+$.

A process related to $\beta\beta$ is the double-beta-plus decay $\beta^+\beta^+$. Analogue to the single-beta-plus decay, competing decay modes are *double-electron capture* $\epsilon\epsilon$ and electron capture positron emission $\epsilon\beta^+$. This process has three decay modes with two neutrinos $\beta^+\beta^+(2\nu)$, $\epsilon\beta^+(2\nu)$, and $\epsilon\epsilon(2\nu)$ and three — in the SM forbidden — neutrinoless modes $\beta^+\beta^+(0\nu)$, $\epsilon\beta^+(0\nu)$, and $\epsilon\epsilon(0\nu)$ (see Figure 2.9). Due to the low Q-values of $\beta^+\beta^+$, its decay rates is even smaller than that of $\beta\beta$. Hence, this process is of minor significance in the search for Majorana neutrinos.

2.4.1 Double-beta candidate isotopes

In total, 35 isotopes are predicted to undergo double-beta decay [11]. From experimental considerations, three factors are of importance when selecting a suited candidate [14]. Firstly, the Q-value should be large as the decay rate is correlated with it — because of the phase space — and moreover, a high Q-value separates the $\beta\beta(0\nu)$ signal from radioactive backgrounds. Secondly, the natural abundance of the isotope and ease of enrichment, since the low decay rate requires a large quantity of the candidate isotope. Lastly, the availability of a suited detection technique.

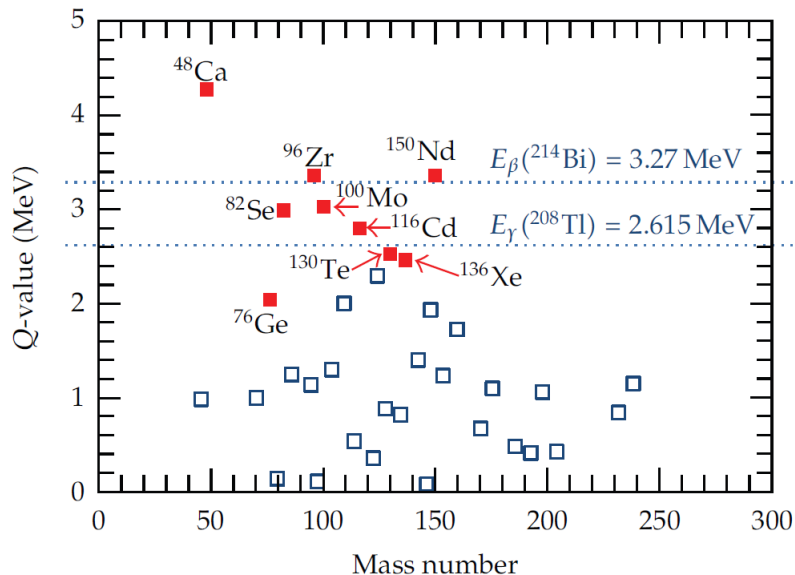


Figure 2.10: The Q-values of the 35 double-beta candidates. The nine candidates of most interest are highlighted in red. These candidates are split in three groups by two background relevant energies — the beta spectra of ^{214}Bi and the gamma line of ^{208}Tl . Graph from [14].

Considering these criteria, there are nine candidates of major interest (see Figure 2.10). They are split in three groups of three by the two background relevant gamma lines of ^{214}Bi and ^{208}Tl . The isotopes of the first group — ^{48}Ca , ^{96}Zr , and ^{150}Nd — have the highest Q-values, all above the background lines. However, their natural abundance is the smallest of all candidates (see Table 2.3), and moreover, these isotopes cannot be enriched by centrifuges. The isotopes of the second group — ^{82}Se , ^{100}Mo , and ^{116}Cd — have Q-values between the two gamma lines. These isotopes have a modest abundance and can be enriched. The isotopes of the last group — ^{76}Ge , ^{130}Te , and ^{136}Xe — have the lowest Q-values among these nine candidates. However, they have a modest to high abundance, are relatively cheap to enrich, and most of all they are excellent

candidates to build good detectors (see Subsection 2.4.2). (This is probably the only reason why ^{76}Ge is of interest.) Due to this fact, most experiments have been conducted with the isotopes of the third group — despite their relatively low Q-values.

Candidate isotope	Q-value (MeV)	Phase space G_{01} (yr^{-1})	Isotopic ab. (%)	Enrichable by centrif.	Indicative cost norm. to Ge
^{48}Ca	4.27226 (404)	6.05×10^{-14}	0.187	No	—
^{76}Ge	2.03904 (16)	5.77×10^{-15}	7.8	Yes	1
^{82}Se	2.99512 (201)	2.48×10^{-14}	9.2	Yes	1
^{96}Zr	3.35037 (289)	5.02×10^{-14}	2.8	No	—
^{100}Mo	3.03440 (17)	3.89×10^{-14}	9.6	Yes	1
^{116}Cd	2.81350 (13)	4.08×10^{-14}	7.5	Yes	3
^{130}Te	2.52697 (23)	3.47×10^{-14}	33.8	Yes	0.2
^{136}Xe	2.45783 (37)	3.56×10^{-14}	8.9	Yes	0.1
^{150}Nd	3.37138 (20)	1.54×10^{-13}	5.6	No	—

Table 2.3: Summary of the most relevant characteristics of the nine candidates of interest. Table from [14].

2.4.2 Detection techniques

To measure the double-beta decay is an experimental challenge. Several factors have to be considered when designing such an experiment. Firstly, to minimise the backgrounds in the detector, it has to be built from extremely pure materials — from the radioactive point of view. Secondly, a good energy resolution is needed to discriminate the signal from the remaining background and to separate the signals from the $\beta\beta(2\nu)$ mode from that from the $\beta\beta(0\nu)$ mode. Thirdly, to overcome the very low decay rate of double-beta decay, detectors with many moles of the candidate isotope (> 100 kg) are required. Hence, to minimise the size of a detector, it is of advantage if the candidate isotope can be used as detection media, as well as as the source. Lastly, if the event topology can be reconstructed with the detector, the capability to discriminate between signals from double-beta decay and from gamma induced background is enhanced.

For the double-beta candidates of the third group — ^{76}Ge , ^{130}Te , and ^{136}Xe — such detection techniques exist. With ^{76}Ge pure crystals can be grown. These crystals are used in high purity Ge-detectors which provide a superb energy resolution. Moreover, new detector designs — with segmented read-out — in combination with pulse shape analysis, allow to reconstruct the event topology. Some experiments conducted with this isotope are the Heidelberg-Moscow experiment — which made the controversial claim to have observed $\beta\beta(0\nu)$ [40] — and the GERDA experiment. With ^{130}Te pure TeO_2 crystals can be grown. At temperatures of a few milli Kelvin, TeO_2 has a small heat capacity. Therefore, TeO_2 crystals can be used to build bolometers. CUORE is an ongoing experiment using this technique. ^{136}Xe is a noble gas. To purified it, it can be recirculated through filters. Xenon can be used in ionization chambers — such as *Time Projection*

Chambers TPC's (see Subsection 2.4.3) — which can be operated with gaseous or liquid xenon. A TPC can reconstruct the event topology in three dimension. Current experiments investigating xenon are EXO (see Chapter 3) — which uses a TPC filled with liquid xenon — and KamLand-Zen — which use xenon dissolved in liquid scintillator. In particular, ^{136}Xe is the only candidate for which the identification of the daughter could be feasible in real-time. This could be used as a strong background rejection tool (see Section 3.3). EXO is pursuing R&D in view of exploiting this feature in a next phase of the experiment. Isotopes where no specific detection technique exists are mostly studied by the NEMO experiment. This experiment uses electron trackers in combination with calorimeters and can reconstruct the angular distribution of the distinctive two electron decay configuration, but with relatively small total isotope masses.

2.4.3 The time projection chamber

The *Time Projection Chamber TPC* is a particle detector type based on the detection of ionization. A TPC consist of three components (see Figure 2.11). Firstly, a detection volume which is filled with a gaseous or liquid detection medium. Secondly, a field cage which limits the detection volume and generates an electric field in it. The field cage is made from a cathode, an anode, and several field shaping rings in between. Ring by ring, the electric potential is reduced from the cathode towards the anode, generating a homogeneous electric field. Thirdly, the anode consists in a read-out plane. The read-out plane is usually divided into two wire planes — however a variety of other techniques are used (e.g. segmented read-out plains). The wire plane close to the

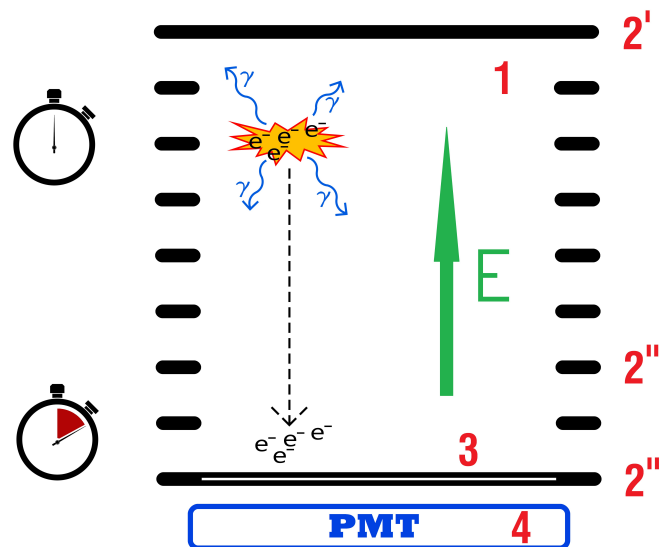


Figure 2.11: The basic components and the working principle of a TPC. The TPC consists from a detection volume (1) filled with a medium, a field cage (2) — with a cathode (2'), an anode (2''), and several field shaping rings (2''') — a read-out plane (3), and if applicable a light collection system (4). At t_0 , an ionizing particle hits the detection medium and generates free charge and scintillation light. The light is instantly registered with the light detection system. Somewhat later, the electrons arrive at the read-out plane. From the drift time t_d the position in z can be reconstructed.

detection volume is called the induction plane. The second wire plane is the so-called collection plane. The wires of the two planes are rotated by an angle θ . They are read-out either in bundles or individually. (In EXO-200 $\theta = 60^\circ$ and the wires are read-out in bundles of three, while in EXO-100 $\theta = 90^\circ$ and the wires are read-out individually.) Additionally, to detect the scintillation light, photo sensors can be placed around the field cage.

An ionizing particle in the detection volume ionizes, as well as excites, atoms of the detection medium. The electric field hinders the ions and free electrons from recombining, and moreover, it forces the positive charged ions to drift towards the cathode and the electrons towards the read-out plane. At the read-out plane, the electrons drift past the induction wires, where they induce a signal, and are collected at the collection wires. From the signals of the collection wires the energy deposited in ionization can be measured. In gas, charge multiplication around thin anode wires is possible, increasing not only the charge signal, but also that on the induction wires. In combination with the signals from the induction wires, the position of an interaction can be reconstructed in the x - y plane — which is oriented perpendicular to the drift direction z . The position in z can be reconstructed from the drift time

$$t_d = t' - t_0 \quad (2.19)$$

where t_0 is the time of the interaction and t' time of arrival of the electrons at the read-out plane. Together with the known electron drift velocity v_e the position in z is given as

$$z = t_d \cdot v_e. \quad (2.20)$$

To determine t_0 , a light detection system is required. (Otherwise, only a relative positioning in z is possible.) This allows to measure the prompt light flash from scintillation and recombination (with a time constant $\tau \ll t_d$). Moreover, the light channel contains additional information on the deposited energy. Recording this channel improves the detector's particle identification capability using the light to ionization ratio, as well as its energy resolution. A detailed description of the working principle of a TPC can be found in [41].

Generally, TPC's can be operated with various detection media. Probably the most fundamental demand on a detection media is that it allows for electron drift. Therefore, the detection medium must not be electronegative — electronegative atoms capture free electrons and diminish the signal. For this reason commonly (but not exclusively) noble gases are used. Additionally, noble gases are inert, and thus, can be purified with filters, do not lead to ageing of the detector, and are harmless to the environment. For some applications a detection media with a high density is desired. In these cases TPC's filled with liquefied noble gases are an option. However, the normal boiling point of noble gases spans a range from 4.2 K to 165 K for He and Xe, respectively. Consequentially, the use of liquid noble gases requires sophisticated cryogenic detectors.

A TPC has several striking features which make it a well suited detector for the search of neutrinoless double-beta decay. The two main features are that a TPC allows for three dimensional positioning and for particle identification. The positioning of an event in all three dimensions allows to fiducialise the detection volume. This has the advantage that the outermost part of the detection volume — where most background events occur — can be excluded. Moreover, three dimensional positioning allows to segment the detection volume. EXO takes advantage of this to distinguish $\beta(\beta)$ from γ interactions. Predominantly, γ 's Compton scatter in the detector, and thus, have multiple sites of interaction. In contrast, $\beta(\beta)$'s predominantly deposit their energy in a single site. The separation of *single site SS* and *multi site MS* events yields two energy

spectra. The background is suppressed in the SS spectrum and dominates the MS spectrum (for the two spectra of the EXO-200 detector see Figure 3.4). In addition, particles can be identified by studying the stopping power dE/dx (described by the Bethe-Bloch formula) and by the charge-light ratio. In particular, α 's generate much more light per deposited energy than $\beta(\beta)$'s and γ 's. Additionally to these two features, high pressure noble gas TPCs can achieve very good energy resolution — however not as good as the solid state (Ge and Te) devices. In liquid xenon, due to the anti-correlation of these competing energy deposition processes, by combining light and charge information, improved energy resolution can be achieved (with EXO-200, almost 1% at the Q-value).

The Enriched Xenon Observatory

In this Chapter an overview of the Enriched Xenon Observatory project is presented. An emphasis is put on the concept of barium tagging, its importance as a background rejection tool, and on the different possible tagging techniques. Finally, some open questions regarding properties of the barium ion relevant for barium tagging are formulated and a possible way to address them is presented.

3.1	EXO-200	19
3.2	nEXO	23
3.3	Ba-tagging: the ultimate background rejection technique	25
3.3.1	The Ba-tagging techniques	27
3.3.2	Ba ion properties relevant for Ba-tagging	27
3.3.3	The uranium series and the concept of Po-tagging	28

The *Enriched Xenon Observatory EXO* is a multi-stage project searching for the neutrinoless double-beta decay of ^{136}Xe . EXO makes use of TPC's filled with xenon — enriched in the isotope ^{136}Xe . The current stage of the project — a prototype called EXO-200 — uses 200 kg of liquid xenon (100 kg in the active volume). Ultimately, its sensitivity is limited, and thus, the next stage — the *next Enriched Xenon Observatory nEXO* — is being developed. Moreover, intense R&D efforts are performed to develop a novel background rejection tool — the so called barium tagging.

3.1 EXO-200

The EXO-200 detector is made from two TPC's joined at the cathode (see Figure 3.1). Charge is read-out at one of two read-out planes located at either end of the drift volume. Each readout plane is made from two wire planes — an induction plane (V-wires) and a collection plane (U-wires). The angle between the V-wires and the U-wires is 60° . To detect the scintillation light, behind the wire planes 468 (twice 234) *Large-Area Avalanche Photo Diodes LAAPD's* are located.

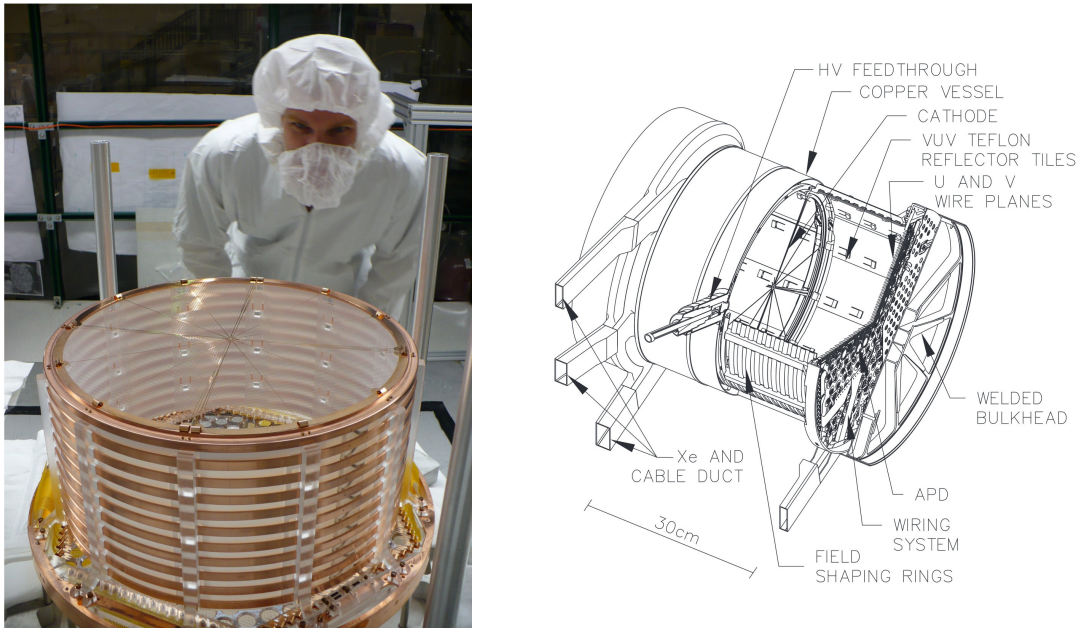


Figure 3.1: The EXO-200 TPC. Left, a photograph of one TPC. On top the cathode mesh can be seen. Right, cutaway view of the EXO-200 TPC with the main components identified. (Graph and caption from [43].)

The detector is encapsulated in a copper vessel which is immersed in HFE7000 — a high purity heat transfer fluid. The HFE7000 is used to cool the copper vessel and acts as a shield against external radioactivity. The HFE7000 fluid is contained in a double wall cryostat made from clean

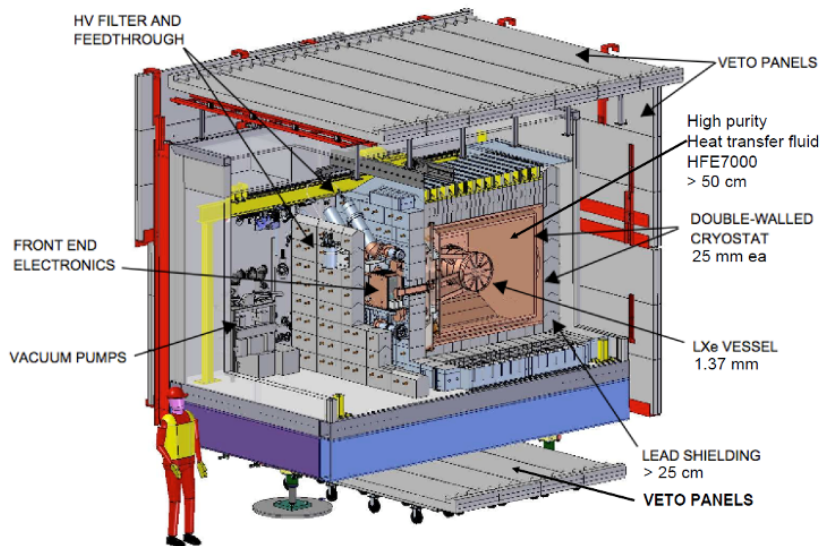


Figure 3.2: An artistic view of the EXO-200 detector.

copper. The inner chamber is cooled by three heat exchangers. The double walled copper cryostat and the lead shield surrounding it (see Figure 3.2) hinder external radioactivity from reaching the detector. All materials and components which were used to build the EXO-200 detector underwent strict radio purity screening [42]. To reach a purity of the liquid xenon sufficient for electron drift, it is recirculated through heated getters¹. More details on the detector are given elsewhere [43].

EXO-200 is located 655 m below ground (1600 m.w.e), at the *Waste Isolation Pilot Plant WIPP* in New Mexico, USA (see Figure 3.3).



Figure 3.3: Location of the EXO-200 detector at WIPP.

With the EXO-200 TPC, charge and scintillation light of an event are recorded and the energy is derived from these channels. Events induced by α radiation have a very different charge-light ratio than events from β or γ radiation, hence α 's can be tagged. However, β and γ radiation deposit their energy with the same charge-light ratio, and hence, γ radiation cannot be rejected with this criteria. To separate these events, EXO-200 uses the concept of *Single Site SS* events — mostly β 's — and *Multi Site MS* events — dominated by Compton scattering and finally photoelectric absorption of γ 's. The corresponding energy spectra are shown in Figure 3.4. The signal from $\beta\beta(0\nu)$ would appear in the SS spectra in a region centred around 2.45 MeV — the Q-value of ^{136}Xe — with a width of roughly twice the energy resolution (FWHM), namely 150 keV. This region is called the *Region Of Interest ROI*. Even in a SS spectrum, it is possible that a γ ray deposits energy within the ROI. Therefore, the contribution of these events to a possible signal can only be approximated through careful study of backgrounds outside the ROI. These background events limit the sensitivity of the experiment, in particular the gamma line of ^{214}Bi within 10 keV of the Q-value.

¹SAES, <http://www.saespuregas.com/>

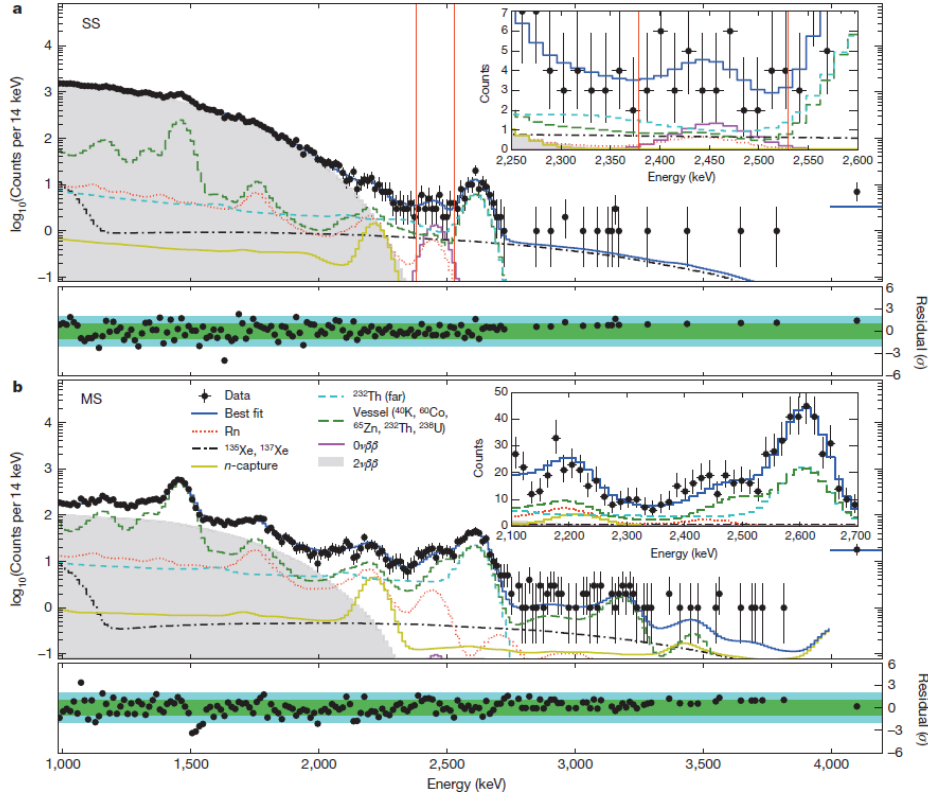


Figure 3.4: Energy spectra after two years of data taking with EXO-200. a) the SS spectrum and b) the MS spectrum. In the SS spectrum, the region of interest is indicated by two red lines. A model including all the known background sources and the hypothetical $\beta\beta(0\nu)$, as well as the allowed $\beta\beta(2\nu)$, is fitted to the data. The various contributions are shown. Graph from [2].

EXO-200 started operations in 2011 and took data for about two years. Thereafter, operations had to be interrupted due to two serious incidents at WIPP [44, 45]. Nevertheless, with data from EXO-200 the $\beta\beta(2\nu)$ decay in ^{136}Xe was discovered [46] and a precision measurement of its half-life was made [1]. It was found to be

$$T_{1/2}^{2\nu} = (2.165 \pm 0.016(\text{stat}) \pm 0.059(\text{sys})) \times 10^{21} \text{ yr.} \quad (3.1)$$

Today, this is the most precise measurement of any $\beta\beta(2\nu)$ half-life, and moreover, it is the slowest directly observed process in nature. Furthermore, with EXO-200, the lower limit on the $\beta\beta(0\nu)$ decay could be pushed up to [2]

$$T_{1/2}^{0\nu} > 1.1 \times 10^{25} \text{ yr at 90\% C.L.} \quad (3.2)$$

Even though EXO-200 will soon be running again, its sensitivity is limited. Hence, a detector upgrade is planned which will increase the sensitivity (see Figure 3.5). However, even with this upgrade it is unlikely that $\beta\beta(0\nu)$ will be observed with enough significance to claim a discovery.

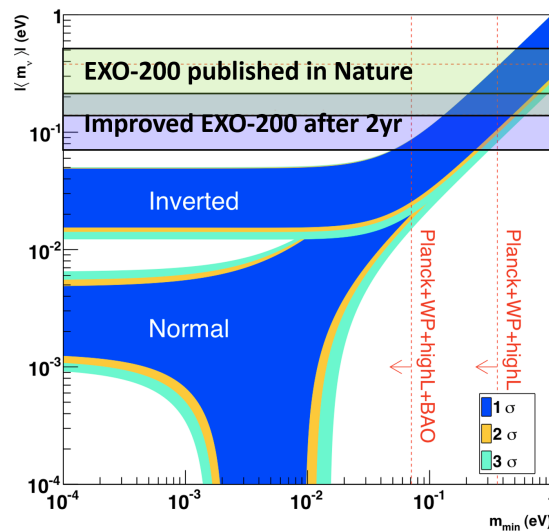


Figure 3.5: The current sensitivity of the EXO-200 detector and the estimated sensitivity after detector improvement. The current bound is somewhat less constrained than that published earlier due to statistical fluctuations presumably.

3.2 nEXO

The nEXO detector will be a multi-ton liquid xenon TPC. Its concept is similar to EXO-200 — a TPC inside a single vessel filled with liquid xenon. The large mass of nEXO will increase the

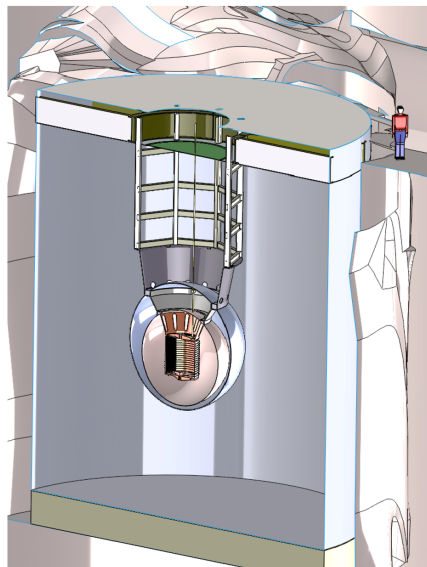


Figure 3.6: Artistic view of a nEXO detector concept. The inner part of the cryostat is cooled with HFE. To hinder external radioactivity from entering the detector, two water shields are placed around it. On top of the inner water shield enough space is foreseen to upgrade nEXO with a barium tagging mechanism.

potential $\beta\beta(0\nu)$ activity in the detector. Furthermore, the self-shielding of liquid xenon will help to reduce the background from external radioactivity. nEXO is still in the concept phase. One such concept is shown in Figure 3.6. Currently, the favoured location for nEXO is SNOLAB in Sudbury, CA (see Figure 3.7) — 2070 m below ground (6000 m.w.e.).

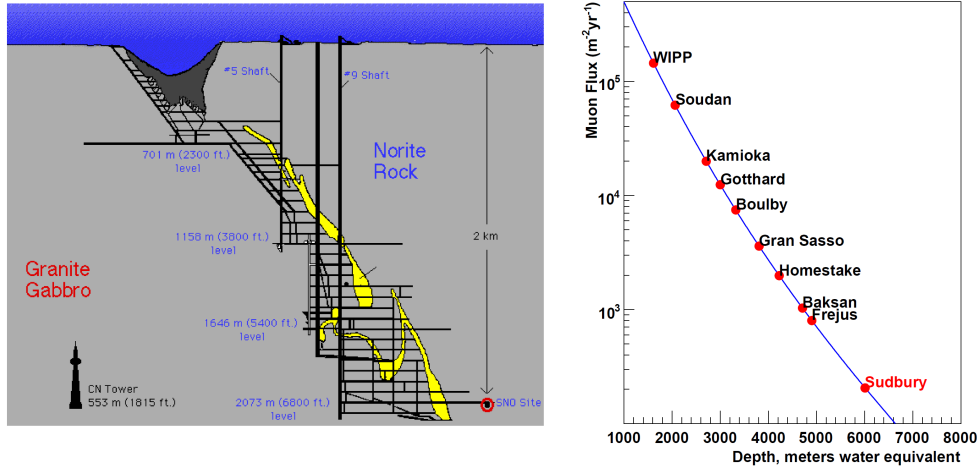


Figure 3.7: The SNO site is located in the Creighton mine 6800 ft. below ground. Left, the structure of the mine is shown and the SNO site is highlighted in red. Right, the muon flux at the SNO site is compared with the muon flux at other underground laboratories including WIPP — the location of EXO-200. (Graphs from [47]).

It is planned that nEXO starts operation around 2020. After five years of data taking the sensitivity of nEXO is expected to be enough to scan the full parameter space of the inverted-hierarchy (see Figure 3.8). If at this point no evidence for $\beta\beta(0\nu)$ will be found, a new approach will be needed. A further scaling by a factor 10 is not feasible, due to the world production

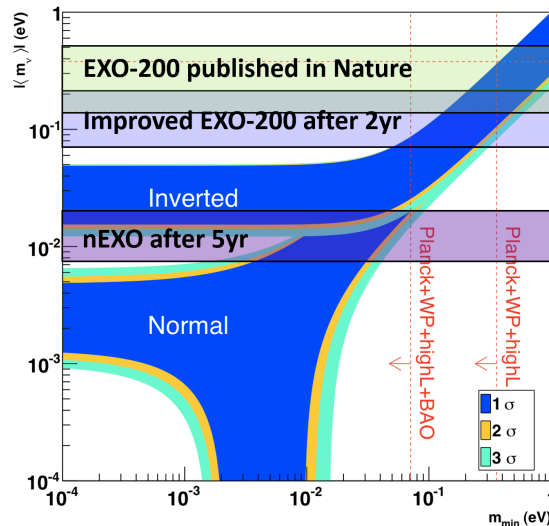


Figure 3.8: The estimated sensitivity of nEXO after five years of data tacking.

rate of xenon, the enrichment rate, and the cost of enriched xenon. It however appears possible to improve the sensitivity by reducing further the background with a novel technique, barium tagging.

3.3 Ba-tagging: the ultimate background rejection technique

The scheme of barium tagging is to detect the ^{136}Ba ion in coincidence with the two electrons emitted in double-beta decay. This will vastly improve the signature of double-beta decay events and lead to an important background suppression. Barium tagging would reject all backgrounds not related to double-beta decay, and hence, it is considered to be the ultimate background rejection technique. As shown in [48], for an experiment with backgrounds that scale linearly with Nt — where N is the number of ^{136}Xe nuclei in the detector and t is the measurement time — the neutrino mass sensitivity scales proportional to $1/\sqrt[4]{T_{1/2}^{0\nu}} \propto 1/\sqrt[4]{Nt}$. However, the neutrino mass sensitivity of a background free experiment scales with $1/\sqrt{Nt}$. Hence, for detectors of large mass, such as nEXO, barium tagging would be a huge advantage (see Figure 3.9).

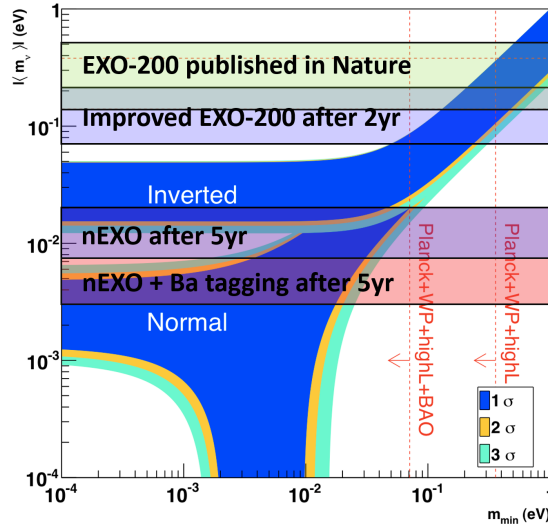
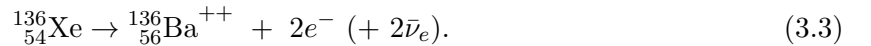


Figure 3.9: The estimated sensitivity of nEXO upgraded with barium tagging after five years of data taking.

A ^{136}Xe atom undergoing double-beta decay does not only deposit energy in the ROI, but moreover, a ^{136}Xe atom is transformed into a ^{136}Ba ion,



The idea of barium tagging is to verify in real time if indeed a barium ion is present at the location of an event with energy in the ROI.

In 1991, Moe [49] proposed to use barium tagging as a background rejection tool for ^{136}Xe double-beta decay experiments. The basic concept is to use lasers to stimulate a singly ionized Ba^+ ion to fluoresce. A laser with 493 nm wavelength is used to excite the electron from the $6^2S_{1/2}$ state to the $6^2P_{1/2}$ state [48, 50, 51] (see Figure 3.10). From the $6^2P_{1/2}$ state, there is a

30% chance for the electron to decay to the $5^4D_{3/2}$ state under the emission of a photon with wavelength of 650 nm. The $5^4D_{3/2}$ state is meta stable, and hence, the electron is trapped in this state. A second laser with 650 nm wavelength is needed to re-excite the electron back to the $6^2P_{1/2}$ state. From where it can decay — with a probability of 70% — back to the ground state under the emission of a photon with wavelength 493 nm. Detection of this wavelength indicates that a barium ion is present in the apparatus. With the help of these two lasers, the fluorescence process can be repeated up to 10^7 times per second, yielding the same amount of 493 nm photons. In 1980, more than a decade prior to Moe’s proposal, this technique was demonstrated by Neuhauser et al. [52] (see Figure 3.11). In 2007, the EXO Collaboration detected single barium ions [53] trapped in a linear ion trap [54].

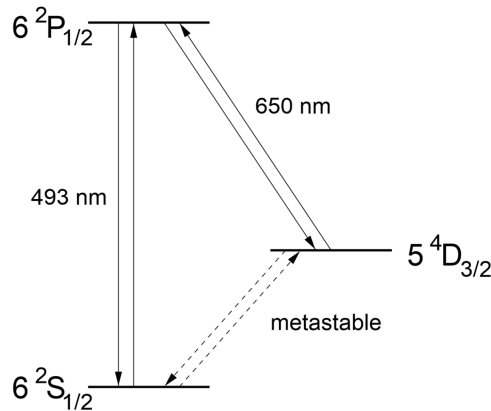


Figure 3.10: Excitation levels of singly ionized barium. See text for more details. Graph from [48].

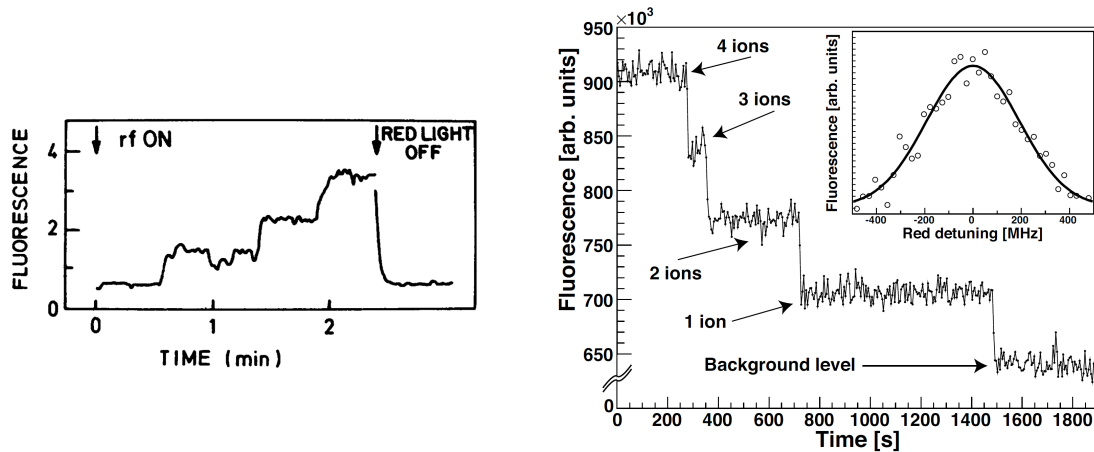


Figure 3.11: The fluorescence power of Ba^+ in arbitrary units versus time. Left, measurement performed in 1980 by Neuhauser et al [52]. The three steps indicate the presence of 0, 1, 2, and 3 Ba^+ in the apparatus. Right, measurement performed in 2007 by the EXO Collaboration [53].

To identify barium with the above described method, it is desired that the barium is present in the singly ionized state Ba^+ — and not Ba nor Ba^{++} — due to its level scheme. Even-though,

in the double-beta decay of ^{136}Xe the barium is produced in the Ba^{++} state, in xenon it is readily converted to the Ba^+ state due to its ionization potentials while immersed in liquid xenon.

3.3.1 The Ba-tagging techniques

The EXO Collaboration has been conducting intense R&D on barium tagging [48, 50, 51, 55, 56]. Currently, several different schemes are under consideration. All presently employed schemes extract the barium ion by an electrostatic grabbing probe. The grabbing probe is inserted into the TPC near the location of the decay, the barium ion is electrostatically attracted to the probe, and subsequently the probe is extracted from the TPC, where laser tagging is done. The presence of the barium in the ionized state is crucial for efficient barium grabbing.

An effort towards ion extraction has been performed by the EXO Collaboration. To build a grabbing probe, three different techniques are explored, the cold-probe, the hot-probe, and the *Resonant Ionization Spectroscopy* RIS-probe. The cold-probe can freeze xenon on its tip. This probe attracts the barium ion electrostatically on its tip. Thereafter, the ion is captured in a thin layer of solid xenon. The ion is released in the ion trap by melting the thin xenon layer. In one variation of this probe, an optical fibre is included and the tagging can be done while the barium is on the probe. At the moment, this technique is the most promising. The hot-probe attracts the barium ion electrostatically to its tip. The probe is extracted from the TPC and guided to the ion trap. To release the barium from the probe, it is heated above 1000 K. In most cases, the barium gets ionized due to the high temperature. The RIS-probe attracts the barium ion electrostatically onto the surface of a semiconductor (e.g. silicon). In the ion trap the barium atom is released from the probe using an ablation laser and RIS lasers to ionize only the barium atom.

Another technique — related to gas TPC's — is the extraction of barium ions from high pressure xenon into vacuum [57]. In this case, after a suspected $\beta\beta(0\nu)$ decay in the TPC, the drift field is changed to allow the ion to drift towards an extraction port. At this port the ion is flushed out of the high pressure xenon through a ion-funnel into vacuum. Subsequently, the ion can be trapped in a RF Paul trap and be tagged.

3.3.2 Ba ion properties relevant for Ba-tagging

Independent of the specific grabbing and tagging techniques, three properties of barium are important to understand its behaviour in the moments after a decay. These are the probability of barium ion to get neutralised right after the decay, the ion lifetime, and the ion drift speed. Firstly, all grabbing techniques require the barium to be ionized. Hence, the probability that the barium is present in an ionized state is essential for the efficiency of these techniques. Moreover, the laser tagging described before is designed to detect Ba^+ and not Ba. Secondly, the ion lifetime is important as all grabbing techniques require some time to reach the location of the barium ion. The anticipated reaction time for the probe is of the order of a minute. Lastly, measuring the ion drift speed allows to calculate the position of the ion at any given time after the decay — e.g. at the time when the probe is in position. The ion mobility of Ba^+ , Tl^- , and Th^+ has been measured and ranges from $0.133 \text{ cm}^2 \text{ kV}^{-1} \text{ s}^{-1}$ to $0.280 \text{ cm}^2 \text{ kV}^{-1} \text{ s}^{-1}$.

3.3.3 The uranium series and the concept of Po-tagging

The study of these three properties of barium requires to tag the barium. However, due to the complexity of barium tagging, the study of these properties of barium is difficult. An alternative is to study them for naturally occurring radioactive isotopes. This has the advantage that a nucleus reveals its position multiple times — once for each decay. The ^{238}U series contains a sequence which is particularly interesting (see Figure 3.12). Starting with ^{222}Rn it contains three alpha decays and two beta decays. Due to the different charge-light ratio of an alpha decay signal in a TPC compared to signals from gamma and beta decays, the alpha decays can be identified and are clearly separated from beta and gamma backgrounds. Moreover, the mono-energetic nature of alpha decay allows to assign each alpha decay to a nucleus in the sequence. The two beta decays have a continuous energy spectrum and the same charge-light ratio as the background. However, the beta decay of ^{214}Bi is followed by the identified alpha decay of ^{214}Po . The appearance of a beta decay followed almost immediately — mostly within one *Data Acquisition DAQ* frame (2 ms) — by an alpha decay at the same position in the detector is an unambiguous sign of the $^{214}\text{Bi} \rightarrow ^{214}\text{Po} \rightarrow ^{210}\text{Pb}$ sequence. The only decay of the sequence which cannot be identified is the beta decay of ^{214}Pb . Hence the sequence is broken into two sub-sequences:



and



For two reasons, the study of the first sub-sequence (3.4) with a TPC is very promising. Firstly, from the position and time of the two alpha decays, it is possible to measure the before mentioned properties for ^{218}Po . However, ^{218}Po is generated through an alpha decay — which has different kinematics than double-beta decay. Hence, due to the large ionization density produced in an alpha decay, the probability of the polonium ion to get neutralised right after the decay may be different than that of barium ions. The other properties are suspected to be similar for all ions. Secondly, the half-life of ^{218}Po — 3.1 min — is of the order of the time it takes to grab an ion from a TPC. Therefore, this sub-sequence is suited to test ion grabbing techniques without the need for the complex barium tagging mechanism.

The concept of polonium tagging is that the alpha decay $^{222}\text{Rn} \rightarrow ^{218}\text{Po}$ is detected in a TPC and identified in real-time. A grabbing probe is displaced to the location of the ^{218}Po and the ion

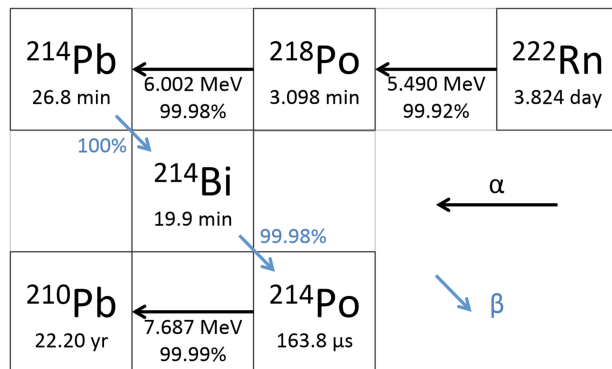


Figure 3.12: Extract from the ^{238}U series. For all decays, the branching ratio and half-life is reported. Note that due to the high branching ratios of all involved decays, the total branching ratio for the sequence is 99.87%. For the α decays, the α 's energy is reported — not the Q-value. Graph from [4].

is extracted from the TPC. Thereafter, the probe is placed in front of an external alpha detector and the subsequent alpha decay $^{218}\text{Po} \rightarrow ^{214}\text{Pb}$ is used to verify the presence of the nucleus.

Combining the first sub-sequence with the second sub-sequence would allow to measure indirectly the probability of the ^{214}Bi to get neutralised right after the ^{214}Pb beta decay. To combine the two sub-sequences is only possible in the case where both the ^{218}Po alpha decay and the ^{214}Pb beta decay result in neutralised daughters. Otherwise, the nuclei drifts in the electric field of the TPC and leaves the detector prior to its decay. Due to the short half-life of ^{214}Po , the beta transition of ^{214}Bi cannot be used to directly measure the probability under discussion.

The study of the sequence shown in Figure 3.12 is very promising in view of barium tagging. Hence, the emphasis of this theses is devoted to it. In the Chapters 4 & 5, the advances on the EXO-100 R&D set-up and its detector are shown. In Chapter 7, a study of the $^{222}\text{Rn} \rightarrow ^{218}\text{Po} \rightarrow ^{214}\text{Pb}$ sequence with data from EXO-200 is presented.

4

The EXO-100 cryogenic R&D facility

In this Chapter the EXO-100 cryogenic R&D facility is presented. It is a very useful tool which allows for a wide range of R&D activities. The facility consists of four subsystems: the cryostat, the gas handling-system, the slow control system, and the safety systems and emergency handling. These subsystems are described in detail.

4.1	The EXO-100 cryostat	33
4.2	The gas handling system	41
4.3	The EXO-100 slow control system	44
4.4	The safety systems and the emergency handling	48

Despite EXO-200’s excellent performance in the search for neutrinoless double-beta decay, this detector is not suited for the study ion properties in liquid xenon nor to test ion extraction from a TPC. When working with EXO-200, there are three main factors leading to these limitations. Firstly, for EXO-200 the search for neutrinoless double-beta decay will remain the highest priority for the next few years. Moreover, this search is based on precision measurements under as stable as possible operating conditions. Therefore, in EXO-200 it is undesirable to change the drift field, which is an interesting parameter when studying the properties of ions. Secondly, in EXO-200 a notable effort was made to reduce all natural radioactive backgrounds to an absolute minimum. This effort strongly affects the isotopes of the so-called ^{238}U series, and thus, their abundances in the EXO-200 detector are suppressed. However, ^{222}Rn and its daughters — which are part of the uranium series — are the preferred candidates to study ion properties in liquid xenon. Therefore, when studying ion properties in liquid xenon, a high abundance of ^{222}Rn is desired. Lastly, in EXO-200 no space was foreseen to install the instrumentation needed to study ion extraction from the TPC. Hence, ion extraction cannot be studied.

Considering these limitations, a dedicated R&D set-up is needed to pursue the mentioned research. Therefore, we built a cryogenic set-up dedicated to nEXO R&D, and specifically, to the study of ions in liquid xenon (see Figure 4.1). The main aim of this set-up — named EXO-100 — is to allow operation of a TPC in liquid xenon with an ion extraction and displacement device. Furthermore, this set-up can be used to perform a variety of measurements not directly related

to Ba-ion tagging (e.g. study of ion properties in liquid argon, measurement of electron drift in liquid CF_4 , or test of high voltage breakdown in liquid xenon).

The core of our set-up is the main chamber with enough space to install a TPC and an ion extraction device. The temperature of this chamber must be precisely controlled to condense xenon in it before a measurement campaign, to maintain the xenon liquid during the campaign, and to evaporate the xenon from the chamber once the campaign is finished. Due to the boiling temperature of xenon (165.1 K at 1 bar), the chamber must be cooled down from room temperature by about 130 K. Therefore, the main chamber is enclosed in a vacuum tight outer vacuum vessel, the ensemble forming the EXO-100 cryostat. The EXO-100 cryostat and the slow control system are described in details in Section 4.1 and Section 4.3, respectively. The original design of the cryostat was developed at the *Haute Ecole d'Ingénierie et de Gestion du Canton de Vaude (HEIG-VD)* in Switzerland [61]. Since then several modifications were made to adapted, as well as improve, the cryostat to changed needs (e.g. operation with liquid argon). In the following the present version is described.

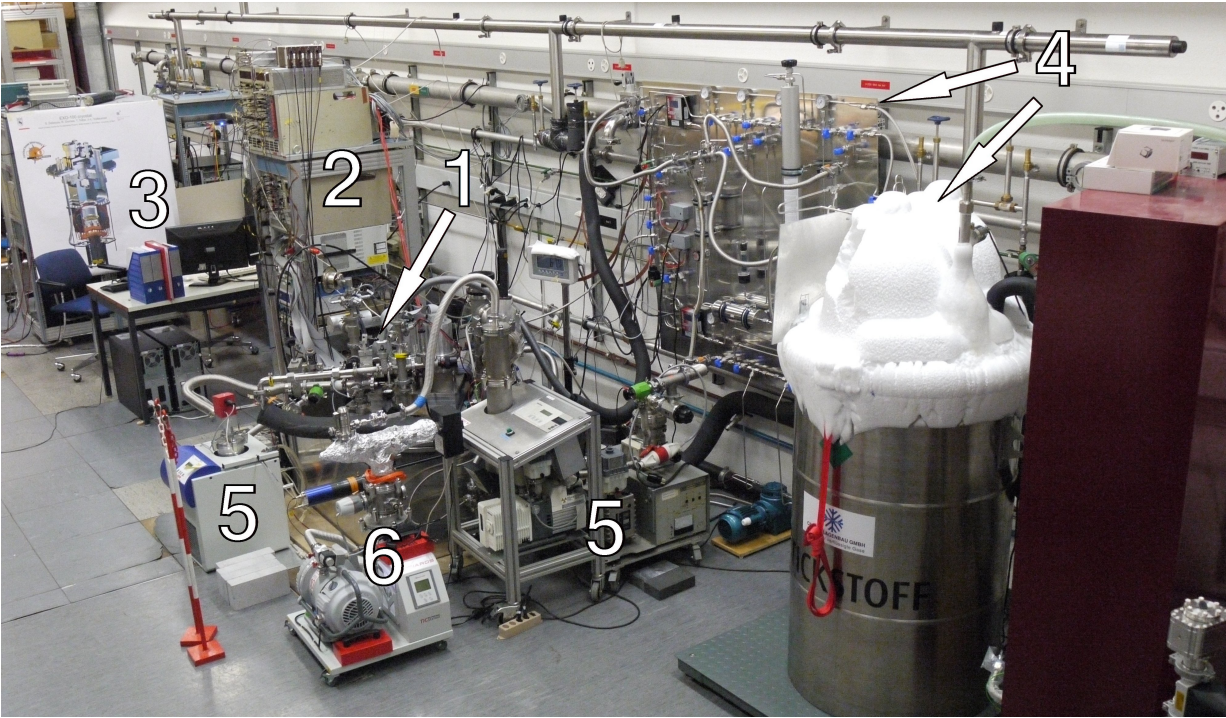


Figure 4.1: Photograph of the EXO-100 set-up: 1 - EXO-100 cryostat with the muon veto, both lowered into the hollow floor, 2 - electronic rack with instrumentation of the slow control system and the *data acquisition DAQ* system, 3 - control centre with PC's for slow control and data acquisition, 4 - gas handling system with gas panel and recovery system, 5 - pump stations, and 6 - *residual gas analysis unit RGA*.

To operate a TPC the purity of the detection medium, as well as the detection medium itself, is crucial. The handling of the detection media varies significantly from operation with xenon or tetrafluoromethane to operation with argon. Xenon and tetrafluoromethane are stored pressurised in gas bottles and need to be condensed in the chamber. Subsequently, to purify them a small fraction of the liquid is evaporated and circulated through filters. Thereafter, the

purified gas is re-condensed in the chamber. In contrast to xenon and tetrafluoromethane, argon cannot be condensed in the chamber due to its low boiling temperature. Consequently, argon has to be poured liquid into the chamber, and thus, argon cannot be circulated. To purify the argon, it can only be filtered during the filling of the chamber. Moreover, xenon is very valuable and tetrafluoromethane (CF_4) is a potent greenhouse gas. Losses of these gases must be minimised. This requires a closed gas handling system, with a recovery system. In contrast, argon is neither particularly valuable nor a greenhouse gas, and thus, the evaporated argon is not recovered but simply released to air. Details on the gas handling system can be found in Section 4.2.

Xenon is a very valuable element. In early 2013, when we purchased our xenon, the price of xenon was about 1 CHF per gram (totally almost 100 kCHF) and has since increased significantly. Thus, any loss of xenon must be prevented. When the xenon is liquefied in the cryostat, the risk of xenon loss is particularly high. A malfunction of the cryostat could lead to loss of cooling power. Thereafter, the xenon would start to warm up and evaporate. Thus, prior to xenon operation, a layer of safety was added to the cryogenic set-up to protect the xenon in case of a system failure. These safety measures include some fully automated processes (e.g. xenon recovery), inform the user via mobile phone in case of irregularities, and allow remote users to measure, switch and control critical components. These safety systems are described in Section 4.4.

4.1 The EXO-100 cryostat

The key task of the EXO-100 cryostat is to regulate the temperature of its main chamber to any requested temperature within the cryostat's operation temperature range. In brief, the functioning principle of the cryostat is that the main chamber is installed between the warm top flange of the vacuum vessel — acting as a heat source — and a cold liquid nitrogen tank — acting as a tunable heat sink. Hence, the temperature of the main chamber can be regulated by tuning the heat sink. In reality, the working principle is a bit more sophisticated. However, for the sake of simplicity, the cryostat can be subdivided by function into three main components: the chamber for the experiment, the liquid nitrogen tank with the exhaust lines, and the vacuum vessel (see Figure 4.2).

The main chamber has to provide optimal conditions for the experiment. In particular, purity of the detection medium is essential when operating a TPC. Therefore, the chamber has to be cleaned prior to filling with the detection medium. Generally, contaminants, such as residual gases and vapours, are best removed by evacuating the chamber to high-vacuum. Therefore, a pump port is connected directly to the chamber. Moreover, it is

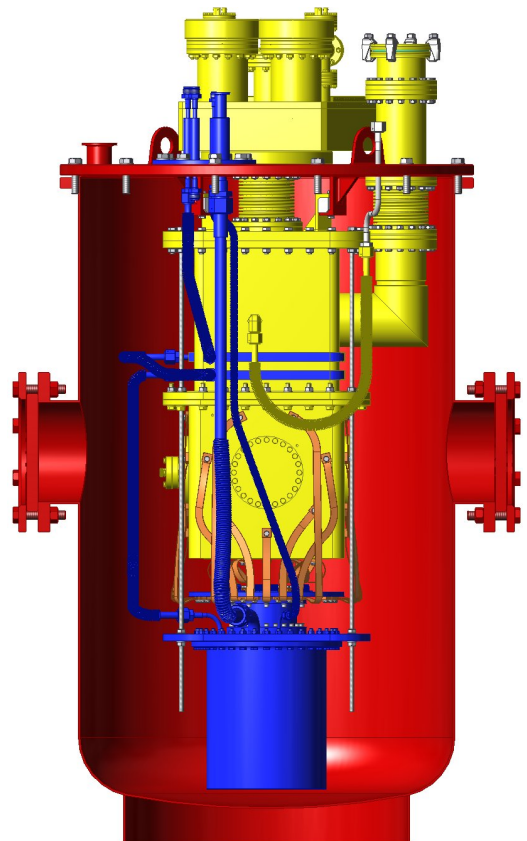


Figure 4.2: Schematic view of the EXO-100 cryostat: yellow - chamber, blue - liquid nitrogen tank with exhaust lines, red - outer insulation vacuum vessel.

equally important to hinder additional gas from entering the chamber. Gas can enter the chamber through leaks, permeate through materials, and from internal sources — out-gassing components and virtual leaks. To hinder gas from leaking into the chamber, it is sealed vacuum tight. In the EXO-100 cryostat a variety of seals is used (see Appendix A for more details). Furthermore, to avoid permeation of gas through the chamber’s walls and to reduce the out-gassing, the chamber was built entirely out of metals.

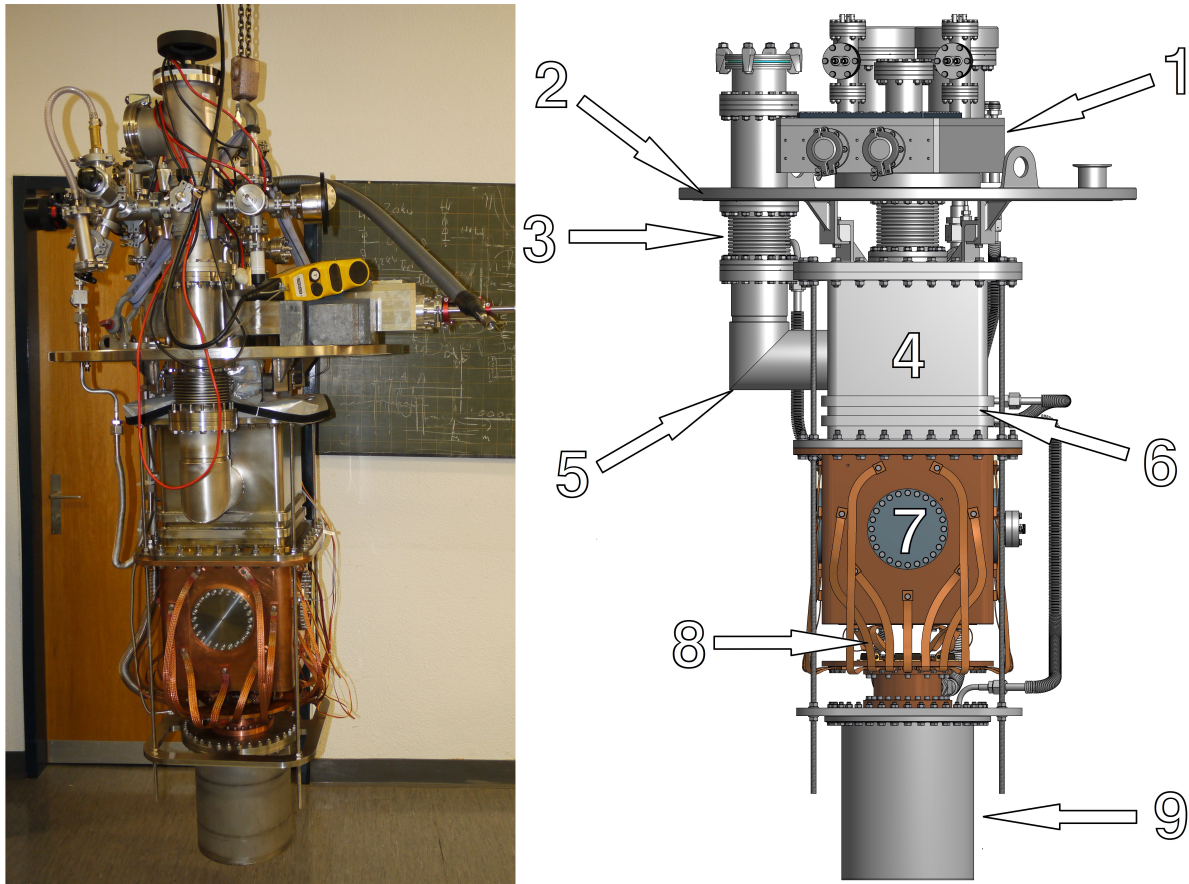


Figure 4.3: Photograph and *Computer-Aided Design CAD* render of the inner cryostat. 1 - Interface box. 2 - Top flange of the vacuum insulation vessel. 3 - Thermal barrier. 4 - Upper section of the inner chamber. 5 - Pump port and gas outlet. 6 - Cooling loops. 7 - Lower section of the inner chamber with flanges. 8 - Copper threads. 9 - Liquid nitrogen tank.

The main chamber is split into three parts, namely, the inner chamber with its lower and upper sections, and an interface box (see Figure 4.3). In the lower section of the inner chamber the TPC can be installed and operated. Therefore, this section is filled with the liquid phase of the detection medium. However, in the case of xenon, the normal boiling point is only 3.8 K above the freezing point — the triple point of xenon is 161.36 K at 0.8162 bar [62]. To avoid freezing of the xenon, the temperature difference across the lower section has to be less than 3.8 K. Consequently, the lower section is made of 1.5 cm thick copper. Copper has a high thermal conductivity (in the temperature range of the cryostat: $350 \text{ W m}^{-1} \text{ K}^{-1}$ to $400 \text{ W m}^{-1} \text{ K}^{-1}$), and thus, tends to quickly equalise its temperature. However, as a result of the high heat conductivity,

it is particularly difficult to weld copper. Moreover, copper is a soft metal. However, copper can be work hardened when formed below its recrystallisation temperature [63, 64]. Therefore, the copper chamber is cold moulded and electron beam welded.

On each side of the chamber's lower section a flange with a diameter of 100 mm is machined. To seal the chamber, each flange is closed by a lid with an indium seal. Several different lids with various configurations were made, and thus, the copper chamber can easily be adapted to changing demands (see Figure 4.4).

In the upper section of the inner chamber, enough space is foreseen to install an ion extraction device. Therefore, this section, as well as the interface box above it, is filled with the gas phase of the detection media. Consequently, the temperature of this section is uncritical. This section is made from stainless steel (thermal conductivity in the temperature rang of the cryostat: $16 \text{ W m}^{-1} \text{ K}^{-1}$ to $24 \text{ W m}^{-1} \text{ K}^{-1}$) in order to minimise the heat conductance between the lower section of the chamber and the warm vacuum vessel. To further reduce the heat conductance, the inner chamber is suspended through a thermal barrier to the top flange. The thermal barrier, as well as the combination of copper and stainless steel, minimises the heat flow and guarantees an even temperature on the copper vessel (see Figure 4.5).

To efficiently clean the chamber, a pump port with a diameter of 100 mm is mounted directly on the inner chamber. Furthermore, this port is used as outlet for the gas circulation to be described later. To fill the medium into the chamber, a separate inlet is mounted on the stainless steel chamber. Finally, multiple threaded holes are placed in the top flange of the inner chamber to support any instrumentation (see Figure 4.6).

The inner chamber is connected via a bellow to the interface box. The purpose of this box is to interface instruments inside the chamber with components installed outside in the laboratory. Hence, several mechanical and electrical feedthroughs penetrate the wall of the interface box. In fact, when this box was designed, it was not decided how the ion extraction device will be driven. Two possible approaches were under discussion. The movement of the ion extraction device can either be generated inside the cryostat with ultra clean cryogenic stepper motors or

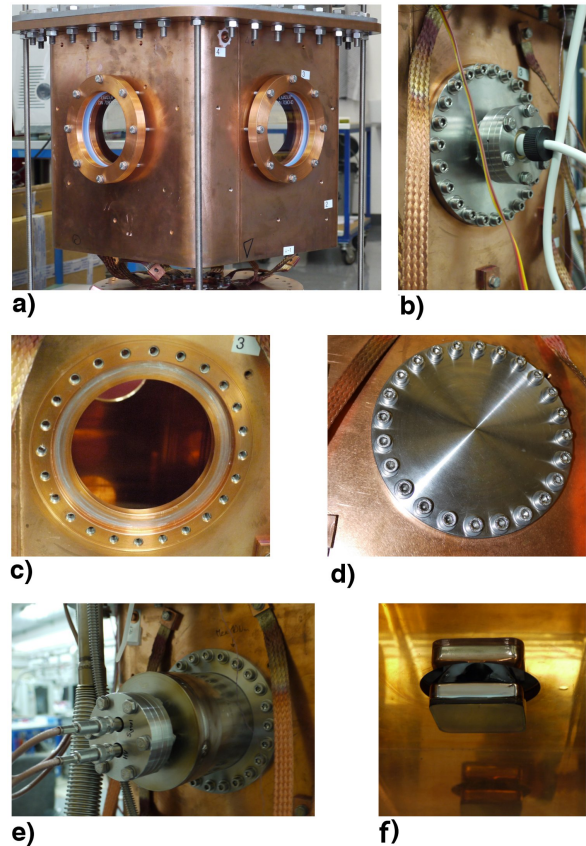


Figure 4.4: Photographs of the different lids: a) The window lids are mounted to the copper chamber. b) A lid with a CF-40 flange on which a high voltage feedthrough is mounted. c) A flange of the copper vessel with out a lid. d) A flange is capped with a blank lid. e) An extension box allowing for sideways installation of a *photo multiplier tube PMT*. f) The PMT seen from inside the chamber.

a mechanical device can divert an external movement into the cryostat and down to the ion extraction device. Due to this uncertainty, the interface box was designed to cope with both approaches. It is possible to add additional electrical feedthroughs to drive multiple stepper motors, and furthermore, enough space and support possibilities for a mechanical device are foreseen in the interface box (see Figure 4.7). Clearly, the chamber is specifically designed to meet the requirements to test ion extraction from a TPC. Nevertheless, the design of the chamber is kept as adaptive and flexible as possible, and thus, the EXO-100 cryostat is also suited for various other applications.

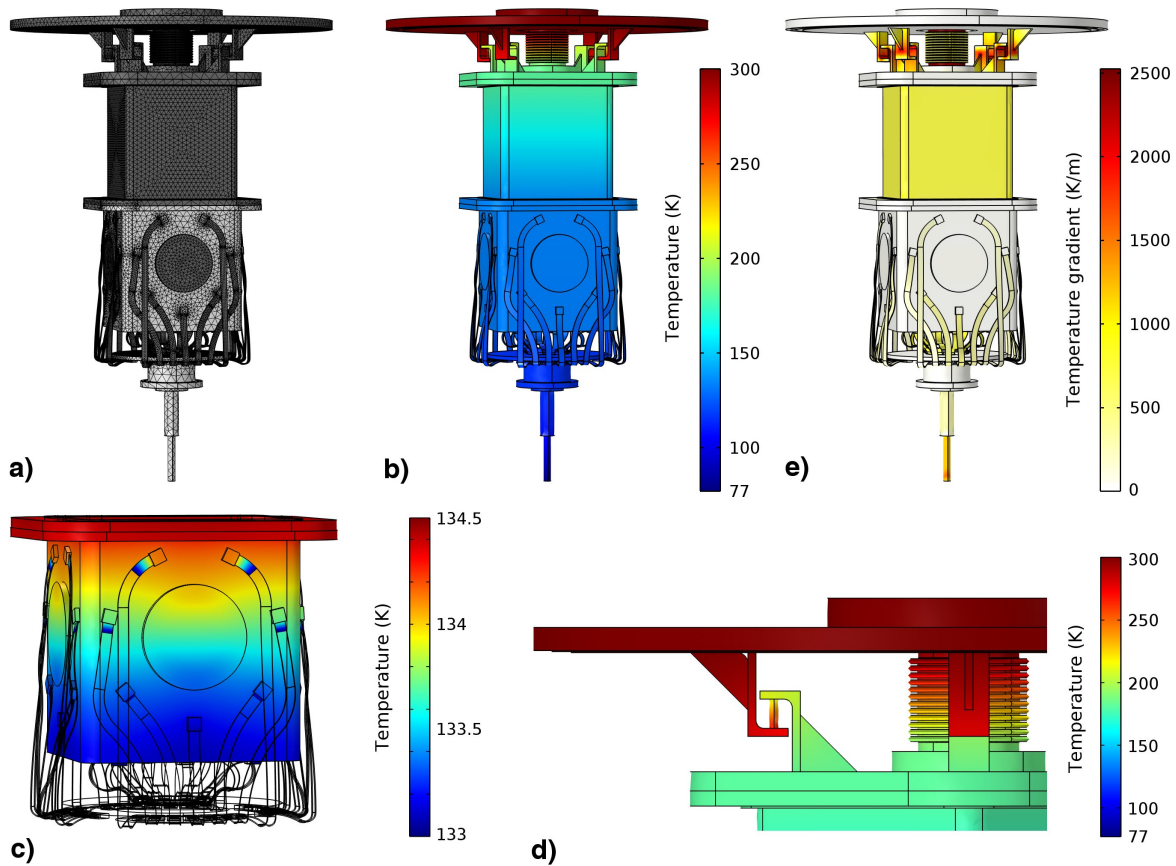


Figure 4.5: Finite element heat transfer simulation of the EXO-100 cryostat (boundary conditions: top flange at 300 K and lowest part of the copper finger at 77 K): a) The mesh and the materials used for the simulation (light gray- copper, dark gray- stainless steel). b) Simulated temperature distribution across the full cryostat. The lower chamber is almost as cold as the copper plate below. c) It can be seen, that indeed the temperature gradient over the copper vessel is less than 1.5 K. d) An abrupt temperature change develops over the thermal barrier. e) Simulated temperature gradient.

Another component of the EXO-100 cryostat is the liquid nitrogen tank (see Figure 4.8). The function of the liquid nitrogen tank is to cool down in a controlled way the copper chamber. Precise temperature regulation is achieved as a result of multiple steps: passive cooling, active heating, and measuring of the actual temperature of the copper chamber and giving a feedback to the heating circuit. To passively cool the inner chamber, the tank is filled with liquid nitrogen through a filling line. The liquid level in the tank is measured and an electromagnetic valve is used to control the inflow. Thereby, the liquid nitrogen in the tank is maintained at a constant level. A copper rod — referred to as a cold finger — is installed in the middle of the tank. The cold finger is mounted on a massive copper flange, which seals the tank and acts as a thermal bridge. On top of the flange a copper plate is mounted. This plate is thermally connected via several copper threads to the copper chamber. During operation of the cryostat, the cold finger is partially immersed into liquid nitrogen, and thus, cools down the copper plate on top of the tank. The inner chamber is cooled via the copper threads. Depending on the targeted temperature of the chamber, the cooling power of the liquid nitrogen tank can be tuned roughly by changing the level of the liquid nitrogen. The liquid level is set in such a way that the chamber is passively cooled slightly below the targeted temperature. To actively regulate the temperature of the chamber, six power resistors are mounted on the copper plate. They allow to dissipate up to 120 W of heat on the plate, and therewith, the chamber can be heated above the targeted temperature. To reach exactly the targeted temperature, a PID feed-back loop is implemented. Several temperature sensors are placed all over the cryostat. Five of which are installed on the copper chamber and are used to give a feed-back to the heating circuit.

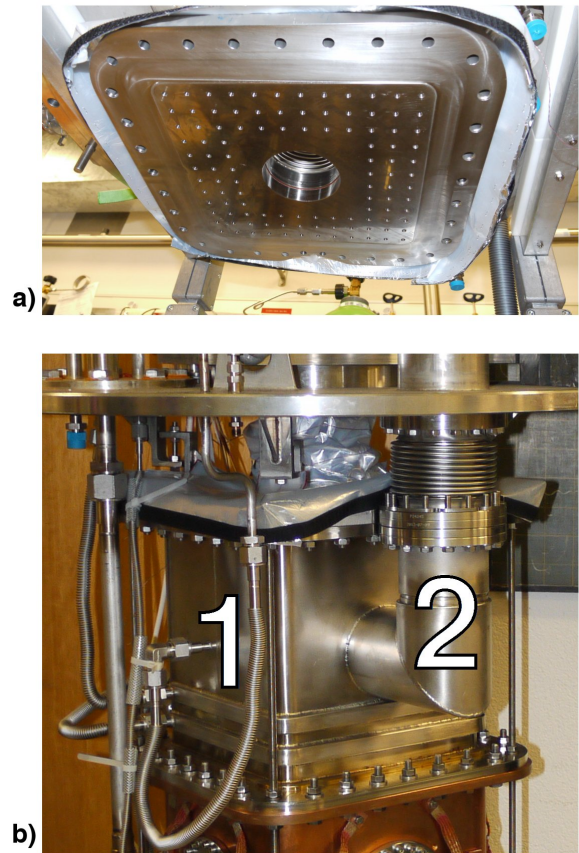


Figure 4.6: Photographs of the upper section of the inner chamber: a) Multiple threaded holes are placed in the top flange of the inner chamber. The hole in the middle connects the inner chamber with the interface box. b) The upper section is made from stainless steel. 1 - The gas inlet port. 2 - Pump port and gas outlet.

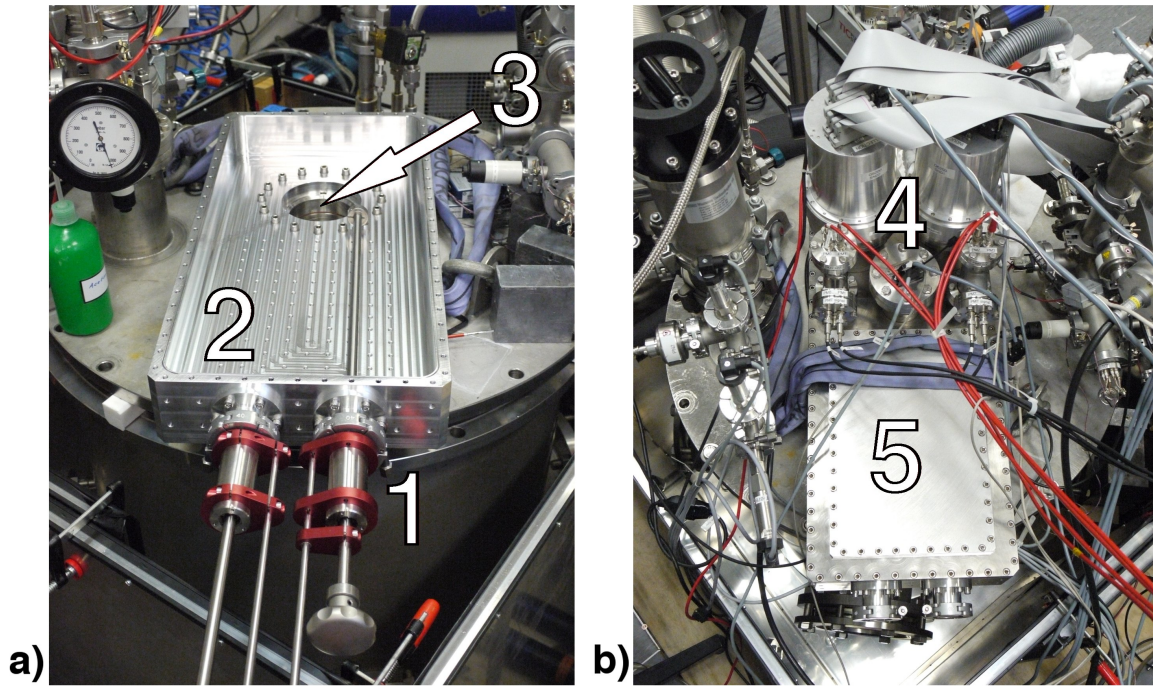


Figure 4.7: Photographs of the interface box: a) The opened interface box: 1 - Mechanical feedthroughs to drive a displacement device. 2 - Pattern with threaded holes to mount instrumentation needed to bring the linear movement to the displacement device. 3 - connection to the inner chamber. b) The closed and fully instrumented interface box: 4 - Various electrical feedthroughs used for the signals of the TPC and PMT's. The pre amplifiers are mounted directly onto the feedthroughs. 5 - A separate lid allows to get access to the inner part of the linear feedthroughs without the need to detach any cabling from the electrical feedthroughs. To seal both lids, indium seals are used.

The cooling power of the cryostat is taken from the latent heat of vaporisation of the liquid nitrogen. Therefore, constantly nitrogen is evaporated in the liquid nitrogen tank. The nitrogen vapour can be evacuated either through a direct exhaust line or through two cooling loops welded onto the inner chamber. The latter allows to use the cold nitrogen gas to additionally cool the chamber. This allows for fast cool down, lower target temperatures, and effective condensation of the detection media. Furthermore, two big resistors are installed on the bottom of the tank. Each of them can dissipate 300 W, and thus, boil off liquid nitrogen. If the nitrogen vapour is led off through the direct exhaust line, these resistors can be used to actively lower the level in the tank. Consequently, the cooling power of the liquid nitrogen tank is reduced. However, if the nitrogen vapour is exhausted through the cooling loops, the cooling power can be significantly increased by boiling off additional nitrogen. Outside of the cryostat, each exhaust line can be shut with a valve. This allows to manually select the desired exhaust line. Finally, the nitrogen gas passes a flow meter and is evacuated through some piping into a yard where it is released to air. The flow meter allows to measure the consumed amount of liquid nitrogen.

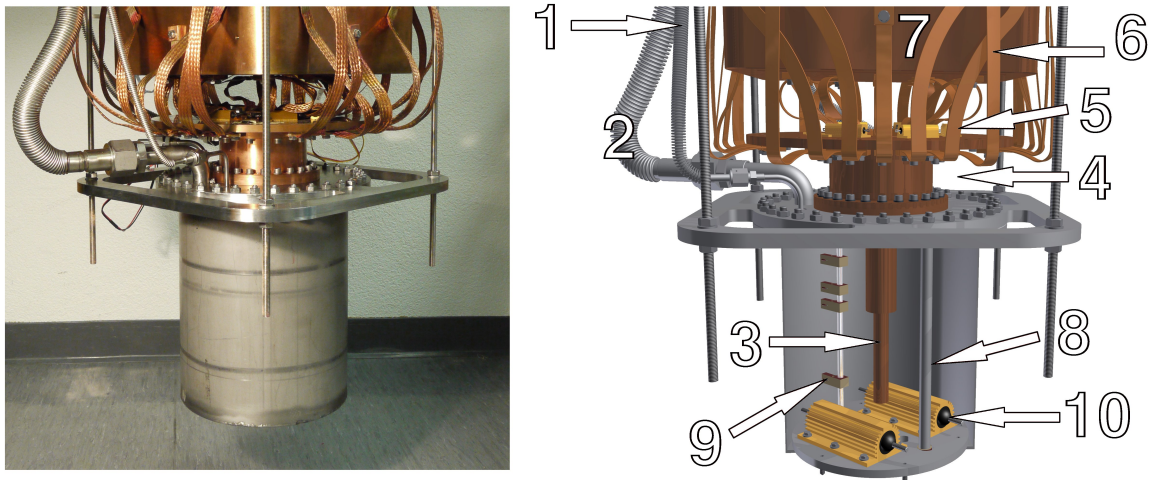


Figure 4.8: Photograph and CAD render of the liquid nitrogen tank. 1 - Liquid nitrogen inlet. 2 - Direct exhaust line (the exhaust line to the cooling loops is hidden). 3 - Cold finger. 4 - Massive copper flange. 5 - Copper plate with temperature regulation resistor. 6 - Copper threads. 7 - lower section of inner chamber. 8 - Capacitive level meter probe. 9 - Resistive level meter probe. 10 - Resistors to force nitrogen evaporation.

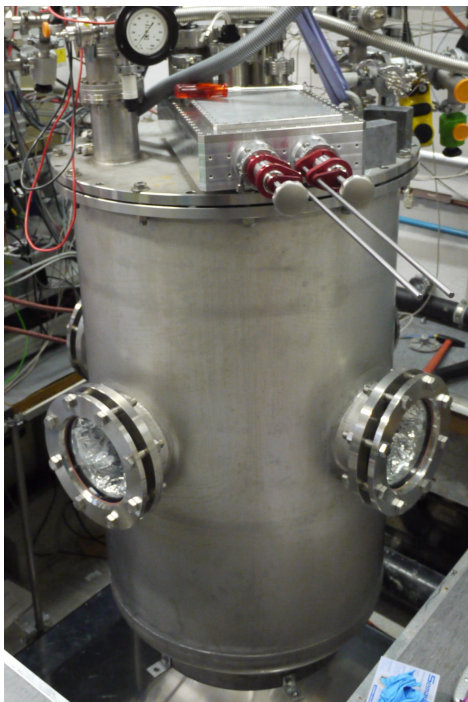


Figure 4.9: Photograph of the outer vacuum vessel. Through the view ports the super insulation foil can be seen.

In short, liquid nitrogen plays a central role for the operation of the set-up. Therefore, liquid nitrogen can be supplied to the EXO-100 set-up in two independent ways: with dewars or with a liquid nitrogen supply line. The dewars in our lab have a capacity of 100 l to 200 l. Depending on the operation temperature of the cryostat, a 200 l dewar lasts for about 1 day to 3 days, barely long enough for operation over a weekend. Therefore, we upgraded the laboratory infrastructure with a liquid nitrogen supply line. This line is connected to an existing liquid nitrogen facility. This facility filters nitrogen out of air and liquefies it at a rate of about 30 l h^{-1} of liquid nitrogen. Subsequently, the liquid nitrogen is stored in a tank with a capacity of 10 m^3 . The liquid nitrogen supply line allows to operate the set-up independently over weeks. Nevertheless, as a back-up two filled dewars are constantly placed next to the set-up. In case of a malfunction the liquid nitrogen supply can manually be switched to these dewars.

The last component of the EXO-100 cryostat is the outer insulation vacuum vessel (see Figure 4.9). It insulates the cold chamber, as well as the liquid nitrogen tank, from the warm surrounding. A reduced heat flow leads to a better temperature homogeneity of the cop-

per chamber and reduces the liquid nitrogen consumption of the cryostat. Heat can be exchanged between those parts through three mechanisms: convection, heat conduction, and heat radiation. The heat exchange due to convection and conduction of gas in the insulation space can almost be stopped by evacuating the insulation vacuum vessel to high vacuum. However, the heat exchange due to heat radiation cannot be stopped, but only be suppressed. Generally, thin metallised boPET film — commonly known as super insulation foil — is used to reduce the heat radiation. Therefore, the vacuum insulation vessel is lined with 6 layers of super insulation foil (see Figure 4.10). Additionally, a special coat is put over the cold parts of the cryostat. This coat is made from ten layers of super insulation foil packed between two protection layers. All these layers are loosely held together by metal staples. For easy mounting and dismounting of the coat, several hook-and-loop fasteners are used (see Figure 4.11).

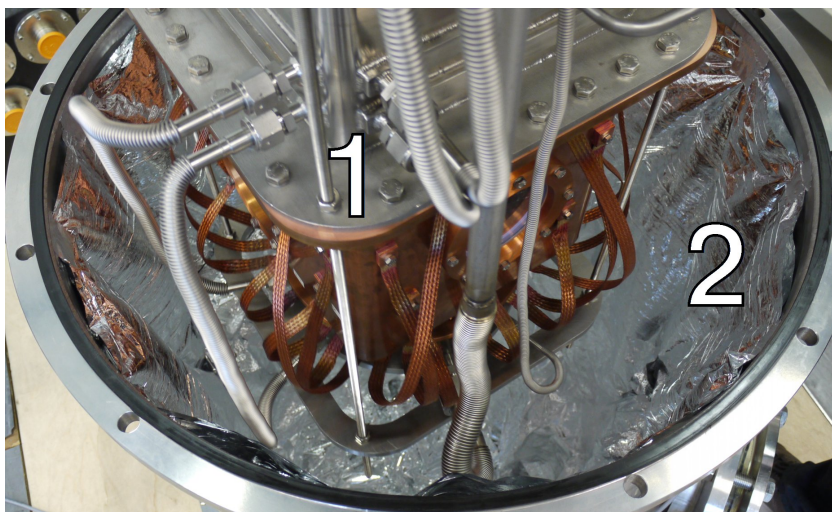


Figure 4.10: Photograph made during the closing of the cryostat: 1 - the inner chamber, 2 - super insulation foil.

Around the insulation vacuum vessel four view ports are placed. These view ports can be aligned with the flanges on the copper chamber. If the ports at the chamber are closed with the window lids, one can see straight through the inner chamber.

The cryostat with its slow control system allows to set the temperature of the chamber to any targeted temperature within the range from 310 K down to 100 K. This wide temperature range, of more than 200 K, allows to condense not only xenon but various other detection media. The normal boiling point of xenon, tetrafluoromethane (CF_4), krypton, and argon is 165.1 K, 145.1 K, 119.7 K and 87.3 K ¹, respectively.

¹data from *National Institute of Standards and Technology NIST*, www.nist.gov

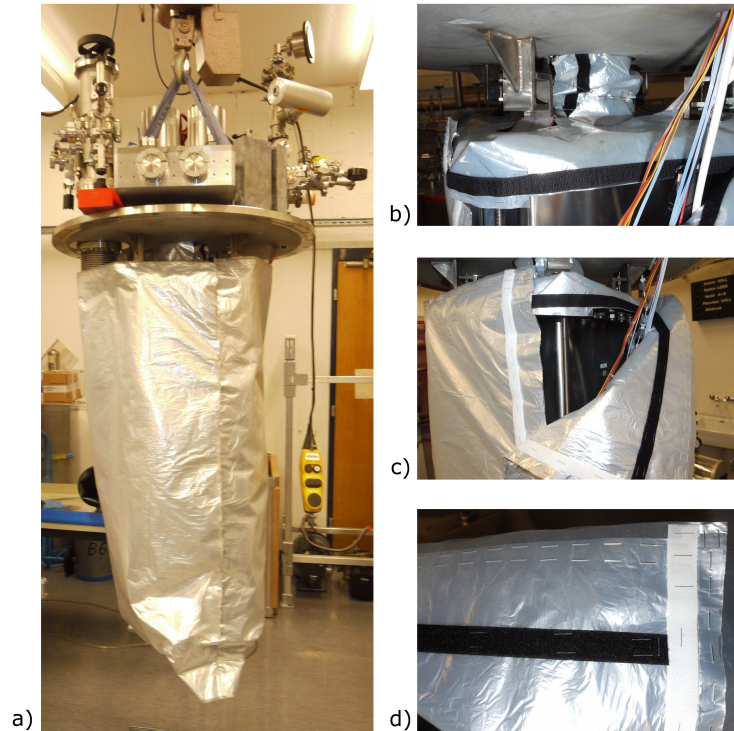


Figure 4.11: Photographs of the super insulation coat: a) - The coat is wrapped around the inner chamber and the liquid nitrogen tank. The cryostat is ready for closing. b) - Close view on the upper part of the coat. The top flange of the inner chamber is covered with a permanently installed cap. Furthermore, a removable collar is put around the bellow connecting the inner chamber with the interface box. c) The main part of the coat is attached to the cap which hook-and-loop fasteners. d) The protection layers, the super insulation foil and the hook-and-loop fasteners are hold together with metal staples.

4.2 The gas handling system

The main components of the gas handling system are the gas panel and the recovery system with the storage bottles (see Figure 4.12 and 4.13). The gas panel allows to inject gas from external gas bottles to the system, to fill gas from the storage bottles to the cryostat, to circulate and filter the gas, and to recover the gas to the storage bottles. To inject the xenon into the system, an injection section is added to the gas panel. This section allows to attach external gas bottles and to inject gas from them into the system (e.g. xenon) or to flush the panel with clean gas (e.g. argon). Gas from external bottles can be injected either directly to the cryostat or to the storage bottles. In both cases, the gas can be led through the filters or by-pass them. Three filters remove contaminants from the gas and guarantee a high purity at the outlet of the panel. In direction of flow, the first filter is a large Oxysorb filter (manufactured by Alphagaz) with a capacity of 9l and 45l of oxygen and humidity, respectively. It removes oxygen and water to below 5ppb and 30ppb, respectively. The second filter is a small Oxysorb filter (manufactured by Alphagaz) which removes the same impurities as the first filter. However, this filter is transparent, and thus, the granulate of the filter substance can be seen. The filter substance changes its color once it is

saturated. Therefore, the second filter acts as an indicator for the saturation of the first filter. The third filter is a Micro Torr filter (manufactured by SAES, model MC700-902FV). This filter is intended to purify noble gases. It removes the following impurities. Firstly, H_2O , O_2 , CO , CO_2 , and H_2 to less than 100ppt. Secondly, acids (e.g. SO_2 , NO_x , and H_2S) and organics ($C > 5$, Toluene) to less than 1 ppt. Lastly, bases (NH_3 and amines) to less than 5ppb. This series of filters guarantees pure gas — less than 0.1ppb of critical impurities — at the outlet of the panel.

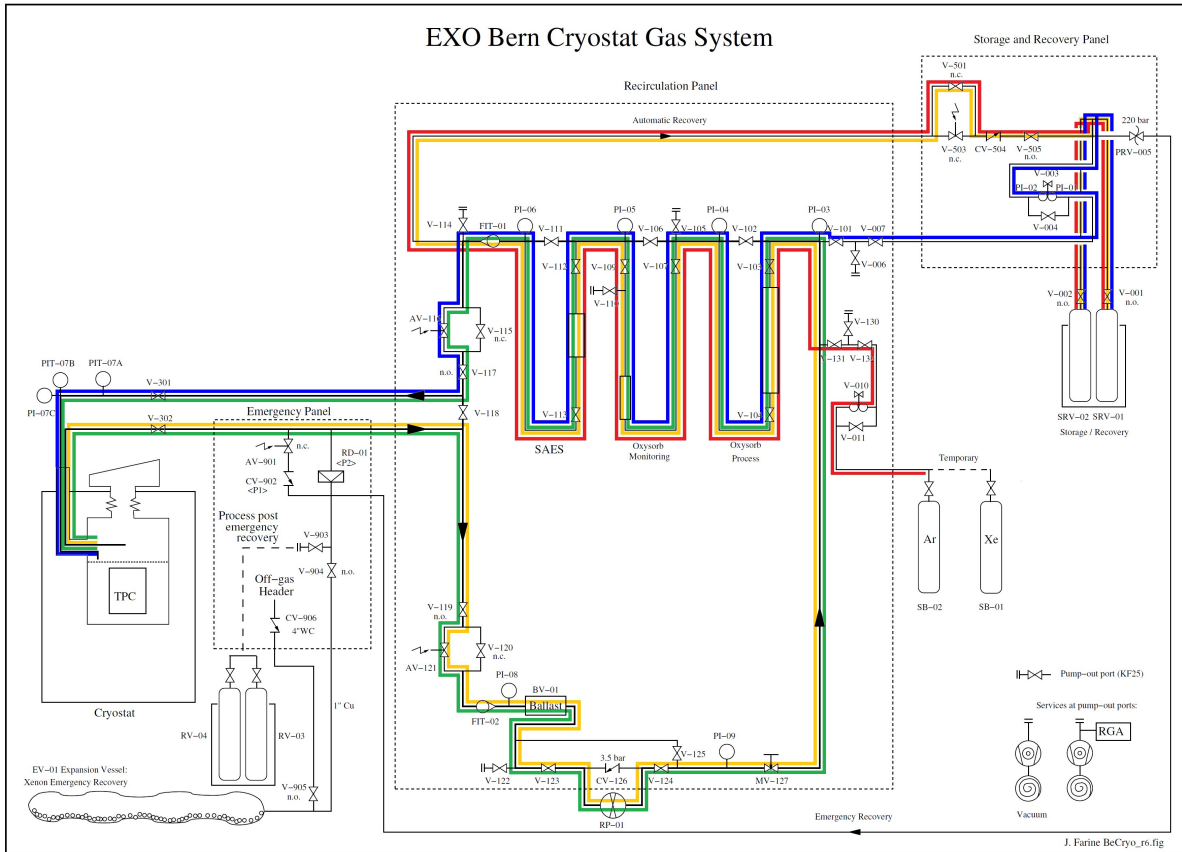


Figure 4.12: Scheme of the gas handling system with the gas flow highlighted for the following tasks: red - gas injection from external bottles, blue - filling from storage bottles to the cryostat, green - gas circulation, and yellow - gas recovery. For all tasks, each filter can individually be by-passed.

To fill gas from the storage bottles (SRV-01 and SRV-02) to the cold cryostat, the gas bottles have to be opened (V-001 and V-002) and the pressure at the pressure regulator (V-003) has to be set in the range from 1 barg to 2 barg. Thereafter, the gas flows (through the filters) via a flow meter (FIT-01) into the cryostat where it condenses. The average condensation rate is about 25 SLPM. Once the cryostat is filled, the pressure regulator has to be closed. To circulate the gas, the inlet of the gas panel (V-302) has to be opened and the circulation pump (diaphragm gas circulation pump by KNF) (RP-01) is started. The circulation pump generates a pressure gradient over it self and forces the gas to circulate through the filters back to the cryostat. The pump generates a pulsed flow which disturbs the reading of the second flow meter (FIT-02). To

smooth out the flow in the flow meter, a ballast volume (BV-01) is added between the flow meter and the pump. To recover the gas back to the storage bottles, the recovery dewar has to be filled with liquid nitrogen. The level of the liquid nitrogen is measured and maintained at a set level by commercial level meter.

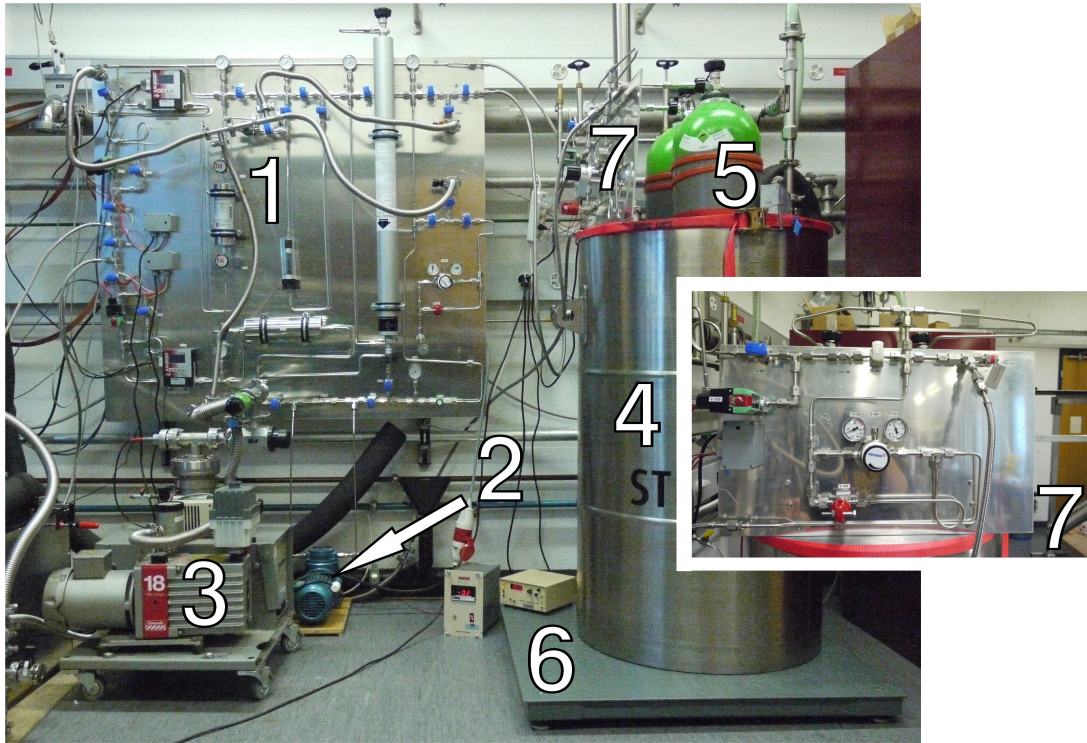


Figure 4.13: Photograph of the gas handling system. 1- the recirculation panel, 2- the recirculation pump, 3- a turbo molecular pump, 4- the recovery dewar, 5- the storage and recovery bottles, 6- the balance, and 7- the storage and recovery panel.

The cold storage bottles freeze the xenon, and thus, allow to cryo-pump the gas. To start manual [automated] recovery, the valve V-501 (V-503) has to be opened. The xenon is then pumped through a check-valve (CV-504) into the bottles. This check-valve protects the system from a pressure burst in case the storage bottles warm up. To allow for xenon accounting, the recovery system is placed on a balance. During the filling phase and after a completed recovery, the amount of xenon in the storage bottles can be estimated by the weight indicated by the balance. To monitor the system during operation, several manometers are installed on the gas handling panel (PI-01, PI-03, PI-04, PI-05, PI-06, PI-08, and PI-09). Hence, an operator can check the state of the system on a glance — even during a power outage. Furthermore, to evacuate and thus clean the gas panel, five pump-out ports are added to the panel. These ports are connected via KF-16 bellows which are then connected to a turbo molecular pump.

During operation with liquid argon, the gas handling scheme is much simpler (see Figure 4.14). Liquid argon is poured via a large Oxysorb filter into the chamber. In the chamber the argon slowly evaporates and is evacuated through a check-valve to air. The liquid argon level drops about 10 cm per day, and hence, argon needs to be refilled every 1-2 days.

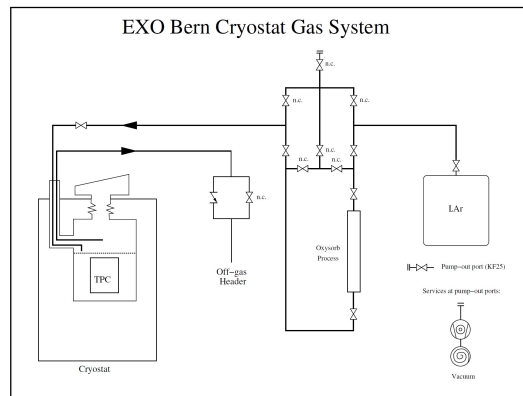


Figure 4.14: Scheme of the argon handling system.

4.3 The EXO-100 slow control system

During operation of the EXO-100 set-up, the state of the cryostat has to be monitored, and moreover, the temperature of the chamber has to be controlled. For this purpose, the EXO-100 set-up is instrumented with different kinds of sensors. These sensors are read-out by the EXO-100 slow control program which is written in LabView. The slow control program processes the information from the sensors and controls valves and heating elements. Moreover, the slow control program writes the state of the set-up to log files. Figure 4.15 shows the EXO-100 control centre.

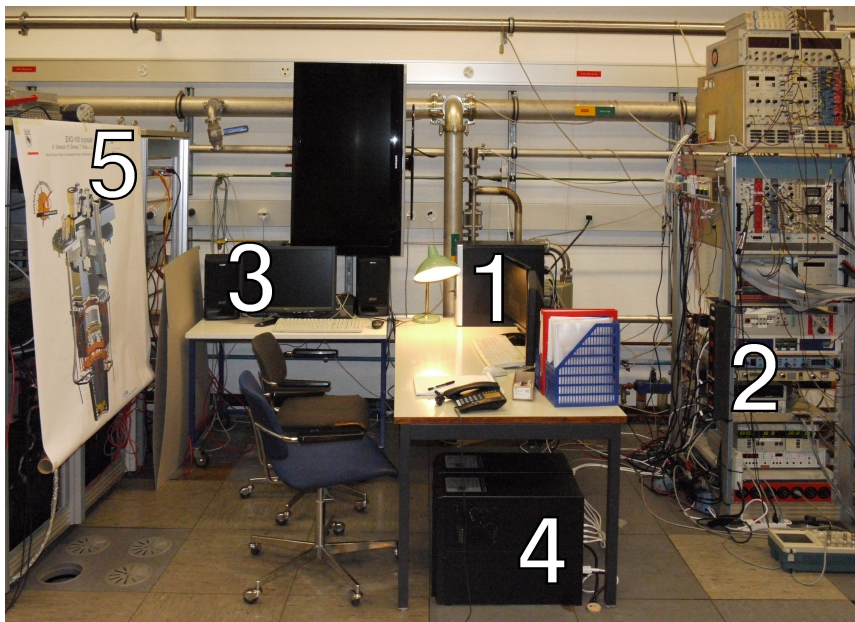


Figure 4.15: Photograph of the EXO-100 control centre. 1- PC running the slow control program, 2- electronic rack with read-out modules of most sensors, 3- PC used for data acquisition, 4- uninterrupter power supplies, and 5- technical drawing of the EXO-100 cryostat.

The monitored parameters are the temperature of the cryostat, the pressure in the three separated volumes — main chamber, liquid nitrogen tank, and insulation space —, the liquid levels — in the liquid nitrogen tank and the chamber —, and the gas flow — inlet and outlet of the chamber, liquid nitrogen tank, and recovery dewar. The temperature of the cryostat is measured with up to 10 *platinum resistance thermometers Pt-100s* and 4 *thermocouples TCs*. These temperature sensors are distributed over the inner chamber and the liquid nitrogen tank. Two temperature controller units are used to read-out the Pt-100s (Oxford Instruments, model MercuryITC and model ITC-503). Together these units allows to read 10 sensors and have four independent heater out puts. The heater out puts can be used to control the temperature of a cryo-camera (see Chapter 6). The TCs are read-out with a thermocouple input module (National Instruments, model NI 9211) which is inserted into a chassis (National Instruments, model NI cDAQ-9172). All three units are separately interfaced with the slow control program, and thus, the temperature reading contains redundancy. The current values of each sensor, as well as its history, is displayed in one of the slow control program's windows (see Figure 4.16). Each sensor can be labelled, however, only the label "regulation" has a function. Sensors labelled as "regulation" are used to calculate (mean of all "regulation" sensor) the temperature of the cryostat.

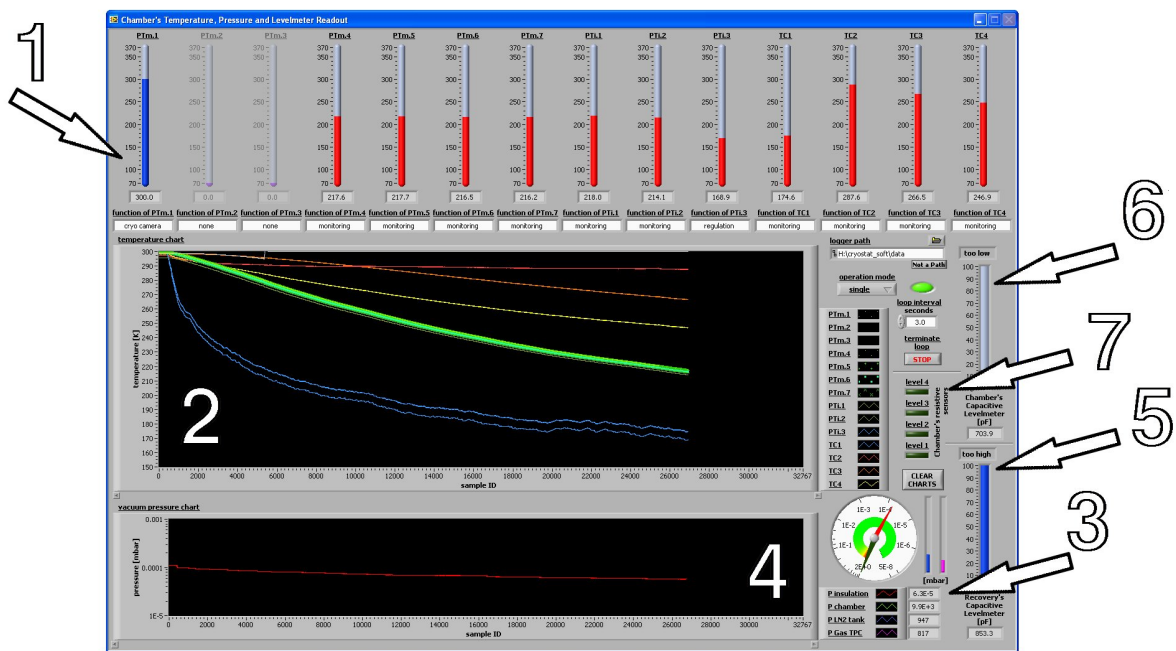


Figure 4.16: The "Temperature" window of the EXO-100 slow control program. 1 - The current temperature of a sensors and its label, 2 - chart with the temperature history, 3 - the current pressure, 4 - chart with the pressure history, 5 - CLM of the recovery dewar, 6 - CLM of the chamber, and 7 - RLM of the chamber.

Depending on the pressure range, the pressure is measured with one of three different types of pressure gauges. Piezo transmitters (Pfeiffer-Vacuum, model APR-266), Pirani gauges (Pfeiffer-Vacuum, model TPR-010), and cold cathode gauges (Pfeiffer-Vacuum, model IKR-050) for the pressure ranges of 10 bar to 1 mbar, 1 bar to 8×10^{-4} mbar, and 5×10^{-3} mbar to 2×10^{-9} mbar,

respectively. To measure the vacua in the chamber and the insulation space, both are instrumented with a pair of a Pirani and a cold cathode gauge. These gauges are read-out with a pressure gauge controller (Pfeiffer-Vacuum, model TPG 300) which automatically selects the appropriate gauge type. To measure the over-pressure in the chamber and the liquid nitrogen tank, both volumes are instrumented with Piezo transmitters. Due to the importance of the pressure in the chamber (see Section 4.4) four independent transmitters are mounted to the chamber volume. The five transmitters are read-out with three controllers (Pfeiffer-Vacuum, model 252 A). One sensor per volume is interfaced with the slow control program. The remaining three are used by the safety system.

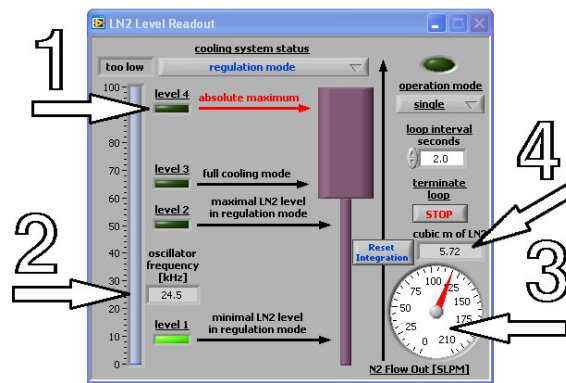


Figure 4.17: The "LN2 Level" window of the EXO-100 slow control program. 1 - The RLM of the liquid nitrogen tank, 2 - CLM of the liquid nitrogen tank, 3 - current gas flow at the exhaust line of the liquid nitrogen tank, and 4 - integrated nitrogen consumption.

Two different level meter probe types are used to measure the liquid levels in the liquid nitrogen tank, the chamber, and the recovery dewar (see Appendix B). The chamber and the liquid nitrogen tank are both instrumented with a *resistive level meter RLM* and a *capacitive level meter CLM*. These level meters are read-out by custom made circuits and interfaced to the slow control program with a multifunction DAQ unit (National Instruments, model NI USB-6009). To prevent overheating, the RLM in the chamber is interlocked with the pressure gauge of the chamber. The RLM is automatically turned off if the pressure in the tank is lower than 0.7 bar. The recovery dewar is only instrumented with a CLM which is read-out with a liquid level controller unit (American Magnetics, Model 180). This unit controls the filling valve of the recovery dewar — independently from the slow control program. The level meters of the chamber and the recovery dewar are displayed in the same window of the slow control program as the temperatures and pressures (see Figure 4.16). The level meters of the liquid nitrogen tank are displayed in a separate window (see Figure 4.17).

To measure the consumption of liquid nitrogen, the flow of the evaporated nitrogen is measured. Therefore, at the exhaust of the liquid nitrogen tank and at the recovery dewar a flow meter is installed (Teledyne Hastings, laminar flow element model L-5S and mass flow transducer model HS-10S). These flow meters are interfaced to the slow control program where the actual flow and the integrated flow are displayed (see Figure 4.17 and 4.18). Furthermore, two digital mass flow meters are mounted on the gas handling panel (Aalborg, model DFM37). These flow

meters measure the flow of the detection medium at the inlet (FIT-02) and outlet (FIT-01) of the panel. In addition, these flow meters measure the temperature and pressure of the gas.

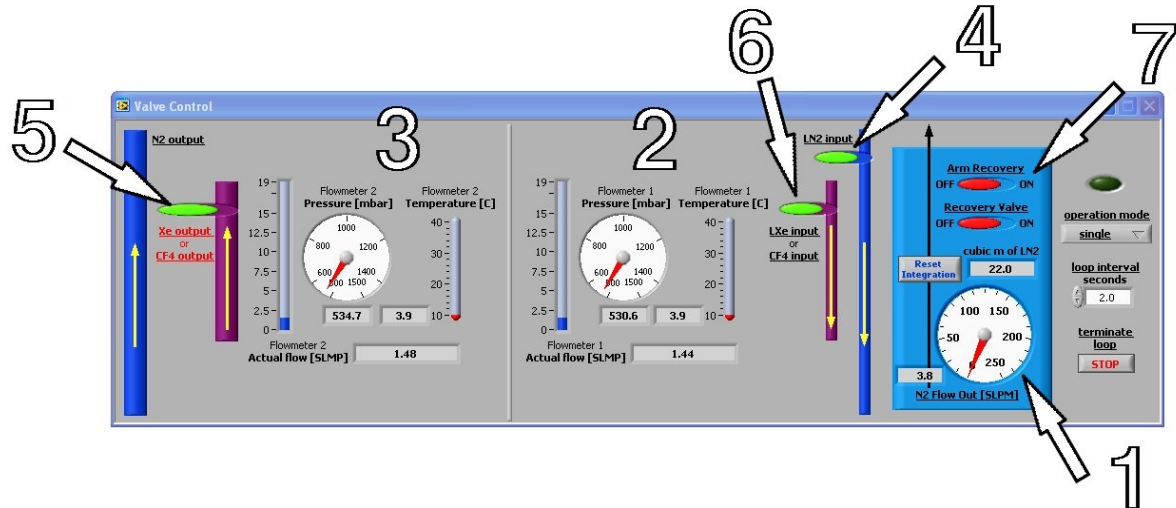


Figure 4.18: The "Valve Control" window of the EXO-100 slow control program. 1 - The current nitrogen gas flow at the recovery dewar, 2 - data from flow meter FIT-01, 3 - data from FIT-02, 4 - control of the filling valve of the liquid nitrogen tank, 5 - control of valve AV-121, 6 - control of valve AV-116, and 7 - manual control of auto recovery (V-503).

The slow control program allows to control four electric valves. Firstly, the filling valve of the liquid nitrogen tank. However, the filling valve is interlocked with the pressure gauge of the liquid nitrogen tank. The valve is automatically forced close if the pressure in the tank is higher than 1.3 bar. Secondly and thirdly, the inlet (AV-121) and outlet (AV-116) valves at the gas handling panel (see Figure 4.12. And lastly, the automated recovery valve at the recovery dewar (V-503). To prevent accidental recovery, the recovery needs to be armed before it can be opened. Furthermore, two sets of heaters can be controlled by the program (see Figure 4.19). To precisely regulate the temperature of the chamber, the regulation resistors at the copper plate are connected to a regulated power supply (Siemens, model SITOP power flexi). With the slow control program, the dissipated heat can be set between 0 W to 120 W. The second heaters are the evaporation resistors in the liquid nitrogen tank. They are powered with a power supply (Electronic Measurements INC., model EMS 20-50) which can supply up to 50 A at 20 V. Thus, the evaporation resistors can dissipate up to 600 W into the liquid nitrogen tank. With the slow control program these resistors can be switched on or off.

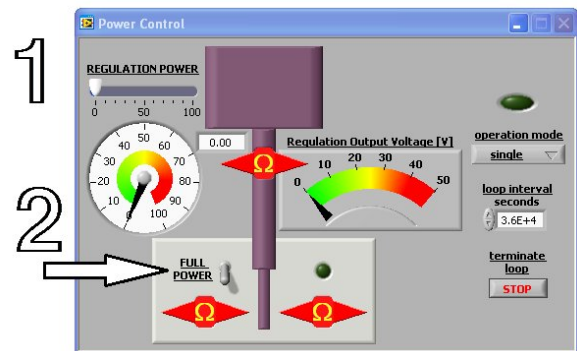


Figure 4.19: The "Power Output" window of the EXO-100 slow control program. 1 - Control of the regulation resistors and 2 - control of the evaporation resistors.

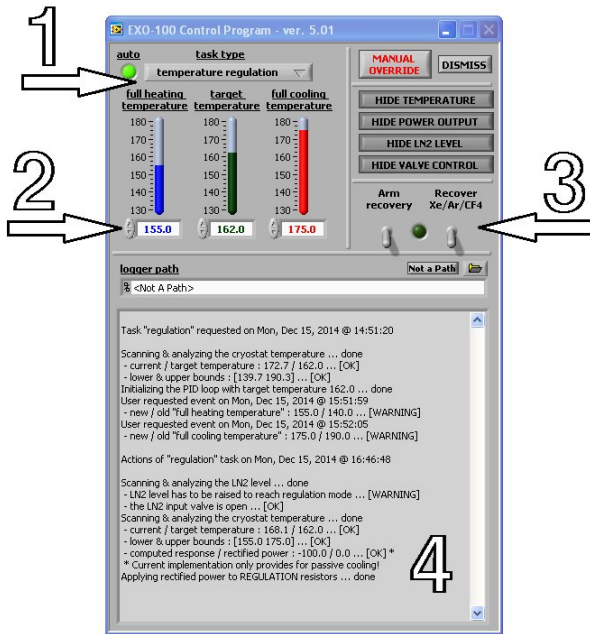


Figure 4.20: The main window of the EXO-100 slow control program. 1 - Task selector, 2 - setting of the three temperatures, 3 - engaging auto recovery during automated operation, and 4 - report of the programs status.

nitrogen level between level 1 and level 2 of the RLM (the lowest two). Thereafter, the program uses a *proportional-integral-derivative PID* feedback loop to control the regulation resistors, and thus, matches the current temperature of the cryostat with the set "target temperature". If for any reason the cryostat temperature leaves the defined range, the program will quit the task and return to "idle". If the "strong heating" task is selected and the cryostat temperature is below the "full heating temperature", the program closes the filling valve and puts the maximal power to the regulation resistors. Once the cryostat temperature exceeds the "full heating temperature", the task is stopped and the program returns back to "idle". Finally, if the "full automation" task is selected, the program analyses the current temperature and selects the appropriate task. Furthermore, the program can adapt to a changing cryostat temperature and automatically switch between tasks.

Users present in the lab can use the EXO-100 control centre to monitor and control the set-up. Moreover, remote users can connect to the *Virtual Private Network VPN* of the University. Thereafter, they can use a *Remote Desktop Protocol RDP* to connect to the EXO-100 control centre. Consequently, remote users can gain full control over the set-up.

4.4 The safety systems and the emergency handling

During operation of the EXO-100 set-up, a failure of any critical component can lead to an undesired or even dangerous state of the set-up. To protect personnel in the laboratory and

The slow control program does not only allow to manually control these valves and heaters but it also provides some fully automated tasks. In the main window of the program (see Figure 4.20) the user can select one of five task: idle, strong cooling, temperature regulation, full heating, and full automation. Furthermore, three temperature points have to be set: full heating temperature, target temperature, and full cooling temperature. If "idle" is selected, no actions are taken by the program, however, all sensors are read-out and their values are logged. If "strong cooling" is selected, the program fills the liquid nitrogen tank up level 3 (2nd from top) of the RLM and shuts off all heating elements. The program will remain in this state until the current temperature (mean of all sensors defined as "regulation") of the system drops below the set "full cooling temperature". Thereafter, the program resets the task to "idle". If "temperature regulation" is selected and the current temperature of the system is between the "full cooling temperature" and the "full heating temperature", the program sets the liquid

to prevent any loss of xenon some safety features are added to the set-up. The main dangers for personnel is that of suffocation and of a rupturing component (e.g. cryostat and gas panel). Suffocation is imminent if a lot of gas is exhausted to the laboratory, and thus, air is displaced. To protect against suffocation, the oxygen concentration in the laboratory is monitored and a siren is activated if the oxygen content drops below 18%. In this case, personnel in the laboratory has to open all windows and leave the room until the oxygen content recovers to normal. During the alert condition, the liquid nitrogen line is shut off to prevent additional nitrogen from displacing air in the laboratory. Furthermore, an over-pressure building up because of an uncontrolled temperature increase may lead to the explosion of a component with parts flying through the laboratory. This can occur if liquefied gas is trapped and warms up.

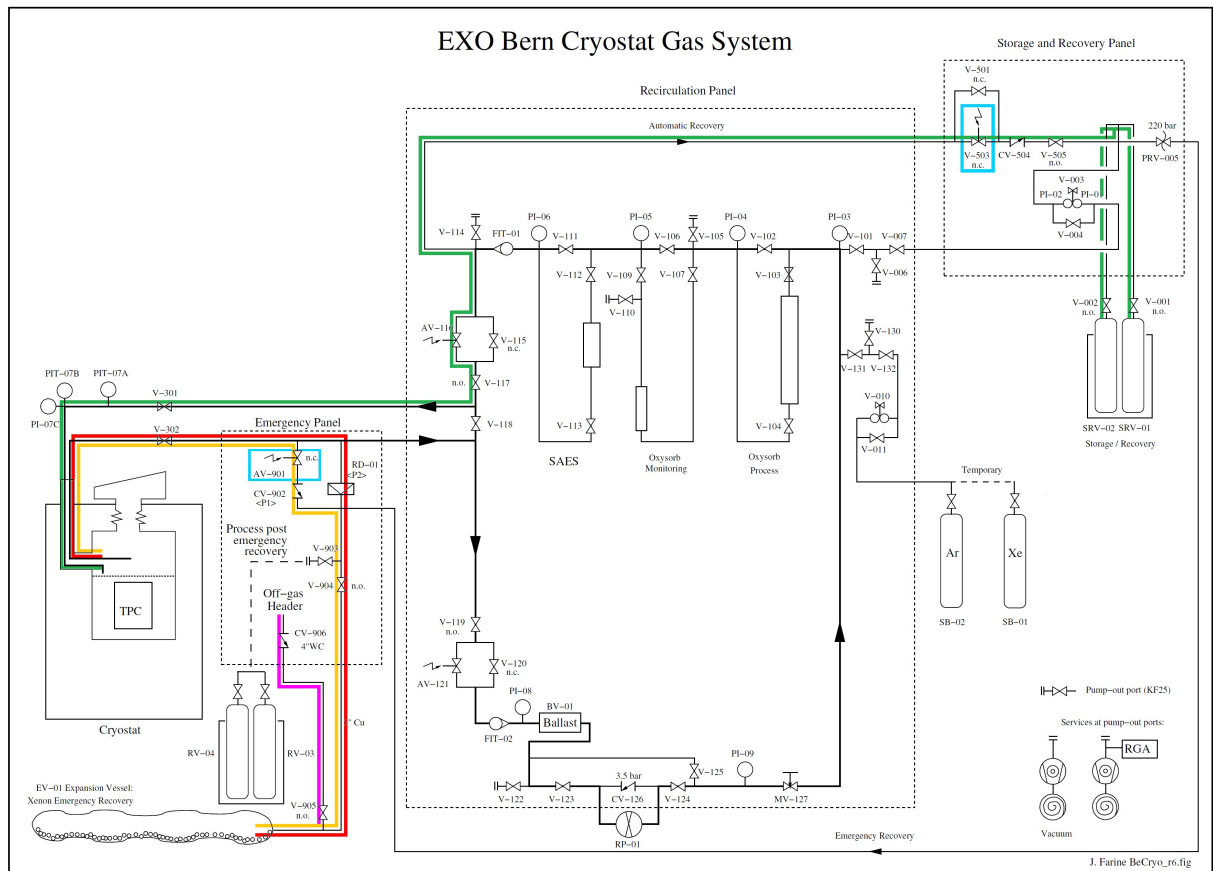


Figure 4.21: Scheme of the gas handling system with the gas flow highlighted for the following emergency levels: green - automated recovery, yellow - partial dump to balloon, red - complete dump to balloon (rupture disk), and pink - release to air. The two automated valves are highlighted in blue.

The EXO-100 set-up has three separate volumes in which a high pressure could lead to a catastrophic failure. Firstly, pressure could build up in the liquid nitrogen tank of the cryostat if the exhaust line freezes or if accidentally the valves of both exhaust lines (direct and cooling loop) are closed. Therefore, the tank is protected with an overpressure valve. Secondly, pressure could build up in the vacuum vessel if the chamber or the liquid nitrogen tank suddenly fail and

release their cryogenic liquids in the warm vacuum vessel. Therefore, also the vacuum vessel of the cryostat is protected with an overpressure valve. Lastly, pressure could build up in the chamber or the gas handling system. Rupturing of any component in this gas cycle would lead to loss of xenon, as well as potentially harm personnel. However, as any loss of xenon has to be prevented, a sophisticated emergency handling scheme is implemented for the chamber. Details on the emergency handling scheme are described later in this section.

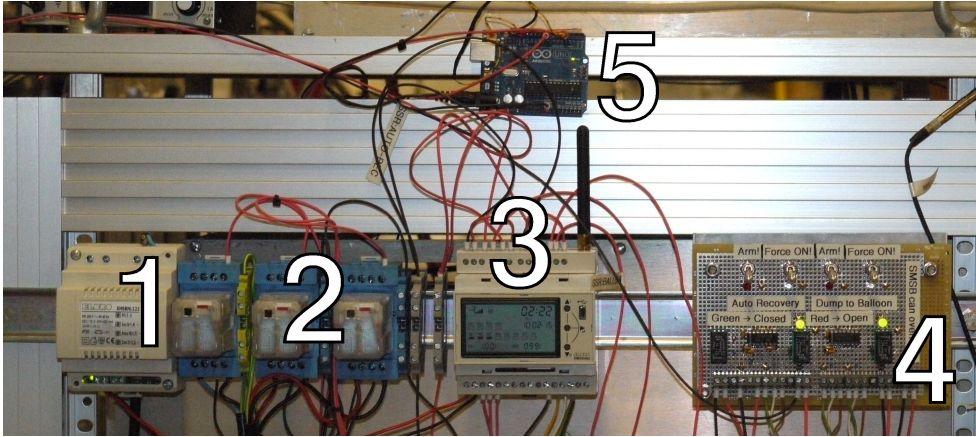


Figure 4.22: Photograph of the safety system control. 1- power supply, 2- relays being switched in case of an anticipated failure mode, 3- the text message control and notification device, 4- control PCB allowing to arm and manually control the two automated valves, and 5- an Arduino UNO monitoring the slow control PC and switching a relay (2) in case the PC crashed.

To prevent any loss of xenon, we performed a failure mode and effects analysis of the set-up. Failures which may endanger the xenon can be categorised in two types: leaks and failures leading to loss of temperature regulation. A leak in the gas handling system or in the chamber of the cryostat clearly leads to loss of xenon. To be sure that no leak is present — leading to a total leakage rate larger than $1 \times 10^{-6} \text{ mbar l s}^{-1}$ — the chamber and the gas handling system are carefully checked for leaks with a helium leak detector. The chance of a large leak opening within the tested pressure range was assessed to be unlikely. Hence, no automated action is foreseen to deal with such a scenario. Moreover, during operation of the set-up with xenon, the level of the

Emergency level	Condition	Action
0	$p_v < 2 \text{ bar}$	normal operation
1	$2 \text{ bar} \leq p_v < 3 \text{ bar}$	auto recovery
2	$3 \text{ bar} \leq p_v < 4 \text{ bar}$	auto recovery + partial dump to balloon
3	$4 \text{ bar} \leq p_v$	auto recovery + rupture disk
4	full balloon	release to air

Table 4.1: Overview of the emergency levels of the EXO-100 gas handling system with their corresponding actions.

liquid xenon is constantly monitored. Any major loss of xenon would be detected with the level meters and the cryo-camera. The second type of failure leads to an uncontrolled temperature of the chamber. Depending on the failure mode, the chamber is either cooled down below the targeted temperature or warmed up. Various failure modes lead to overcooling of the chamber (e.g. failure of the resistive level meter in the liquid nitrogen tank, failure of the liquid nitrogen filling valve, failure of the regulation resistors, or failure of the slow control software). In these cases, the xenon gets cooled and will soon start to freeze. Consequently, the operation of the TPC, as well as the data acquisition, is affected and needs to be stopped. However, freezing of the xenon does not lead to any loss of it. Hence, failure modes leading to uncontrolled cooling were assessed to be harmless, and thus, no automated action is implemented to handle these failures. However, failure modes leading to warming of the xenon, as well as the chamber, may result in a catastrophic state of the system if no countermeasures are taken in time. The most critical and likeliest failure modes leading to warming are: power outage in the lab, crashed PC or slow control software, and lost connection to temperature sensor read-out module. To get through a power outage, two *uninterrupted power supplies UPSs* are added to the set-up. Their capacity is large enough to power all essential parts of the set-up for more than an hour. Furthermore, a text message notification and control device (Elbro, model SMS-Butler SMSB482) is added. This device monitors the power line and the state of the slow control program (see Figure 4.22). In case of a failure, it sends distinct text messages to a group of users. Consequently, these users are alerted and can try to rectify the fault.

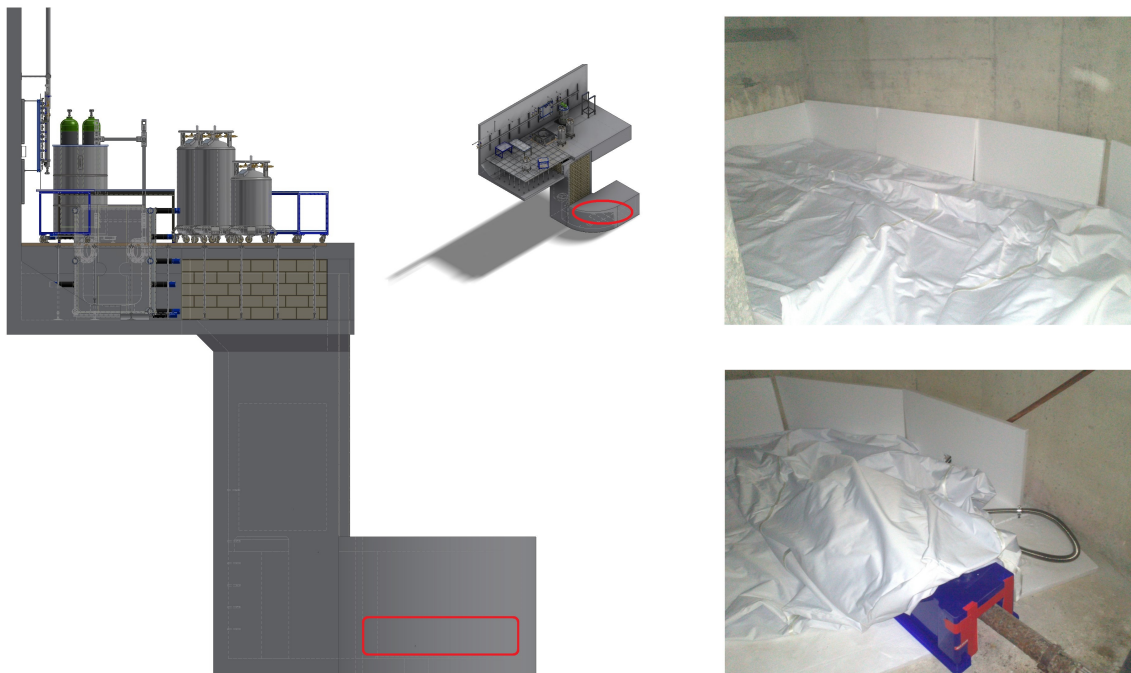


Figure 4.23: A shaft leads to a cavity located 6 m below the laboratory floor. In the cavity the balloon is installed (marked in red). The balloon is made from $150\ \mu\text{m}$ (6 mil) thick polyurethane. To protect it from mechanical damage, it is wrapped into a nylon sleeve. Furthermore, the cavity is lined with plates made from expanded polystyrene.

In case a failure cannot be rectified in time, the xenon will warm up and the *vapour pressure* p_v will increase. Therefore, p_v is used as the indicator for the state of the system. Based on p_v , several emergency levels are defined (see Table 4.1). If p_v exceeds 2 bar, the electro magnetic valve *AV-503* is opened and the system starts to recover xenon to the storage bottles. This valve remains open until p_v drops below 1.9 bar. In case the automated recovery is not sufficient to stabilise p_v , and thus, p_v eventually exceeds 3 bar, the electro magnetic valve *AV-901* is opened and xenon is partially dumped to a balloon *EV-01* (see Figure 4.23). This valve remains open until p_v drops below 2.9 bar. If the partial dump and the automated recovery are not sufficient to limit p_v , the rupture disk *RD-01* opens at about 4 bar and the xenon is released to the balloon. The capacity of the balloon is 10 m³ while the total amount of xenon in the system is 16 m³. Therefore, xenon is released to air if the balloon is totally filled. The system informs the users via text messages when p_v crosses 2 bar or 3 bar. Furthermore, users can request the current p_v and remotely open or close the two valves by sending text messages to the system. In order for the system to automatically response to an increased p_v , these automated actions need to be armed at the control *printed circuit board PCB*.

The EXO-100 detector

The central component of the EXO-100 detector is a Time Projection Chamber TPC (see Section 5.1). With the TPC, radioactive decays and cosmic rays can be detected and studied. To separately study internal radioactivity and short lived radioactivity induced by cosmic rays, as well as cosmic rays themselves, the TPC is surrounded by a muon veto (see Section 5.2). To select and to acquire the desired data type, signals from the TPC and from the muon veto are combined in a trigger logic. Whenever the trigger logic triggers on an event, data is acquired from the TPC with a Data Acquisition DAQ system (see Section 5.3). To study ion extraction from the TPC, it is planned to instrument the current detector with a displacement device — on which an ion grabbing probe can be mounted — and with an external alpha detector. Both devices are not yet built. In Appendix C the current status of the R&D performed for the displacement device is shown.

5.1	The EXO-100 time projection chamber	53
5.1.1	The detection volume	55
5.1.2	The charge-collection system	58
5.1.3	The light-collection system	62
5.2	Muon veto and muon trigger	64
5.3	DAQ and trigger logic	67

5.1 The EXO-100 time projection chamber

The EXO-100 TPC is installed in the inner chamber of the EXO-100 cryostat (see Figure 5.1). It is suspended from an aluminium plate with many threaded holes. This plate functions as the base for all internal instrumentation (i.e. TPC, level meters, displacement device, and alpha detector), thus it is named base plate. The base plate itself is supported with four threaded rods via thermal barriers from the top flange of the inner chamber. To ground the base plate, one of the thermal barriers is by-passed with a wire. During operation of the TPC, the chamber is filled

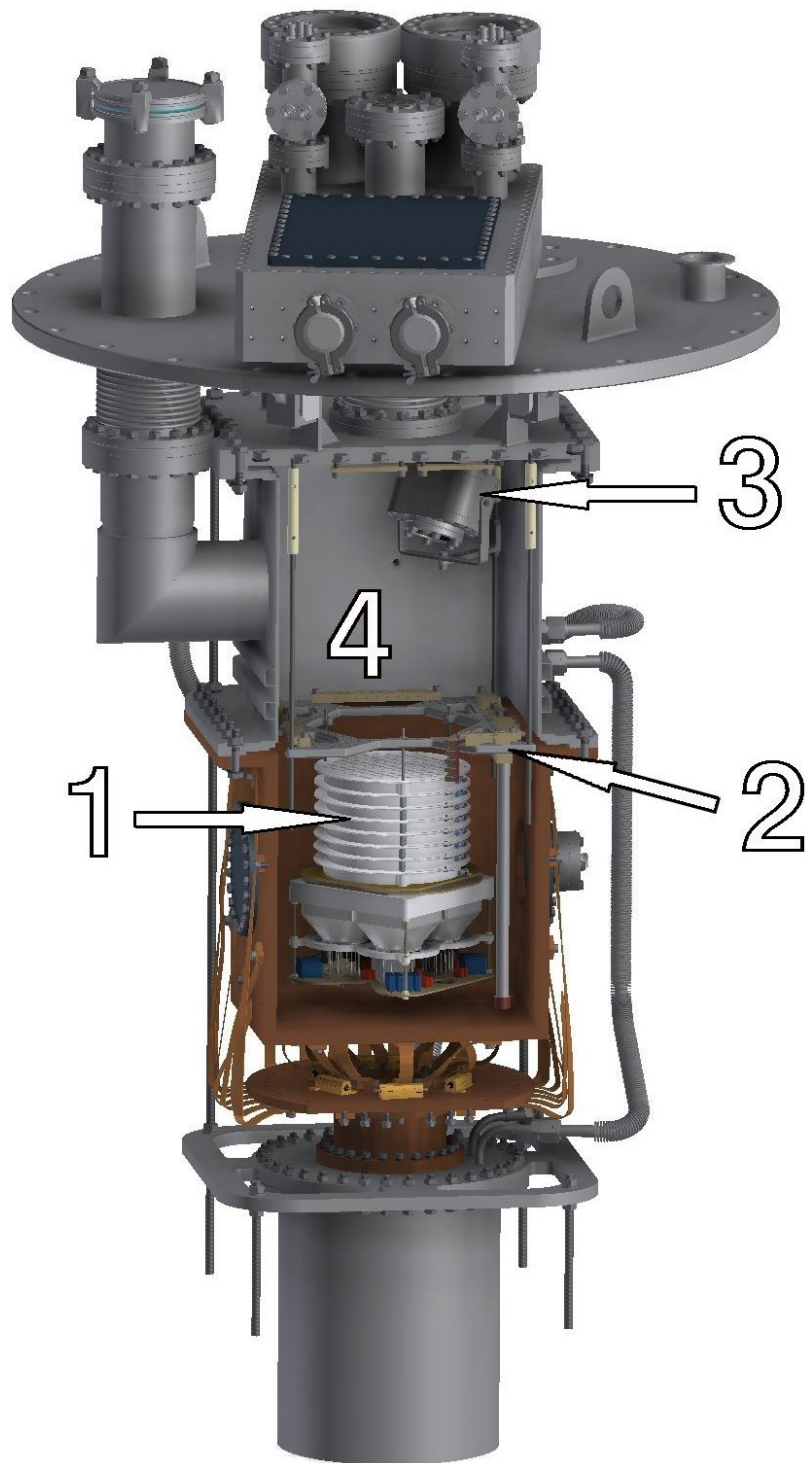


Figure 5.1: CAD render of the EXO-100 cryostat. The inner chamber is cut open to reveal the TPC (cables are omitted). 1- the TPC, 2- the base plate with attached level meter probes, 3- the cryo-camera, and 4- reserved space for the displacement device.

up to the base plate with the liquid phase of the detection medium. Hence, the TPC is fully immersed in the liquid detection medium. The TPC consists of three components: the detection volume, the charge-collecting system and the light-collecting system (see Figure 5.2).

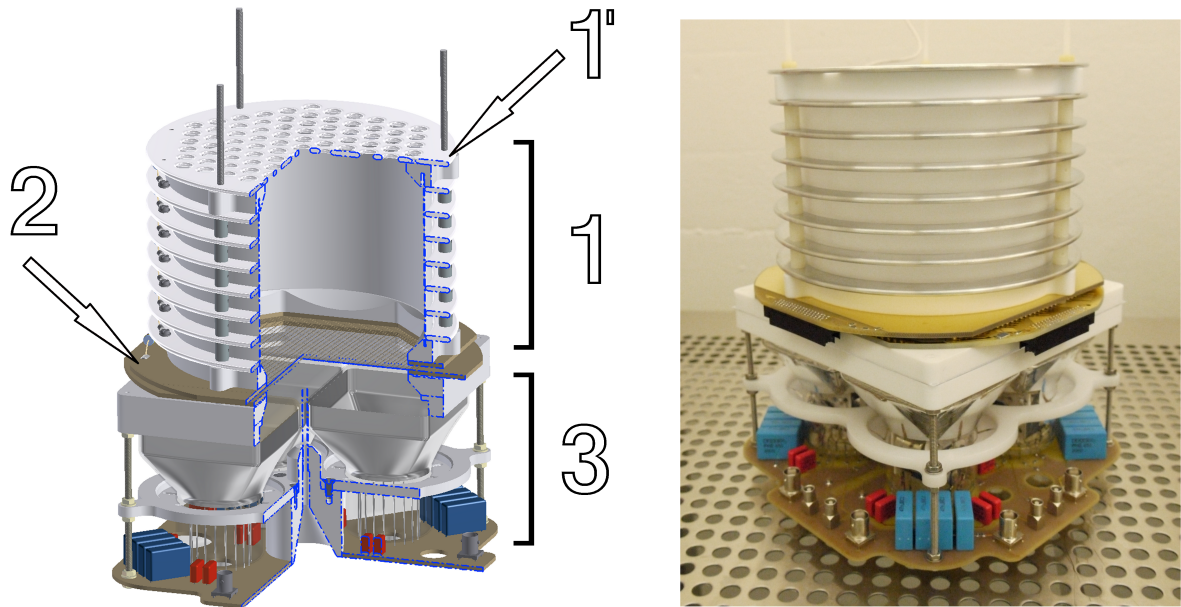


Figure 5.2: The EXO-100 TPC. Left, section view of the TPC: 1- detection volume, 1'- cathode, 2- charge-collecting system, and 3- light-collecting system. Right, photograph of the assembled TPC.

5.1.1 The detection volume

An electrical field is applied to the detection volume to drift the deposited charge towards the charge read-out planes. To create the electric field, a field cage is used. It is made from a cathode, an anode, part of the read-out planes, and several metal field-shaping rings which form the boundary of the detection volume. The field cage is specifically designed to give the displacement device access to any region in the detection volume (see Figure 5.3). Depending on the orientation of the field cage, the displacement device accesses the detection volume either through the cathode or through a gap between two rings. To allow for access through the cathode, several holes are made in it. To allow for access between rings, the field shaping rings are separated by a large gap between them while still providing a homogeneous drift field (see Figure 5.4). The field cage design is modular, and thus, the length of the field cage is variable. Due to the field cages accessibility, as well as its modular design, another group from Bern University showed interest in the TPC. Spare parts were given to them so they could replicate the EXO-100's TPC and test their UV laser calibration system with it [65].

To generate a homogeneous electric field in the detection volume — as seen in Figure 5.4 — the components of the field cage (e.g. the cathode and the rings) have to be at coherent electric potentials. A high voltage supply (Spellman, model SL60PN150/DPM4/FCV/230) is used to control the potential at the cathode (see Figure 5.5). The high voltage from this supply unit is lead via a low pass filter into the vacuum insulation space of the EXO-100 cryostat. From there it

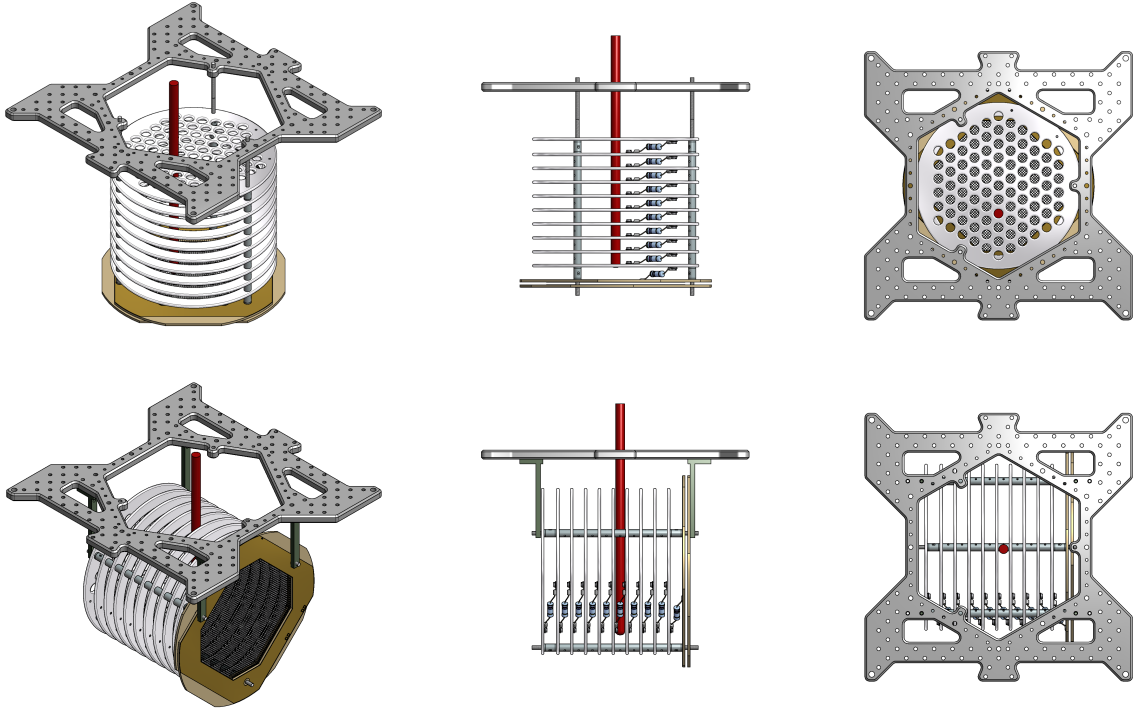


Figure 5.3: Sketch of the field cage and the charge-collecting system. The ion extraction probe — in red — has access to the detection volume. In the top row, the TPC is mounted vertically. The probe accesses the volume through holes in the cathode. In the lower row, the TPC is mounted horizontally. The probe accesses the volume through a gap between two rings. Neither the resistive voltage divider nor any of the pillars block the probes access.

is fed through one of the lids on the copper chamber directly into the liquid phase of the detection medium. This path avoids the gas phase of the detection medium, and thus, reduces the risk of breakdown. In the chamber a PTFE coated cable is used to apply the potential to the cathode. To reduce the potential from ring to ring, a resistive voltage divider is used (see Figure 5.6). To electrically connect neighbouring rings, as well as the cathode with the top ring, resistors are mounted between the rings. The last ring is connected via a resistor to the induction plane PCB (see Subsection 5.1.2). To compensate for the thickness of the induction plane PCB, a small voltage divider is soldered on the PCB. To control the potential at the induction plane, a high voltage supply (channel A of Iseg, model NHQ 222M) is connected via a filter and a feedthrough to the induction PCB. This assembly guarantees a homogeneous electrical drift field independent of the applied cathode and induction potentials. However, due to the filters and the constant current through the voltage divider, the potentials at the induction wire plane diverges from the potential set at its supply unit. Therefore, the potential from both wire planes is measured directly with voltage probes. Lastly, to control the potential of the collection wire plane, and thus to control the electric field between the two wire planes, a high voltage supply (channel B of the Iseg supply) is connected via a filter and a feedthrough to the collection PCB.

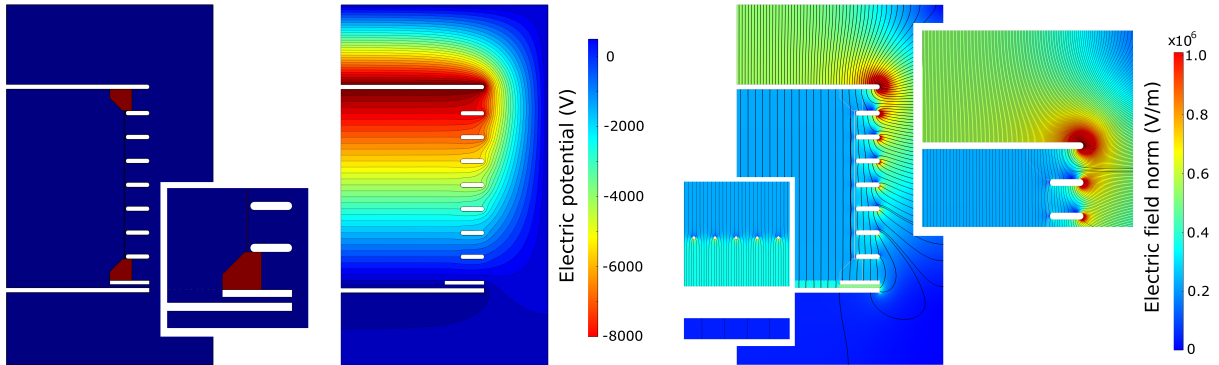


Figure 5.4: Finite element electro-static simulation of the EXO-100 TPC (axial symmetric). On the left the structure of the TPC is shown: white- the cathode, the field shaping rings, and the charge collecting-system, red- the PTFE light reflector, and blue- liquid xenon. In the middle the electric potential is shown. Potentials of -8 kV , 0 kV and $+0.36\text{ kV}$ are applied to the cathode, induction-plane, and collection-plane, respectively. Every 250 V an iso-potential lines is drawn. On the right side the electric field is shown. The color represents the field strength. In black field lines are drawn. The field in the detection volume is homogeneous. At the edge of the cathode the strongest fields occur. However, even there the field in the detection volume is only weakly distorted. A close view on the anode shows the increased field strength between the wire planes.

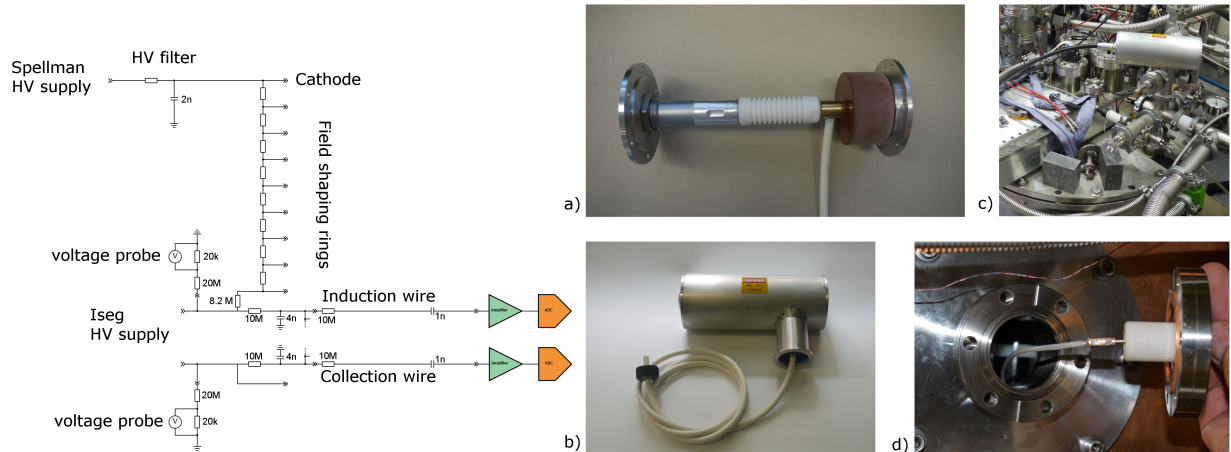


Figure 5.5: The high voltage circuit of the EXO-100 detector. Left, schematic of the circuit. If not indicated, the resistors have a resistance of $47\text{ M}\Omega$. Right, photographs of the high voltage cabling. a) Low-pass filter during assembly. b) Assembled filter with vacuum feedthrough. To prevent discharges in the filter, it is filled with SF_6 gas. c) The filter is mounted on the vacuum insulation space. d) A high voltage feedthrough is used to feed the HV from the vacuum insulation space into the chamber of the cryostat.

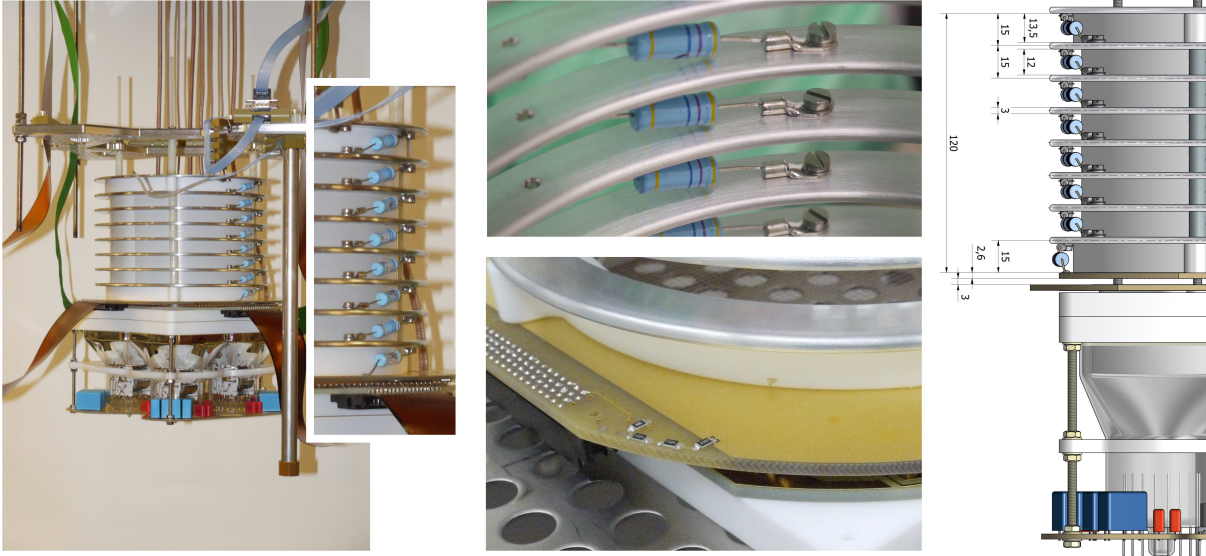


Figure 5.6: The resistive voltage divider distributes the electrical potential coherently over the field cage. Left, photograph of the fully assembled TPC with a zoom of the voltage divider. The last resistor is soldered on to the upper side of the induction-wire plane. Middle top, the resistors are mounted between the rings — in a region with a modest electric field strength. Middle down, on the induction-wire plane, a small voltage divider connects the upper side (last resistor) and lower side (induction potential). Right, technical drawing of the field cage with the voltage divider. The spacing between rings (all dimensions are in mm) leads to a regular resistance-per-length ratio, and thus, to a regular drift field.

5.1.2 The charge-collection system

Negative charge (electrons) generated in the detection volume — due to ionizing radiation — drifts towards the charge read-out planes. To let the electrons drift through the induction-plane, the electric field strength between the wire planes has to be higher than in the detection volume. A field ratio of about 1.8 makes the induction-plane transparent to the electrons. The electrons pass the induction-plane and get collected at the collection-plane. Electrons passing the induction-plane induce a bipolar signal — negative polarity during approaching the plane and positive when departing — on the induction-wires in their vicinity. Thereafter, they get collected at the nearest collection-wire, where they generate a signal with a negative polarity. Examples of the different signal types and the corresponding muon event are shown in Figures 5.7 & 5.8, respectively.

The induction-plane and the collection-plane are identical (see Figure 5.9). They consist of a PCB with 63 metal (98% Cu, 2% Be) wires, each with a diameter of $125\ \mu\text{m}$. The spacing between wires is 2 mm. Each wire is connected on one side with a resistor to the corresponding plane potential. On the other side, a decoupling capacitor of 1 nF connects the wire to the signal read-out cable. The induction-plane is mounted below the field cage. After a gap of 3 mm, the collection-plane is mounted (upside down and rotated by 90 degree). Therefore, the wires of the two planes are oriented orthogonally to each other, allowing to reconstruct the electrons position in x and x . This assembly instruments an area of $147\ \text{cm}^2$. Considering the drift distance of 12.3 cm in the standard configuration, the fiducial volume of the EXO-100 TPC is 1.811 or

5.34 kg of liquid xenon.

To connect the signal channels of both planes — twice 63 channels — to their amplifiers, four flat cables are used. A cable made from Kapton and a commercial ribbon cable are installed per plane. Considering the out gassing of the cables, the Kapton cables are favoured. However, for technical reasons, these Kapton cables are not suited to carrying the induction and collection potentials. The cables are connected to two custom-made feedthroughs mounted on the interface box. On the outer side of the feedthroughs, two transimpedance amplifiers are directly plugged (see Figure 5.10). Thereafter, the amplified signals are connected to the DAQ system (see Section 5.3).

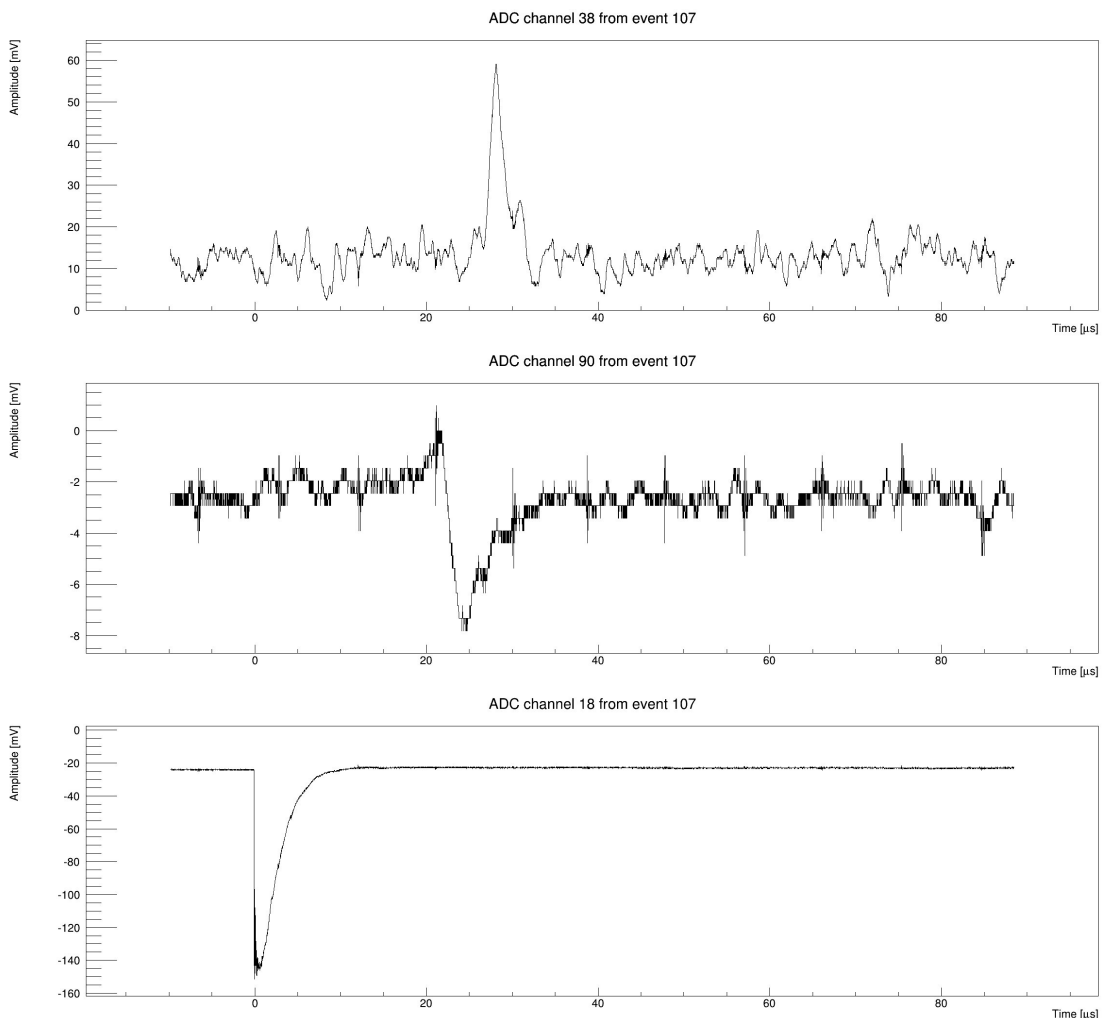


Figure 5.7: Typical amplified signals of a muon event in liquid argon in the EXO-100 TPC — with a drift field of 1 kV cm^{-1} . Top, unipolar collection signal. Middle, bipolar induction signal. Bottom, signal of a PMT at the output of the integrating amplifier. Note that the amplifiers of the collection and induction signals are inverting. These waveforms correspond to three channels of the muon event shown in Figure 5.8.

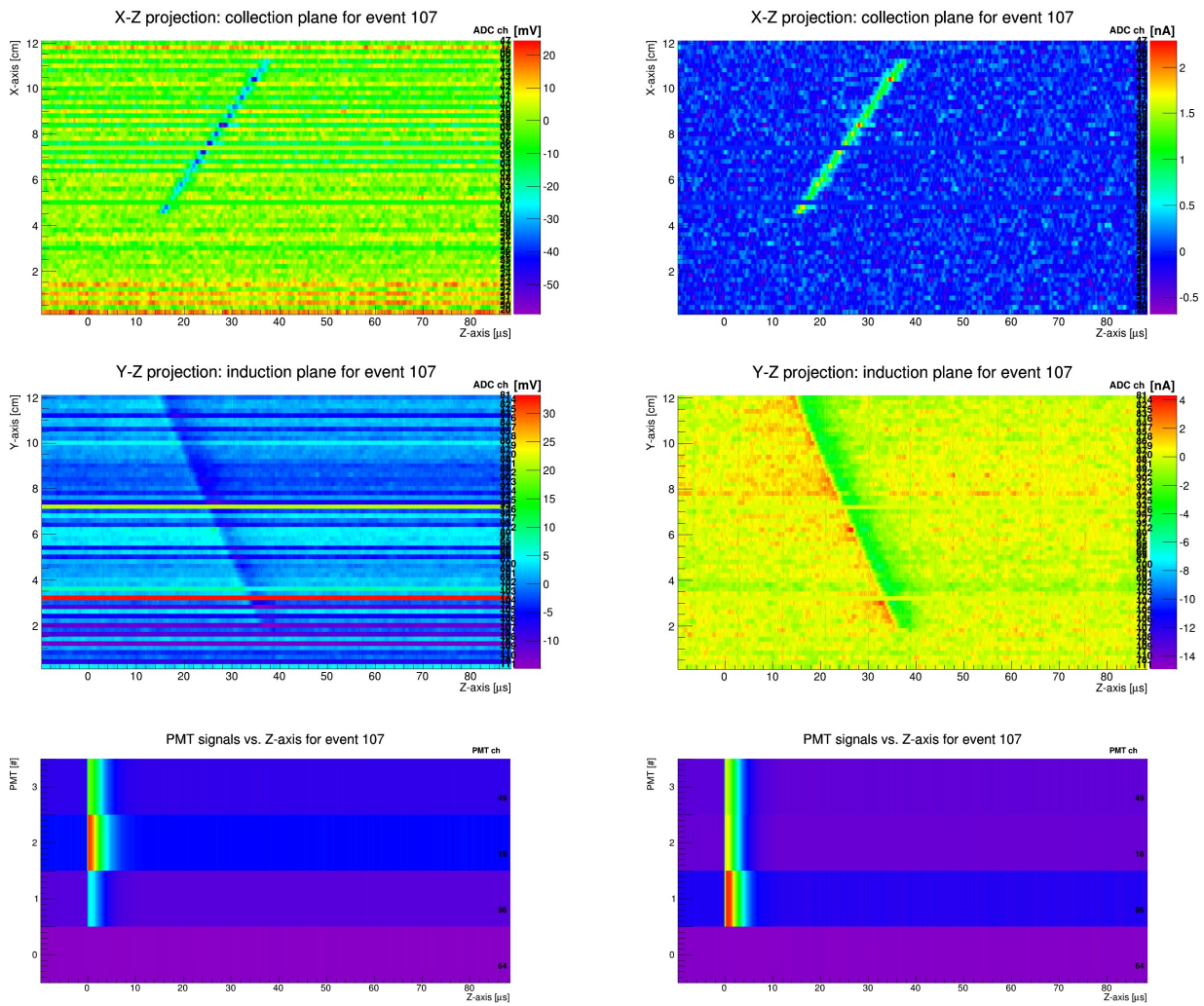


Figure 5.8: A muon event as seen with the EXO-100 detector. As detection medium, liquid argon is used. On the left, the raw signals in mV are shown. On the right, the gain and offset corrected signals in nA are shown. Top row, the signals from the collection channels. Middle row, the signals from the induction-channels. Bottom row, the signals from the four PMT's. The PMT at channel 0 is not functioning.

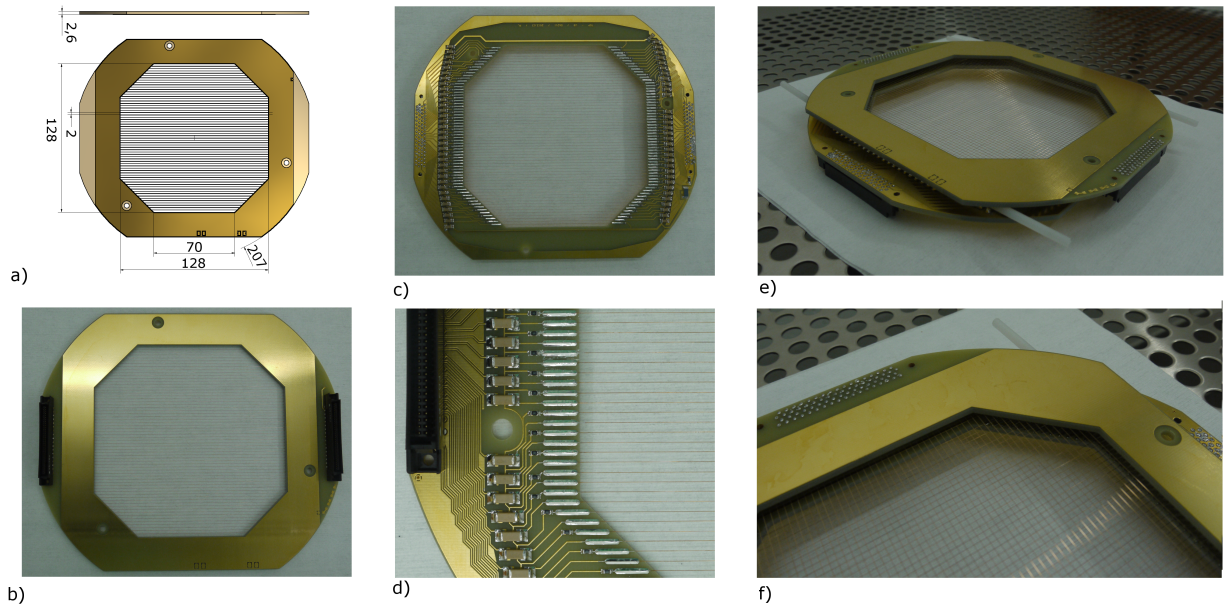


Figure 5.9: The wire planes of the charge-collection system. a) Technical drawing of the PCB (all dimensions in mm). b) The upper side of the wire plane. On the side, two black connectors are mounted. c) The lower side of the wire plane. d) A zoom of the lower side. The decoupling capacitors and the coupling resistors are shown. e) The two wire planes stacked on each other. f) The wires from the two planes are oriented orthogonally to each other.

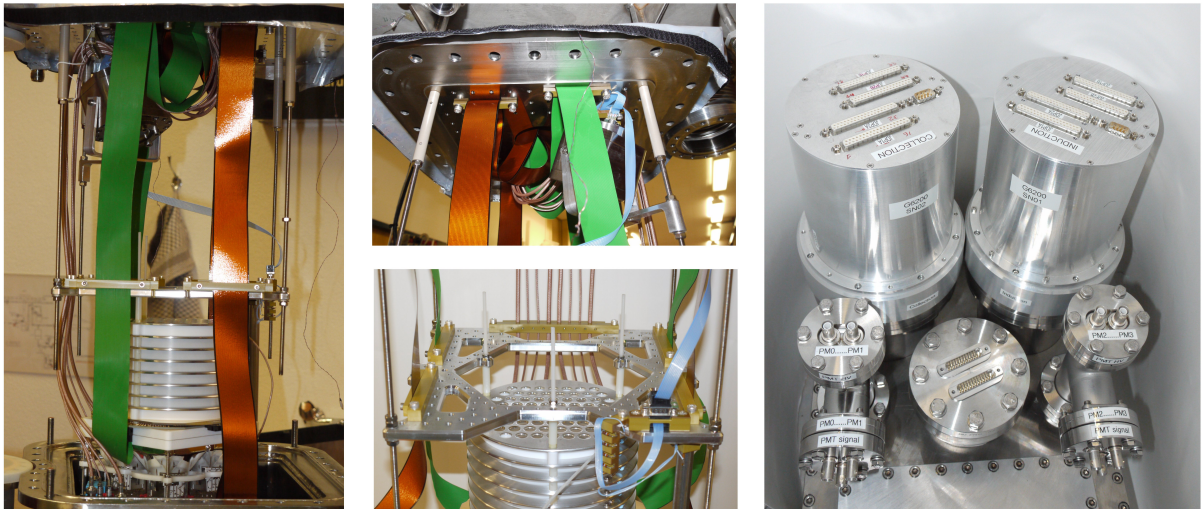


Figure 5.10: Photographs of the cabling of the TPC. Left, the cables of the charge-collection and light-collection system are guided to the top of the inner chamber. The brownish cables are made from Kapton. Middle down, the cables are fixed on the base plate with parts made from PAI. Middle top, the cables are fed through the bellow into the interface box. Right, view on the interface box with the electrical feedthroughs. The charge amplifiers are mounted directly on the feedthroughs.

5.1.3 The light-collection system

The last component of the EXO-100 TPC is the light-collection system. After ionization, scintillation light is emitted isotropically in all directions. To detect the scintillation light, four *Photo Multiplier Tubes PMT's* are installed 1.5 cm behind the collection-wire plane. To detect scintillation light which is not emitted directly on the PMT's — and thus to increase the light detection efficiency — the field cage is lined with a reflector. The reflector is made from *Polytetrafluorethylene PTFE* — better known under its trade name Teflon of the manufacturer DuPont. PTFE is a diffuse reflector for all wave lengths of interest [66]. Moreover, the reflector blocks light from outside of the field cage, which is thus not detected with the PMT's. Therefore, radiation ionizing the detection medium outside of the field cage does neither affect the charge channels nor the light channels of the TPC.

The scintillation light of liquid xenon and liquid argon peaks at a wave length of 175 nm and 124 nm, respectively. However, the PMT model used (Hamamatsu, model R6237-01 MOD with platinum underlay) is not sensitive to wave lengths below 250 nm. Therefore, *TetraPhenyl-Butadiene TPB* is used to shift the wave length of the scintillation light into the visible range. The emission spectra of TPB matches the spectral sensitivity of the PMT (see Figure 5.11). A thin sheet of *Poly(methyl methacrylate) PMMA* — also known as acrylic glass — is placed between the collection-wire plane and the PMT's. The surface of the acrylic glass facing the wire-plane is coated with a thin *Polystyrene PS* film doped with TPB. The acrylic glass with the coating is transparent in the visible, and thus, converted photons pass it and are detected with the PMT's. To increase the UV-photon conversion efficiency, some parts of the PTFE reflectors are coated with a pure TPB coating (see Figure 5.12). To coat PTFE, a special coating technique was applied (see Appendix D for additional information on TPB coating).

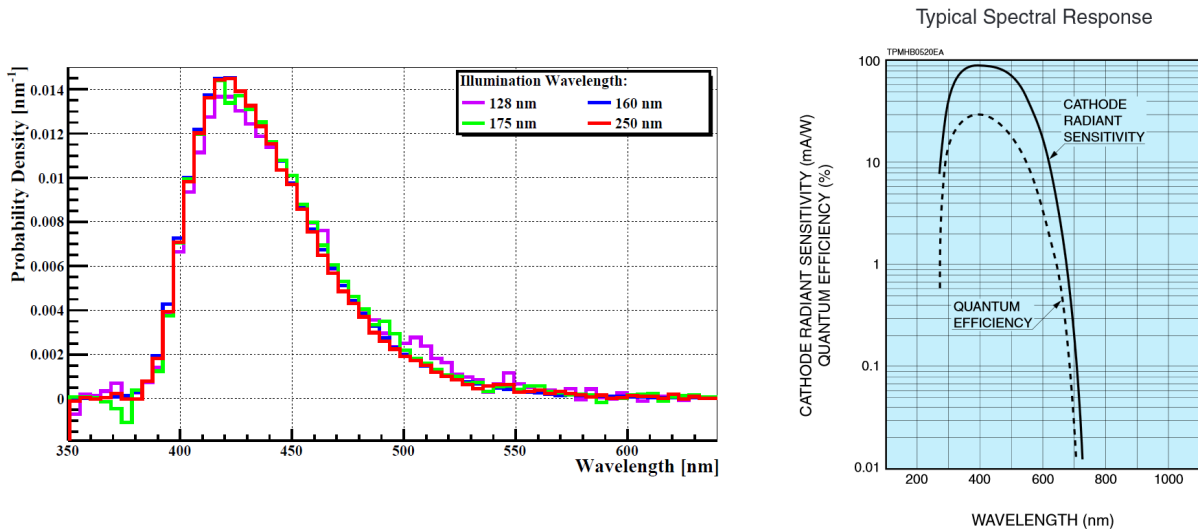


Figure 5.11: The emission spectra of TPB matches the sensitivity curve of the R6237-01 MOD PMT. Left, TPB emission spectra when illuminated with light of different wavelengths [67]. Right, sensitivity curve of the PMT (reprint from corresponding data sheet).

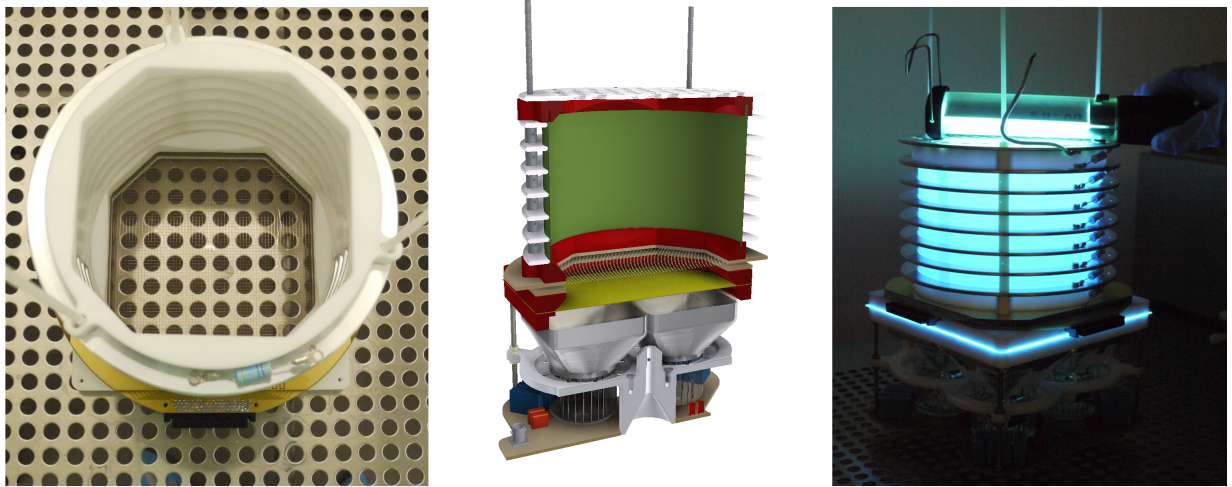


Figure 5.12: The reflectors and wave length shifter of the light-collecting system. Left, photograph of the opened field cage. Middle, schematic section view: red- reflectors made from PTFE without a coating, green- PTFE sheet coated with TPB, and yellow- PMMA glass coated with TPB. Right, the light-collecting system illuminated with UV light.

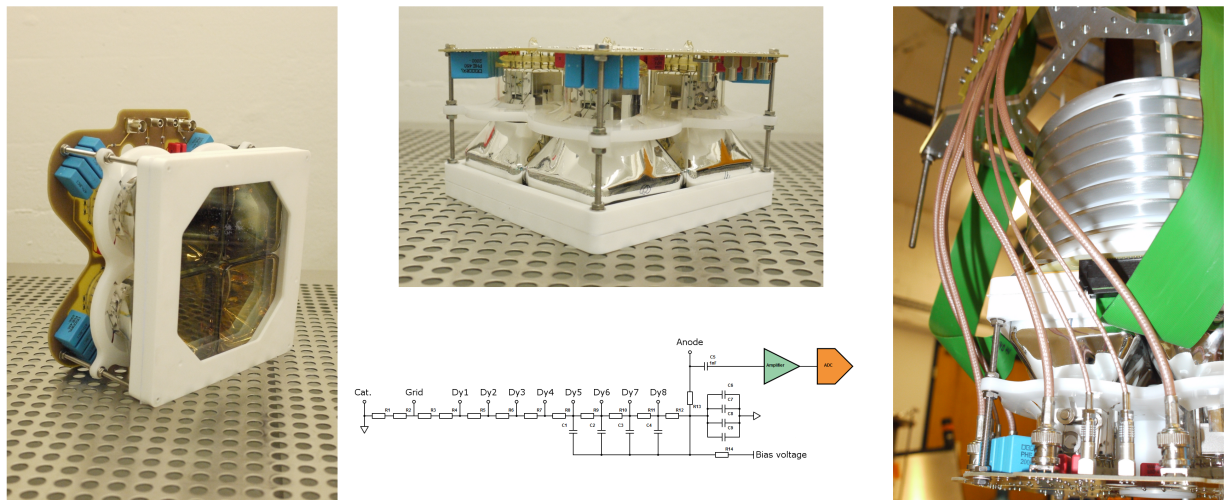


Figure 5.13: The light-collecting system without the reflectors and the field cage. Left, photograph of the assembled system. A PMMA glass is placed in front of the photo cathodes. Middle top, photographs from the side of the assembly. The PMT's are stacked between the PCB with the bases and the reflectors. Middle down, scheme of the PMT base (one of four channels). All resistors have $1\text{ M}\Omega$ resistance. All capacitors, if not marked otherwise, have 47 nF capacity (C1-C4, WIMA MKP4 0.047 / 630 and, C5-C8, RIFA PHE 450 2000 47 nF). Right, the fully assembled TPC. Eight cables (4 bias voltage and 4 signal) are connected to the PCB and guided to the interface box.

The four PMT's of the light-collecting system are soldered on a PCB (see Figure 5.13). For each PMT, the PCB provides a resistive voltage divider. To individually set the gain of a PMT, its bias voltage can be adjusted at a 4-channel high voltage power supply (CAEN, model N1470). To reduce noise and to stabilise the bias voltage, each channel is filtered directly on the PCB. Moreover, to not affect the charge collection on the nearby collection-wires, the PMT's photo cathodes are set to ground potential. Consequently, the signals of the PMT's, as well as the anodes, are at positive high voltage. Capacitors are used to decouple the signals from the bias voltages. To connect the bias voltage cables and the signals cables, connector sockets are soldered on the PCB. Eight coaxial cables are plugged to these sockets and connect the channels to four feedthroughs at the interface box. The signals are amplified with integrating pre amplifiers (Ortec, Model 113) before they are connected to the DAQ system.

5.2 Muon veto and muon trigger

The EXO-100 set-up is located at Bern, Switzerland at an altitude of 555 m above sea level in an aboveground laboratory. The flux of cosmic rays through the set-up is about $400 \text{ s}^{-1} \text{ m}^{-2}$. When a cosmic ray crosses the chamber of the EXO-100 cryostat, it deposits energy in the form of ionization and of scintillation. Depending on the selected trigger scheme of the TPC's DAQ, — i.e. trigger on light or on charge — either the scintillation light or the free electrons will trigger

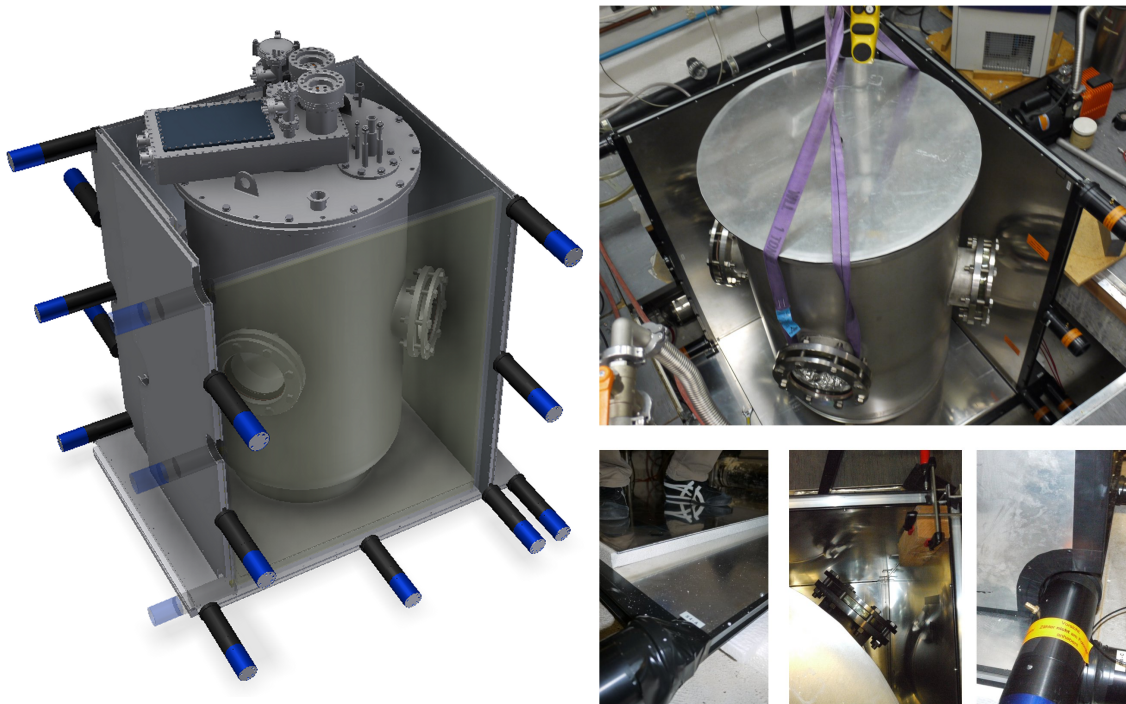


Figure 5.14: To detect cosmic rays, six panels made from plastic scintillator are placed around the EXO-100 cryostat. The panels are instrumented with 16 PMT's. Left, a CAD render of the EXO-100 cryostat with the panels placed around it. Right, photographs taken during the assembly of the muon veto.

the DAQ. However, depending on the desired type of data, the cosmic rays are considered an unwanted background — studies of the natural radioactivity, or measurements with an external source — or they are considered the desired signal. More information on the different types of data is given in Section 5.3.

To build a trigger which can clearly separate signals induced by cosmic rays from signals independent of cosmic rays, six panels made from 2.0 cm thick plastic scintillator (NE 102A) are installed around the EXO-100 cryostat (see Figure 5.14). These panels were previously built for the Orpheus detector [68]. If a cosmic ray crosses a panel, it excites the scintillator which then emits scintillation light. The light is reflected on the walls of the panel until it is collected by a PMT. Each panel, depending on its size, is instrumented with two or three PMT's. In total 16 PMT's are used to instrument 7.8 m² of scintillator — resulting in a muon veto with close to 100% geometrical efficiency for thoroughgoing cosmic rays. To supply the bias voltage to each PMT, a high voltage power system (LeCroy model HV4032A) is used which allows to separately set the bias voltage for each PMT. The signals of these PMT's are used to build a muon veto and a muon trigger which rejects or selects events induced by cosmic rays, respectively.

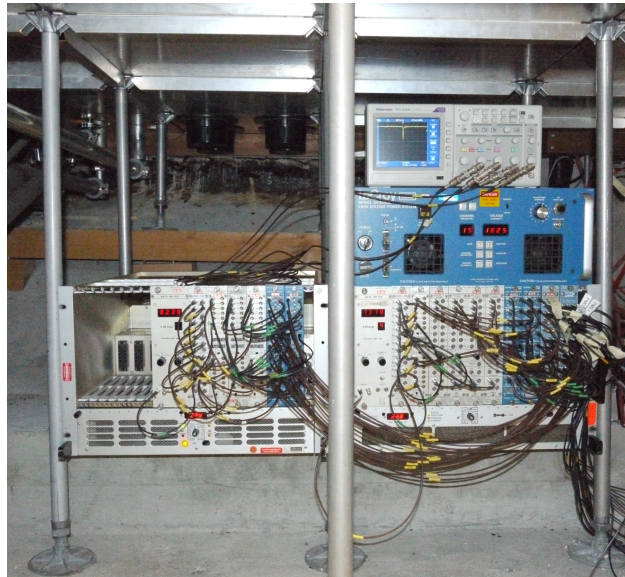


Figure 5.15: Photograph of the muon veto's electronic crates. The left crate contains the NIM modules of the muon trigger and the right crate contains those for the muon veto and the two PMT amplifiers. On top of it, the high voltage system and an oscilloscope for test purposes is placed.

The muon veto has to efficiently reject all cosmic events even if it rejects some other events. However, the muon trigger has to trigger purely on cosmic events even if it misses some of them. To build both an efficient muon veto and a pure muon trigger, two independent logic schemes are realised. To duplicate, as well as amplify by a factor 10 all 16 signals, two 12-channel PMT amplifiers with a fan-out function (LeCroy model 612) are used. One set of signal is used in the logic of the muon veto while the other set is used in the logic of the muon trigger. The logic of the muon veto and muon trigger is placed in two *Nuclear Instrument Module NIM* crates (see Figure 5.15).

The logic of the muon veto is split in three levels (see red arrows in Figure 5.16). Firstly, two octal discriminator units (LeCroy model 4608C) are used to set a threshold of -100 mV on each of the 16 signals. For signals above threshold, the discriminator produces a 100 ns long pulse. Secondly, to declare that

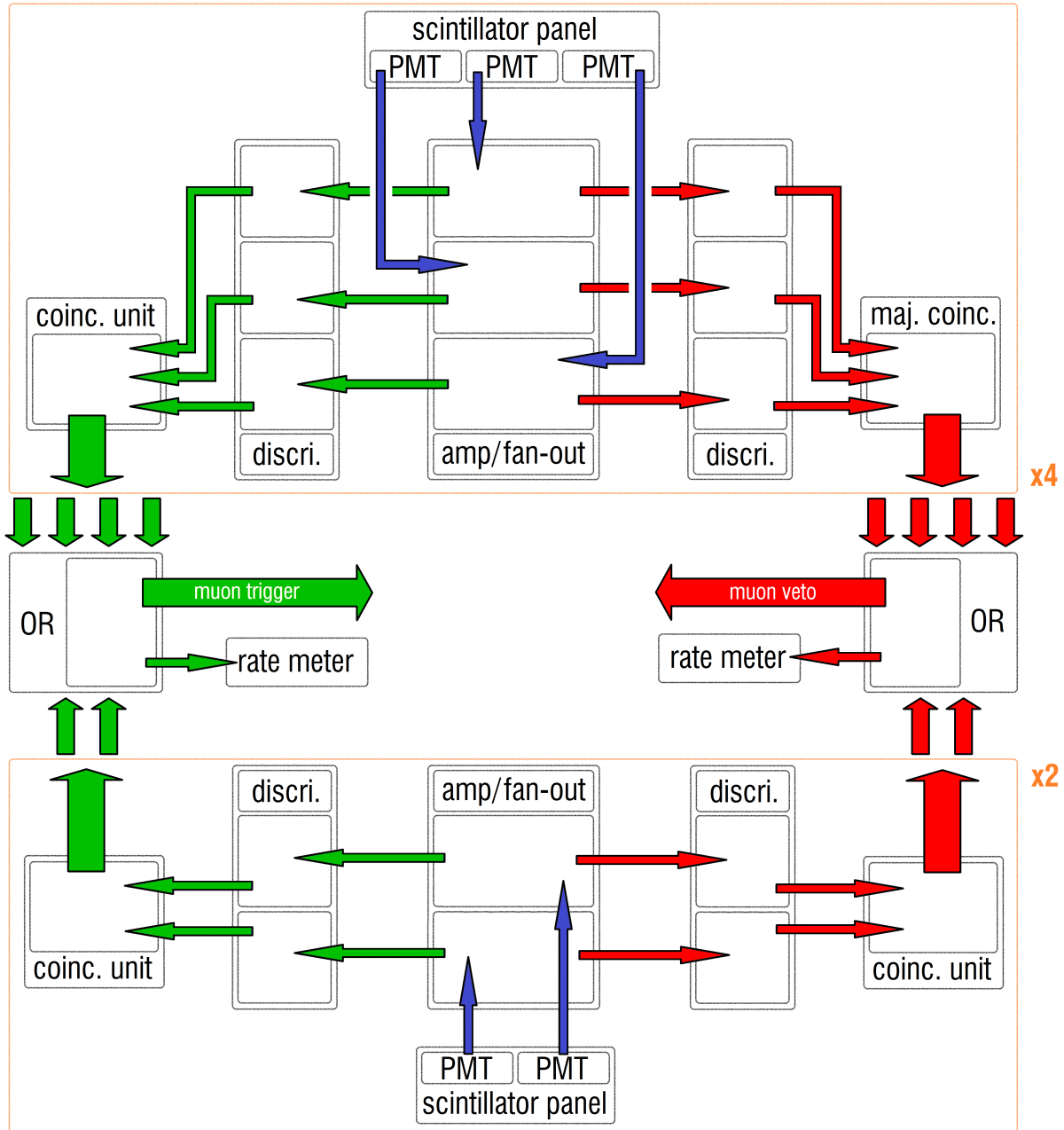


Figure 5.16: Diagram of the muon veto and trigger scheme. The signals of the PMT's (blue arrows) are amplified and duplicated before they are used in the muon veto (red arrows) and the muon trigger (green arrows). All components in an orange box are realised once per scintillator panel. See text for details.

a cosmic ray may have passed a scintillation panel, and hence, to consider this panel as trigger, coincidences between signals from the same scintillation panel are demanded. To trigger one of the four panels instrumented with 3 PMT's, simultaneously two or more of its PMT's have to trigger. For the signals of these panels, four majority coincidence units are used (model UB/C16). The coincidence level at these units is set to 2. However, to trigger one of the two panels instrumented with 2 PMT's, simultaneously all of its PMT's have to trigger. For the signals of these panels, a coincidence unit (model UB/C10) is used. A triggered panel generates a 200 ns long pulse, for the duration of which the panel is considered triggered. Finally, to trigger the muon veto it is enough if one of the six panels is triggered. Therefore, the six signals of the panel are OR-ed with a logic unit (model UB/L1). If any of the panels is triggered, this unit generates an output pulse with a duration of 500 ns. This signal is then integrated into the DAQ trigger scheme which is described in Section 5.3. Moreover, a rate meter (model UB/SC5) is used to measure the rate of muon veto triggers — which is about $1.7 \times 10^4 \text{ s}^{-1}$.

The logic of the muon trigger is built similar to the logic of the muon veto (see green arrows in Figure 5.16). The logic of the muon trigger is also split in three levels. Firstly, two octal discriminator units (LeCroy model 4608) are used to set a threshold of -5 V on each of the 16 amplified signals. In case a signal passes the threshold, its corresponding output of the discriminator produces a 100 ns long pulse. Secondly, to declare that a cosmic ray has passed a scintillation panel, and hence, to consider this panel as triggered, coincidences between signals from the same scintillation panel are demanded. To trigger any of the scintillator panels, simultaneously all of its PMT's have to be triggered. For the signals of all panels, three coincidence unit (model UB/C10) are used. A triggered panel generates a 100 ns long pulse. Finally, to trigger the muon trigger it is enough if one of the six panels is triggered. Therefore, the six signals of the panel are OR-ed with a logic unit (model UB/L1). If any of the panel is triggered, this unit generates an output pulse with a duration of 300 ns. This signal is then integrated into the DAQ trigger scheme which is described in Section 5.3. Moreover, a ratemeter (model UB/SC5) is used to measure the rate of muon triggers — which is about 270 s^{-1} . For details on the performance of the muon veto and trigger see Appendix E.

5.3 DAQ and trigger logic

The EXO-100 *Data Acquisition DAQ* system consists of a *Versa Module Europa VME* crate, a PC, and an optical link between them. The VME crate (Wiener, model 6U VME 195 Mini) contains two 64-channel ADC boards (CAEN, model V1740) and an interface board (CAEN, model V2718). From the 128 ADC channels, 62 are connected to the amplifiers of the induction wires, another 62 are connected to the amplifiers of the collection wires, and 4 are connected to the pre amplifiers of the PMT's. The VME crate is linked to the DAQ PC with an optical fibre. The DAQ PC runs the *Maximum Integrated Data Acquisition System MIDAS* framework — the DAQ PC acts as the frontend node and the backend node. The main components of the MIDAS are the web server application, the frontend program, and the data logger. The MIDAS web server application allows to control the run (e.g. start and stop it), to modify the settings of the VME module (e.g. frame size, pre trigger ratio, internal trigger, thresholds on groups of channels, etc.), and much more. However, to communicate with the hardware the frontend program is required. The frontend program has direct access to the hardware and can write to and read from the register of the ADC boards. It writes the settings to the VME module, controls

the status of it, and fetches data from it. After it transferred the data to the DAQ PC, the data logger writes the data in the MIDAS event format from the memory to the hard drive. A full description of the MIDAS framework can be found elsewhere.¹ The acquired data is temporarily stored on the DAQ PC before it is manually copied to a *Network Attached Storage NAS*.

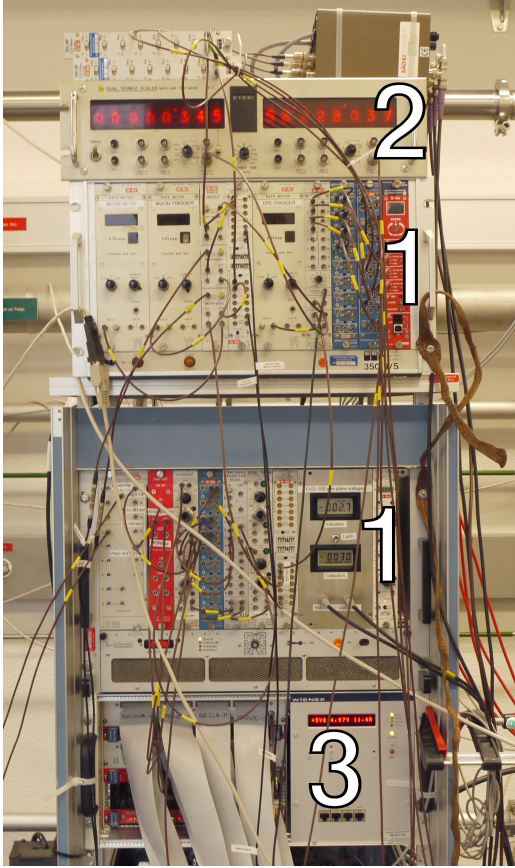


Figure 5.17: The electronics of the data acquisition system and the trigger scheme. 1- two NIM crates with the units used to build the trigger logic. 2- a scaler, two delay units, and the integrating pre-amps of the PMT's. 3- the VME crate with the two ADC boards and the link card.

channels. If any of these channels passes the threshold, the internal trigger is generated and is fed out to a discriminator (LeCroy model 4608). This discriminator is used because it has a veto function. Secondly, the signals from the four PMT's from the light-collecting system are used. They are duplicated (LeCroy model 428F) and one set is fed to the ADC boards. The other set is fed to a discriminator (LeCroy model 4608C) where a threshold on the PMT signals can be set. Thereafter, the logic signals from the four tubes are combined with a majority coincidence

The ADC boards can be triggered in two separate ways. Either by an internal trigger on the channels or by an external trigger. Because the DAQ system contains two ADC boards, the internal triggering is disabled. However, the internal triggers of both ADC boards are feed out of each board — without triggering it — where they are integrated into a sophisticated trigger logic. The output of the trigger logic is then used to simultaneously trigger the external triggers of both ADC boards.

The trigger logic is designed for three different types of data. The three event types of interest are internal alpha decays (e.g. ^{222}Rn and ^{218}Po), cosmic events (e.g. muons and electromagnetic showers), and internal gamma interactions induced by external calibration sources. The internal alpha events are the main source of interest when studying the properties of ions. However, the purity of the detection medium can be measured with muon tracks crossing the full length of the TPC's detection volume. Furthermore, the TPC's response can best be characterised by gamma interactions from well known calibration sources. Therefore, the trigger logic offers a distinct trigger for each of these event types, and furthermore a manual trigger for test purposes. The trigger logic is installed in two NIM crates (see Figure 5.17). In Figure 5.18, a diagram of the trigger logic is shown. In the following this logic is described in detail.

The trigger logic uses five input sources to generate these four distinct triggers. Firstly, the signals from the collection wires and induction wires are feed to two ADC board. With the MIDAS web server a threshold can be defined for groups of 8

¹<https://midas.psi.ch/htmldoc>

unit — to form the so-called *TPC light trigger*. Thirdly, the signal from the muon trigger is used. Fourthly, the signal from the muon veto is used. Lastly, the manual trigger is used.

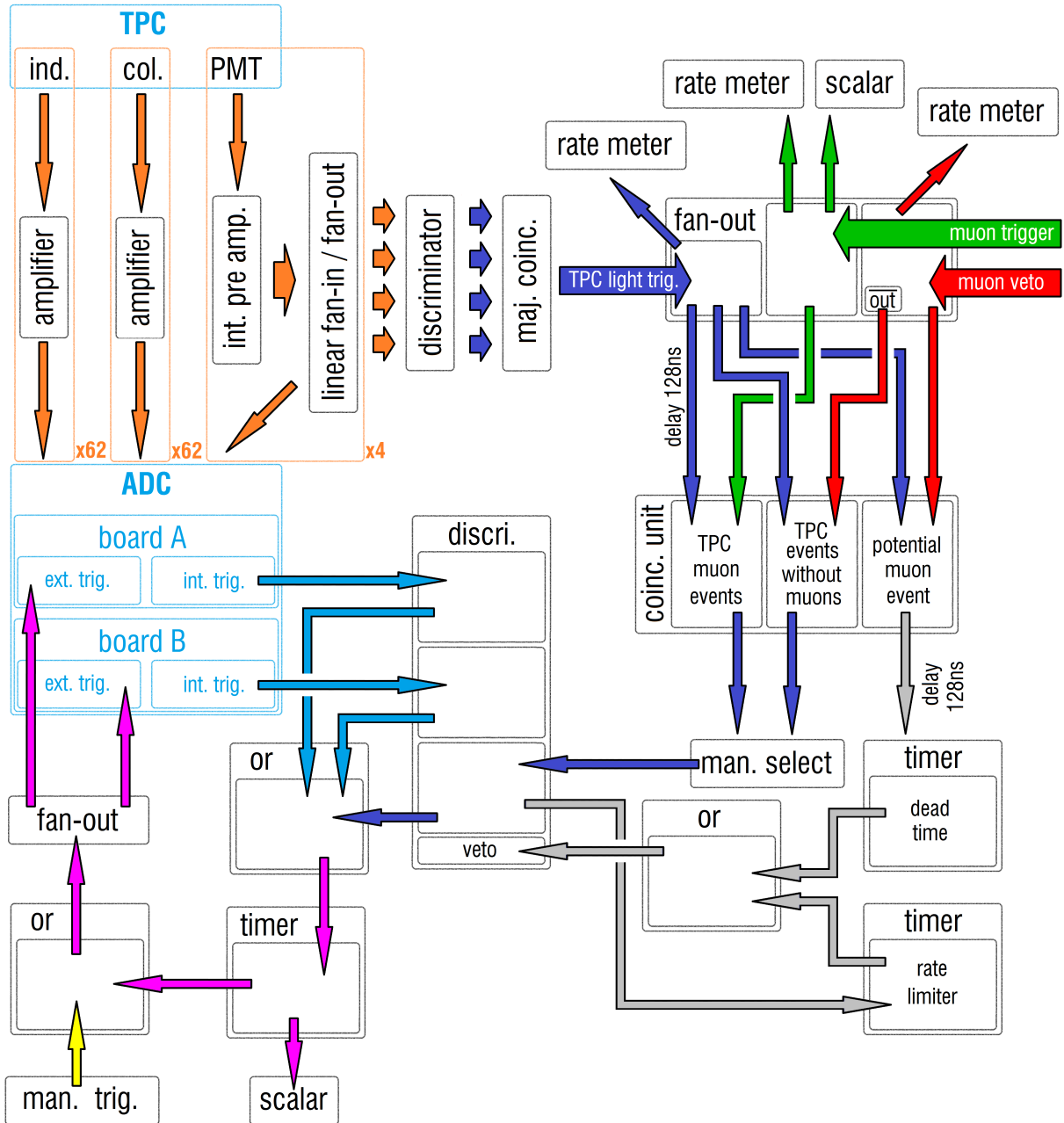


Figure 5.18: Diagram of the trigger logic. See text for details.

To generate a trigger for internal alpha events — the energy of an alpha decay is mainly deposited in the light channels — the TPC light trigger is combined with the inverted muon veto from the muon veto system in a coincidence unit. To select this trigger, the corresponding output of the coincidence unit has to be plugged ("man. select") into the discriminator with the

veto function. If this discriminator is not vetoed, the signal from the *TPC events without muons* is fed through an OR unit to start a timer. This timer generates a gate of $1\ \mu\text{s}$, which is then fed through another OR unit and doubled with a fan-out unit. Finally, a duplicate of the gate is used to generate the external trigger of each of the ADC boards. On the other hand, if the discriminator is vetoed, the pulse is not forwarded, and thus, the boards are not triggered by it. The veto of the discriminator is turned on in two situations. Firstly, every successful trigger starts a timer which vetoes the discriminator for a set dead time. This mechanism limits the maximal trigger rate, and therefore, is used to eliminate problems related to a too high data transfer rate in the optical fibre. Secondly, every potential muon event — coincidence between the TPC light trigger and the muon veto — starts a dead time of $500\ \mu\text{s}$. This avoids that delayed radioactivity

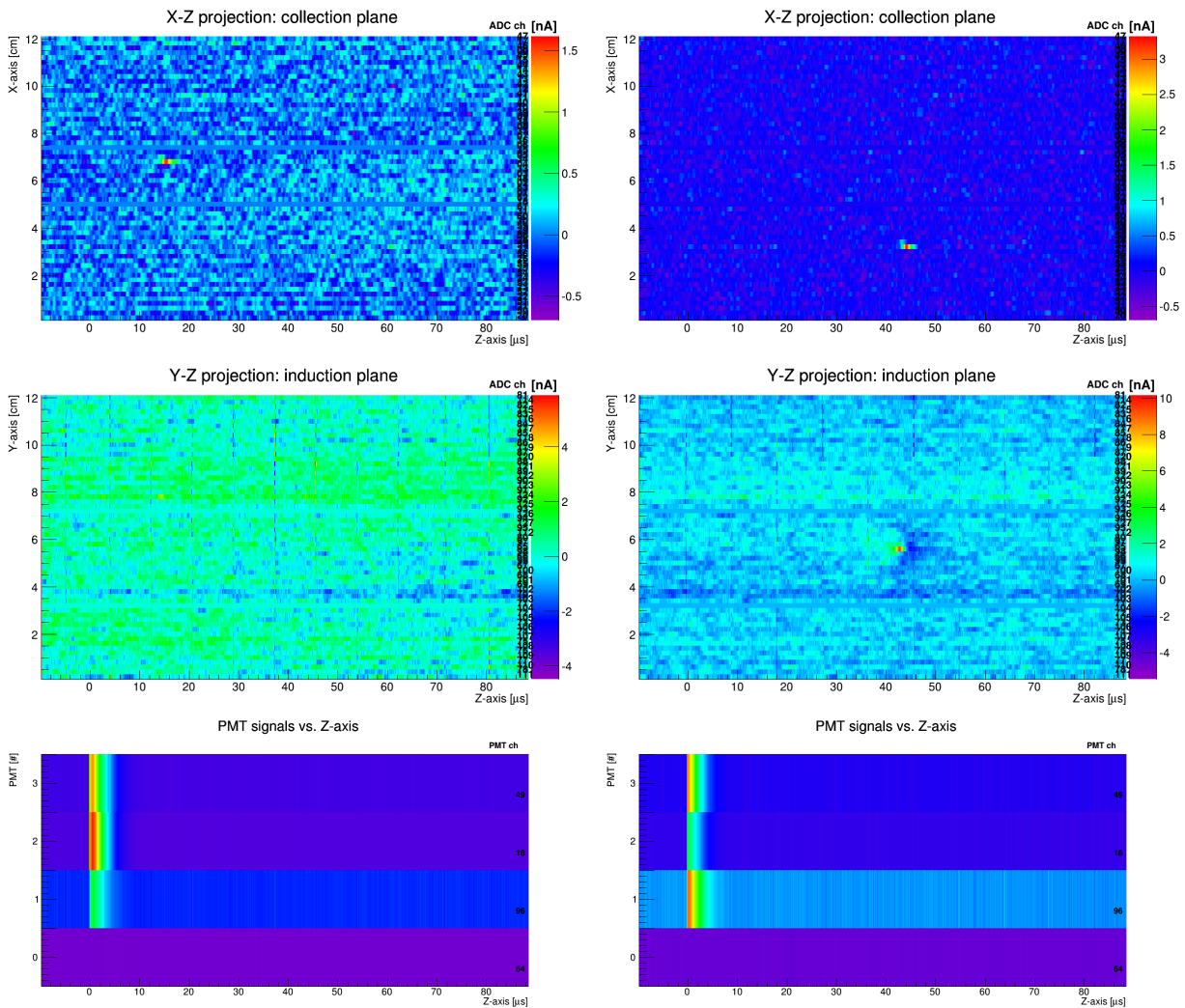


Figure 5.19: Two events triggered by the internal alpha event trigger — in liquid argon. The light pulses are at $t = 0$ — the moment of triggering. (A pre trigger of 10% is set.) The charge drifts to the read-out planes, and thus, arrives delayed. Left, the induction signal does not allow to localise the event in y direction. Right, the event can be localised in all three dimensions. (PMT0 is out of order.)

which was induced by muons is misinterpreted as internal radioactivity. Independently of the selected trigger, these two veto mechanisms are active. For the trigger on internal alpha decays, at the MIDAS web server the thresholds of the internal triggers are disabled, effectively set to -999 mV. A post trigger of 10% is set when recording waveforms. An example of such an event is shown in Figure 5.19.

To generate the trigger for muon events, the TPC light trigger is combined with the muon trigger from the muon veto system in a coincidence unit. To select this trigger, the corresponding output of the coincidence unit has to be plugged ("man. select") to the discriminator with the

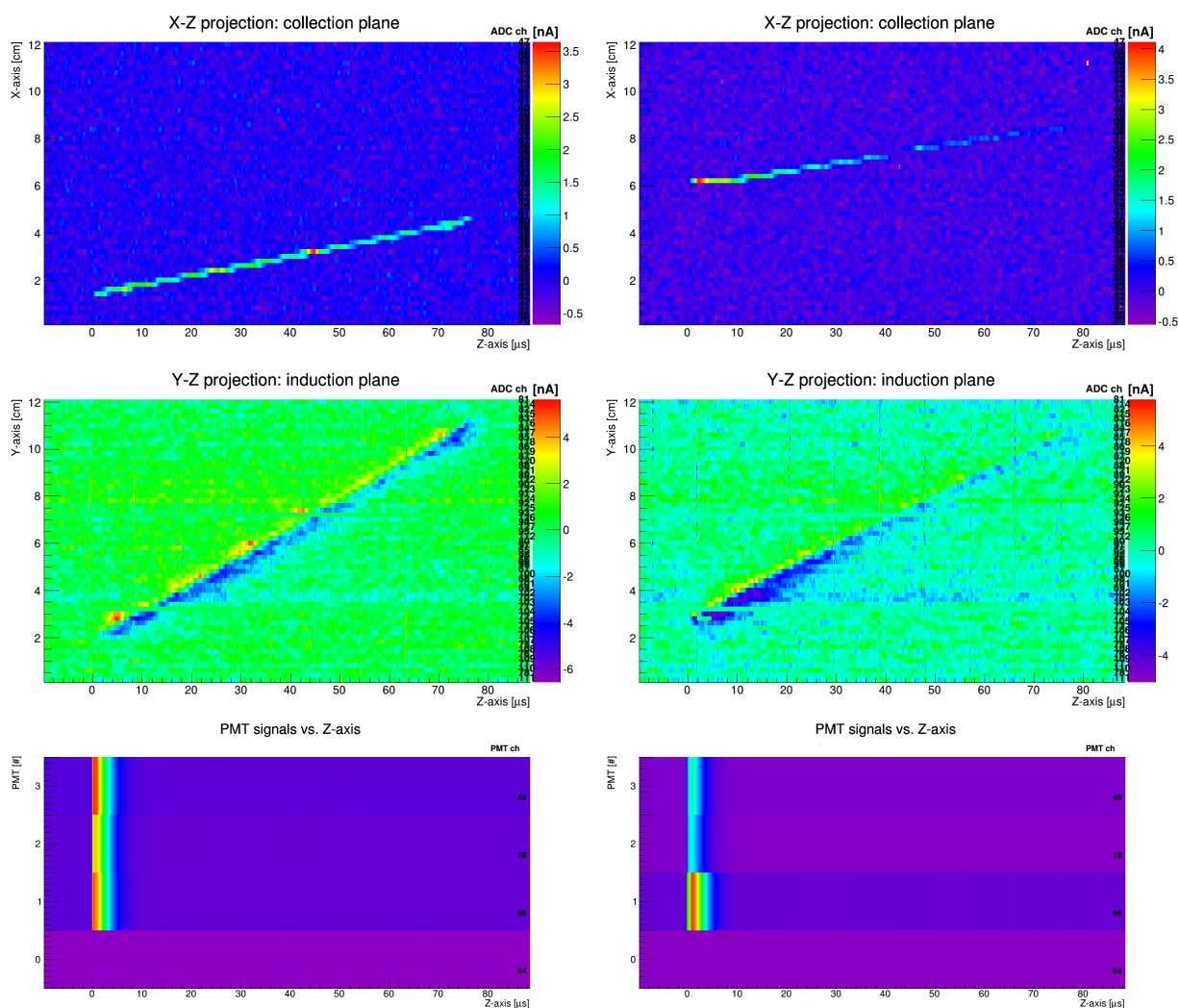


Figure 5.20: Two events triggered by the muon trigger — in liquid argon. The light pulses are at $t = 0$ — the moment of triggering. (A pre trigger fraction of 10% is set.) Both muons cross the full drift volume. Left, the apparent ionization density along the track is homogeneous. This indicates that the argon purity is good. Right, the apparent ionization density decreases with the drift distance. This indicates that the argon purity is poor. (PMT0 is out of order.)

veto function. The remaining part of the logic is identical to the trigger logic for internal alpha decays. However, for this trigger it is important to notice the 128 ns delay of the second veto mechanism. This delay is needed to avoid vetoing the muon event itself. For the trigger on muons, at the MIDAS web server the thresholds of the internal triggers are disabled — set to -999 mV — and a post trigger of 10% is set. Two examples of such events are shown in Figure 5.20. Sometimes, events recorded with this trigger contain electromagnetic showers or other spectacular interactions. A selection of such events is shown in Appendix F.

To generate the trigger for gamma rays of a source — the energy of a gamma ray is mainly deposited in the charge channels — neither the *TPC muon events* nor the *TPC events without*

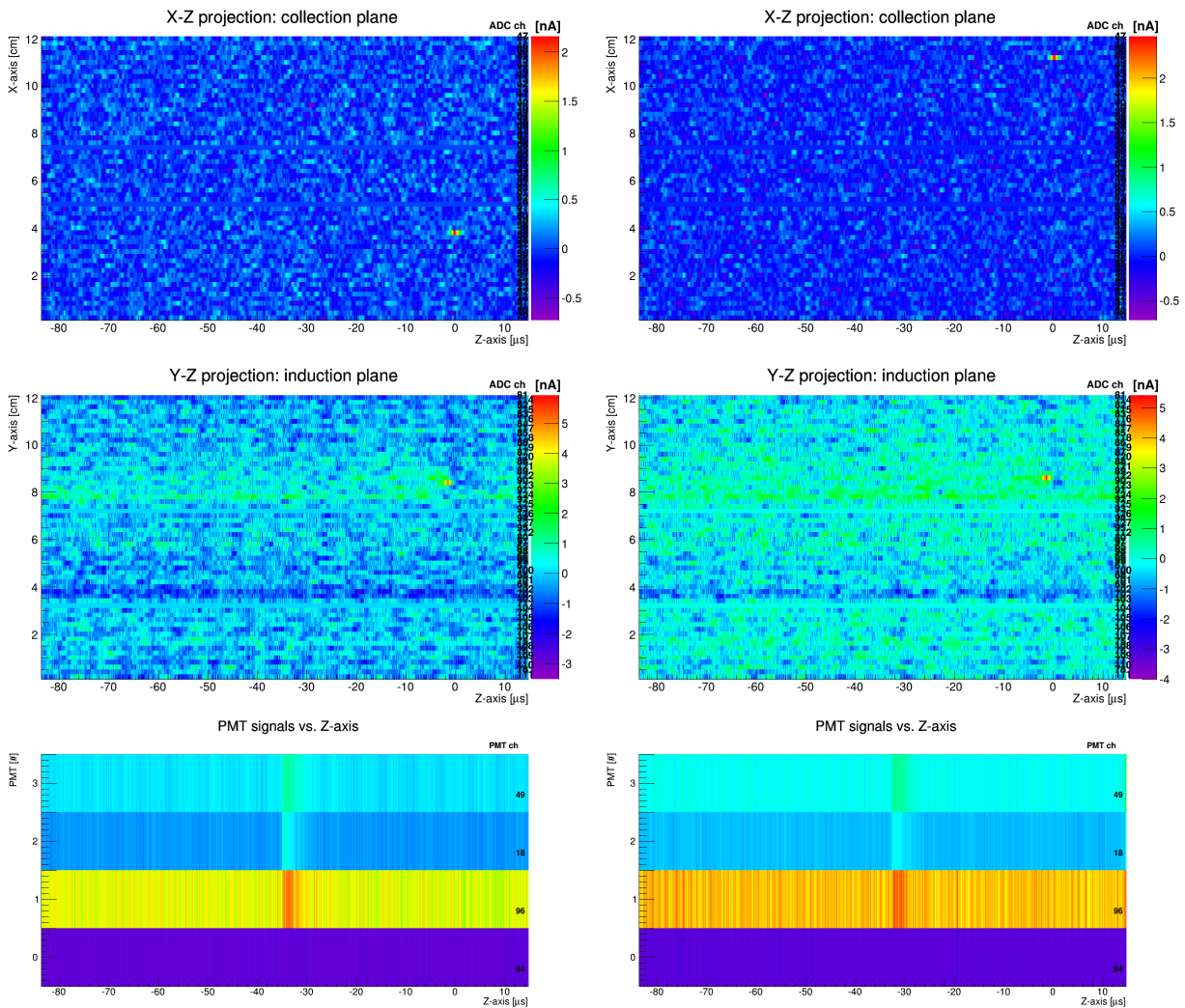


Figure 5.21: Two events triggered by the source trigger — in liquid argon. The charge arrives at $t = 0$ — the moment of triggering. The light pulses occurred before the charge gets collected. Hence, a pre trigger fraction of 90% is set. Both events can be localised in all three dimensions. (PMT0 is out of order.)

muons is plugged ("man. select") to the discriminator with the veto function. Hence, all events are triggered by the ADC boards. For this trigger, at the MIDAS web server the thresholds of the internal triggers on the charge collection channels are enabled — set to e.g. 30 mV — and a post trigger of 90% is set. In this trigger logic, the veto mechanism is enabled, which rejects delayed radioactivity induced by muons. Examples of such events are shown in Figure 5.21.

Independently of the selected trigger logic, the ADC boards can manually be triggered at any time. This trigger is not affected by any veto.

The cryo-camera

In this chapter the design of a temperature controlled and vacuum tight camera casing containing a digital camera is presented. The so-called cryo-camera was designed specifically for the use in the EXO-100 cryostat. Parts of this chapter were published [3] in a scientific journal.¹ In the last section of this chapter, high voltage tests performed on a miniaturised copy of the EXO-200 TPC are presented. These tests illustrate the usefulness of the cryo-camera and the EXO-100 cryostat for general R&D applications.

6.1	The design of the cryo-camera	76
6.2	Tests of the cryo-camera	80
6.3	An investigation of high voltage discharges in EXO-200	83
6.3.1	The miniEXO mock-up	83
6.3.2	High voltage tests	84
6.3.3	Simulation of the electric field in the miniEXO	87
6.3.4	Conclusions of the tests with miniEXO	89

During operation of the EXO-100 set-up, the chamber of the cryostat is sealed. Hence, instrumentation inside the chamber — such as the EXO-100 detector with the displacement device and the ion grabbing probe, as well as the chamber itself — is hidden in the cryostat. However, for several reasons a view inside the chamber is desired. A view inside the chamber allows to calibrate both level meter probes in the chamber — which are both media dependent — to monitor the displacement device, to spot high voltage break downs, and to inspect the general condition in the chamber (e.g. to detect frozen xenon). Therefore, a camera is installed inside the cryostat. This camera has to withstand low temperatures and allow for high vacuum. However, few camera models could be found to meet these demands. Therefore, a temperature controlled and custom made camera casing was developed to house a conventional digital camera. In Figure 6.1 a photograph of the so-called cryo-camera is shown.

¹The content of this chapter is partially copied from that publication — of which the author of this thesis is the corresponding author.



Figure 6.1: Photograph of the cryo-camera.

6.1 The design of the cryo-camera

The digital camera used is a C525 model manufactured by Logitech. This model was chosen because of its compact design and low price. Its most important specifications are summarised in Table 6.1.

Feature	Description
HD video capture	up to 1280 x 720 pixels
Photo capture	up to 8 megapixels (software enhanced)
Audio	built-in mic
Interface	Hi-Speed USB 2.0

Table 6.1: Specifications of the Logitech HD Webcam C525 ¹.

To keep the camera within its operating temperature range (between -30°C and 50°C), active temperature regulation is needed. The ITC-503 temperature controller unit from Oxford Instruments is used together with a *platinum-100 PT-100* sensor and two heating resistors (each with a resistance of $39\ \Omega$ and rated for 25 W, in parallel) to form a PID-controlled temperature regulation system. Good thermal contact between camera, PT-100, and heating resistors is required for the temperature regulation system to work. Therefore, the camera is inserted in a small aluminium casing with a lid (see Figure 6.2). The choice fell on aluminium because of its good thermal conductivity. The PT-100 — inserted into a copper support — and the heating resistors are attached with screws to the bottom of the aluminium casing, guaranteeing a good thermal contact. This inner unit is maintained at a constant temperature by the temperature controller. At this controller, the target temperature and the PID-parameters are set.

¹Logitech; www.logitech.com/en-ch/product/hd-webcam-c525

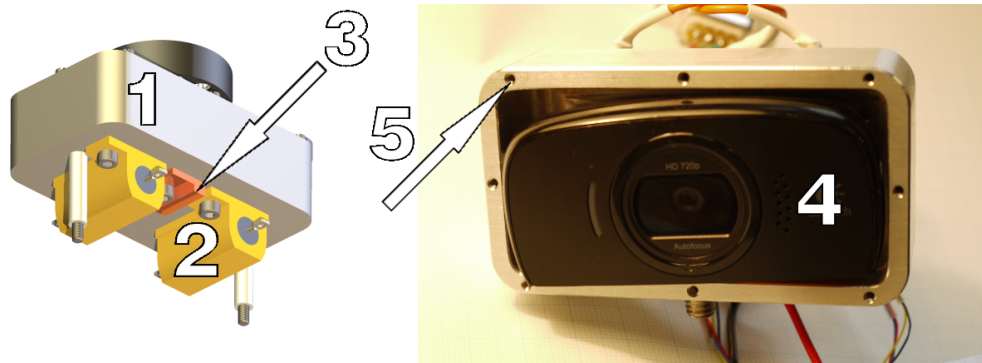


Figure 6.2: Left: CAD render, worm's eye view of the inner unit: 1- inner aluminium casing, 2- two heating resistors, 3- copper support for PT-100 sensor. Right: photograph of the inner casing with removed lid: 4- camera with removed stand, 5- threads to close the lid.

To regulate the temperature of the inner unit the ITC-503 provides power to the two heating resistors. Ultimately, the energy is dissipated to the environment and should therefore be kept small. The required heating power can be minimised by thermally insulating the inner unit from the environment. Therefore, special attention was paid to minimising the heat radiation. The inner aluminium casing forms a heat radiation barrier between the environment and the camera. The barrier is only broken for the lens of the camera. To reduce the heat exchange between the inner unit and the outer body, the inner unit is completely wrapped in five layers of super insulation (metallised boPET film). A small hole is left at the position of the lens (see Figure 6.3).

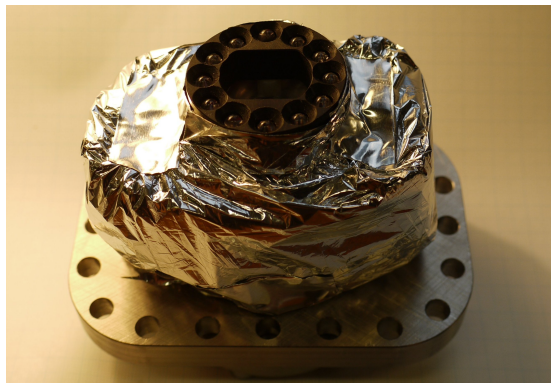


Figure 6.3: Photograph of the inner unit wrapped in five layers of super insulation.

The camera's out gassing rate is expected to be severe due to its plastic frame and *printed circuit board PCB*. However, a high out gassing rate makes it almost impossible to reach a good vacuum in the environment of the camera and certainly contaminates the detection medium. Therefore, the inner unit — containing the camera — is encapsulated in a camera body (see Figure 6.4). The camera body is vacuum tight and built out of stainless steel, which is a material well suited for high vacuum (e.g. low out gassing and gas permeation). The camera body's parts are shown in Figure 6.5.

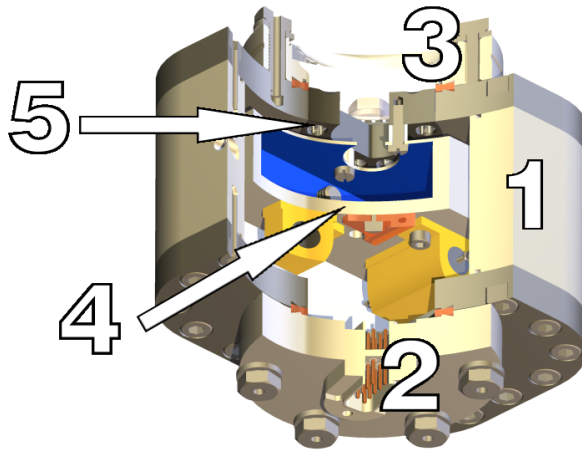


Figure 6.4: Cutaway view of the cryo-camera: 1- vacuum tight camera body, 2- Sub-D feedthrough, 3- borosilicate window, 4- inner unit with space for the camera (blue), 5- lighting system.

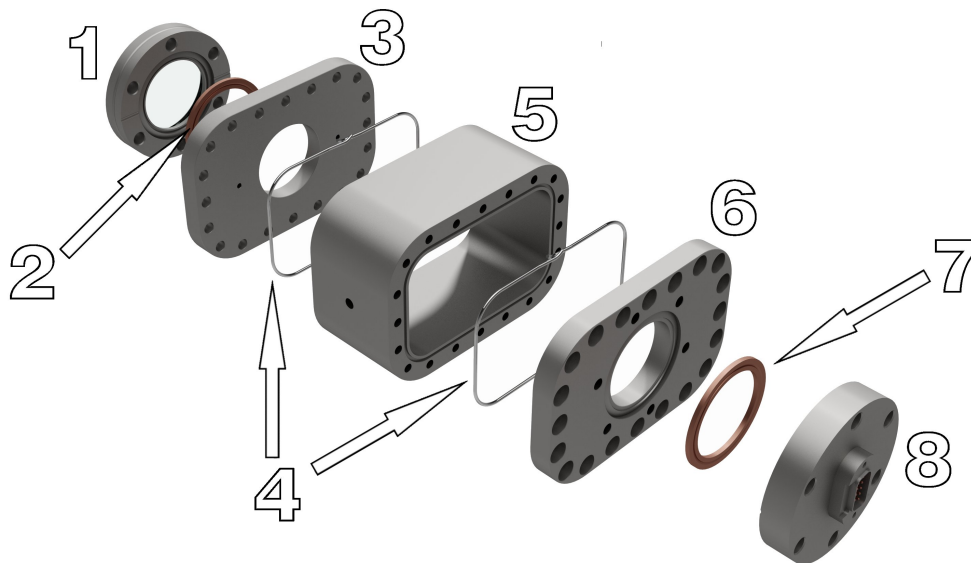


Figure 6.5: CAD exploded view of the vacuum tight camera body (screws are omitted): 1- borosilicate window on CF-40 , 2- soft baked copper gasket, 3- upper flange, 4- indium wires, 5- body piece, 6- lower flange, 7- copper gasket, 8- Sub-D feedthrough on CF-40.

To connect the individual parts together two well known vacuum sealing techniques are used [69]. A borosilicate window and a Sub-D feedthrough are mounted to the flanges with a CF-40 soft baked copper gasket and a normal copper gasket, respectively. The seals between the flanges and the body piece are made with indium wires [70]. To avoid virtual leaks vacuum screws are used.

When mounted inside the EXO-100 cryostat a lighting system is needed to illuminate the

scene. Twelve LED's are mounted on a support ring made of black anodised aluminium. This ring is fixed onto the inner unit inside of the vacuum tight camera body (see Figure 6.4). In the middle of the support ring a hole was cut out to leave the view of the camera free. The LED's can be dimmed or turned off from an external control unit.

The gas filling the inner volume of the camera body may condense or freeze on the camera body's inner walls once it is cooled down to cryogenic temperature. Therefore, there are the risks that the pressure in the inner volume drops significantly (which could lead to overheating of the camera) and that the borosilicate window becomes misted. To avoid these problems, an adequate gas is chosen to fill the inner volume and a simple gas purification system is included. The choice for a filling gas depends on the cryo-camera's application — the expected coldest body temperature — and is lead by a compromise between good thermal insulation (e.g. argon, xenon, or nitrogen) and low condensation temperature (e.g. helium 4 K, nitrogen 77 K, argon 86 K, or xenon 165 K; at 1 bar). Even though helium is a very inefficient insulator, its low condensation temperature and the ability to easily leak check it, makes it the preferred candidate. Regarding thermal insulation, argon is the better choice for most cryo-camera's applications. Unwanted residual components with high freezing temperatures (e.g. water) are still present after the inner volume is filled with helium gas and can still mist the borosilicate window. These residuals originate from impurities in the filling gas and out gassing from the camera parts. A simple purification system is integrated in the camera body to remove these residuals from the filling gas. The purification system consists of two parts (see Figure 6.6). Firstly, a hole is milled in the upper flange reducing locally the wall thickness to 0.5 mm and thus lowering locally the heat resistance. Therefore, this will be the coldest point inside the camera body once the cryo-camera is at cryogenic temperature. The residuals will condense at this point. Secondly, this hole is filled with silica gel to efficiently remove water vapour from the filling gas.

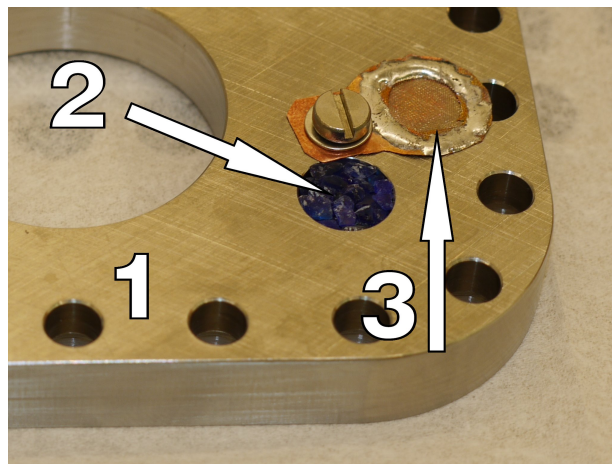


Figure 6.6: Photograph of the gas purifying system: 1- upper flange, 2- hole filled with silica gel, 3- cover with a thin mesh to close the hole.

6.2 Tests of the cryo-camera

To test the vacuum tightness of the camera body the cryo-camera was placed inside a small vacuum chamber. The vacuum chamber was equipped with three devices: a turbo molecular pump to evacuate the chamber, a vacuum gauge to measure the pressure, and a helium leak checker to detect leaks in the camera body. A first test was done with the empty chamber. Thereafter, the chamber was reopened and the cryo-camera was installed. The results of the two runs are shown in Table 6.2.

Condition of the chamber	Pressure [mbar]	Leakage rate [mbar · l/s]
Empty	$1.1 \cdot 10^{-6}$	$1.4 \cdot 10^{-10}$
With cryo-camera	$1.7 \cdot 10^{-6}$	$3.3 \cdot 10^{-10}$

Table 6.2: Results of the vacuum tightness test.

For operation in environments where high purity is required (e.g. TPC's) the values shown in Table 6.2 are sufficient. After these tests, the cryo-camera was operated inside the EXO-100 cryostat (see Figure 6.7). With the TPC, tracks of cosmic muons in liquid argon were observed. The analysis of these tracks confirms that the cryo-camera does not pollute its environment.

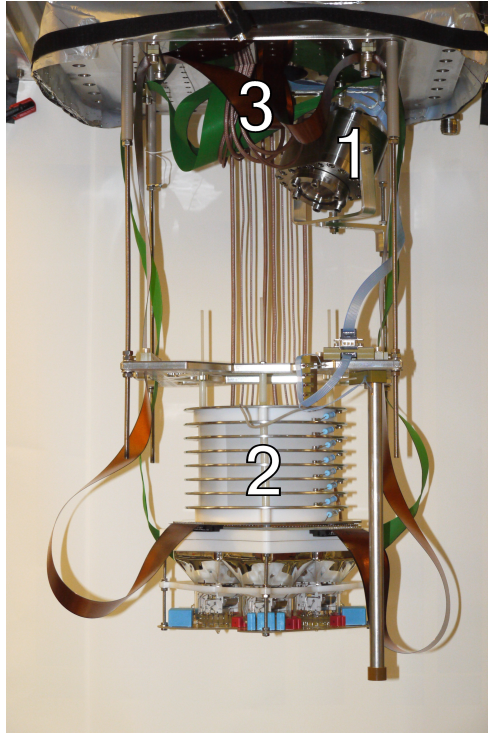


Figure 6.7: Photograph of the EXO-100 detector with the mounted cryo-camera: 1- cryo-camera, 2- time projection chamber, and 3- signal cables.

Important parameters for applications of the cryo-camera are the operation temperature range, the temperature stability, and the dissipated power. To measure these quantities under demanding conditions the cryo-camera was immersed in liquid nitrogen. During this procedure, the temperature controller measured the temperature of the inner unit and maintained it at a given target temperature T_t . A computer was connected to the temperature controller — via RS-232 interface — to record the temperature curve of the inner unit and the voltage of the temperature controller’s heating output. Thereafter, the heating power was calculated from the heating output voltage — over a total resistance of $19.5\ \Omega$. The heating power is systematically underestimated due to temperature dependence of the resistance. Figure 6.8 shows the recorded data.

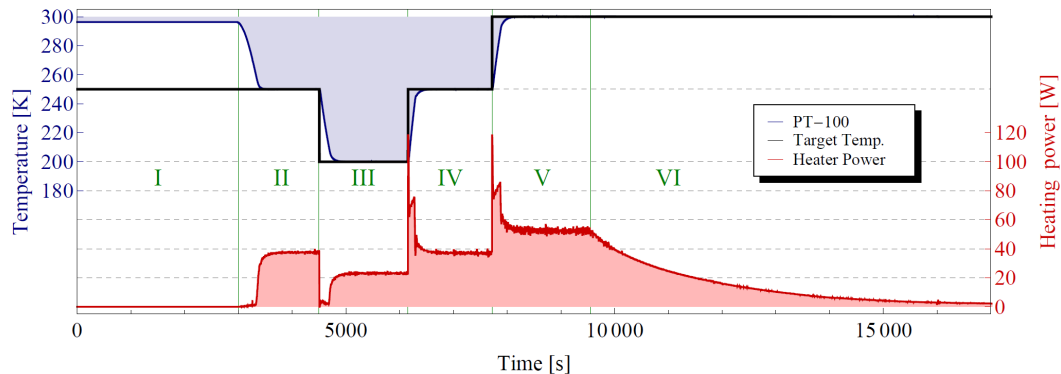


Figure 6.8: Temperature of the inner unit and the required heating power: I- cryo-camera at room temperature ($T_t = 250\ \text{K}$), II- cryo-camera immersed into liquid nitrogen ($T_t = 250\ \text{K}$), III- T_t lowered to $200\ \text{K}$, IV- T_t increased back to $250\ \text{K}$, V- T_t increased to $300\ \text{K}$, VI- cryo-camera extracted from liquid nitrogen to air ($T_t = 300\ \text{K}$).

In this test, target temperatures of the inner unit between $200\ \text{K}$ and $300\ \text{K}$ were reached. Below $250\ \text{K}$ the contrast of the image was reduced and at $200\ \text{K}$ the camera stopped working. However, the camera fully recovered after warming up the inner unit to $250\ \text{K}$. During earlier tests, the inner unit was cooled down to $77\ \text{K}$ and the camera also fully recovered after warming up. Similar behaviour was reported by Seddon et al. [71] who used a CCD camera to visualise cryogenic flow. At $250\ \text{K}$ the camera works without any image degradation, and thus, this temperature was chosen as the nominal operation temperature. The data from this test show a precise temperature regulation and an excellent temperature stability ($T = T_t \pm 0.1\ \text{K}$). However, the absolute temperature accuracy depends on the sensor calibration at the ITC-503. In this case the uncertainty is $\pm 1\ \text{K}$. Better accuracy can be reached by carefully calibrating the PT-100 sensor.

The required heating power P_h to maintain the inner unit at a certain T_t is shown in Table 6.3. During camera operation ($T_t = 250\ \text{K}$) $38\ \text{W}$ are constantly dissipated into the liquid nitrogen. Hence, the nitrogen constantly boils and produces bubbles at the surface of the camera body. To reduce boiling, the target temperature can be set to a lower temperature while the camera is not in operation — e.g. $T_t = 200\ \text{K}$ for fast recovering within minutes or $T_t < 77\ \text{K}$ to avoid any boiling. This will significantly lower the power dissipated into the liquid nitrogen. Furthermore, operation of the cryo-camera in liquid nitrogen is considered a demanding condition, therefore, these values represent the worst case scenario. During operation in the vapour phase, as in the case of the EXO-100 detector, less heat is lost and no bubbles are produced in the liquid phase

underneath the cryo-camera.

T_t [K]	P_h [W]
300 ± 1	52 ± 3
250 ± 1	38 ± 3
200 ± 1	23 ± 3

Table 6.3: Heating power P_h required to maintain the inner unit at a certain target temperature T_t (cryo-camera immersed in liquid nitrogen).

The cryo-camera's imaging performance was tested under two conditions. In a first test, the cryo-camera was exposed to short-term harsh conditions (for a few hours, immersed in liquid nitrogen). In a second test, the cryo-camera was installed in the EXO-100 cryostat and operated under long-term mild conditions (for several weeks, above liquid argon in the vapour phase). In both cases, the target temperature of the inner unit was set to $T_t = 250$ K at the ITC-503. During these tests several pictures and videos were recorded with the cryo-camera. Two pictures are shown in Figures 6.9 and 6.10.

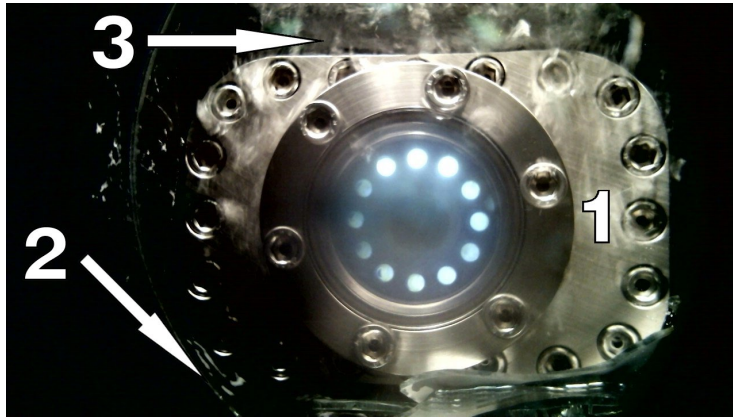


Figure 6.9: Picture taken with the cryo-camera while immersed in liquid nitrogen. A mirror was placed 10 cm in front of the cryo-camera and a self portrait was taken: 1- cryo-camera, 2- round three times magnifying shaving mirror, 3- bubbles produced by the cryo-camera due to heat dissipation

Under both conditions, the cryo-camera performed well and no image degradation was observed. However, three problems occurred. Firstly, the light of the lighting system is reflected on the front window and disturbs the outer part of the camera's view field. A possible improvement would be to replace the current window with one having an anti-reflection coating. This would lower the intensity of the reflected light and thus reduce the undesirable effect. Secondly, sometimes impurities condensed and froze on the inside of the window during operation in liquid nitrogen. This reduces or blocks the view of the camera. Thirdly, the dissipated heat of the heating resistors induces boiling in liquid nitrogen. Therefore, the cryo-camera has to be oriented horizontally as otherwise the bubbles disturb the camera view field. The last two problems only

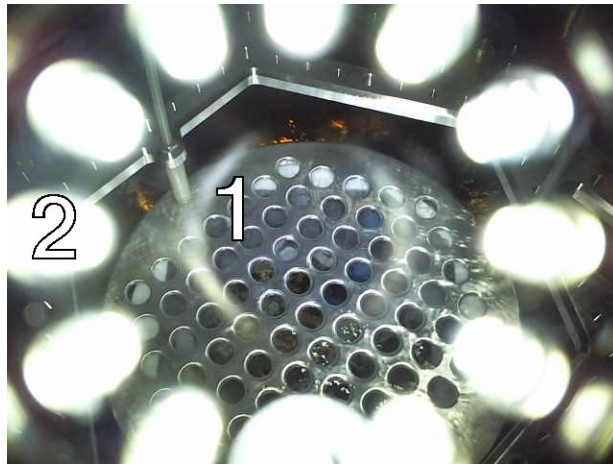


Figure 6.10: Picture taken with the cryo-camera while installed in the EXO-100 cryostat. Bird’s eye view onto the EXO-100 TPC filled with liquid argon: 1- the cathode of the EXO-100 TPC and 2- reflections of the LED’s of the cameras lighting system on the borosilicate window.

occur during operation in liquid nitrogen (and most likely in liquid argon). Operation in the gas phase is free of these problems.

6.3 An investigation of high voltage discharges in EXO-200

The EXO-200 TPC is designed to hold up to -75 kV at the cathode without provoking any discharges. However, during the commissioning of the EXO-200 detector, spikes — so-called glitches — were detected with an oscilloscope capacitively coupled to the high voltage line. These glitches appeared at a potential at the cathode of -10 kV and seem to produce light inside the TPC. To allow for data taking, as well as to protect the detector against discharges, the nominal operation potential of the EXO-200 cathode was set to -8 kV — almost an order of magnitude less than the designed maximal rating. The physics of these glitches was never fully understood, however it is assumed that they are an omen of an imminent breakdown. A detailed description on the high voltage problem in EXO-200 can be found in [72] (in the section related to EXO).

6.3.1 The miniEXO mock-up

The understanding of the glitch phenomenon is important for both the operation of EXO-200 and the design of nEXO. However, it cannot be studied with EXO-200 as a high voltage discharge could damage parts of the detector (e.g. the *Large-Area Avalanche Photo Diode LAAPD*). The loss of some LAAPD would deteriorate the detector’s performance. In the worst case, the EXO-200 cryostat would need to be opened to replace the LAAPD’s. This would cause a delay of several month. Hence, the EXO high voltage task force decided to build a minimised model of the EXO-200 TPC — the so-called miniEXO — and to use it to study the glitch phenomenon (see Figure 6.11). The design of miniEXO defers from that of EXO-200 field cage only in the used materials and in the outer diameter of its rings — 19 cm, the half of EXO-200. The mechanical designed was realised at SLAC national accelerator laboratory and Stanford University², in the

²Namely by: Larry Bartoszek, Michelle Dolinski, Peter Rowson, and Knut Skarpaas.

USA. The EXO-100 cryostat is well suited for this test as it allows for operation in liquid xenon, and moreover, to spot high voltage breakdowns, it can be equipped with cryo-cameras.

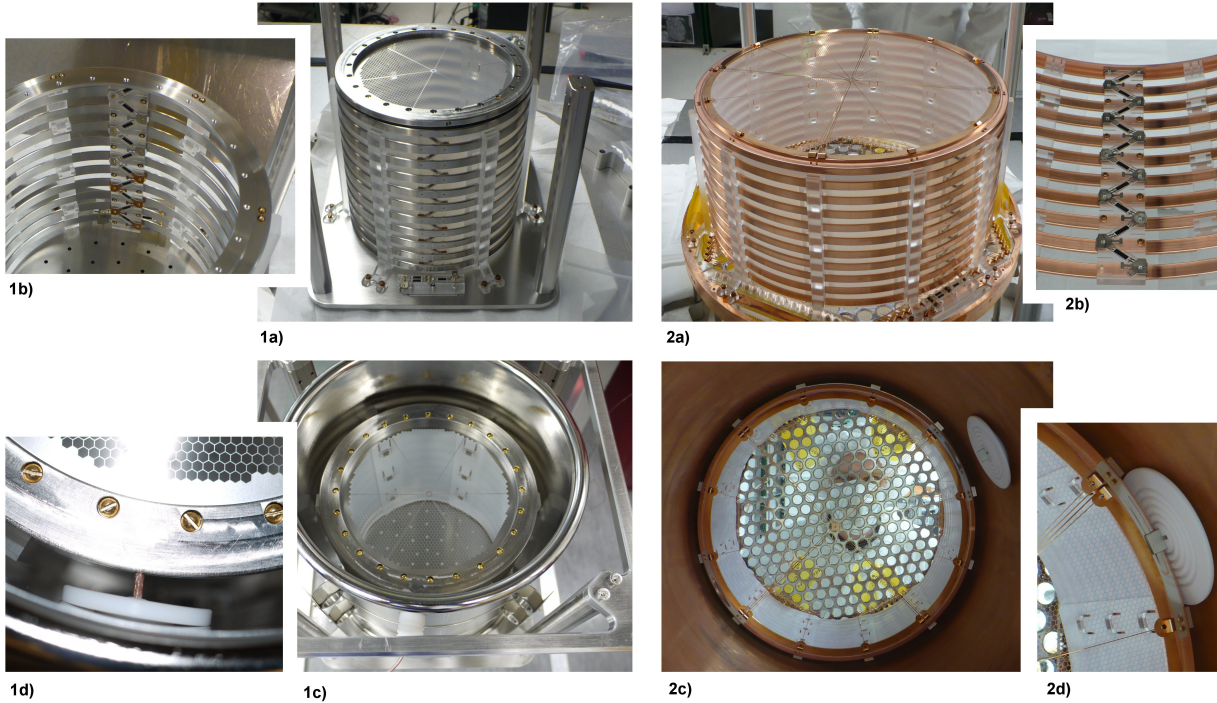


Figure 6.11: Photographs of the miniEXO mock-up (1) and of one half of the EXO-200 TPC (2). a) The field cage of the miniEXO is made from stainless steel and the field cage of EXO-200 from radio pure copper. b) Inside the field cage the voltage divider is mounted on an acrylic bar. From the outside of the field cage, 6 and 12 acrylic struts hold the field shaping rings of miniEXO and EXO-200, respectively. The struts of the miniEXO are from the same batch as those of the EXO-200 TPC. c) The shroud is mounted around the miniEXO and the EXO-200 TPC is installed in its cryostat. d) Details of the high voltage connections.

As an explanation for the phenomenon of the glitches, three hypotheses were evaluated. Firstly, the field shaping rings of the EXO-200 TPC are mounted on supports made from acrylic glass. To minimise the out gassing of these struts, they were stored for years in dry nitrogen gas. This nitrogen treatment reduces the natural spark suppression one may expect from absorbed air (i.e. O_2 and H_2O) in the material. Thus, the acrylic glass could change its electrical properties. This could lead to discharges from one field shaping ring to another along or inside the struts. Secondly, the discharges could happen between a field shaping ring and the grounded cryostat walls. Lastly, the discharges could originate from the voltage divider.

6.3.2 High voltage tests

To test these hypotheses independently from each other, a shroud made from stainless steel — aka the *Shroud of Bern-in* — was machined which can be mounted around the miniEXO. It defines the electric potential outside the field cage, in the same way the cryostat does in EXO-200. The shroud was carefully polished and the ends formed to reduce edge fields. The distance

between the shroud and the rings is 11 mm, the same as in EXO-200. The miniEXO was tested in two different configurations. Firstly, without the shroud, and secondly, with the grounded shroud mounted. In both configurations, two cryo-cameras were mounted above the miniEXO to monitor the level of the liquid xenon and to spot high voltage discharges (see Figure 6.12).

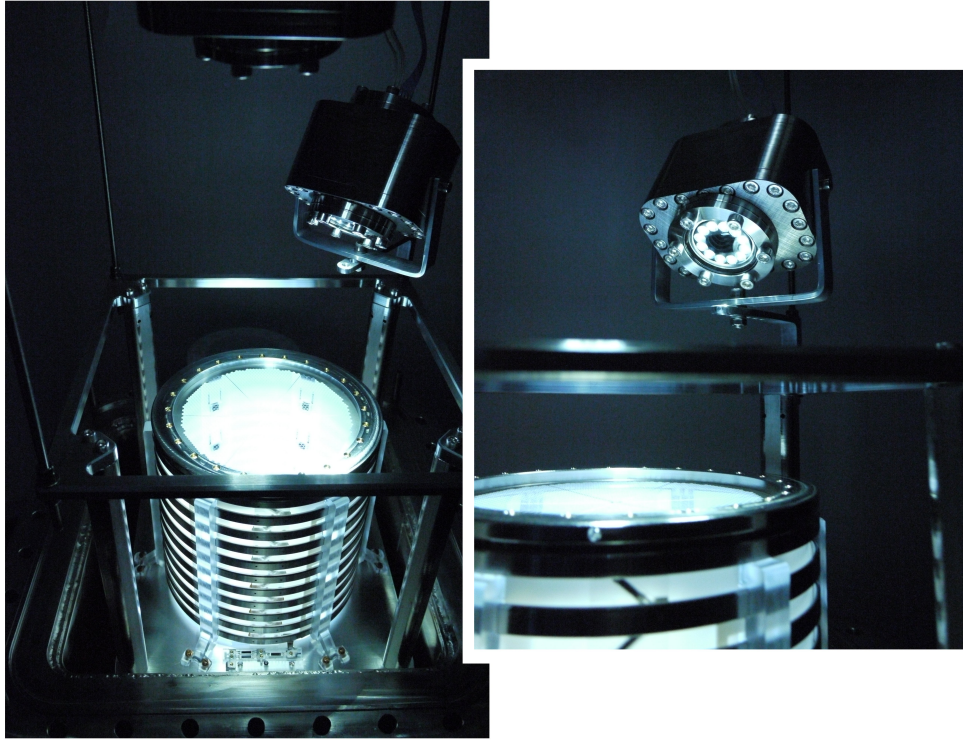


Figure 6.12: Photographs of the cryo-cameras and miniEXO. Two cryo-cameras were installed in the EXO-100 cryostat. One camera was focused on the high voltage divider and the other was mounted on top to have the full assembly in its field of view. In both photographs, the scene is illuminated by the lighting systems of the two cameras.

For the first test run, the high voltage was connected to the cathode of miniEXO as described in Figure 6.13. The high voltage filter described in Figure 5.5 was used. The anode of miniEXO was connected to a glitch detector which kept the anode potential at a virtual ground. Furthermore, an oscilloscope was connected to the glitch detector which allowed to monitor the high voltage line. In this test, glitches with negative polarity were observed during the ramp-up of the high voltage — starting at -5 kV. These glitches vanished after several minutes of operation at a fixed voltage. At -16 kV, glitches with positive polarity — indicating discharges on the high voltage side of the voltage divider — started to occur. These glitches got stronger until at -22 kV frequent discharges occurred inside the high voltage filter, and thus, this voltage could not be kept for longer periods. However, no discharges related to miniEXO could be observed during this test run — as far as we could tell essentially all of the discharges and glitches originated externally in the HV feedthrough. These results rule out the hypotheses that the problem in EXO-200 is due to the voltage divider or due to discharges between the field shaping rings. However, the purity of the liquid xenon — which was certainly worse than in EXO-200 — could not be measured in

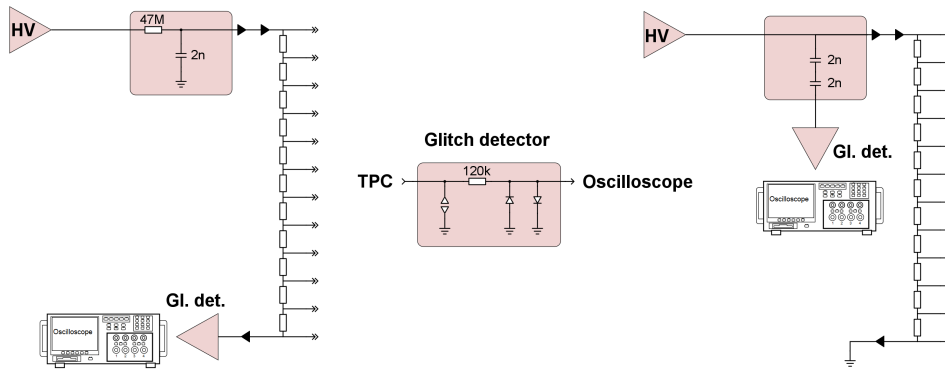


Figure 6.13: Electrical diagram of the high voltage tests. If not noted differently, resistors have a resistance of $1\text{ M}\Omega$. A black filled arrow head indicates a feedthrough. Left: the diagram for the first test. Middle: diagram of the glitch detector. Right: diagram of the second test. The output impedance of the high voltage unit is omitted. The oscilloscope was set on $100\text{ M}\Omega$ input impedance.

this run. It is the main uncertainty when interpreting these results as impurities may quench discharges.

For the second test run, the high voltage filter was replaced by a new feedthrough and a high voltage decoupling box was added (see Figure 6.13). This box allowed to connect the glitch

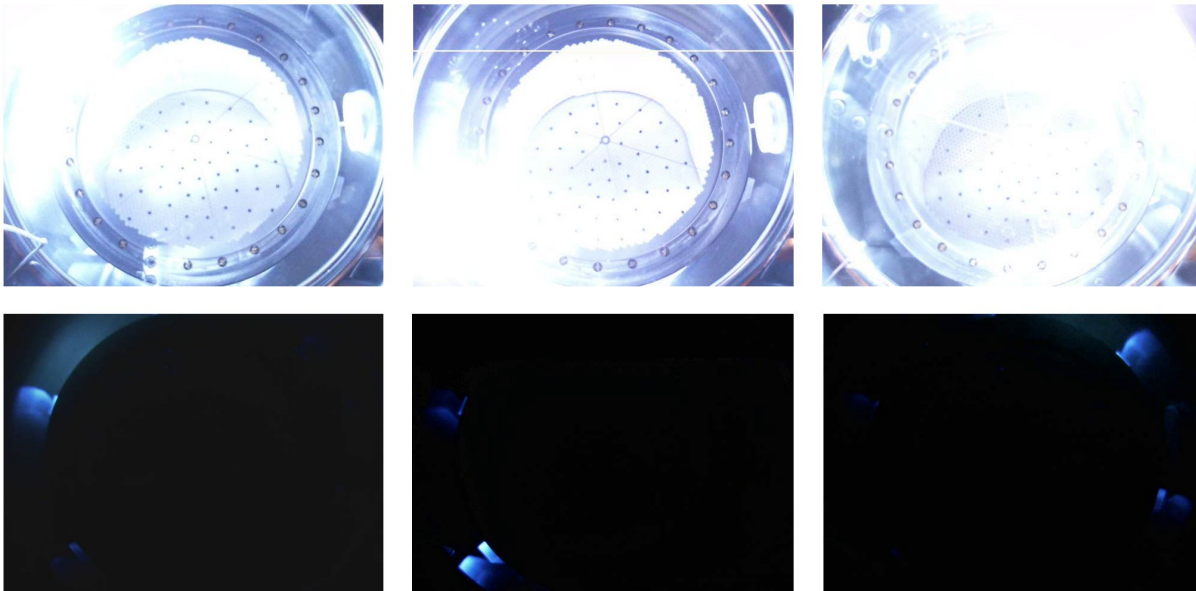


Figure 6.14: Photographs taken with the cryo-cameras of discharges in miniEXO. The upper row shows three photographs captured at the moment of a discharge. In the lower row, the afterglow of these discharges are shown — the acrylic struts show phosphorescence (decay times $> 1\text{ s}$) apparently excited by UV light generated in the spark.

detector at the high voltage side of miniEXO — as is done in EXO-200. The anode and the shroud were connected to ground. Furthermore, two simple purity monitors were installed in the chamber allowing for qualitative purity measurements. During this test run, discharges in miniEXO could be provoked at -38 kV and at higher voltages. Some of these discharges were captured by the cryo-cameras (see Figure 6.14). All observed discharges took place between the shroud and miniEXO. From a careful analysis of the videos taken with the cryo-cameras, it is clear that the discharges happen at the end of miniEXO to which the high voltage is applied. Moreover, it seems that most discharges occur close to or on an acrylic strut — a precise localisation was not possible. However, when ramping-up the high voltage very gently, a cathode potential of -50 kV was reached without observing large glitches on the oscilloscope. The signals from the purity monitors indicated that the xenon purity must have been high enough to drift free electrons — generated in liquid xenon by alpha and beta rays by ^{241}Am and ^{90}Sr , respectively — in a drift field of 70 V cm^{-1} over a gap of 1.4 cm . During this test one of the purity monitors inadvertently connected miniEXO’s virtual ground to true ground. Therefore, the glitch detector could not be used as before and was less sensitive.

6.3.3 Simulation of the electric field in the miniEXO

For completeness, the electric fields in the two test configurations were simulated. To minimise the required computing power, a simplified structure of miniEXO was used for these simulations. The miniEXO design is essentially axial symmetric, and hence, the simulation is reduced to two cut surfaces (see Figure 6.15). The first cut surface goes through the central axis of miniEXO and passes between two acrylic struts. This cut surface represents the situation far from the struts. The second cut surface goes through the central axis and through the middle of an acrylic strut. Hence, this cut surface represents the situation at a strut. For these two cut surfaces, a simulation without the shroud — the situation of the first test run — and a simulation with the shroud — the situation of the second test run — are shown in Figure 6.16. The maximal electric fields occurring in these simulations are summarised in Table 6.4. The absolute maximal electric field occurs in the situation with the shroud. At the struts, the maximal field is 23% higher than away from them. This is in agreement with the location of the discharges observed during the second test run.

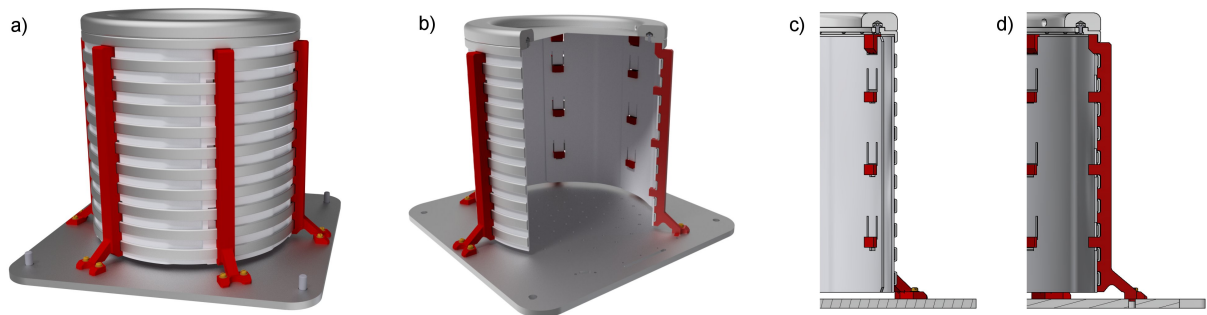


Figure 6.15: Renders of miniEXO. The acrylic struts are highlighted in red. a) The full model is almost axial symmetric. Only the struts break the symmetry. b) A cut away view of miniEXO. The cuts define two cut surfaces: c) a cut surface representing the situation away from the struts and d) a cut surface at a strut. These two cut surfaces are used for the following electric field simulations.

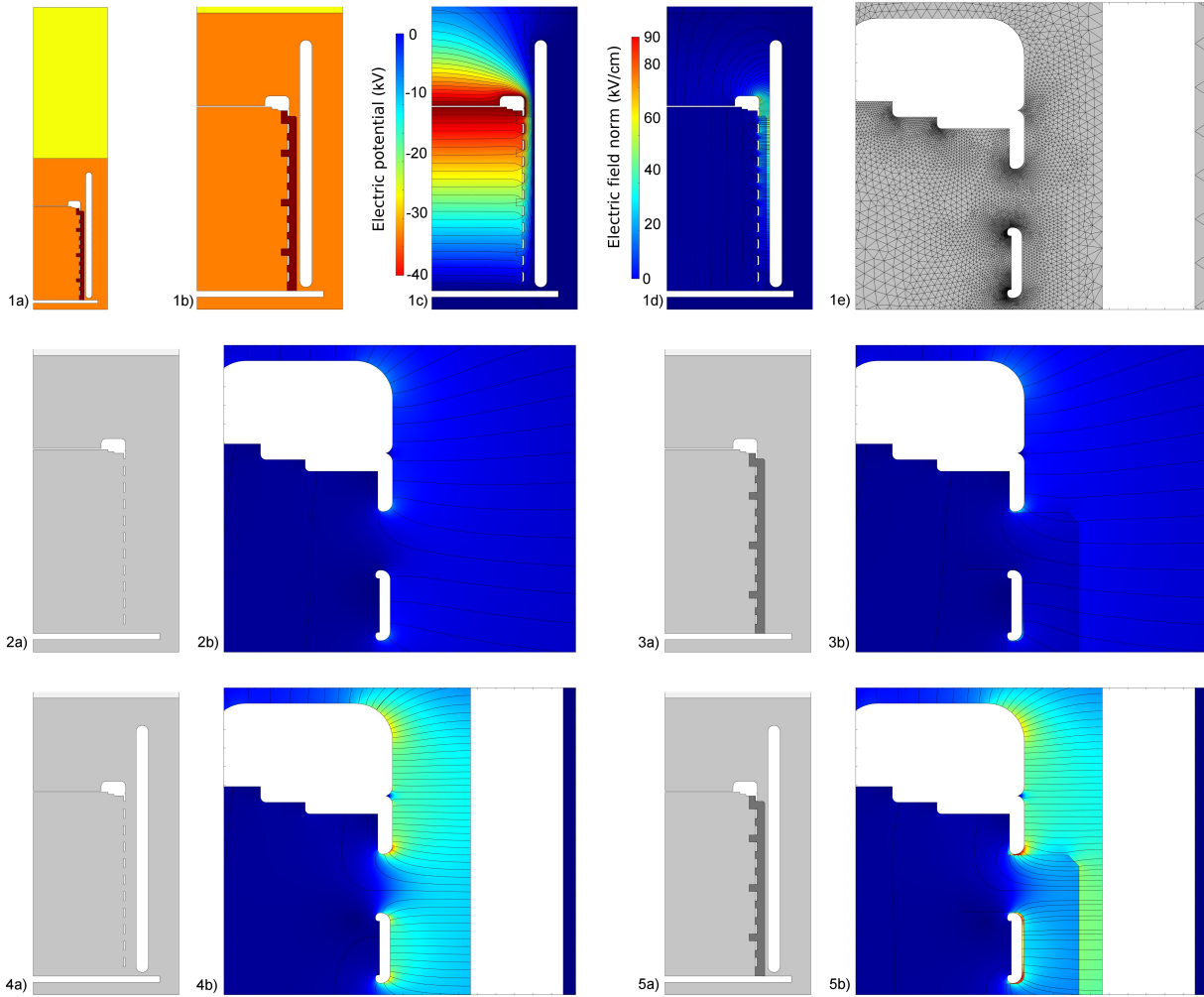


Figure 6.16: Finite element simulation of the electric field in miniEXO. 1a) The simulations are performed with two dimensional axial symmetric models — the symmetry axis is along the left border of the picture. For all cases, miniEXO is placed in the chamber of the EXO-100 cryostat. Yellow- gaseous xenon ($\epsilon_r = 1$), orange- liquid xenon ($\epsilon_r = 1.874$), dark red- acrylic struts ($\epsilon_r = 3.5$), and white- conductor at a given potential. 1b) Zoom of the lower part of the chamber. The upper part is of little interest and is thus not shown here. However, for completeness it was always simulated. 1c) For all simulations shown here, the potential of the cathode was set to -40 kV and the anode to ground. The potential difference from cathode to anode was distributed regularly over the field shaping rings. In black some iso-potential lines are drawn. 1d) The electric field strength is shown. It can be seen that the region with the highest field is close to the cathode. The color legend is valid for all subsequent plots. 1e) The mesh in the high field region is very fine. This simulation was made for four situations. In the following, for these four simulations only the configuration (a) and the electric field in the high field region (b) is shown. 2) The highest field occurs at the lower end of the cathode. 3) The highest field occurs at the lower end of the cathode and at the lower part of the first ring. 4) The highest field occurs at the lower end of the cathode. 5) The highest field occurs at the lower end of the cathode and at the lower part of the first ring. The field between the strut and the shroud is enhanced.

Configuration	Cut surface	Max. electric field
Without shroud	Between two struts	24.6 kV cm ⁻¹
Without shroud	At strut	33.1 kV cm ⁻¹
With shroud	Between two struts	70.9 kV cm ⁻¹
With shroud	At strut	87.2 kV cm ⁻¹

Table 6.4: Maximal electric fields in the four simulations. In reality, some parts of the geometry (e.g. the gaps between the rings and the struts) are not under control. Therefore, care has to be taken when interpreting these values. Nevertheless, they show that the struts increase the maximal field.

6.3.4 Conclusions of the tests with miniEXO

The two test runs with the miniEXO mock-up in combination with the electric field simulations clarified several points. Firstly, the two tests showed that there is no fundamental flaw with the design of the voltage divider. Up to a cathode voltage of -50 kV, no discharges at the voltage divider were detected. Secondly, during these tests no discharges between field shaping rings were observed. This suggests that there is no mechanism that leads to discharges along the struts from ring to ring. Lastly, all observed discharges occurred between the upper end of the field cage and the grounded shroud. These observations are supported by the results of the electro-static simulations. The maximum surface fields in EXO-200 are enhanced by the presence and geometry of the acrylic struts, and it is at these locations where breakdown preferentially occurs.

The data from the glitch detector was not conclusive, and thus, the origin of the glitches could not be found. Nevertheless, these tests demonstrated the usefulness of the EXO-100 set-up and the cryo-cameras for general R&D applications.

Ion tracking with EXO-200 data

For the barium tagging technique some properties of barium in liquid xenon are important. Three properties directly affect the feasibility and efficiency of barium tagging. Firstly, the barium ion fraction — the fraction of the barium which are generated in a charged state $Ba^{+,++}$ after $\beta\beta$ decay. This is critical because all probes described in Section 3.3 can only capture barium ions. Secondly, the ion life-time — defining the time after the decay during which tagging is possible. Lastly, the ion drift speed — defining the time available for the probe to reach the location of the ion. To identify barium is difficult because it requires laser spectroscopy. Instead, these properties were studied with the naturally occurring $^{222}Rn - ^{218}Po$ sequence. In this chapter a data analysis with data from EXO-200 is presented.

7.1	The fully reconstructed data set	92
7.1.1	The populations in the light-charge map	93
7.2	Fiducial cuts	95
7.2.1	Cut in z	95
7.2.2	Cut in x-y	98
7.2.3	Combined fiducial cuts	103
7.3	Identifying alphas	103
7.4	Event linking	107
7.4.1	Verification of the linking algorithm	109
7.5	Radon-222—polonium-218 pairs	111
7.6	Conclusion of the data analysis	117

EXO-200 has accumulated about 2yr of data. However, in EXO-200 the activity of the uranium series is vastly suppressed. For ion tracking, this is a disadvantage. Moreover, EXO-200 was taking data only at one fixed drift field — $380(5) \text{ kV cm}^{-1}$. Thus, the ion properties cannot be studied in dependence of the drift field. However, the advantage of this data is that a large effort was made to analyse it — in the framework of the searches for $\beta\beta(2\nu)$ and $\beta\beta(0\nu)$. The raw data — the waveforms off all channels — was fitted and the position and energy of the events were reconstructed. Due to these efforts and the good performance of EXO-200, this data set

comes with a good energy resolution. For a detailed description of the EXO-200 data set and the event reconstruction, see [1].

7.1 The fully reconstructed data set

The reconstruction of the charge and light signals is essential for the reconstruction of the position and the energy of an event. In some cases, the reconstruction can only partially be achieved. For β and γ events, most of the energy is deposited in the charge channels. In these cases, it is possible that the light signals are too weak, and cannot be reconstructed. The lack of the light signal makes it impossible to reconstruct the z -position of a charge cluster. In EXO-200, 95% of the β and γ events can be fully reconstructed [1]. For α events, most of the light is deposited in the light channels, and thus, all light signals can be reconstructed. However, for the α 's the charge signals are weak. In most of these cases, the signals on the collection channels (U-wires) can be reconstructed. However, the signals of the induction channels (V-wires) can be reconstructed in less than 30% of all α events [4]. Hence, for more than 70% of the α 's it is not possible to reconstruct the position in all three spacial dimensions. Consequentially, the light signals of these events cannot be light map corrected.

In the analysis presented in this section, only the fully reconstructed events were considered. The use of the fully reconstructed data set has its advantages and drawbacks compared to the full data set. The advantages are that the position of all events is known in all three dimensions. The position of the events is needed to identify consecutive alpha-alpha or beta-alpha decays, called here pairing. Moreover, knowing the position of a decay allows to correct the energy deposited in the light channel — depending on the event location more or less light is detected

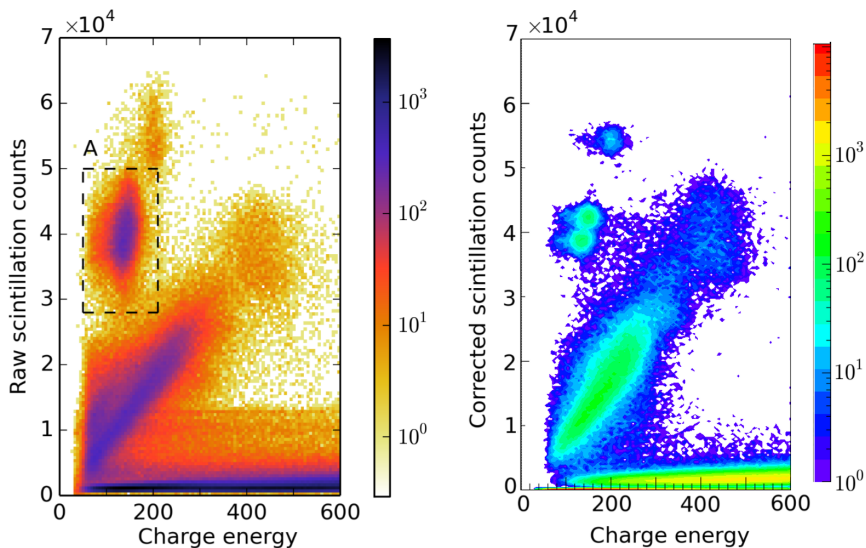


Figure 7.1: Charge-light maps of EXO-200 data. Left, raw scintillation counts versus charge energy. The events in region A correspond to ^{222}Rn and ^{218}Po α decays. The two populations cannot be distinguished in this plot (Figure modified from [4]). Right, corrected scintillation counts versus charge energy. The two α populations can be separated (the lower region corresponds to ^{222}Rn and the upper to ^{218}Po).

with the LAAPD's. The so-called light map correction allows to increase the energy resolution in the light channel, and thus, allows to separate the different α decays in the charge-light map — a two dimensional histogram in which the charge energy is plotted versus the light energy. Figure 7.1 shows how the ^{222}Rn and ^{218}Po populations are overlapping with the raw light signal, and how they can be separated using the light map. The drawback of the fully reconstructed data set is that it is only a small sub set of the full data set. To find a pair, both α 's have to be fully reconstructed. However, the probability for this is less than 9% — considering that the probability for a single α to be fully reconstructed is less than 30%. An analysis on the full data set had been made in parallel to the analysis presented here [4]. The fully reconstructed data has a smaller uncertainty in the pairing process, and it yields information on the displacement of ions in all spacial dimensions. In this sense it is complementary.

7.1.1 The populations in the light-charge map

In the light-charge map of the fully reconstructed data set, several populations can be distinguished (see Figure 7.2). Population 1 corresponds to β , $\beta\beta$, and γ events. This population has been studied in detail [1, 2, 46]. Population 2 are α events occurring on the surface of the cathode (2a & 2b) and the anode (2b) (see Figure 7.3). Population 2a is identified to be ^{214}Po decays. The nature of population 2b remains unclear. Population 3 are the three α decays of ^{222}Rn (3a), ^{218}Po (3b), and ^{214}Po (3c).

The events of the fully reconstructed data set are not homogeneously distributed in the detector. Their position is shown in Figure 7.4. Most events are located close to the anodes and the cathode.

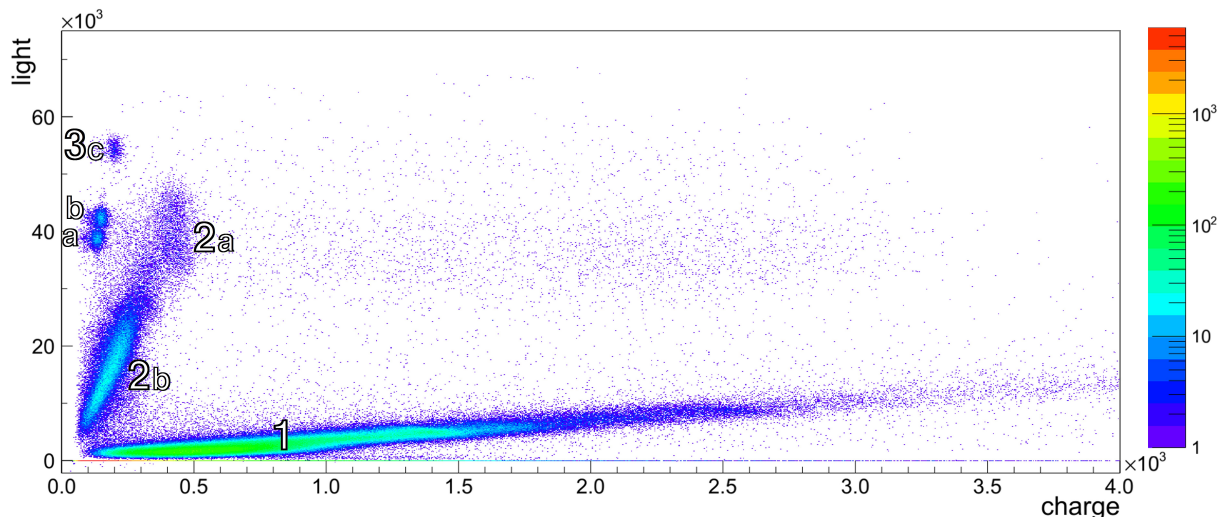


Figure 7.2: Charge-light maps of EXO-200 data. The various populations are identified. For MS the charge energy is summed. See text for details.

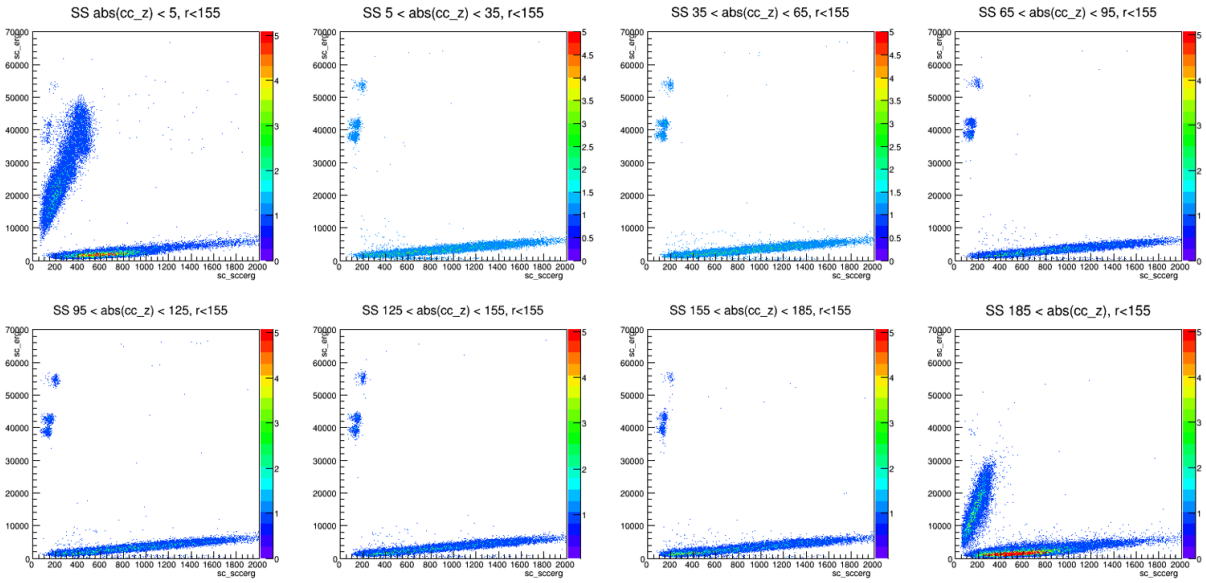


Figure 7.3: Charge-light maps of EXO-200 data. The data set is divided in slices along the z -axis. Top left, the first 5 mm around the cathode. All populations are visible. Note that population 1 is much stronger than in other slices, even though this slice is thinner. This is due to radioactivity on the cathode mesh. Left to right, top to bottom, slices of 30 mm from the cathode towards the anode. Population 2 is not present in these regions. Right bottom, events close to the anode. Population 2a is not present. Furthermore, from the α populations only the ^{222}Rn is visible. The decays of ^{218}Po and ^{214}Po — occurring later in the uranium series — are absent. These two isotopes predominantly drift towards the cathode before they decay. Due to the radioactivity on the anode, population 1 is enhanced.

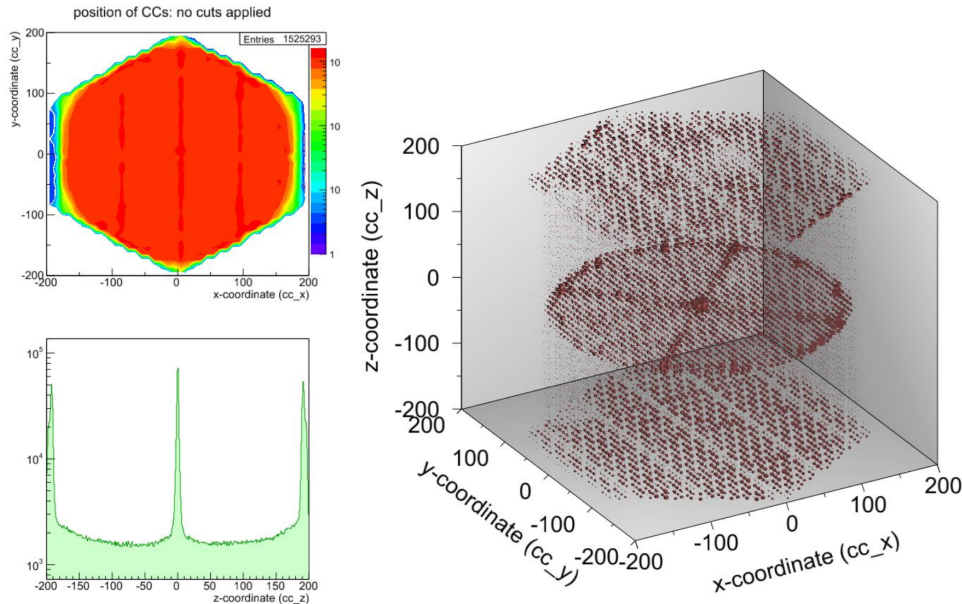


Figure 7.4: Position of all charge clusters in the fully reconstructed data set of EXO-200. In the x - y plane, the hexagonal shape of the instrumented area is shown. In the z -projection, the increased radioactivity at the cathode and the anodes can be seen. In the 3 dimensional plot, the structure of the cathode mesh is visible. All axis are in mm.

7.2 Fiducial cuts

A large fraction of the events in the EXO-200 data set are located close to or on the surfaces of the detector. For three reasons, it is advantageous to exclude these events from the analysis. Firstly, to measure the ion drift velocity, ion neutralisation fraction, and ion lifetime, only alpha events in the bulk are of interest. Alphas at the surface are at rest, and thus, do not bear any information on these quantities. Moreover, these events could distort the measurement if not correctly identified. Secondly, the detection efficiency close to the surfaces of the detector is unknown. Lastly, applying spacial cuts allows to define well a fiducial volume. Therefore, two cuts on the position of an event are applied. The first cut fz is applied on the z -coordinate of a charge cluster and the second fh on its x - y coordinates.

7.2.1 Cut in z

A view on the z -coordinate of all *Charge Cluster's (CC)* reveals an enhanced event rate at the cathode and the anodes (see Figure 7.5). These events originate mostly from γ and β decays on the surfaces. Nevertheless, the cut in z is defined as the regions where these surface events contribute less than 1% to the constant event rate in the bulk. To find these points, the following function is fitted to the cathode and anode regions (see Figures 7.6 & 7.7):

$$f(z) = \exp(p_0 + p_1 \cdot z) + p_2 \quad (7.1)$$

where p_0 is proportional to the amplitude, p_1 is related to the absorption coefficient of xenon and to the detector resolution in z , and p_2 represents the homogeneously distributed signal in the bulk. Thus, the data set is cut where:

$$z = \frac{\ln(p_2/100) - p_0}{p_1}. \quad (7.2)$$

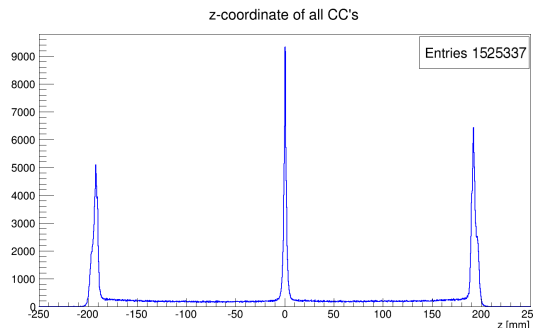


Figure 7.5: Histogram of the z -coordinate of all CC's.

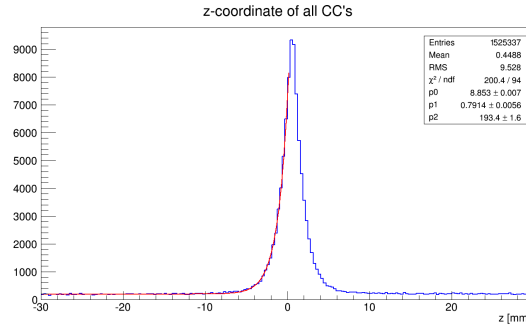


Figure 7.6: Histogram of the z -coordinate of the CC's close to the cathode. Function (7.1) is fitted to determine the cut in this region.

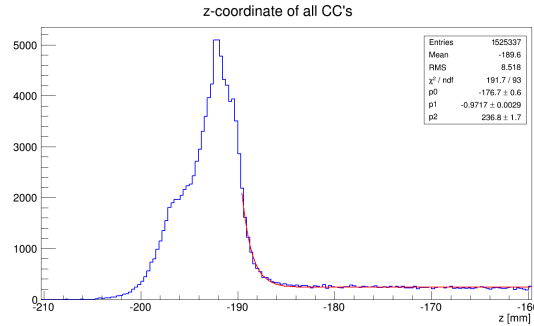


Figure 7.7: Histogram of the z -coordinate of the CC's close to an anode. Function (7.1) is fitted to determine the cut in this region.

The parameters from the four fits lead to the following acceptance intervals for z :

$$\begin{aligned}
 & [(10.95 \pm 0.10)\text{mm}, (182.37 \pm 0.17)\text{mm}] \\
 & \quad \text{OR} \\
 & [(-182.63 \pm 0.82)\text{mm}, (-10.353 \pm 0.074)\text{mm}]
 \end{aligned} \tag{7.3}$$

However, the cathode is not exactly at $z = 0$ (see Figure 7.8). Therefore, the z -axis has to be shifted. To obtain the desired shift correction z_{off} , a Gauss function — without the normalisation part — plus an offset was fitted in the cathode region:

$$f(z) = p_0 \cdot \exp(-0.5((z - p_1)/p_2)^2) + p_3 \tag{7.4}$$

where p_0 is the amplitude of the Gauss function, p_1 is the mean, p_2 the variance, and p_3 the offset.

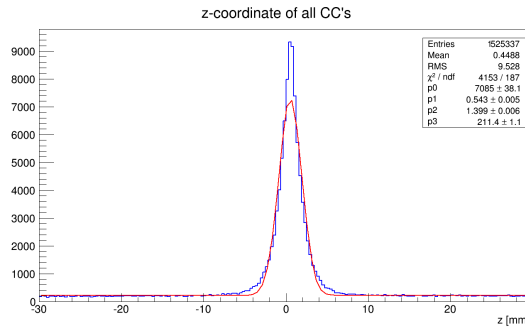


Figure 7.8: The cathode is not located exactly at $z = 0$. To determine the shift correction z_{off} , a Gauss function is fitted to the cathode events.

The mean of the Gauss function determines the shift correction

$$z_{off} = 0.543(5)\text{mm}, \quad (7.5)$$

and thus, the shifted z -coordinates z' are given as

$$z' = z - z_{off}. \quad (7.6)$$

Therefore, the acceptance intervals (7.3) have to be shifted:

$$\begin{aligned} & [(10.41 \pm 0.10)\text{mm}, (181.83 \pm 0.17)\text{mm}] \\ & \quad \quad \quad \text{OR} \\ & [(-183.17 \pm 0.82)\text{mm}, (-10.896 \pm 0.074)\text{mm}]. \end{aligned} \quad (7.7)$$

Considering the errors of the fit parameters and the resolution of the detector (6 mm in z) the cut in z is defined as:

$$fz := \{z' \in \mathbb{R} \mid 11\text{mm} \leq |z'| \leq 181\text{mm}\}. \quad (7.8)$$

The inverse cut is defined as $ifz := \Omega - fz$. The effect of these cuts on the full data set and on selected alpha events is summarised in Table 7.1 & 7.2, respectively. A look at events close to the cathode reveals the structure of the cathode mesh (see Figure 7.9).

Applied cut	CC's remaining	%
none	1 525 293	100.0
fz	590 605	38.7
ifz	934 688	61.3

Table 7.1: The fiducial cut fz applied on the full data set.

Applied cut	CC's remaining	%
none	7 241	100.0
fz	6 782	93.7
ifz	459	6.3

Table 7.2: The fiducial cut fz applied on the on the 3σ ^{222}Rn - ^{218}Po region. These regions are described in Subsection 7.3.

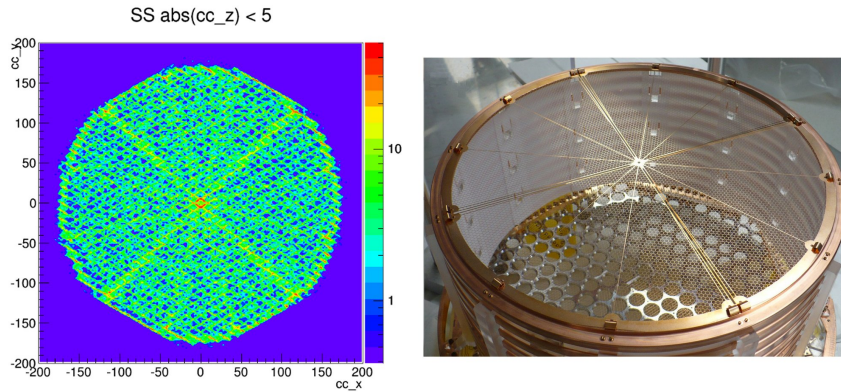


Figure 7.9: The radioactivity at the cathode. Left, the CC's located 5 mm around the cathode reveal the structure of the cathode mesh. Right, a photograph of the cathode mesh.

7.2.2 Cut in $x-y$

To reject events close to the field shaping rings, a cut in the $x-y$ plane is applied. To define such a cut, some characteristics of the read-out planes have to be considered. Due to the U and V wire orientation, the instrumented area of the TPC's have a hexagonal shape (see Figure 7.11). Therefore, a hexagonal cut is used. However, the x and y coordinates of a CC are reconstructed from the U and V wire where the CC was detected. This leads to some artefacts which need to be treated with special care (see Figure 7.10).

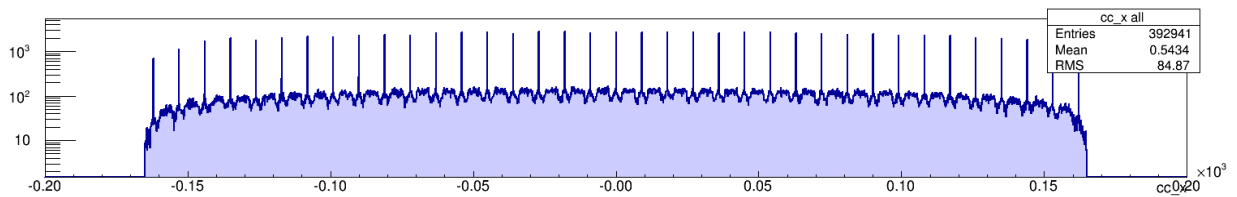


Figure 7.10: Histogram of the x coordinates of all CC's. For a CC detected only with one U triplet and one V triplet, the position is artificially reconstructed as the middle of the triplets. The y coordinates show a similar pattern.

The read-out wires are bundled and read-out in groups of three. For a CC detected with only one U-wire triplet, its U coordinate is reconstructed as the middle of this U-triplet. Thus, for

these CC's, the position reconstruction results in discrete positions. Only if a CC is detected with more than one U wire triplet, its U coordinate can be reconstructed between these discrete steps (see Figure 7.12). The same considerations apply to the V coordinate.

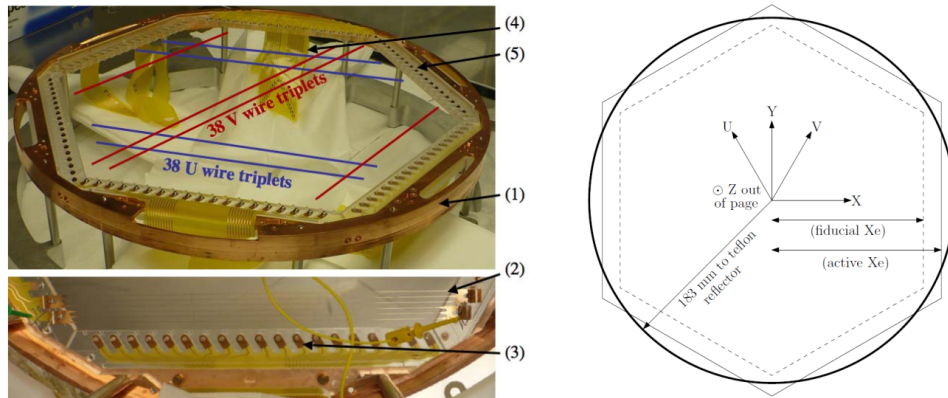


Figure 7.11: The coordinate systems in EXO-200. Left, a copper support ring (1) holds six acrylic blocks in a hexagonal pattern. U wires (2) are mounted on one side of the acrylic blocks and V wires (not shown) are mounted on the opposite side (3) providing a spacing of 6 mm between the wire planes. Four flexible cables (4) make the electrical connections to platinum plated 0-80 UNF screws which anchor the wire triplets to each of four of the acrylic blocks. Un-plated 0-80 UNF screws (5) serve to anchor the other end of the wires and are not used for electrical connection. (Figure and caption from [43].) Right, the scheme of the coordinate systems. (Figure from [1].)

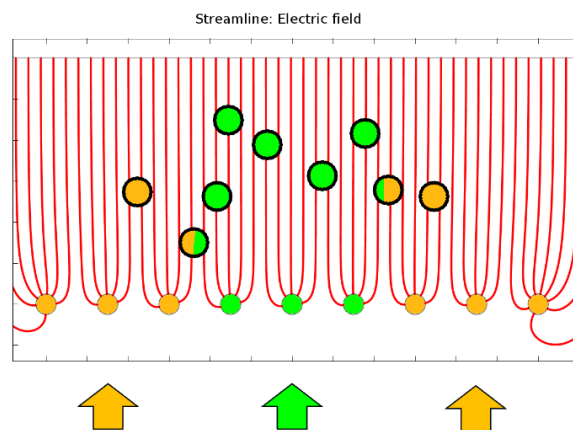


Figure 7.12: Artefact in the position reconstruction. CC's drift along the electric field lines (in red) towards the read-put plane. Some of them are collected on only one wire, and thus, have their position reconstructed as the middle of a wire triplet (indicated by the arrows).

This effect leads to a chess board like pattern in the U-V plane (see Figure 7.13). Two CC's within a given field have the exact same reconstructed $x-y$ coordinates. As shown in Figure 7.14, this leads to hot spots in the $x-y$ plane. Analysing the data shows that 26.6% of all CC's have their $x-y$ coordinates reconstructed on hot spots. However, for the α events this is 96.2%. Presumably,

the difference is due to the short range of α 's in liquid xenon — several micrometers compared to several millimetres for β and γ interactions. Similar reconstruction effects occur if only 3 triplets detect a CC (see Figure 7.15), in this case the positions are reconstructed on hot lines — the middle of a wire group. If two or more U-triplets and two or more V-triplets detect a CC, its position is reconstructed in the continuous x - y plane.

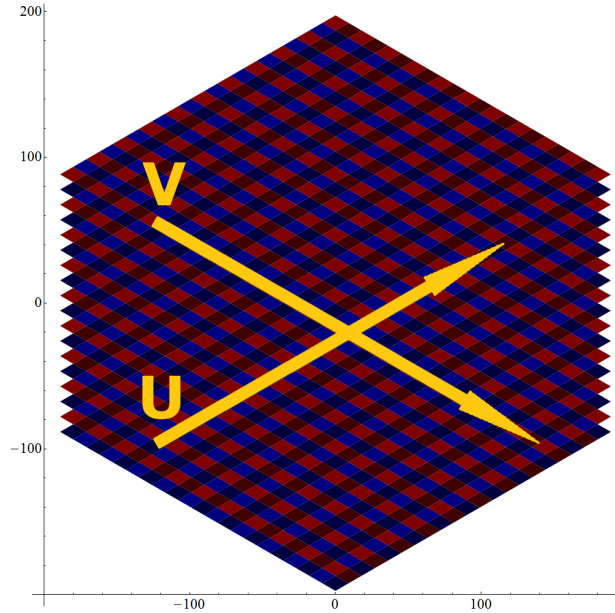


Figure 7.13: Chess board like pattern originating from the U and V wire triplets. In yellow, the orientation of an U and a V wire is shown. Axes in mm.

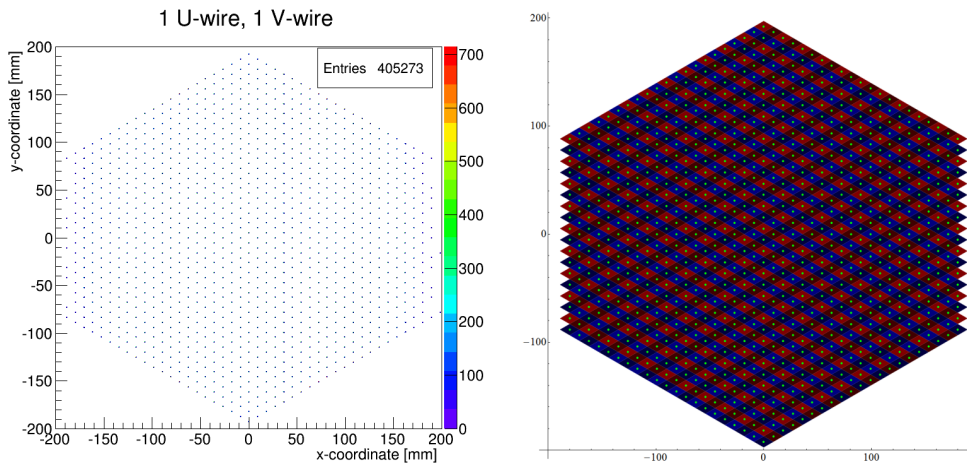


Figure 7.14: Reconstructed position of CC's detected with only one U and one V wire. Left, EXO-200 data. Right, the chess board like pattern with the hot spots marked in the middle of each field.

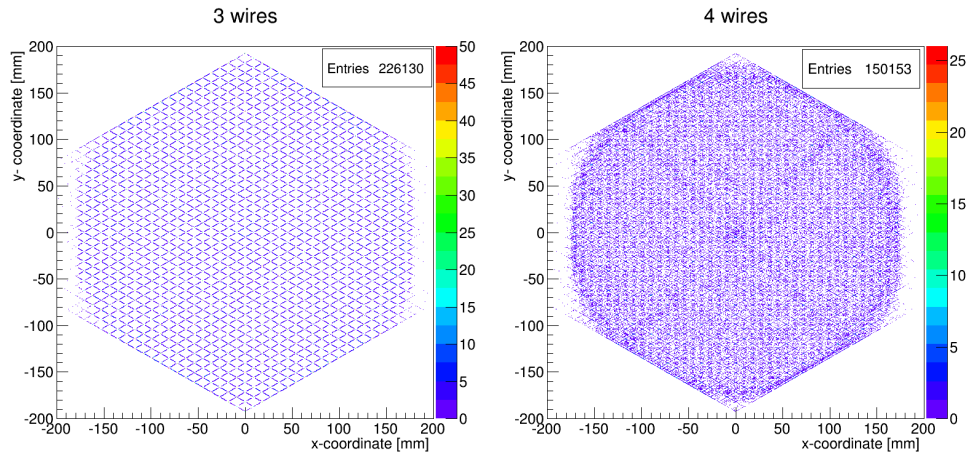


Figure 7.15: Reconstructed position of CC's detected with 3 (left) and 4 (right) wires.

Due to these reconstruction artefacts, using a regular hexagon as cut is not appropriate. A regular hexagon leads to locally asymmetric cut conditions. If the apothem of a regular hexagon is set in such a way that four of the six sides lead to a locally symmetric cut, the other two sides go exactly through the hot spots (see Figure 7.16). Analysing the data shows that 10 670 CC's — 0.7 % of all CC's — are exactly on this cut line. This could lead to a systematic error in the calculation of the fiducial volume. Therefore, an irregular hexagon is used for the x - y cut (see Figure 7.17). Only 18 CC's are located on the cut line of the irregular hexagon.

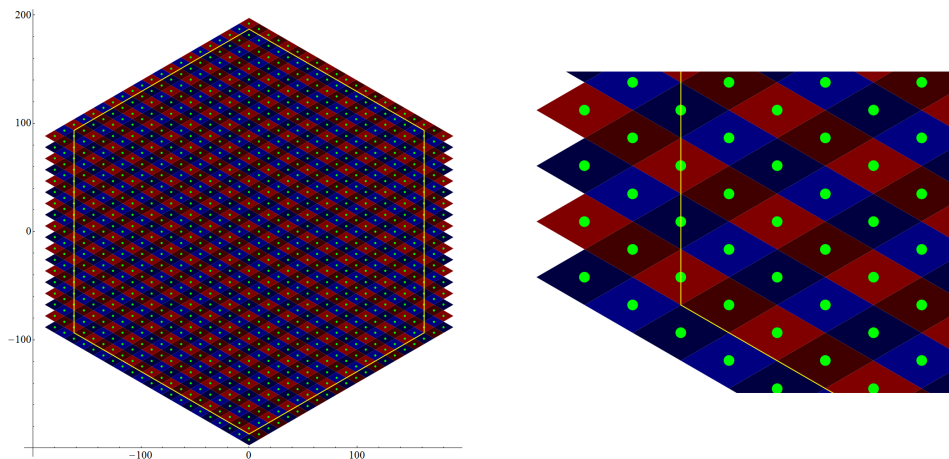


Figure 7.16: Hexagonal cut in the x - y plane. Left, a regular hexagon with an apothem of 162 mm is drawn (in yellow). Right, a close view reveals that this cut goes exactly through the hot spots, and thus, is locally asymmetric.

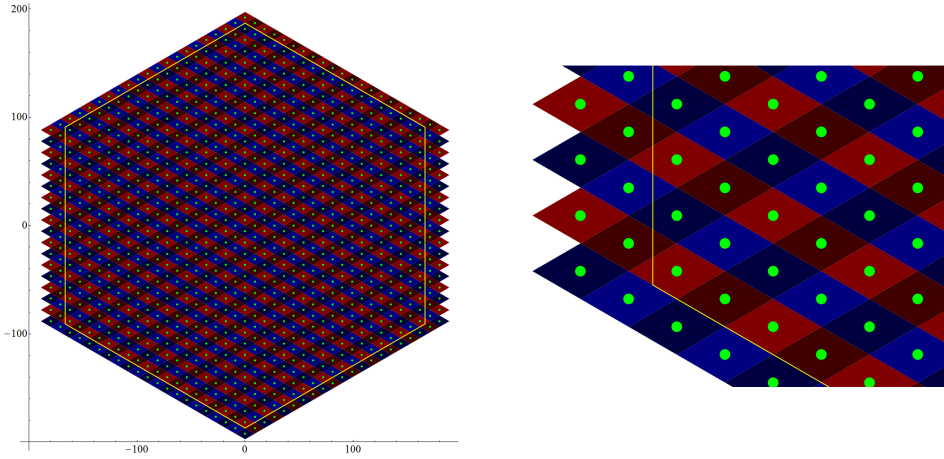


Figure 7.17: Irregular hexagonal cut in the x - y plane. Left, an irregular hexagon with an apothem of 162 mm is drawn (in yellow). Right, on two sides the hexagon is extended by 4.5 mm to establish a locally symmetric cut.

Considering the advantage of the asymmetric extended hexagon, the x - y cut is defined as

$$fh := \left\{ x, y \in \mathbb{R} \mid |y| \cdot \sqrt{3} + |x| \leq 2 \cdot a \text{ AND } |x| \leq a + 4.5 \text{ mm} \right\} \quad (7.9)$$

with apothem $a = 162$ mm. The inverse cut is defined as $ifh := \Omega - fh$. The effect of these cuts on the full data set and on selected α events is summarised in Table 7.3 & 7.4, respectively.

Applied cut	CC's remaining	%
none	1 525 293	100.0
fh	867 327	56.9
ifh	657 966	43.1

Table 7.3: The fiducial cut fh applied to the full data set.

Applied cut	CC's remaining	%
none	7 241	100.0
fh	6 612	91.3
ifh	629	8.7

Table 7.4: The fiducial cut fh applied to the 3σ ^{222}Rn - ^{218}Po region. These regions are described in Subsection 7.3.

7.2.3 Combined fiducial cuts

In the data analysis, the two fiducial cuts fz and fh are used in combination. Additionally to these cuts, all multi site events are rejected, *single site* (ss) events only are accepted. The ss cut affects only a few alpha events (0.6%). However, this simplifies the event linking process as degenerate cases are excluded. The effect of the combined cuts on the full data set and on selected alpha events is summarised in Table 7.5 & 7.6, respectively.

Applied cut	CC's remaining	%
none	1 525 293	100.0
fz & fh (& ss)	396 169 (209 436)	26.0 (13.7)
ifz OR ifh	1 128 524	74.0

Table 7.5: The combined cuts applied to the full data set. In brackets, the addition of the ss cut is shown.

Applied cut	CC's remaining	%
none	7 241	100.0
fz & fh (& ss)	6 194 (6 150)	85.5 (84.9)
ifz OR ifh	1047	14.5

Table 7.6: The combined cuts applied to the 3σ ^{222}Rn - ^{218}Po region. These regions are described in Subsection 7.3. In brackets, the addition of the ss cut is shown.

Combining the two cuts fz and fh selects a fiducial volume of:

$$\begin{aligned}
 Length &= 2 \cdot 17.0(6) \text{ cm} \\
 Area &= 925(25) \text{ cm}^2 \\
 Volume &= 31.47(89) \cdot 10^3 \text{ cm}^3.
 \end{aligned}
 \tag{7.10}$$

7.3 Identifying alphas

After applying the cuts described above, some populations in the charge-light map vanish (see Figure 7.2 and 7.18). In the charge-light map of the reduced data set, the α populations are clearly distinguishable from the others. The three α populations correspond to the decays of ^{222}Rn , ^{218}Po , and ^{214}Po in the bulk of the detector. The ^{214}Po population is separated from the other two, and thus, these events can be identified. However, the ^{222}Rn and ^{218}Po populations overlap. For each of these two populations, a region in the charge light map was defined and characterised.

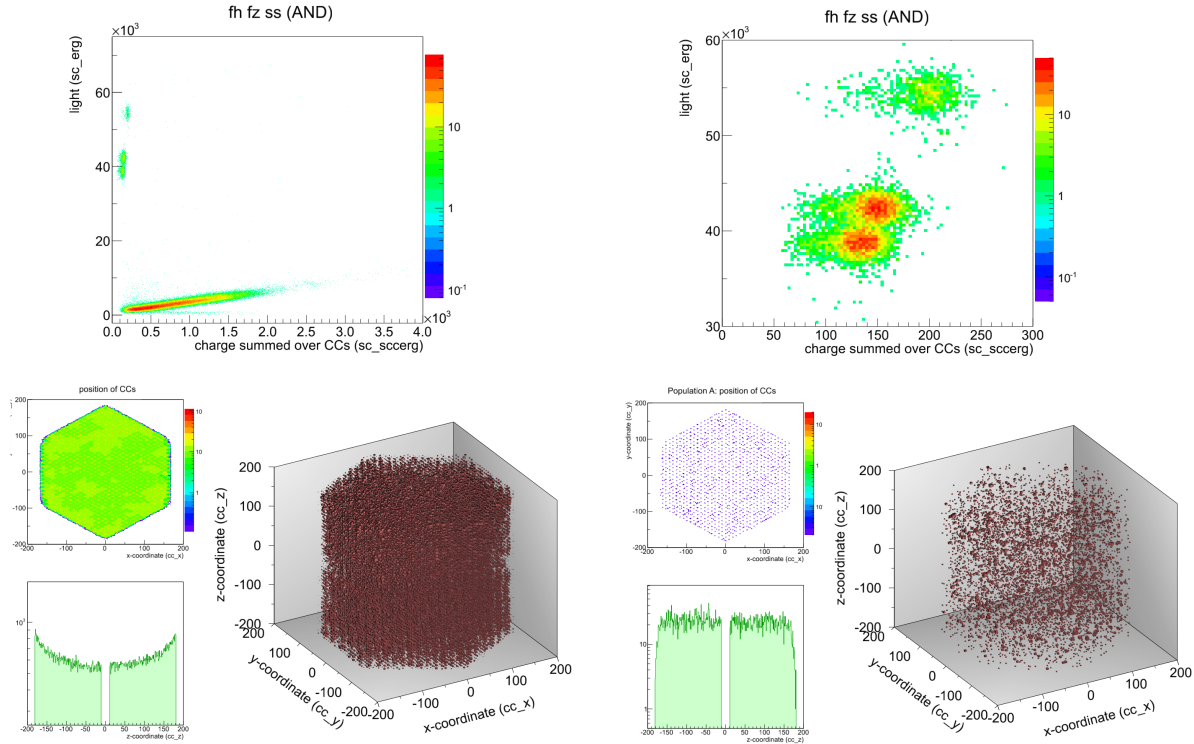


Figure 7.18: EXO-200 data after applying the combined cuts fz , fh , and ss . Top, the charge-light maps. Bottom, the position plots. Left, the full data set. Right, a rough selection of the α events.

To define the ^{222}Rn and ^{218}Po regions, two multivariate normal distributions (see Appendix G) are fitted to these populations (see Figure 7.19). From the fit result, several independent cuts in the light charge map were defined. The resulting ellipses are centred around the peak of the corresponding multivariate distribution and have radii of n sigma. For flexibility, n can be chosen as desired.

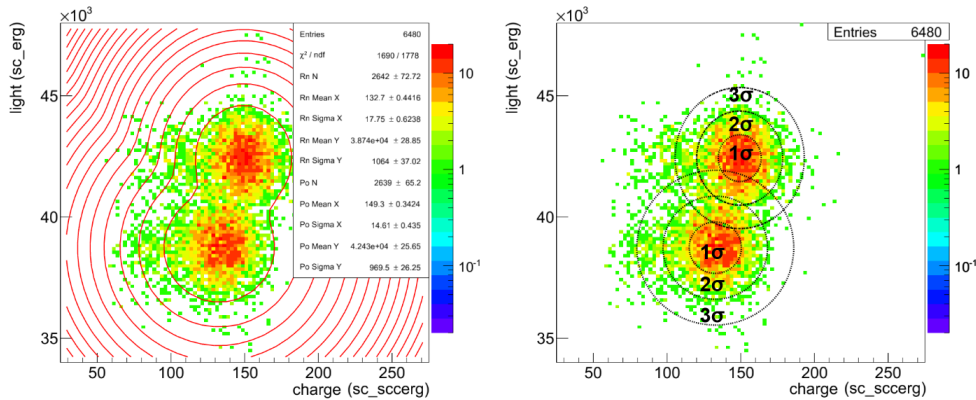


Figure 7.19: The ^{222}Rn and ^{218}Po populations. Left, a multivariate normal distribution is fitted to the data. Right, from the fit parameters several regions around ^{222}Rn and ^{218}Po can be defined.

To determine the efficiency and purity of these regions, theoretical distributions can be plotted (see Figure 7.20). These theoretical distributions allow to calculate separately the contribution of the ^{222}Rn and ^{218}Po populations in any region of the charge-light map. In Figure 7.21, these distributions are presented for the 3σ ^{218}Po region. For the ^{222}Rn and ^{218}Po populations, four regions were defined (see Figures 7.22 & 7.23) and their efficiency and purity was calculated (see Tables 7.7 & 7.8). The ^{214}Po population can be isolated in the charge-light map, and thus, this procedure is not required. For this population a 5σ region is used — which has a purity and efficiency close to 100%.

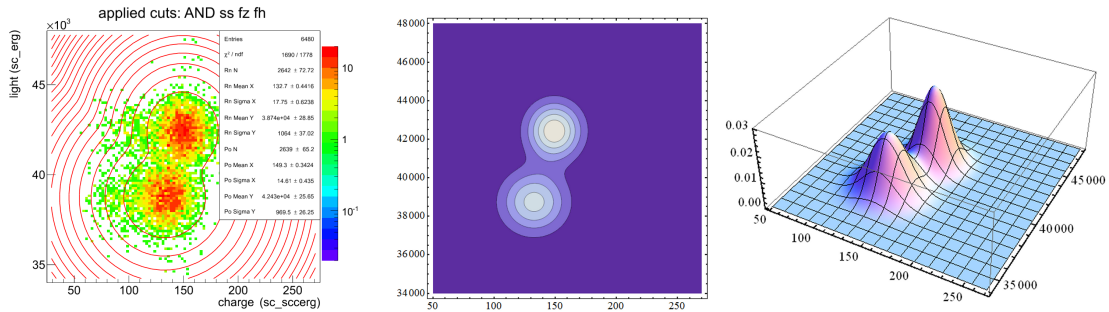


Figure 7.20: The theoretical distributions in the ^{222}Rn - ^{218}Po region. Left, the fitted data. Middle, a contour plot of the theoretical distributions, and right, a three dimensional plot. (The x and y axis are in mm. The z is in arbitrary units.)

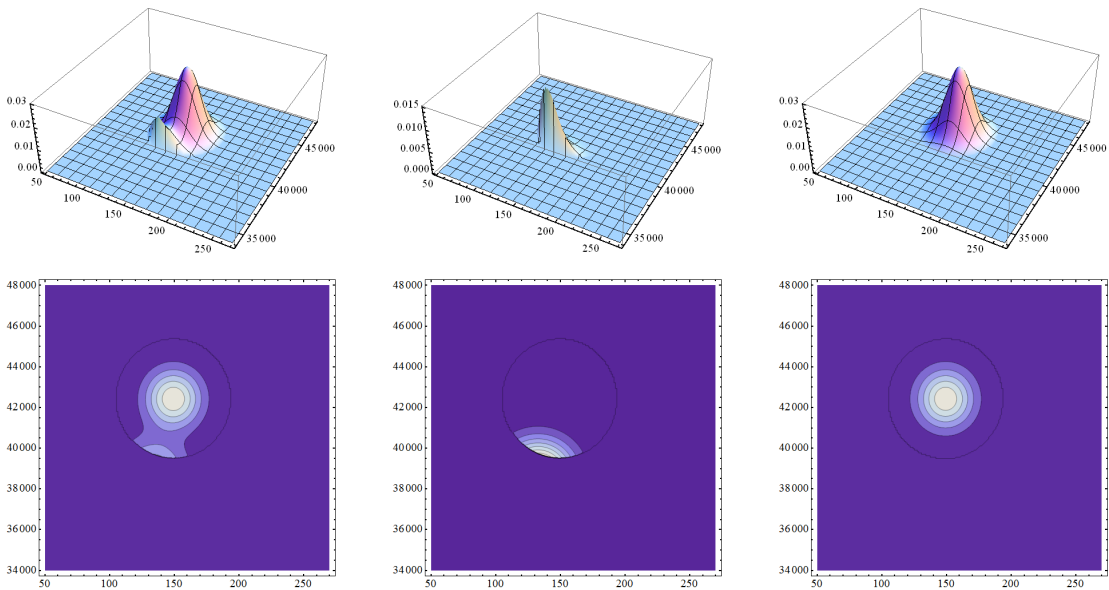
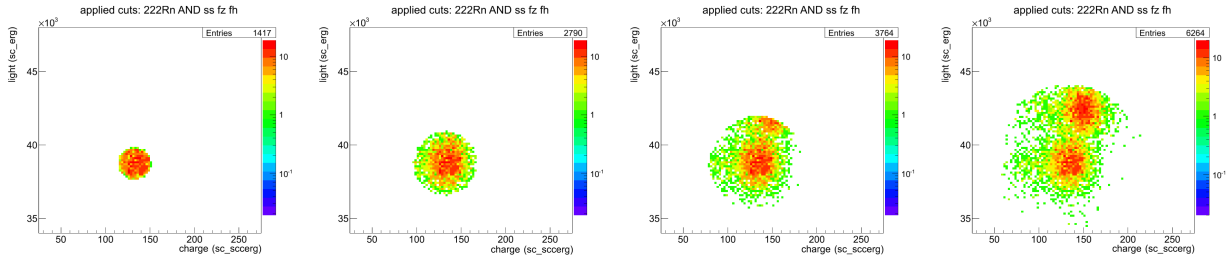
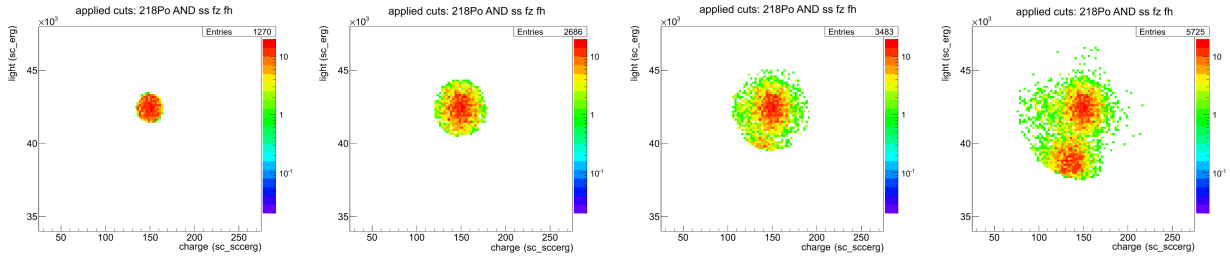


Figure 7.21: The theoretical distributions in the 3σ ^{218}Po region. Left, the two distributions. The integral of this plot yields the total amount of events in this region. Middle, the ^{222}Rn population leaks into the selected region. The integral of this plot yields the impurity. Right, the selected region cuts some of the ^{218}Po events. The integral of this plot yields the efficiency. Top, three dimensional plots, and bottom, contour plots. (The x and y axis are in mm. The z is in arbitrary units.)


 Figure 7.22: Charge-light map of the four regions around ^{222}Rn . Left to right, 1σ , 2σ , 3σ , and 5σ .

Selected region	Events in region	Efficiency [%]	Purity [%]
$^{222}\text{Rn } 1\sigma$	1 417	39.3	99.7
$^{222}\text{Rn } 2\sigma$	2 790	86.5	96.8
$^{222}\text{Rn } 3\sigma$	3 764	98.9	81.8
$^{222}\text{Rn } 5\sigma$	6 264	99.9996	51.9

 Table 7.7: The purity and efficiency of four regions around the ^{222}Rn population.

 Figure 7.23: Charge-light map of the four regions around ^{218}Po . Left to right, 1σ , 2σ , 3σ , and 5σ .

Selected region	Events in region	Efficiency [%]	Purity [%]
$^{218}\text{Po } 1\sigma$	1 270	39.3	99.6
$^{218}\text{Po } 2\sigma$	2 686	86.5	97.5
$^{218}\text{Po } 3\sigma$	3 483	98.9	87.3
$^{218}\text{Po } 5\sigma$	5 725	99.9996	56.1

 Table 7.8: The purity and efficiency of four regions around the ^{218}Po population.

In addition to identifying the α 's, from the fit parameters the charge-light relation for α events can be determined. Plotting the mean values of the three multivariate normal distributions shows that the charge and light follow a linear dependence (see Figure 7.24). The charge-light relation for α events is

$$\begin{aligned}
 l_\alpha &= p_0 + p_1 \cdot ch_\alpha \\
 l_\alpha &= 8.1 \cdot 10^3 + 230 \cdot ch_\alpha,
 \end{aligned}
 \tag{7.11}$$

where l_α is the light and ch_α the charge produced by an α event — in arbitrary but standardised units.

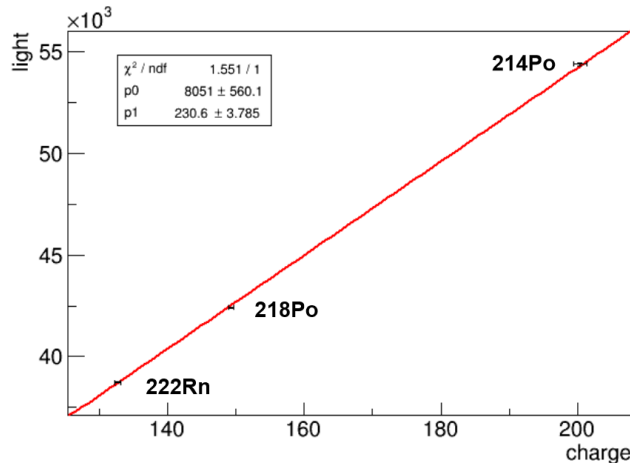


Figure 7.24: The charge-light relation for α events. A linear fit is applied to the three data points (in red).

7.4 Event linking

To measure the properties of interest, the mother and the daughter decays of a single nucleus have to be linked. Thereafter, each successfully linked pair can be analysed. To correctly link two decays — which may occur with a delay of several minutes — a linking algorithm is used. This algorithm follows four steps. Firstly, two candidate populations have to be defined — using the fiducial cuts and selecting a region in the charge-light map. The events in population A are considered decays of the mother while the events in population B are considered decays of the daughter. Secondly, to find the B' candidate corresponding to a given A' candidate, a rough selection of potential B_j candidates is made. Generally, all B_j candidates occurring in a time interval $[t_0, t_0 + 10 \cdot T_{1/2}]$ are considered — where t_0 is the time of the A' event and $T_{1/2}$ is the half-life of the daughter decay. Moreover, all A_i candidates in the interval $[t_0 - 10 \cdot T_{1/2}, t_0 + 10 \cdot T_{1/2}]$ are considered competitors to the A' event in the subsequent linking process. This step is required to avoid that a single B candidate could get linked to two different A candidates. This pre-selection yields n A_i candidates — including A' — and m B_j candidates. Thirdly, the probability $p(A_i, B_j)$ that two candidates belong together is calculated for all A_i and B_j combinations and stored in a $n \times m$ matrix M . The probability $p(A_i, B_j)$ depends on the temporal Δt and spacial $\Delta \vec{x}$ separation of the two events [73]

$$p(A_i, B_j) := p(\Delta \vec{x}, \Delta t). \tag{7.12}$$

The probability $p(\Delta\vec{x}, \Delta t)$ is given as

$$p(\Delta\vec{x}, \Delta t) = p(\Delta\vec{x} | \Delta t) \cdot p(\Delta t) \quad (7.13)$$

where $p(\Delta t)$ is the portability that two events occur with a certain temporal separation and $p(\Delta\vec{x} | \Delta t)$ the probability that they occur with a certain spacial separation given the temporal separation Δt . The probability $p(\Delta t)$ is given as

$$p(\Delta t) \mapsto \begin{cases} \lambda e^{-\lambda|\Delta t|} : & \Delta t > 0 \\ 0 : & \Delta t \leq 0 \end{cases} \quad (7.14)$$

where λ is the lifetime of the daughter decay. In $p(\Delta t)$ two cases are distinguished. If $\Delta t > 0$, the daughter event occurred after the parent decay. If $\Delta t < 0$, the inverse is suggested. This is non-physical, and thus, $p(\Delta t < 0) = 0$. In the case where $\Delta t = 0$, the two events to be linked are the same physical event. Thus, to avoid self-linking, $p(\Delta t = 0) = 0$.

The probability $p(\Delta\vec{x} | \Delta t)$ is given by a n dimensional independent multivariate normal distribution (see Appendix G)

$$\begin{aligned} p(\Delta\vec{x} | \Delta t) &= f(\Delta\vec{x}, \vec{\mu} = 0, \sigma(\Delta t)) \\ &= \frac{1}{\sqrt{(2\pi)^n \sigma(\Delta t)^{2n}}} \exp\left(-\frac{1}{2} \sum_{i=1}^n \left(\frac{(\Delta x_i)^2}{\sigma(\Delta t)^2}\right)\right) \end{aligned} \quad (7.15)$$

with

$$n \mapsto \begin{cases} 2 : & \Delta t \leq 200 \text{ s} \\ 3 : & \Delta t > 200 \text{ s} \end{cases} \quad (7.16)$$

For the first 200s, the daughter could be charged and drift in z . Therefore, during this time only the x and y separation are considered. Thereafter, charged daughters have drifted out of the fiducial volume and only the neutral remain. For them a three dimensional distribution is adequate.

In (7.15), $\sigma(\Delta t)$ is the time dependent spacial uncertainty on the nucleus's position. It is generally given as

$$\sigma(t) = \sigma_0 + \sqrt{t} \sigma_1 + t \sigma_2 \quad (7.17)$$

where σ_0 is the detector's position resolution, σ_1 is the square-root of the diffusion coefficient, and σ_2 the contribution due to liquid xenon flow. The value of the detector resolution σ_0 — which is dominated by the reconstruction artefact discussed above — is set to the wire triplet spacing of 9 mm. The contribution of σ_1 is so small that it is neglected. The value of σ_2 is estimated to be of the order of 0.1 mm s^{-1} — from the liquid xenon circulation speed. In Figure 7.25, $p(\Delta\vec{x}, \Delta t)$ is shown for the one dimensional case.

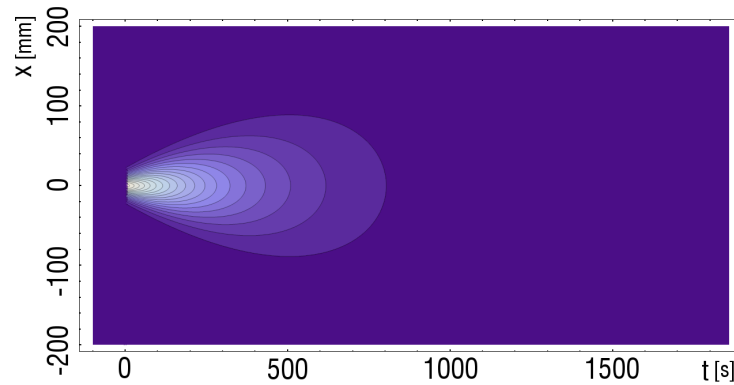


Figure 7.25: The one dimensional linking probability function. The mother's decay is localised at $\Delta t = 0$ and $\Delta x = 0$. A darker color indicates a low probability density.

With (7.12 – 7.17), M can be written as

$$M := \begin{pmatrix} p(A_0, B_0) & p(A_0, B_1) & \cdots & p(A_0, B_m) \\ \vdots & \vdots & & \vdots \\ p(A', B_0) & p(A', B_1) & \cdots & p(A', B_m) \\ \vdots & \vdots & & \vdots \\ p(A_n, B_0) & p(A_n, B_1) & \cdots & p(A_n, B_m) \end{pmatrix} \quad (7.18)$$

The last step in the linking algorithm is to check M for a probable and unambiguous match. In the row of A' the two entries B' and B'' with the highest linking probability are selected. If $p(A', B') > 100 \cdot p(A', B'')$, B' is considered the unambiguous candidate for a match. To be considered a probable match candidate, $p(A', B')$ has to be larger than a minimal probability p_{min} . Only if both conditions are satisfied, B' is considered the favoured link candidate for A' . However, this does not imply that A' is the favoured link candidate for B' . Hence, the same procedure is done in the column of B' . If this yields A' as the preferred candidate, a pair is found.

7.4.1 Verification of the linking algorithm

To be sure that the linking algorithm returns true pairs, it can be tested in two ways. In a first test, the cuts in the charge-light map of the A and B populations are relaxed to include all events in the ^{222}Rn and ^{218}Po region. Thus, both populations are identical. With these populations the linking algorithm is executed. It returns the linked mother decays in the ^{222}Rn region of the charge-light map and the corresponding daughter decays in the ^{218}Po region (see Figure 7.26).

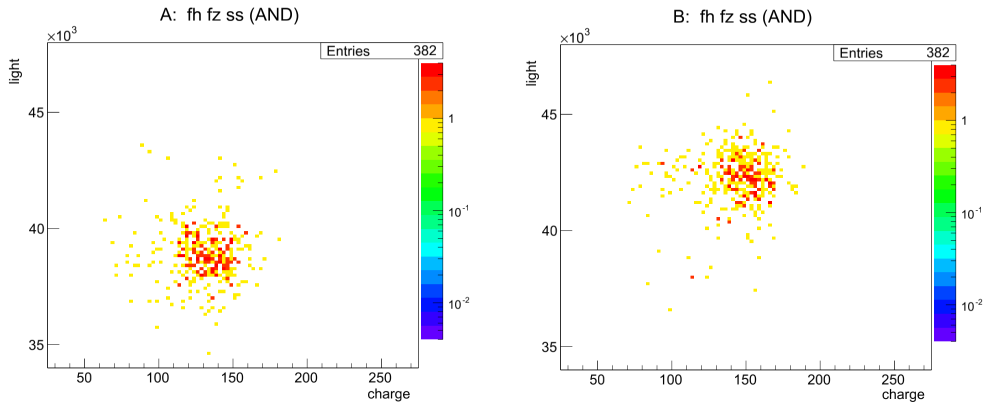


Figure 7.26: Test of the linking algorithm in the charge light map. The mother (left) and daughter decays (right) returned by the linking algorithm are located correctly in the ^{222}Rn and ^{218}Po regions in the charge light map. For this test, no distinction of the A and B candidates is made prior to executing the algorithm.

In a second test, the cuts in the charge-light map are set to ^{222}Rn (2σ) and ^{218}Po (3σ) for the population A and B , respectively. With these populations the linking algorithm is executed. Thereafter, a histogram with the Δt of the pairs is generated. In the histogram an exponential function is fitted to the data in the time interval $[T_{1/2}, 3 \cdot T_{1/2}]$ (see Figure 7.27). (The time interval $[0, T_{1/2}]$ contains charged daughter which drift out of the fiducial volume. Therefore, this interval is excluded.) The fit yields $T_{1/2} = 178(4)$ s. This result is close to the known half-life of ^{218}Po , 183 s. These two tests indicate that the linking algorithm predominantly returns true pairs.

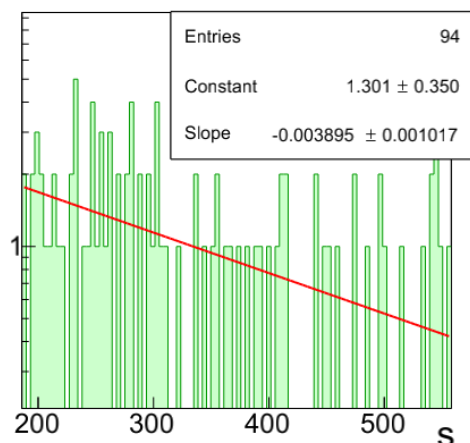


Figure 7.27: Test of the linking algorithm with the decay time. For the time window $[T_{1/2}, 3 \cdot T_{1/2}]$ — which is free from Po ions — the measured half-life is correct.

7.5 Radon-222—polonium-218 pairs

To obtain a set of ^{222}Rn — ^{218}Po pairs (*RnPo*), three steps were made. Firstly, the fiducial cuts (fh and fz) and the single side cut (ss) was applied to the data set. Secondly, the 3σ region of ^{222}Rn was selected as population A, and, the 3σ regions of ^{218}Po as population B. Lastly, the linking algorithm was executed. The linking algorithm found 387 fully reconstructed pairs — in the data of about 2 yr. The ^{222}Rn and ^{218}Po decays (corresponding to these pairs) are homogeneously distributed in the fiducial volume (see Figure 7.28).

From the positions of the mother's and daughter's decays, the ion displacement can be derived. Figure 7.29 shows arrows starting at the mother's decay position and pointing towards the daughter's decay position — thus, these arrows indicate the absolute displacement. Furthermore, the displacement relative to the mother's decay position are shown. It can be seen that a fraction of the ions drifted towards the cathode.

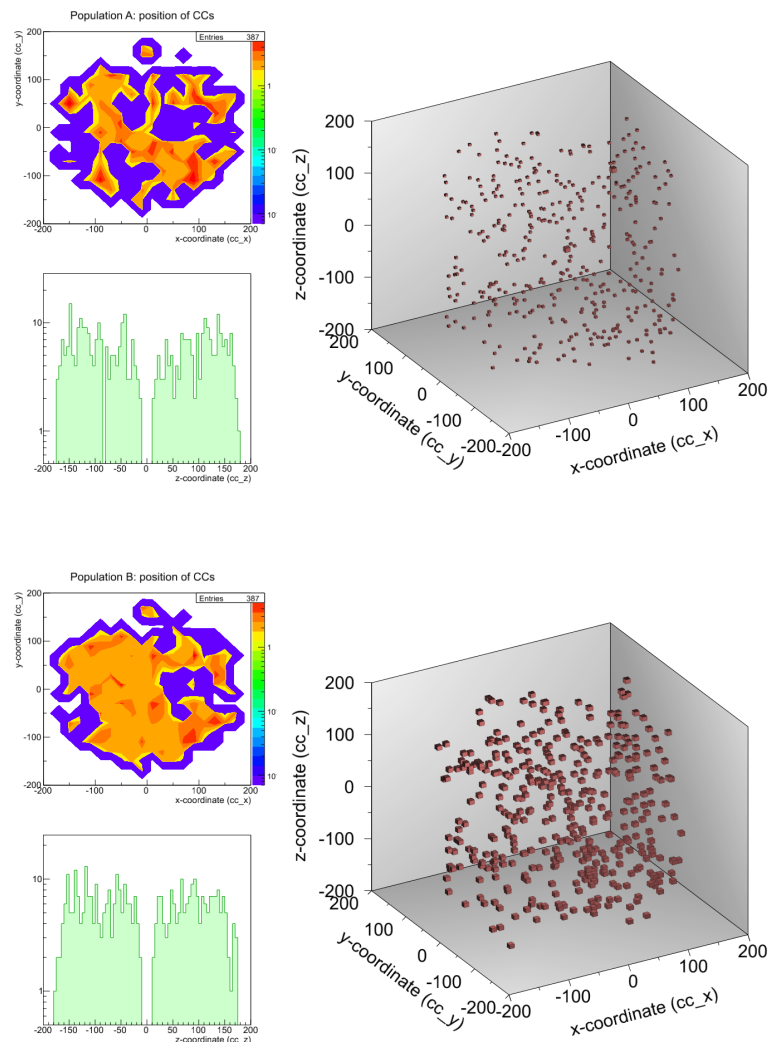


Figure 7.28: The position of the mother decays ^{222}Rn (top) and daughter decays ^{218}Po (bottom).

The velocity of an ion can be derived from the displacement and the time between the mother's and daughter's decay. Figure 7.30 shows arrows indicating the velocity. In the top row, the arrows start at the position of the mother's decay and have a length corresponding to the speed of the ion. In the middle row, the arrows start at $\vec{V} = 0$. For short dt 's, the detectors positioning uncertainty (in particular in z) leads to some arrows with $V_z > 2.5 \text{ mm s}^{-1}$. In these cases the calculated displacement has a large relative uncertainty — which directly affects the uncertainty of \vec{V} . Therefore, these arrows are dominated by the uncertainty and can be rejected by rejecting all pairs with $\Delta t < 5 \text{ s}$ — shown in the bottom row.

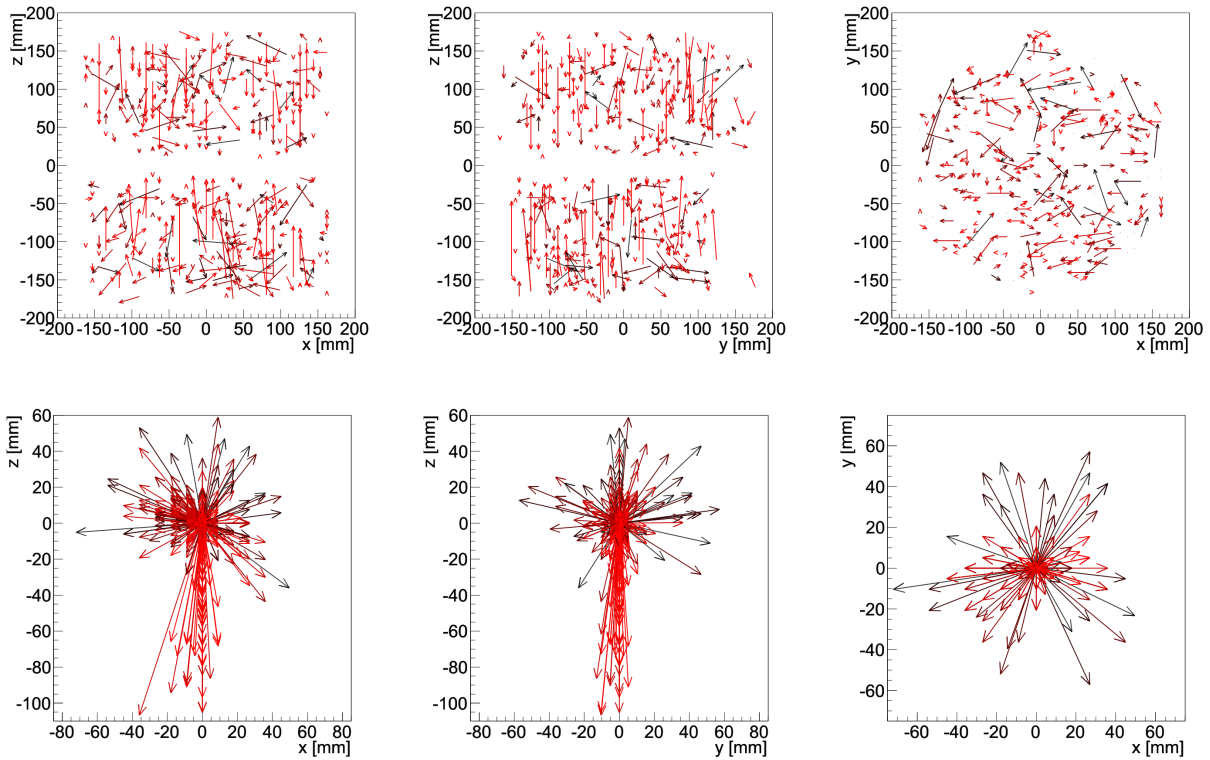


Figure 7.29: Arrows showing the displacement of the polonium during its life-time. In the top row, the arrows start at the position where the ^{222}Rn decayed. Their heads point to the ^{218}Po decay. The arrows are projected onto three planes. The color represents the time between the decays (dark for large Δt), $\Delta t < 10 \cdot T_{1/2}$. In the lower row, the arrows start at the origin of the coordinate system and indicate the relative displacement of the polonium. In both rows, several of the bright red arrows (decay during the first half-life) show a displacement towards the cathode.

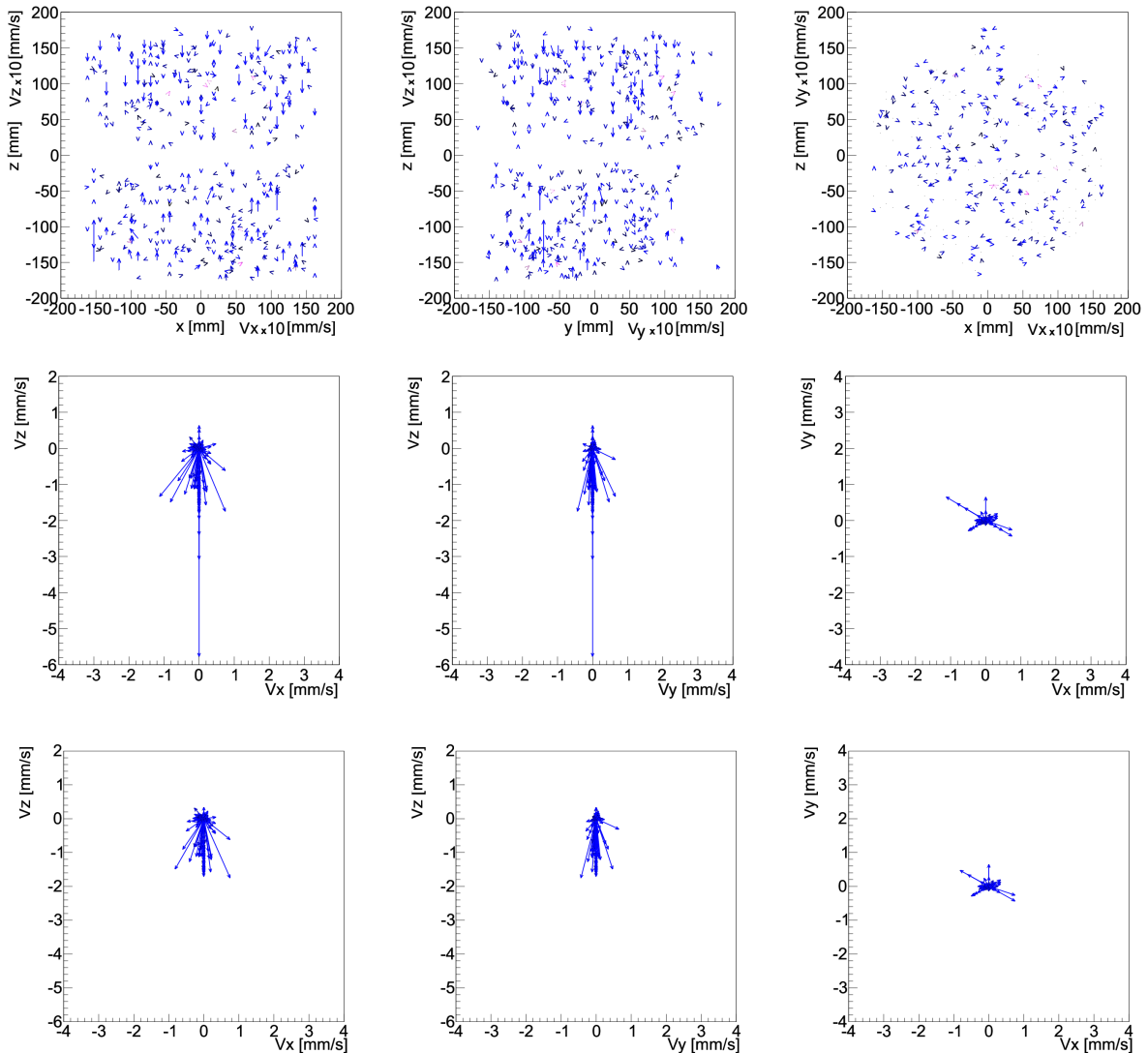


Figure 7.30: Arrows showing the drift speed of the polonium. In the top row, the arrows start at the position where the ^{222}Rn decayed. Their heads point to the ^{218}Po decay and have a length corresponding to the drift speed. The arrows are projected onto three planes. The color represents the time between the decays (short to large Δt 's: blue, dark blue, purple), $\Delta t < 10 \cdot T_{1/2}$. In the middle row, the arrows start at the origin of the coordinate system and show the drift speed of the polonium. In the bottom row, the same is shown but pairs with $\Delta t < 5$ s are rejected.

The z component of the velocity shows two groups (see Figure 7.31). The first group is at rest and the second drifts towards the cathode. The first group originates from ^{218}Po generated in a neutral state. The second group are ^{218}Po generated in a positively charged state. Furthermore, it can be seen that in the decay of ^{222}Rn the ^{218}Po is never generated in a negatively charged state. In Figure 7.31, it seems that the charged group is a minority. However, the charged ions drift out of the fiducial volume and thus a large fraction of them are never linked. In this sense this selection is 'unfair'.

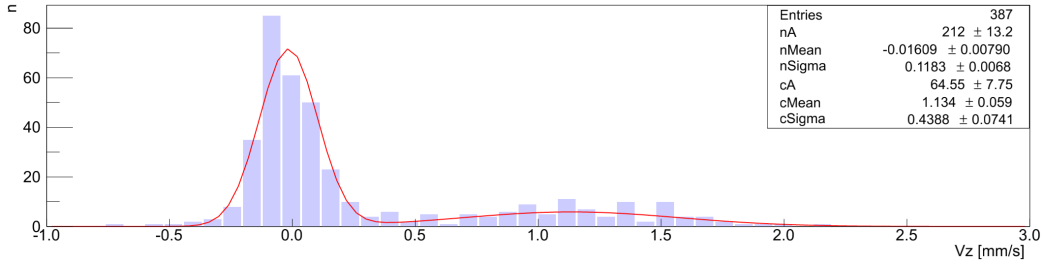


Figure 7.31: Histogram of the z -component of polonium's drift speed. A positive speed indicates motion towards the cathode.

To derive the true neutralisation fraction a 'fair cut' was applied to the pair data set. The concept of the 'fair cut' is to give the neutral and the charged ^{218}Po an equal chance to be selected. To correct for the fraction of ^{218}Po which drift out of the fiducial volume before they decay, only pairs with $dt < \Delta t(z')$ are selected. $\Delta t(z')$ is the time window during which any charged ^{218}Po is still in the fiducial volume. This time window is defined as

$$\Delta t(z') := \frac{|z'| - z_{cut}}{v_{max}} \quad (7.19)$$

where z' is the z coordinate of the ^{222}Rn decay (corrected for the offset, see eq. 7.6), z_{cut} is the fiducial cut along the cathode (11 mm), and v_{max} is the fastest velocity of any ^{218}Po ion. In Figure 7.31, it can be seen that no ion drifts faster than 2.5 mm s^{-1} and thus $v_{max} := 2.5 \text{ mm s}^{-1}$. For those pairs selected by the 'fair cut', the z component of the velocity is shown in Figure 7.32. Fitting the velocity distribution with two Gauss functions allows to determine the ^{218}Po ion and

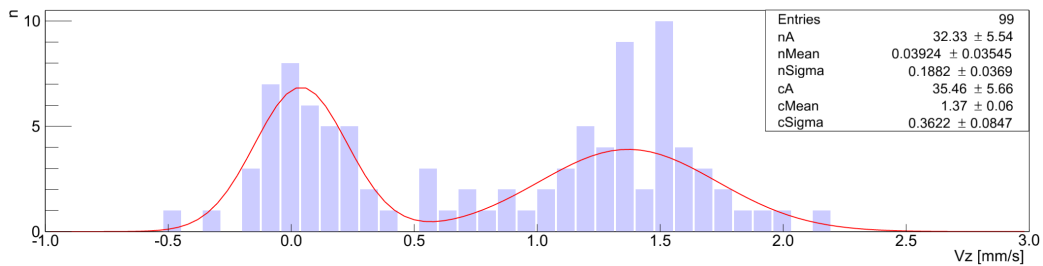


Figure 7.32: Histogram of the z -component of the polonium's drift speed with applied 'fair cut'. A positive speed indicates motion towards the cathode. The charged group is distributed wider than the neutral group (see text for details).

atom fractions:

$$\frac{{}^{218}\text{Po}^+}{{}^{218}\text{Po}^+ + {}^{218}\text{Po}} = 52(10)\% \quad (7.20)$$

$$\frac{{}^{218}\text{Po}}{{}^{218}\text{Po}^+ + {}^{218}\text{Po}} = 48(10)\%. \quad (7.21)$$

Moreover, the ion drift velocity can be determined from the Gauss function fitted to the charged group:

$$v_{ion} = 1.4(4) \text{ mm s}^{-1} \text{ (for a drift field of } 380(5) \text{ kV cm}^{-1}\text{)}. \quad (7.22)$$

In Figure 7.32 it can be seen that the distribution of the speed of the ion is wider than that of the atoms. It was found that this is due to a dependence of the drift speed on the drift time. In Figure 7.33, the displacement and drift speed is plotted versus the drift time. The ion drift speed changes to slower speeds for larger drift times. Because of the low statistics of the fully reconstructed data set, it is not possible to study further this effect with it. However, this effect was studied for pairs of the complete data set [4] — which contains many additional pairs (see Figure 7.34). The change in drift speed can be described by a mathematical model¹. In this model, the ${}^{218}\text{Po}$ ion is generated in a state with drift speed $v_1 = 1.48(1) \text{ mm s}^{-1}$. During the subsequent drift, the ion changes to the slower drift speed $v_2 = 0.83(1) \text{ mm s}^{-1}$. The transition time from v_1 to v_2 is described by an exponential decay

$$p_1(t) = e^{-\tau_v \cdot t} \quad (7.23)$$

¹Initially proposed by W. Fairbank, Colorado State University

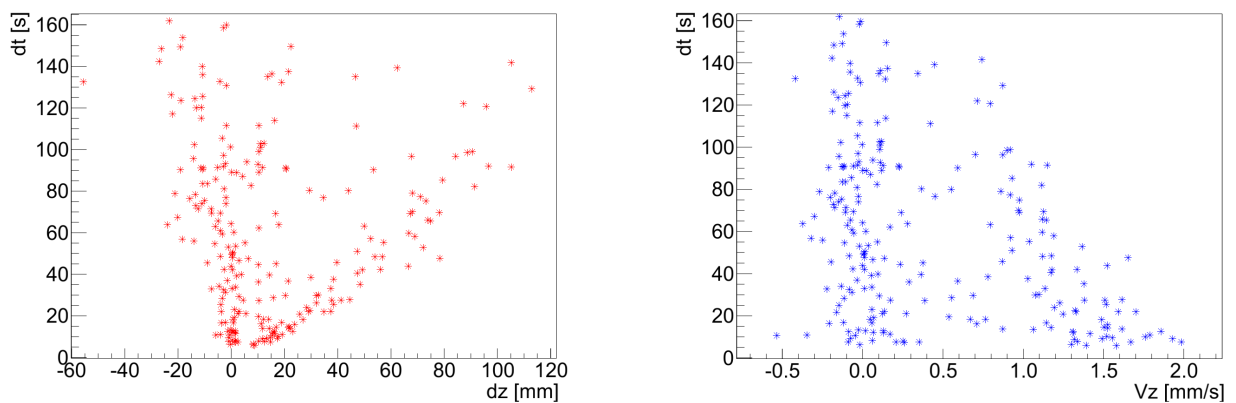


Figure 7.33: Dependence of the drift speed on the drift time. Left, the displacement of the polonium versus the drift time. Right, the polonium drift speed versus the drift time. It can be seen that the drift speed is reduced for longer drift times. However, the low statistics does not allow to study further details.

with a reaction time τ_v . It was found that the reaction time depends on the purity of the xenon (see Figure 7.35). To our knowledge, such a behaviour has never been reported. The physical mechanism leading to this behaviour is unclear. Possible explanations could be that ^{218}Po undergoes a chemical reaction leading to a larger effective mass or that ^{218}Po is generated in the Po^{++} state and changes to the Po^+ state. Furthermore, in Figure 7.34, the ions and atoms are clearly separated. This suggests that the ion life time is large compared to the drift time.

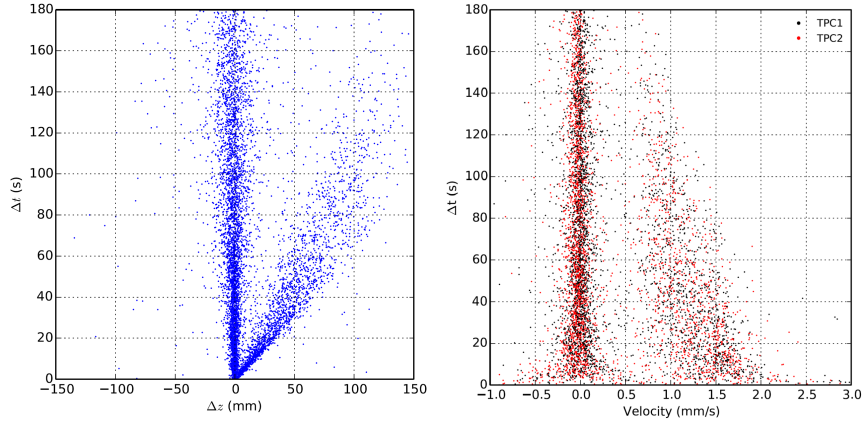


Figure 7.34: Dependence of the drift speed on the drift time, for the full data set. Left, displacement versus drift time. Right, drift speed versus drift time. Around 0.5 mm s^{-1} a gap can be seen. This gap suggests that the ion life time is large compared to the drift time. Figure from [4].

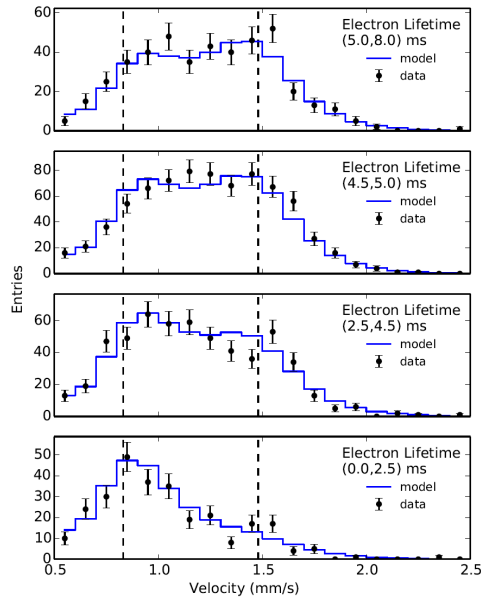


Figure 7.35: Dependence of the reaction time on the xenon purity. With a higher purity the reaction time is longer. Figure from [4].

7.6 Conclusion of the data analysis

In this analysis, the properties relevant to barium tagging were measured for polonium using the delayed coincident of the RnPo sequence. The ion fraction was measured to be 52(10) % (50.3(3.0) % for the analysis in [4]). Moreover, no indication for ion neutralisation during drift was observed. This suggests that the ion life-time is large compared to the drift time. The ion drift speed was measured to be $1.4(4) \text{ mm s}^{-1}$ (for a drift field of $380(5) \text{ kV cm}^{-1}$). However, a careful study of the drift speed revealed a behaviour of the ions never observed before [4]. It could be shown that the ions have two drift speeds — initially $v_1 = 1.48(1) \text{ mm s}^{-1}$, and then changing to $v_2 = 0.83(1) \text{ mm s}^{-1}$ with a transition time τ (for a drift field of $380(5) \text{ kV cm}^{-1}$). Moreover, it was found that τ depends on the purity of the xenon. For the analysis with all data (including partially reconstructed events) these findings were published [4].

Clearly, the results from the analysis with the fully reconstructed events have lower statistics and thus higher uncertainties. However, this method allows for the probability based linking (which e.g. prevents matching the same candidate twice) and the pre-selection in the charge light map, which further reduces systematic uncertainties. The full strength of this method could not be demonstrated with the EXO-200 data — for which the α activity is extremely low, and thus the probability of false matching is small. Nevertheless, this method will allow to study these properties in dependence on the drift field with EXO-100 – at much higher α activities. Moreover, with EXO-100 the fraction of fully reconstructed events is expected to be large because, unlike EXO-200, EXO-100 is designed to detect alpha decays. With this method Rn and Po decays delayed by several half-lives were linked. Moreover, this method allowed to link ^{218}Po with ^{214}Po decays (see Figure 7.36). The low statistics does not allow the make significant statements.

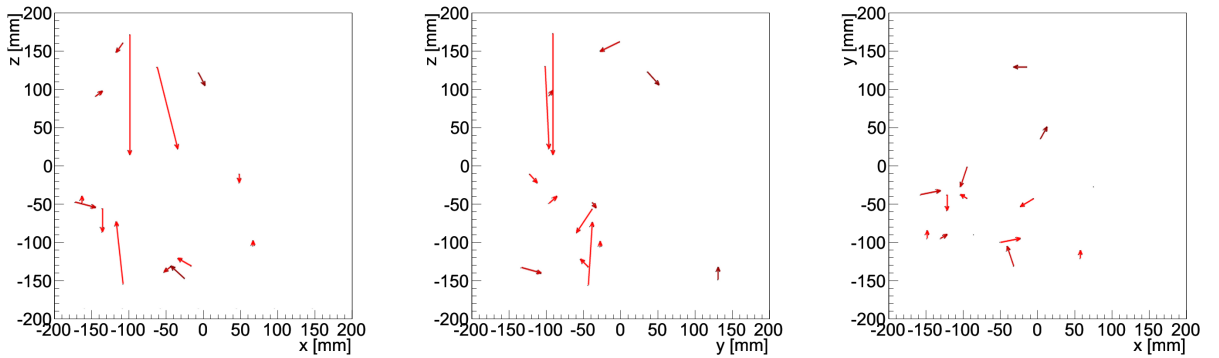


Figure 7.36: Arrows showing the displacement between the ^{218}Po and ^{214}Po decay, for pairs with $\Delta t < 2800\text{s}$, the combined half-life. The arrows start at the position where the ^{218}Po decayed. Their heads point to the ^{214}Po decay. The arrows are projected onto three planes. The color represents the time between the decays (dark for large Δt).

Conclusions and outlook

The framework of this dissertation enabled the construction and successful operation of the EXO-100 cryogenic facility. The cryostat was substantially modified from its original design. Furthermore, the set-up was complemented with a gas handling system, a slow control system, and a safety system. During this dissertation, EXO-100 was operated with liquid argon (87 K), liquid CF_4 (145 K), and liquid xenon (165 K), sometimes uninterrupted for periods of over a month. Along with EXO-100, a novel cryo-camera was developed, and two cryogenic level meter types were realised. As a whole, these developments, extensions, and modifications make the EXO-100 cryogenic facility the ideal tool for research towards barium ion tagging. Within the EXO-collaboration, EXO-100 is a unique R&D facility which allows studies in one cubic foot of liquid xenon. Its strength as an R&D facility for nEXO was demonstrated by the high voltage breakdown tests with the miniEXO mock-up.

The EXO-100 TPC was built and operated in the EXO-100 facility. The TPC was used to take data in liquid argon and liquid xenon. The liquid argon data, induced by cosmic rays and radioactivity, allowed the demonstration of the good behaviour of the TPC, muon veto, and DAQ system. Some very clear tracks from cosmic rays were observed in liquid argon. However, the data taken in liquid xenon was unsatisfactory and indicated that the xenon purity is hardly sufficient for electron drift. Increasing the xenon purity requires an upgrade of the EXO-100 gas handling system, with an evaporator and a condenser. This would significantly improve the efficiency of the xenon purification process. The EXO-100 TPC is specifically designed to allow the insertion of an ion grabbing probe. Moreover, advances were made towards a displacement device which would allow the ion grabbing probe to be moved to the location of a decay. In the near future, the displacement device will be motorised and implemented in the current facility. Polonium tagging can be studied using this device and a grabbing probe. This would be an important step towards barium ion tagging, showing the feasibility of grabbing single ions from a TPC.

Several properties of the ion are of importance to the ion grabbing process. These properties were measured for polonium with the EXO-200 data-set. The ion fraction was measured to be 52(10) %, and no indication was observed of ion neutralisation during drift. This is encouraging,

because it allows a reasonable ($< 52(10)$ %) efficiency to be achieved in the polonium tagging process. Furthermore, the ion drift speed was measured to be $1.4(4) \text{ mms}^{-1}$ (for a drift field of $380(5) \text{ kV cm}^{-1}$). This drift speed is sufficiently slow to give time for the grabbing probe to reach the location of the ion before the ion arrives at the cathode. It is expected that the drift speed of barium ions is similar to that of polonium ions. The ion fraction of beta decay is the main remaining worry for the efficiency of barium tagging. The mechanism leading to a given ion fraction is unknown. However, it is suspected that, due to the differences in the kinematics of alpha decay versus double-beta decay, the ion fraction could be larger for barium than for polonium — this is supported by the findings in [4]. Furthermore, the ion fraction could be influenced by the strength of the drift field. This hypothesis cannot be studied with EXO-200 because the drift field is fixed at 380 kV cm^{-1} during the search for $\beta\beta(0\nu)$, and the event rate is extremely low. However, in the EXO-100 detector the ^{238}U -series is not artificially suppressed, and thus the event rate of RnPo's is much larger. Therefore, EXO-100 could collect data in a short time with similar statistics as the EXO-200 data-set, collected over two years.

Once polonium tagging is realised with EXO-100, it is envisaged that the facility will be moved to Carlton University, Colorado State University or Stanford University where it will be combined with there set-up. A barium ion source will be installed in the EXO-100 TPC. The barium ion can be grabbed and identified with laser spectroscopy.

Indium seals

In the EXO-100 set-up more than 100 seals are used to seal a total length of about 10 m. Depending on the specific situation, various different types of seals are used. Where ever possible, commercial sealing systems, such as KF, ISO-K, NPT, CF and VCR, are used. Details on these sealing systems are given elsewhere [74]. However, in some situation those system are not suited and custom made seals are required. For cryogenic applications, indium seals have been used since decades [69]. They have all the advantages of metal seals (e.g. a low out-gassing rate and almost no permeation of gas through the seal). Furthermore, they can be made in almost any shape and size. The only draw back is that indium seals can only be backed to about 100 °C — the melting point of indium is 157 °C.¹

The basic functioning principle of an indium seal is that indium is placed between two flanges which are pressed together. In case an indium wire is used, in one of the flanges a groove is machined in which the indium wire is placed. While the two flanges are being pressed together, the soft indium

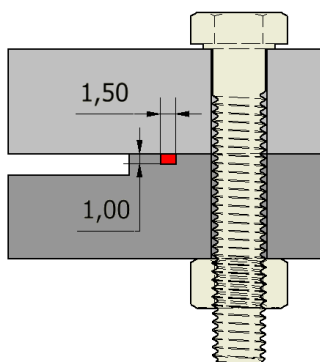


Figure A.1: Cross section view of the groove of an indium seal. Light gray: the upper flange, dark gray: the lower flange in which the groove is milled, red: the groove is 1.5 mm wide and 1.0 mm deep, beige: bolt and nut.

flows along these surfaces and forms a vacuum tight seal. In the EXO-100 cryostat all indium seals are made from indium wire with a diameter of 1.6 mm, however, it is also possible to use different indium wire or thin indium foil.

When designing an indium seal, several aspects have to be considered to guarantee the desired performance of the seal. Critical aspects are the shape and dimension of the groove in which the indium is placed, the number and position of the bolts pressing the flanges together and, the

¹Data from *National Institute of Standards and Technology NIST*, www.nist.gov

thickness and material of the two flanges. For practical reasons, the cross section of the groove used for the indium seal in the EXO-100 cryostat has a rectangular shape. The groove is 1.5 mm wide and 1.0 mm deep (see Figure A.1). Thus, the groove is slightly narrower than the diameter of the indium wire. Hence, once the indium wire is placed by hand in the groove, it will already be held in place. Therefore, even head first assembly of a seal can easily be done. Furthermore, a groove with these dimension has a slightly smaller cross section than the cross section of the indium wire. Consequently, this design guarantees that the indium flows along both sealing surfaces while the flanges are being pressed together. Moreover, the positioning of the bolts holding the two flanges together is of uttermost importance. To understand how to position these bolts, it is important to know how the force a bolt exerts on the flanges affects the whole assembly. A tightened bolt is under tension like a spring. Thus, the spring force acts on the surface where the bolt head or nut gets in contact with the flange. From this point, the force develops in a pressure cone into the material (see Figure A.2).

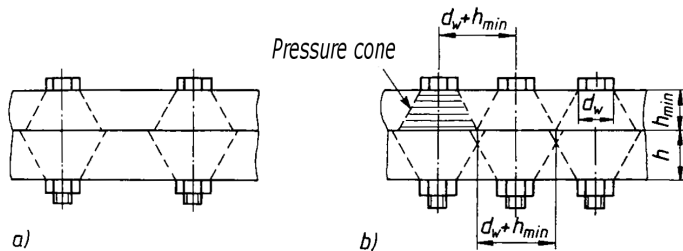


Figure A.2: Schematic view of a flange connection: a) The pressure cones are not overlapping at the junction between the two flanges. The spacing between bolts is too large. Between two bolts the pressure on a indium seal is not sufficient. Consequently, the seal may leak. b) The spacing between bolts is optimised. The pressure cones are overlapping, and thus, the precondition for a tight indium seal are met. Graphic modified from [75].

Furthermore, as a pressure cone develops from the bolt head and from the nut it is of advantage to use flanges of similar thickness. Else, shear forces may develop over the soft indium seal. Furthermore, due to these pressure cones, through going bolts with nuts should be used. If in one flange a threaded hole is machined the cone from this flange will start almost at the sealing surface, and thus, reduce the effective h_{min} . From these considerations it is also clear that the bolts should be placed as close as possible to the groove.

In case the seal is intended for cryogenic applications, additional considerations on the materials of the flanges and the bolt have to be made. It is favourable to make all parts from the same material. Otherwise, the flanges have different thermal expansion, and thus, during cool down additional forces may develop at the seal. Furthermore, if the flanges are made from a material with a larger thermal expansion than the bolt (e.g. copper flanges and steel bolts), during cool down the flanges shrink more than the bolt. Consequently, the bolt can partially relax, and thus, the tension on the seal is reduced. This effect can be compensated by using washers made from molybdenum. Molybdenum has a smaller thermal expansion coefficient than stainless steel.

Therefore, deeper in the flange the force the bolt exerts is distributed over a larger area. To get a good seal, the pressure cones of neighbouring bolts have to overlap at the depth of the sealing surface (see Figure A.3). Consequently, for thick flanges the distance between bolts can be larger than for thin flanges. Generally, the following relation can be used to determine the correct distance between bolts:

$$d = d_w + h_{min} \quad (\text{A.1})$$

where d is the distance between two neighbouring bolts, d_w the diameter of the bolt head and, h_{min} the thickness of the thinner flange. Fur-

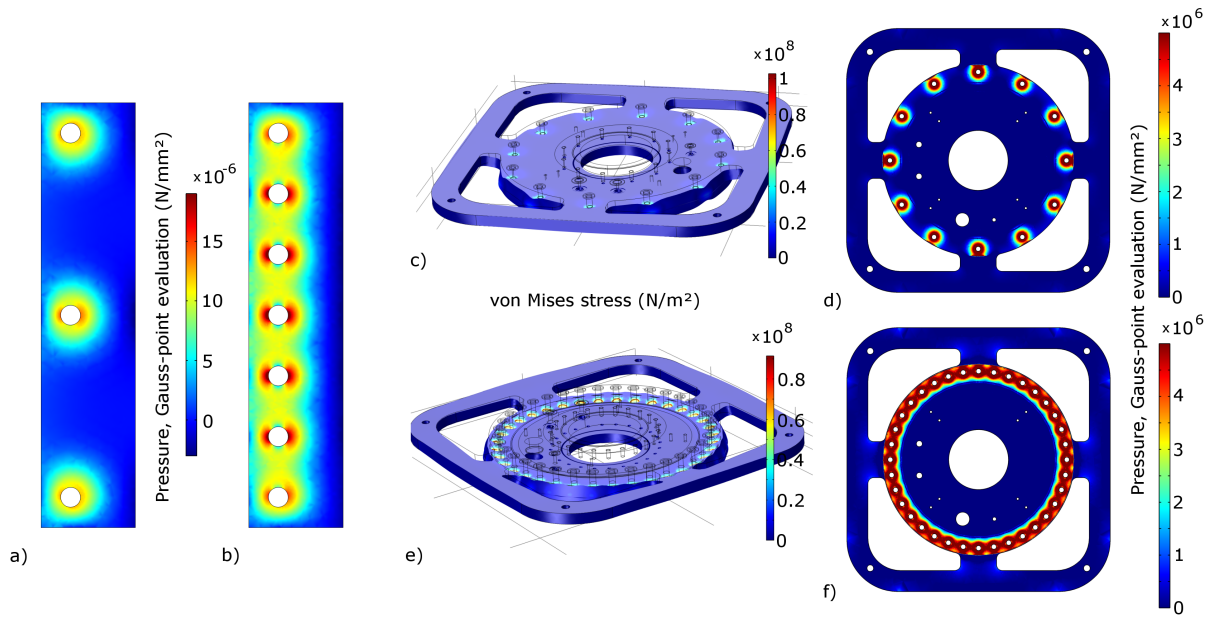


Figure A.3: Finite element simulation of mechanical stress and pressure on a sealing surface: a) The pressure cones are not overlapping. Between two bolts the pressure on the sealing surface is dramatically reduced. b) The same configuration as before but with more bolts. The pressure cones overlap. c) - f) Study of the main indium seal from the liquid nitrogen tank of the EXO-100 cryostat. This study reveals that it was necessary to increase the number of bolts — c) and d) — to make the seal tight — e) and f).

Therefore, molybdenum washers can be used to match the thermal expansion of the assembly with the thermal expansion of the bolt (see Figure A.4).

Even a well designed seal can fail if not enough care is taken during the assembly of the seal. Both sealing surfaces have to be cleaned with acetone to remove dirt and grease. Furthermore, the indium wire has to be cleaned. Depending on the supplier of the indium wire, the indium may have a thin oil layer to protect the bare indium. In this, case acetone can be used to remove the protection layer. If no such layer is present, at the surface of the indium a thin indium oxide layer is formed. Hydrochloric acid can be used to remove this layer, which can affect the performance of the seal. If all components are clean and the indium oxide layer is removed, the indium seal will cold weld the two parts together. However, a seal made in this way will be difficult to open. Therefore, a thin layer of vacuum grease can be put on both sealing surfaces. This will avoid the cold welding and the seal can be opened easily. However, it is not recommended to use vacuum grease for indium seals intended for cryogenic applications if the two flanges are not made out of the same material. Moreover, it is not recommended to reuse indium, even if new wire is formed from it. The indium may be contaminated with grease or indium oxide which both minder the quality of the indium. In Figure A.5 some of EXO-100's indium seals are shown and discussed.

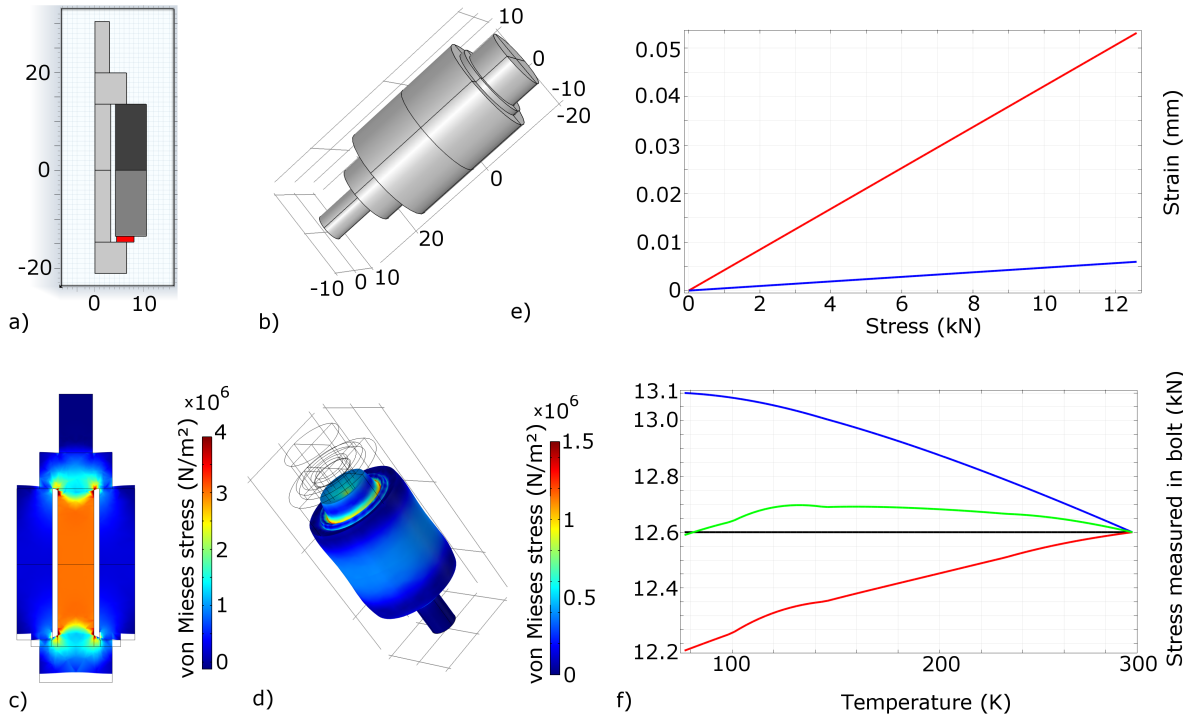


Figure A.4: Finite element simulation of mechanical stress and strain of a simple bolt assembly. a) Two dimensional geometry of the assembly (all dimensions in mm): light gray — bolt and nut, gray — lower flange, dark gray — upper flange and, red — washer. b) Revolved three dimensional geometry. c) and d) Exaggerated deformation of the assembly when a pre-load of 12.6 kN is applied. e) This graph shows the stress-strain curve of the bolt (in red) and the flanges (in blue). f) This graph shows the change of stress in the bolt when cooled down from 300 K to 77 K: Black — all parts made from stainless steel. The temperature has no effect as all parts have the same thermal expansion coefficient. Red — one flange made from copper. Copper shrinks more than steel, thus, the stress is reduced during cool down. Green — one flange made from copper and washer made from molybdenum. The molybdenum washer almost does not shrink and thus compensates for the copper flange. The stress in the bolt can be kept almost constant. Blue — the washer is made from molybdenum. The stress in the bolt increases during cool down. Therefore, molybdenum washers can be used to guarantee good cold seals.

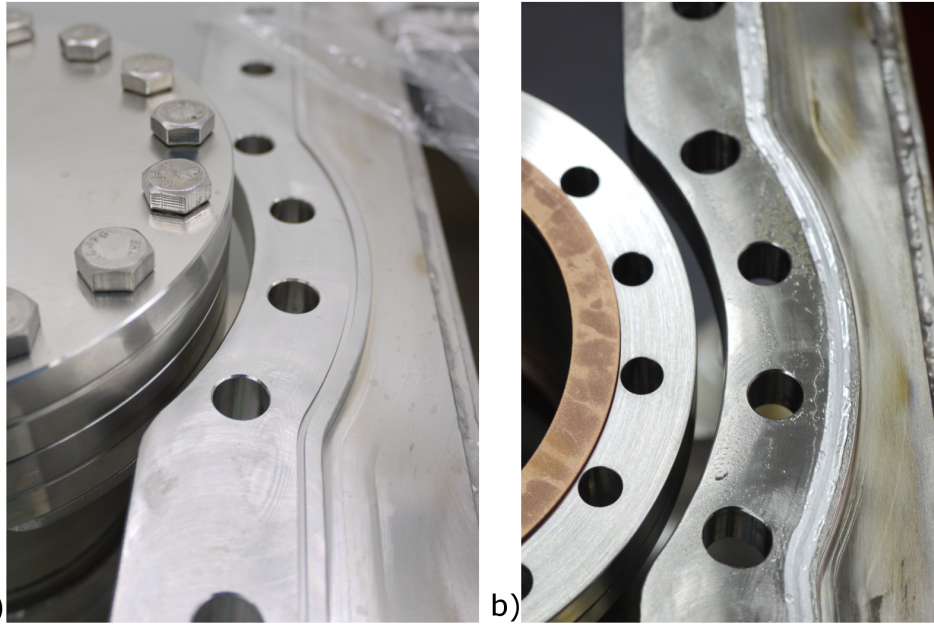


Figure A.5: An examples of an indium seals in EXO-100: a) Example of a well designed indium seal. The bolts are placed close to the indium groove. b) The indium wire is equally pressed along the full length. This example shows that indium seals can be mad in a variety of shapes.

B

Cryogenic level meters

In the EXO-100 set-up, various cryogenic liquids are used as detection medium or as cooling agent. To monitor the amount of detection medium in the chamber and to regulate the cooling power of the recovery dewar and of the liquid nitrogen tank, the levels of these liquids have to be measured. Level meters are widely used in experiments, hence, various commercial products are available. However, no model could be found satisfying exactly our demands. Moreover, applications in which liquid level meters are needed are manifold, and therefore, we decided to develop our own level meters. In the EXO-100 set-up two different types of level meters are in use — *capacitive level meters CLM* and *resistive level meters RLM*.

CLMs are built out of two metal tubes with different diameters (see Figure B.1). The tube with the smaller diameter is inserted into the other one and a gap of about 0.5 mm is left between the two tubes. Thus, these tubes form a coaxial capacitor. The capacity depends on the geometry of the level meter (e.g. length and diameters), and moreover, on the relative permittivity of the medium filling the gap. If the level meter is partially immersed in liquid with a given permittivity, the liquid will fill the gap up to the level to which the level meter is immersed. Accordingly, the capacitance of the level meter increases linearly with the liquid in the gap. Therefore, information on the liquid level can be derived from the capacitance of the level meter. To convert the capacitance into an analogue voltage (e.g. 0 V to 10 V), a read-out circuit is connected to the level meter. In the EXO-100 set-up the CLMs are read-out with commercial read-out modules and with a read-out circuit designed by us.

The second type of level meter is built out of an electrical resistor. This type of level meter uses the fact that some electrical resistors change the resistance depending on their temperature. A resistor with a positive [negative] temperature coefficient will increase [decrease] its resistance when warmed up, and decrease [increase] when cooled down. When such a resistor is immersed into a cryogenic liquid it will cool down and equalise its temperature with the liquid. Accordingly, its resistance will change to R_c . Once the liquid level drops and the resistor is no longer immersed in the cryogenic liquid, it has to warm up in order to change its resistance back to the previous value R_h . However, the temperature of the vapour just above the liquid is close to the temperature of the liquid itself. Consequently, the temperature of the resistor does not change by itself. In order to have a clear temperature change when the resistor is extracted from the cold liquid,

constantly 0.5 W of electric power is dissipated in the resistor. When the resistor is in the liquid phase, the heat generated in the resistor will be lead off due to the high thermal exchange with the liquid. Besides, the resistor acts as a heat source and may thus lead to local boiling of the cryogenic liquid. However, when the resistor is in the gas phase, the heat generated in the resistor will warm the resistor due to a lower thermal exchange with the gas phase. To avoid over heating, attention has to be taken not to operate this type of level meter in vacuum. Nevertheless, this operation scheme allows to clearly distinguish R_h from R_c .

The sensor of the RLM is simply an electrical resistor. To hold it in place a support for the resistor is made (see Figure B.2). Depending on the application, even *surface-mount device SMD* resistors may be considered. In any case, to measure the resistance of the RLM a read-out circuit is needed. The basic functioning principle of such a circuit is that a constant current passes the RLM and the voltage drop over it is measured. Assuming that the current is indeed constant, the voltage over the RLM is proportional to its resistance. During the development of the RLM, multiple attempts to design a reliable read-out circuit were made. In an early attempt, a current

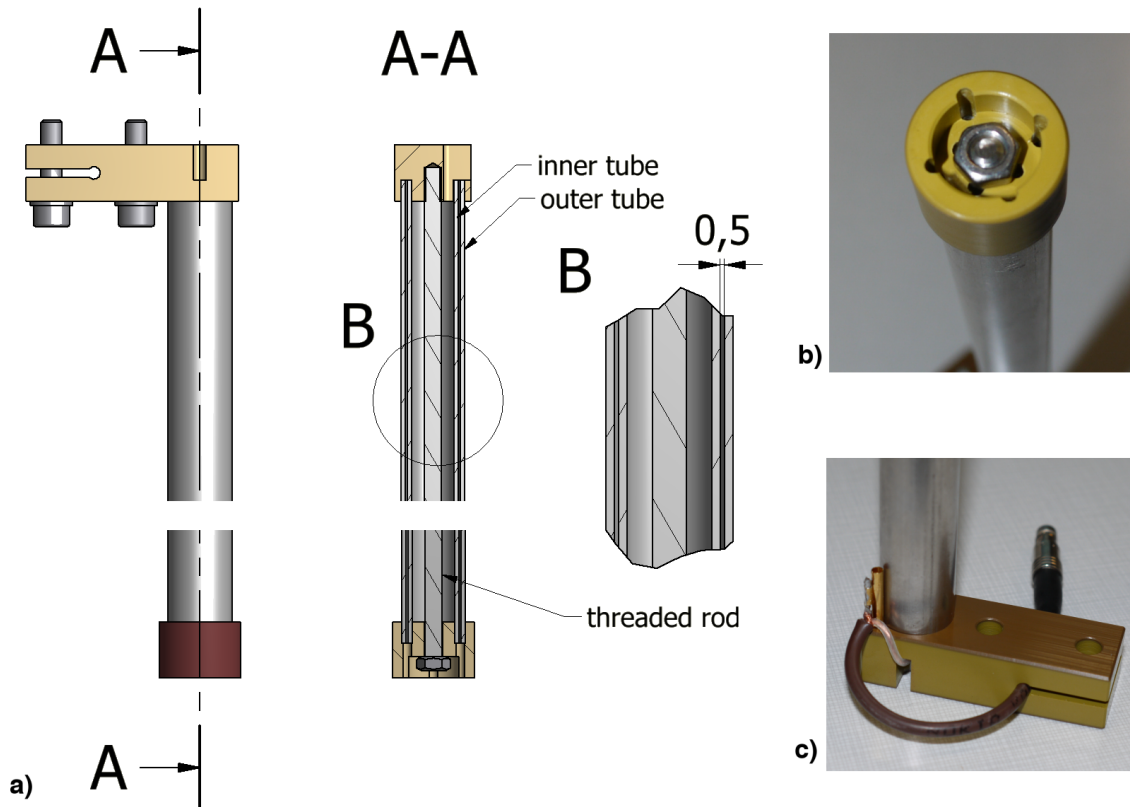


Figure B.1: The design of the capacitive level meter probe: a) Technical drawing of the level meter probe with a cross section view. The inner and outer tubes are positioned by two supports made from *Polyamide-imide PAI* (Torlon). The assembly is hold together by a threaded rod. The two supports guarantee that the gap between the tubes is regular. b) The lower support is fixed with a nut on the threaded rod. To allow the liquid to flow into the gap, several holes penetrate it. c) At the upper support, a coaxial cable is connected to the two tubes. Furthermore, the gap is ventilated on top, otherwise liquid could not flow into the gap.

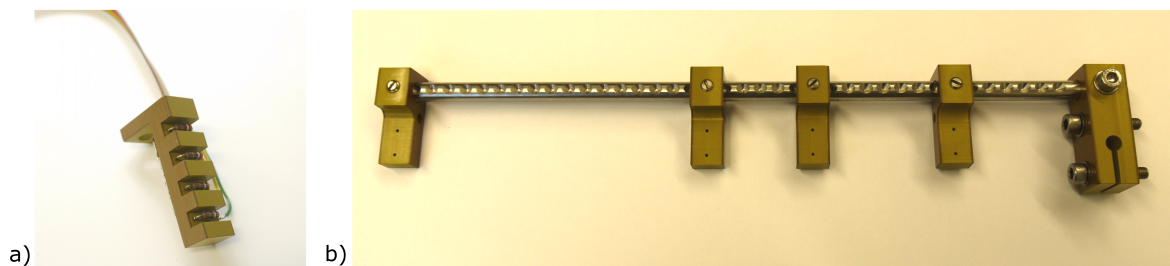


Figure B.2: Two designs of a RLM probe: a) This probe is installed in the chamber and is used as an end switch. The design prevents bubbles from a lower sensor to fake a gas phase in the upper sensor. b) This probe is installed in the liquid nitrogen tank of the EXO-100 cryostat. This design allows to change the height of the four sensors. Both probes are made from PAI and stainless steel.

regulating diode was used to generate the current in the sensor. However, a current regulating diode is not stable enough, and furthermore, the spread within a production series is large. This read-out circuit has a delicate behaviour, and thus, it is not suited. The breakthrough was the use of a regulated current source [76] (see Figure B.3). This circuit allows to precisely adjust the current through the sensor, and hence, the circuit can be used to calibrate the RLM. Subsequently, a voltage comparator is used to compare the voltage across the RLM with an adjustable voltage (threshold). The out put of the comparator is a logical signal indicating that a given level has been reached and passed.

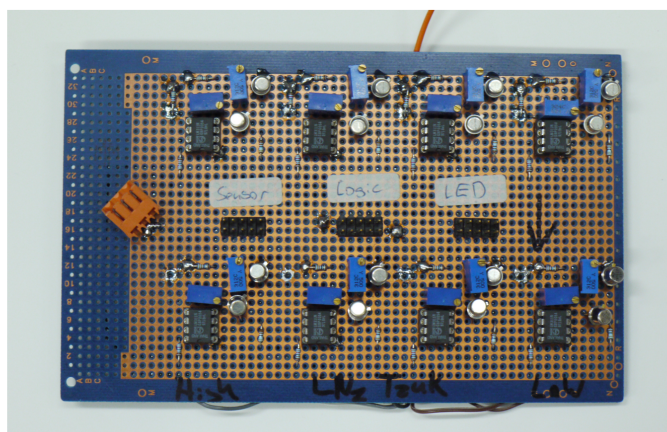
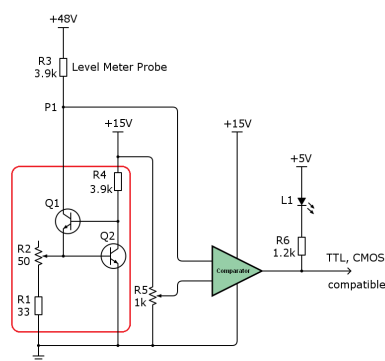


Figure B.3: The read-out circuit of the RLM. Left: circuit diagram of a single channel. The current source (in the red box) can be adjusted at R2. It powers the level meter probe (R3). The current through R3 is independent of its supply voltage (+48V). Thus, if R3 changes its resistance the potential at P1 will change accordingly. P1 is compared with a threshold voltage (set at R5) using a comparator (LM311N). The out-put of the comparator is used to drive a LED and as a logic out-put. Q1 and Q2 are both NPN bipolar junction transistors (2N2222A). Right: a photograph of the RLM read-out circuit board — with 8 channels — used in the EXO-100 set-up.

The CLM and RLM are two fundamentally different types of level meter. Each one has advantages and drawbacks. In Table B.1 the two types are compared. In the EXO-100 set-up, several of these self made level meters are in operation. They have been operated reliably in liquid nitrogen, liquid argon, liquid xenon and, liquid CF₄. Especially, the RLM of the liquid nitrogen tank — which is an essential component for the temperature regulation of the cryostat to work — has repeatedly been operated for periods of several months over the last two years.

Level meter type:	CLM	RLM
Measurement type:	Continuous measurement over the total length of the level meter.	Discrete reading at the sensor's position.
Probe powered by:	AC, induces noise on TPC, cannot be operated during DAQ.	DC, can be low pass filtered, can be operated during DAQ.
Power dissipation:	None.	0.5 W per sensor.
Required space:	Straight cylinder with an outer diameter of 2 cm.	Small, can be installed almost anywhere.
Dependence on medium:	Yes, relative permittivity (known from literature).	Yes, boiling temperature (need to calibrate the current source).
Operation in vacuum:	Yes.	No, risk of over heating.

Table B.1: Comparison of the two level meter types.

Development of a displacement device

In an early sequence of the barium-tagging process (see Section 3.3) the barium ion has to be extracted from the TPC. In this sequence, a displacement device is required to move the ion grabbing probe (see Subsection 3.3.1) to the location of a decay. In the framework of this thesis, advances in the development of such a displacement device were made.

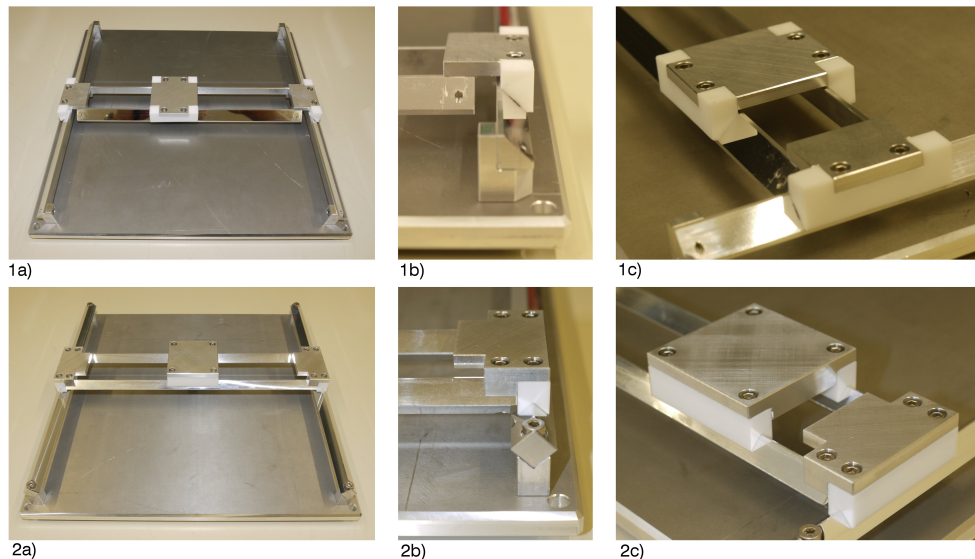


Figure C.1: Photographs of two displacement devices made with different rail designs — 1 & 2. a) The assembly with the two sets of rails and the platform. The assembly is mounted on a base-plate dummy. 1b) & 1c) With the first design the sliders are only positioned on one surface per rail. With this design, the second set of rails and the platform are not well positioned and thus wobble. 2b) & 2c) With the second design, the sliders are well positioned at each rail.

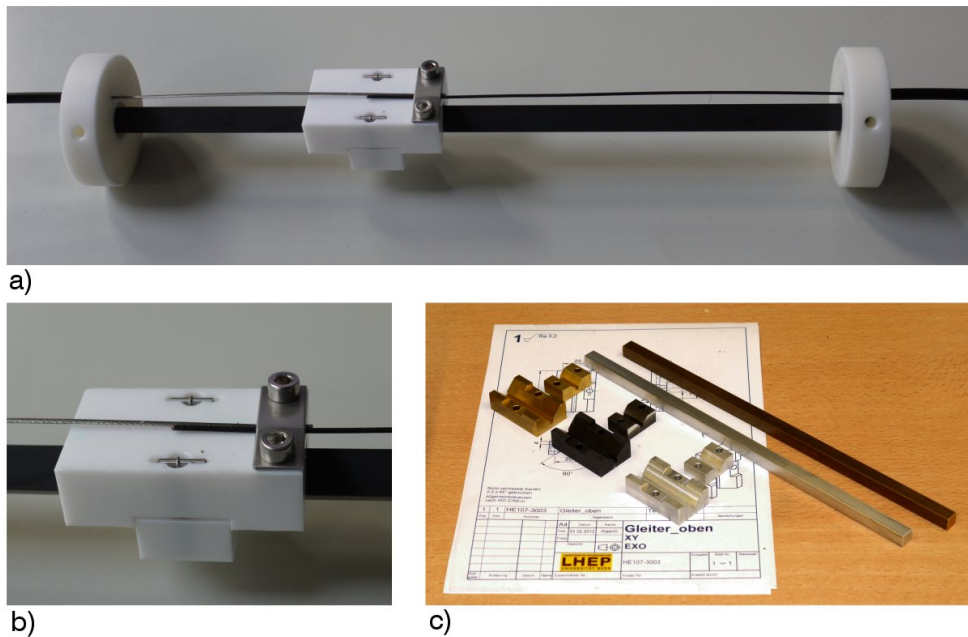


Figure C.2: Photographs of the mono-rail mock-up. a) It consists of a rail and a slider — which is split in an upper and a lower part. b) The two parts are held together by two springs, fitting the rail tightly. To move the slider along the rail, steel wires are fixed to the slider. c) The rail was made from brass, aluminium, and aluminium coated with Teflon. The slider was made from the same materials and additionally from bulk Teflon.

The range of the displacement device has to cover the fiducial volume of the TPC and some parts outside the liquid phase. To accomplish this the displacement device requires at least three degrees of freedom. These degrees of freedom define a coordinate system. Initially, three different coordinate systems were considered; spherical, cylindrical, and Cartesian. Due to the cuboid shape of EXO-100's inner chamber the Cartesian system is most appropriate — the choice may be different for nEXO.

The design of the displacement device — with a Cartesian coordinate system — is based on two sets of rails (e.g. see 1a and 2a in Figure C.1). The first set is fixed to the base plate (from which the TPC is suspended). These rails are oriented in the x direction. The second set of rails

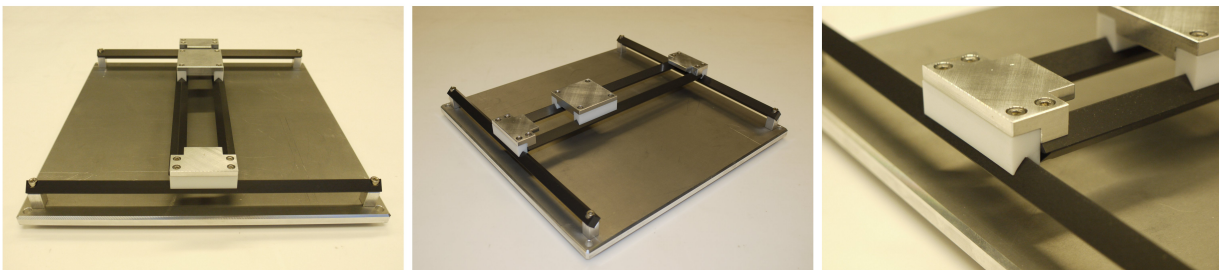


Figure C.3: Photographs of the current version of the displacement device. The rails are made from aluminium coated with Teflon.

is placed on top of the first set, but oriented perpendicular (y direction). On the second rails a small platform is placed. On this platform a mechanism could be installed which holds the grabbing probe and allows to lower the probe into the TPC (z direction).

The displacement device will be located inside the inner chamber. Therefore, it is in contact with xenon and exposed to low temperature. This environment sets particular demands on the design of the device. To allow for electron drift the xenon must be extremely clean. Consequentially, the displacement device should have a low out-gassing rate, be high-vacuum compatible, and not require lubricants. Moreover, the low temperature requires that the device is designed cryo-compatible. Therefore, the shrinking of materials and the availability of cryo-motors has to be considered (such motors exist but they are rather costly). Most plastics shrink significantly when cooled, hence metals are preferred. However, in high vacuum it is possible that metals cold weld on each other [77].

To test several material combinations a mono-rail mock-up was built (see Figure C.2). It was

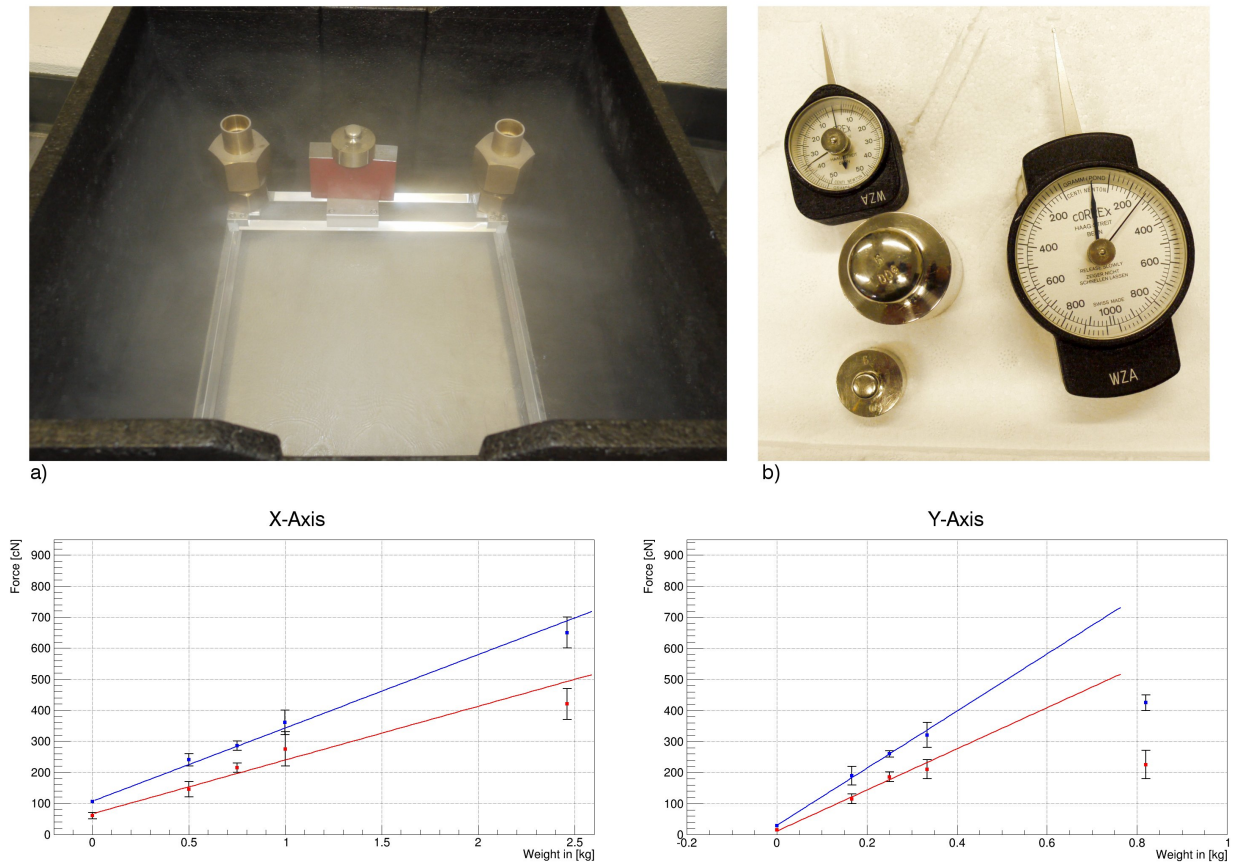


Figure C.4: The power required to drive the displacement device was measured for two temperatures. a) For both conditions, additional weights were put on the device. b) The force was measured using manual force meters. The results of these measurements are shown in the two graphs. Left, the required force versus the additional weight for the x -axis, and right, for the y -axis. The red points were measured at room temperature and the blue at 77 K. (For the linear fit in the y -axis the points at 820 g were ignored.)

found that combinations of metal on Teflon by far yield the smallest friction. However, Teflon undergoes extreme thermal expansion and shrinking. To avoid malfunction, as well as lack of precision, the rails are square. With this rail concept, the shrinking only affects the z direction — where lower precision is required. Two such rail designs were realised and tested (see Figure C.1). In the first design, the Teflon sliders were only positioned on one surface per rail. With this design the movements were wobbly and thus it was abandoned. However, in the second design the sliders were well guided and thus allows for a steady movement. For the second design, the force required to move along the x and y direction was measured (See Figure C.4). It was found that this force gets about 35% higher when the device is cold (77 K). After these measurements, the rails were Teflon coated (see Figure C.3). It is planned to repeat the friction measurements with this version.

Independently of the rail design, two approaches to drive the device are considered. Firstly, to use four cryogenic stepper motors to drive the device directly. Two motors would be used to drive along the x direction — one on each side of the y -rails. For the y and z directions, one motor per direction would be used. Secondly, to use steel wires and linear feedthroughs to guide an externally generated movement to the displacement device (via the interface box, shown in Figure 4.7). With this approach the movement is generated outside the cryostat and the displacement device is moved indirectly. Both approaches have their advantages and disadvantages. With the direct approach, the movement is generated close to the displacement device. This allows for a better accuracy. However, the motors dissipate heat into the inner chamber. Moreover, costly motors and vacuum cables have to be used. With the indirect approach the motors are located outside the cryostat. Thus, they need neither be high-vacuum nor cryo-compatible. This allows for cheap and strong motors — the dissipated heat is of minor importance. However, a clear disadvantage is the complex mechanism required to guide the movement to the displacement device. Moreover, two linear feedthroughs are part of this mechanism. When in motion, these feedthroughs are prone to small leaks. Considering these aspects, the direct approach is currently favoured.

Clearly, more advances have to be made before the displacement device can be used for tagging. Nevertheless, the current version has the potential to be motorised and used for first movement tests. Thus, it is suited to serve as a basis for future developments.

D

TPB coating technique

To convert the scintillation light from the UV in to the visible range some parts of the light-collecting system of the EXO-100 detector (see Subsection 5.1.3) are coated with *tetraphenyl butadiene TPB* — a wave length sifter. Before coating these parts, different coatings were applied on samples of different materials with various coating techniques. To test the coatings, these samples were exposed to high vacuum and cryogenic temperatures.

Three different coatings were used in these tests (see Table D.1). Firstly, a solution of TPB and toluene — referred to as the pure solution — was mixed. A magnetic stirrer was used to mix the solution at 50 °C for several minutes. Secondly, a solution of TPB, *acrylic glass PMMA*, and toluene was mixed. Beforehand, the PMMA was milled to produce swarf. The PMMA, TPB, and toluene were mixed with the magnetic stirrer at 50 °C for half an hour. Thereafter, the PMMA swarf was dissolved and the solution was optically clear. Lastly, a solution of TPB, *polystyrene PS*, and toluene was mixed. The procedure to mix this solution is identical to that of the PMMA solution.

Independent of the coating and coating technique, the solutions have to be applied to the samples and left to dry for several hours. Thus, toluene evaporates and a coating of TPB, TPB in a PMMA matrix, or TPB in a PS matrix is formed on the sample. These three coatings were tested on three materials: glass, acrylic glass, and *Teflon PTFE*.

Name	TPB	Matrix	Toluene
Pure	1.0 g	—	133 ml
PMMA	1.0 g	2.0 g of PMMA	100 ml
PS	1.0 g	3.0 g of PS	100 ml

Table D.1: The three solution used for the TPB coatings.

To test the coatings on glass, microscope slides were used as samples. To apply the coating, the microscope slides were mounted on a turning table (see Figure D.1). A large drop of one of the

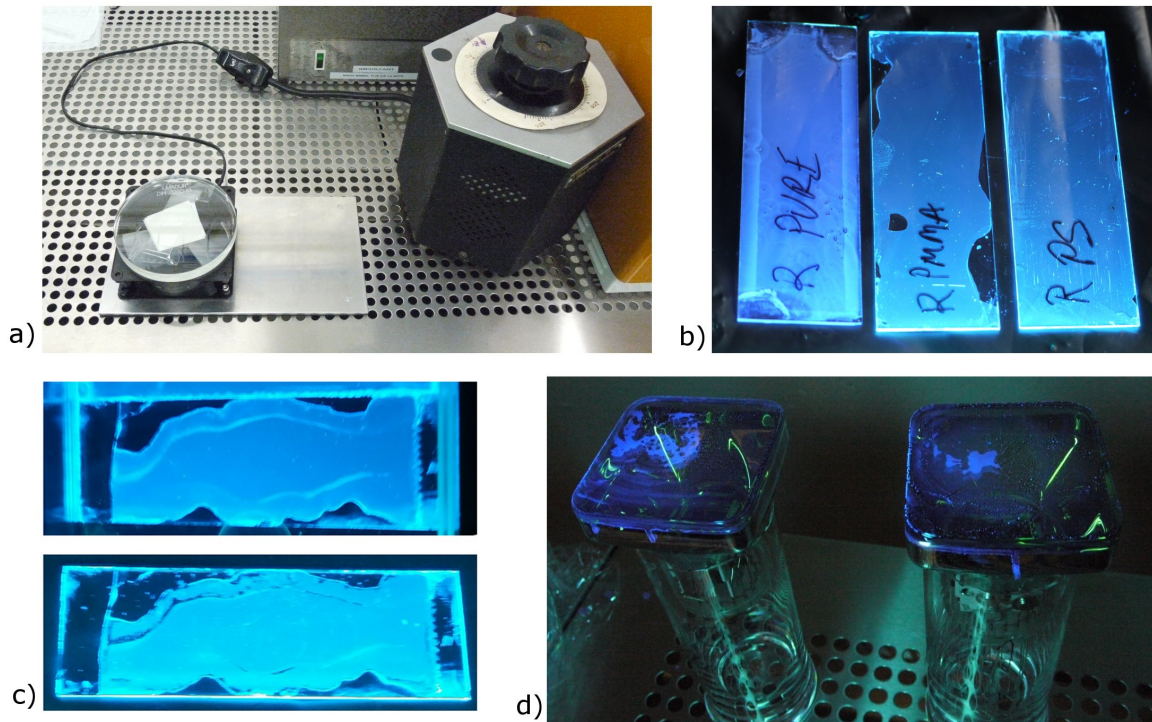


Figure D.1: Photographs of the TPB coating on glass. a) A microscope slide is mounted on the turning table. The rotation speed can be controlled at the autotransformer. b) The three coatings on glass samples. The samples are illuminated with a UV lamp. c) A sample with PMMA coating before (top) and after (down) a cryogenic test. At some spots, the PMMA coating got detached from the glass. d) A pure coating on the PMT's used in EXO-100. The coating is not homogeneous.

mentioned solutions was placed in the middle of the slide and the turning table was started. The rotation speed was set in such a way that the drop spread out over the full sample. After a few seconds, the table was slowly stopped and the samples were removed and left to dry. The result of this procedure were optically transparent coatings for the PMMA solution and the PS solution (see Figure D.1). However, the coating with the pure solution was slightly frosted. In a first test, the samples were placed in a vacuum chamber where they were exposed to a vacuum better than 1×10^{-7} mbar for about 18 h. During a subsequent inspection of the samples by eye under UV illumination, no degradation of any sample could be found. In a second test, the samples were immersed in liquid nitrogen. In this test the samples showed a clear degradation. The PMMA solution and PS solution produced debris, and thus, the coatings were partially destroyed (see Figure D.1). The coating made from the pure solution produced less debris, and thus, this coating was considered for photo cathode of the PMT's. However, the PMT's glass did not allow for a homogeneous coating (see Figure D.1). Other groups reported that it is possible to apply a TPB coating directly on a PMT using an evaporator [78]. However, we had no evaporator at hand, and thus, proceeded with another approach — using an acrylic glass in front of the PMT's. Nevertheless, these coatings have proven to be suited for applications in high vacuum where no cryogenic temperatures are required (e.g. in gas TPC's [79]).

To test the coatings on acrylic glass, 6 cm by 6 cm large pieces were cut out of a 0.5 mm thick acrylic glass plate. These samples were coated with each solution and the same tests as with the glass samples were performed. All three coatings showed no degradation. To coat the acrylic glass plate of the light-collecting system, the choice fell on the PS coating as it is optically the clearest (see Figure D.2).

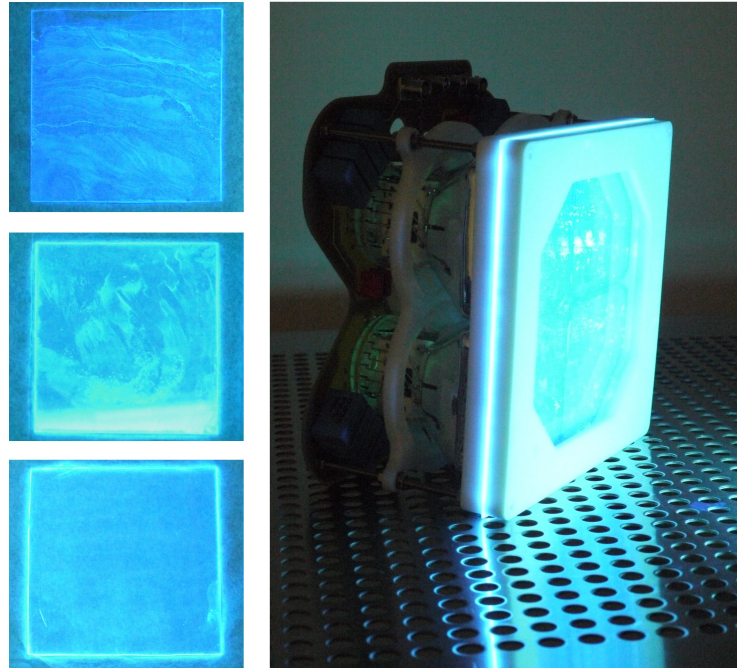


Figure D.2: Photographs of the TPB coating on acrylic glass. Left, the three coatings on acrylic glass sample. From top to down: pure, PMMA, and PS coatings. Right, the light-collecting system of the EXO-100 detector. A acrylic glass with the PMMA coating is placed in front of the PMT's.

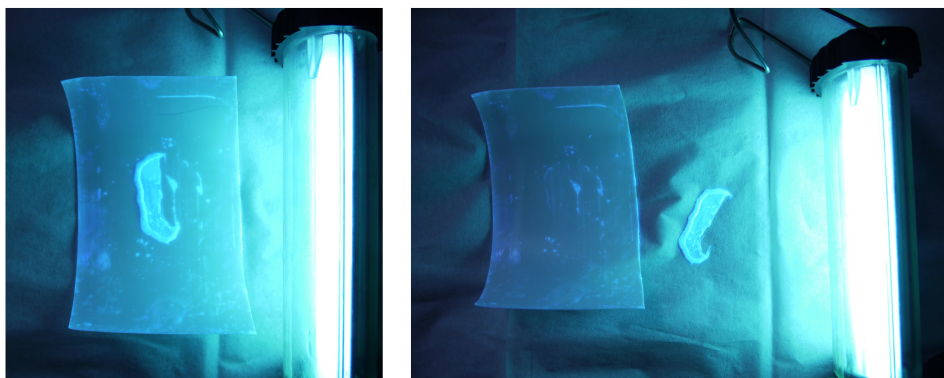


Figure D.3: Photographs of a PMMA TPB coating on Teflon before (left) and after (right) a cryogenic test. The solution formed a drip in the middle. During the cryogenic tests parts of the coating detached.

To test the coatings on Teflon, samples were cut out of a Teflon sheet. In a first approach, samples were immersed in all three solutions. However, none of the solutions is able to wet the Teflon sufficiently. Consequentially, the solutions formed drips prior to drying, and thus, the coatings were not regular. These samples had to undergo the same tests as the others. Exposing the samples to vacuum did not degenerate them. However, the cryogenic temperature made the PMMA and PS coatings detach from the Teflon sheet (see Figure D.3). However, the pure coating was rather resistant against low temperature and mechanical removal, and thus, in a second approach only the pure coating was further scrutinised.

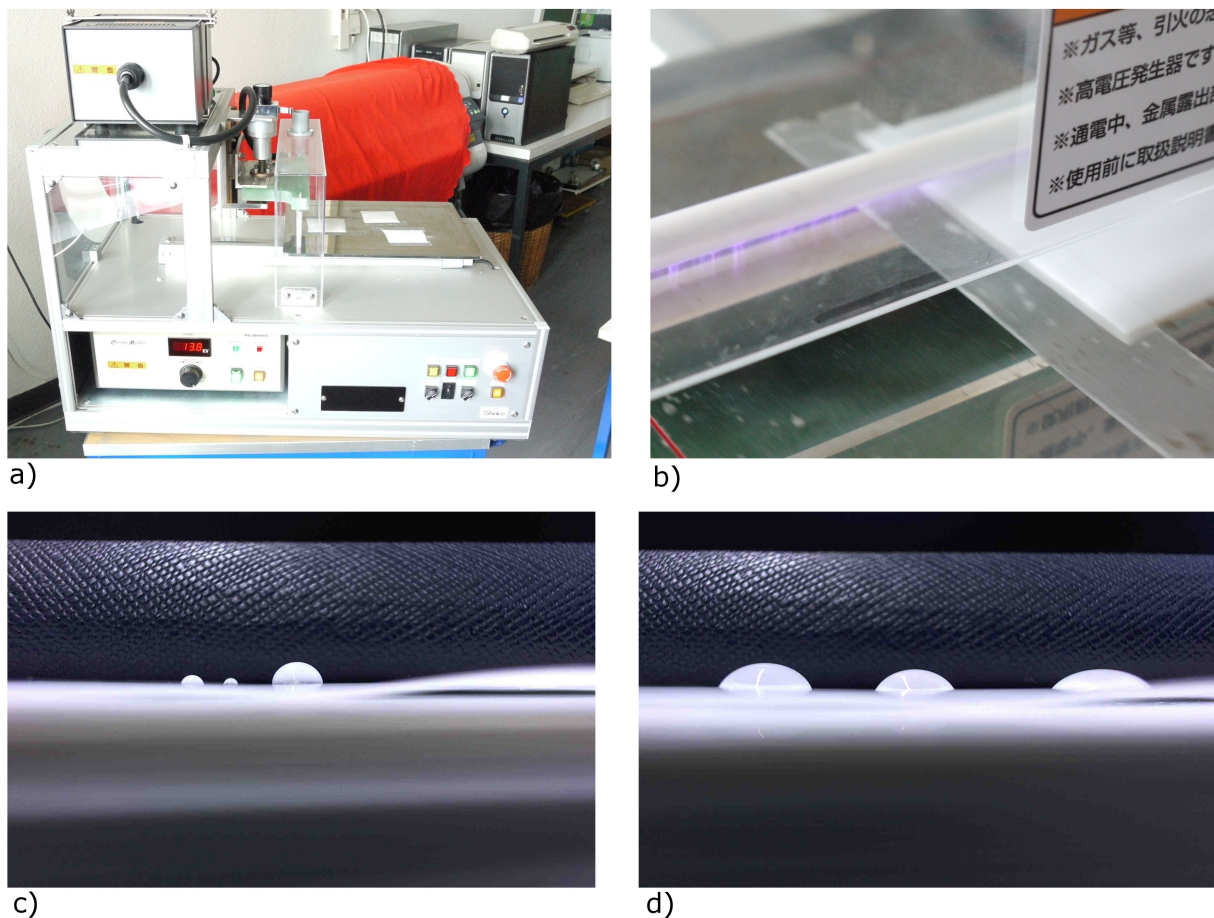


Figure D.4: Photographs of the UVO surface treatment. a) The device used for the UVO treatment. b) To produce UV light and ozone, this device used electrical discharges in air. c) Drops of water on a Teflon sheet without UVO treatment. The contact angle of the drops is larger than 90° . This is an indication for low wettability. d) Drops of water on a Teflon sheet which was UVO treatment. The contact angle of the drops is about 60° . This shows an improved wettability of the Teflon sample after the UVO treatment.

To increase the wetting, the Teflon sheets were treated by *ultra-violet ozone UVO* treatment prior to coating them. UVO treatment is a widely used cleaning and surface modifying technique — which is described in details elsewhere [80]. The UVO treatment device and the effects of UVO treatment on the Teflon sheets are shown in Figure D.4. To increase the surface wettability of

Teflon, 15 minutes of UVO treatment is sufficient. Thereafter, the pure solution forms a regular film when poured on the treated surface. After drying of the solution, a homogeneous coating remains (see Figure D.5). For the coating of the Teflon reflector in the EXO-100 light-collecting system, this technique was used.



Figure D.5: Photograph of a Teflon sample coated with the pure solution. During the UVO treatment, the Teflon sample was fixated at two edges with tape onto the UVO treatment device. Below the tape the sample was not UVO treated, and therefore, the solution could not wet the sample along these edges.

The performance of EXO-100's muon veto

To estimate the performance of the muon veto and the muon trigger, the accidental coincide rate of the PMT's of a panel can be calculated. Assuming random distributed pulses of the PMT's, the rate of n PMT's to be in accidental coincidence R_n is given as [81]:

$$R_n = n \cdot N_1 \cdot N_2 \cdots N_n t^{n-1} + \text{terms in } t^n \quad (\text{E.1})$$

where N_n is the rate of the n -th PMT and t the gate duration. For panels with three PMT's where a coincidence level of 2 is required, the accidental rate is given as:

$$R = R_{AB} + R_{AC} + R_{BC} - 2 \cdot R_{ABC}. \quad (\text{E.2})$$

For the muon veto and the muon trigger the accidental coincidence rates are shown in Table E.1 and Table E.2, respectively. For the muon veto, the accidental coincidence rate is small — at the level of one per thousand — with respect to the total rate. Hence, most events are due to real coincidences, and thus, due to a physical event in a panel. This suggests, that due to the low thresholds in the muon veto, mostly events from gamma interactions, as well as all events from cosmic rays, trigger a panel. For the muon trigger, the accidental coincident rates are minute — at a level of one per million — compared to the total rate. For the two panels with only two PMT's, these rates are a bit higher. The low panel rates when compared with the muon veto, suggest that only the most energetic events — e.g. cosmic rays — are triggering the panels.

PMT nr.	PMT pos.	PMT type	Panel nr.	Panel pos.	PMT rate	Panel rate	Accid. coinc. rate
0.0	Left	56DVP	0		3.7 k s^{-1}		
0.1	Middle	56DVP	0	Floor	3.3 k s^{-1}	2.3 k s^{-1}	7.06 s^{-1}
0.2	Right	56DVP	0		3.3 k s^{-1}		
1.0	Low	56DVP	1		7.3 k s^{-1}		
1.1	Middle	56DVP	1	Right	6.7 k s^{-1}	3.8 k s^{-1}	23.5 s^{-1}
1.2	High	56DVP	1		4.9 k s^{-1}		
2.0	Low	XP2020	2		1.8 k s^{-1}		
2.1	Middle	XP2020	2	Front	7.6 k s^{-1}	2.3 k s^{-1}	9.69 s^{-1}
2.2	High	XP2020	2		3.7 k s^{-1}		
3.0	Low	XP2020	3		2.2 k s^{-1}		
3.1	Middle	XP2020	3	Back	8.5 k s^{-1}	10 k s^{-1}	14.2 s^{-1}
3.2	High	XP2020	3		4.9 k s^{-1}		
4.0	Low	56DVP	4	Left (front)	7.8 k s^{-1}	1.2 k s^{-1}	56.2 s^{-1}
4.1	High	56DVP	4		36 k s^{-1}		
5.0	Low	56AVP	5	Left (back)	6.3 k s^{-1}	1.2 k s^{-1}	5.42 s^{-1}
5.1	High	XP2020	5		4.3 k s^{-1}		

Table E.1: Information on the PMT and scintillator panels used in the muon veto. The positions are given with respect to the render in Figure 5.14. The reported PMT rates are with respect to a -10 mV threshold — corresponding to -100 mV on a 10 times amplified signal (see text for details).

PMT	Panel	PMT	Panel	Accid.
nr.	nr.	rate	rate	coinc. rate
0.0	0	110 s^{-1}		
0.1	0	200 s^{-1}	7 s^{-1}	$1.58 \times 10^{-7} \text{ s}^{-1}$
0.2	0	240 s^{-1}		
1.0	1	670 s^{-1}		
1.1	1	3.2 k s^{-1}	38 s^{-1}	$1.16 \times 10^{-5} \text{ s}^{-1}$
1.2	1	180 s^{-1}		
2.0	2	220 s^{-1}		
2.1	2	1.1 k s^{-1}	9 s^{-1}	$2.69 \times 10^{-6} \text{ s}^{-1}$
2.2	2	370 s^{-1}		
3.0	3	90 s^{-1}		
3.1	3	1.2 k s^{-1}	10 s^{-1}	$1.07 \times 10^{-6} \text{ s}^{-1}$
3.2	3	330 s^{-1}		
4.0	4	450 s^{-1}		
4.1	4	300 s^{-1}	100 s^{-1}	$1.98 \times 10^{-2} \text{ s}^{-1}$
5.0	5	900 s^{-1}		
5.1	5	380 s^{-1}	120 s^{-1}	$6.84 \times 10^{-2} \text{ s}^{-1}$

Table E.2: The reported PMT rates are with respect to a -500 mV threshold — corresponding to -5 V on a 10 times amplified signal (see text for details).

EXO-100 event gallery

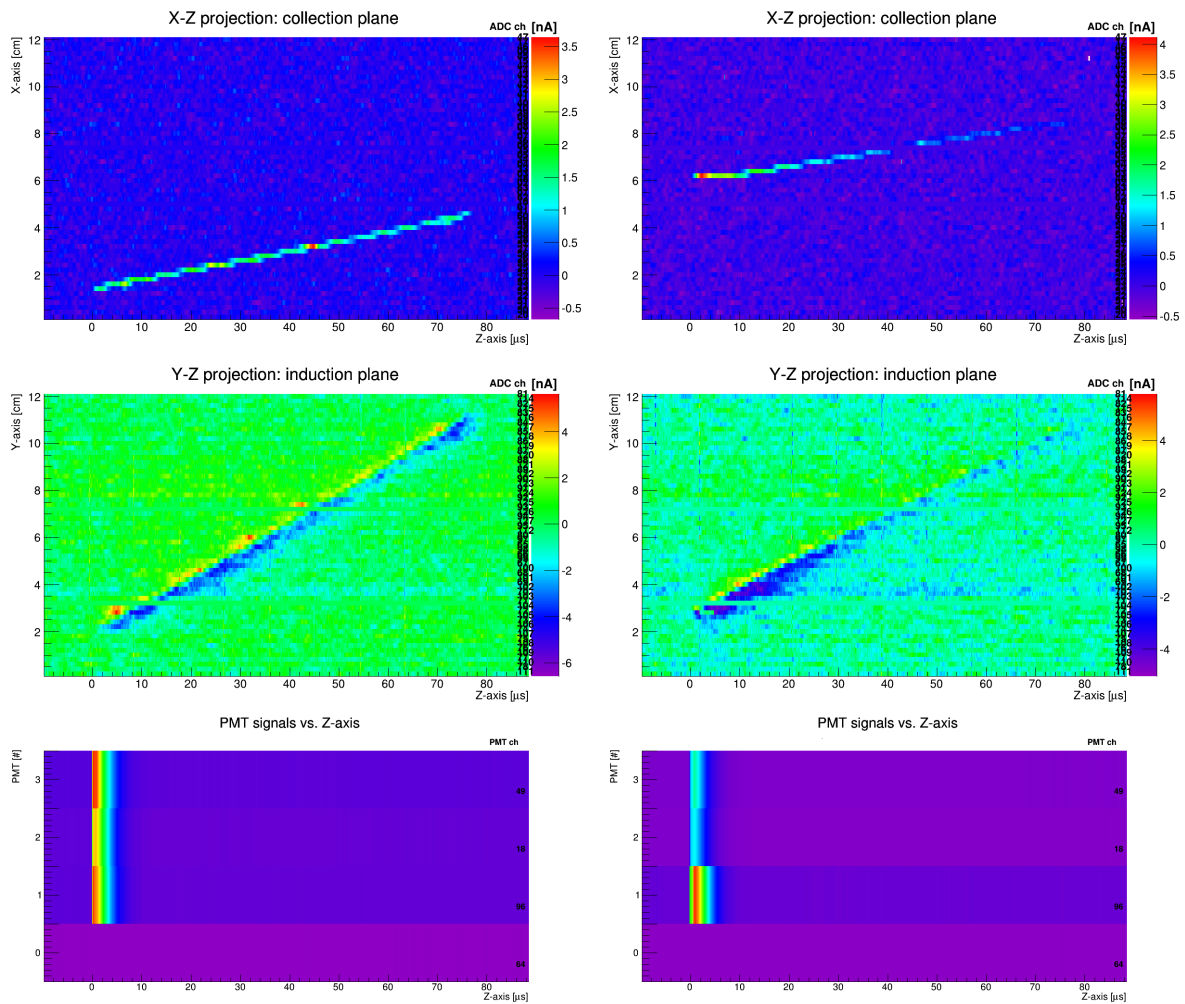


Figure F.1: Plots of events recorded with EXO-100. Left, a muon crossing the entire drift volume. The argon quality is good. Right, another muon crossing the entire drift volume. Due to the impurities in the liquid argon, the muon track is fading for longer drift times.

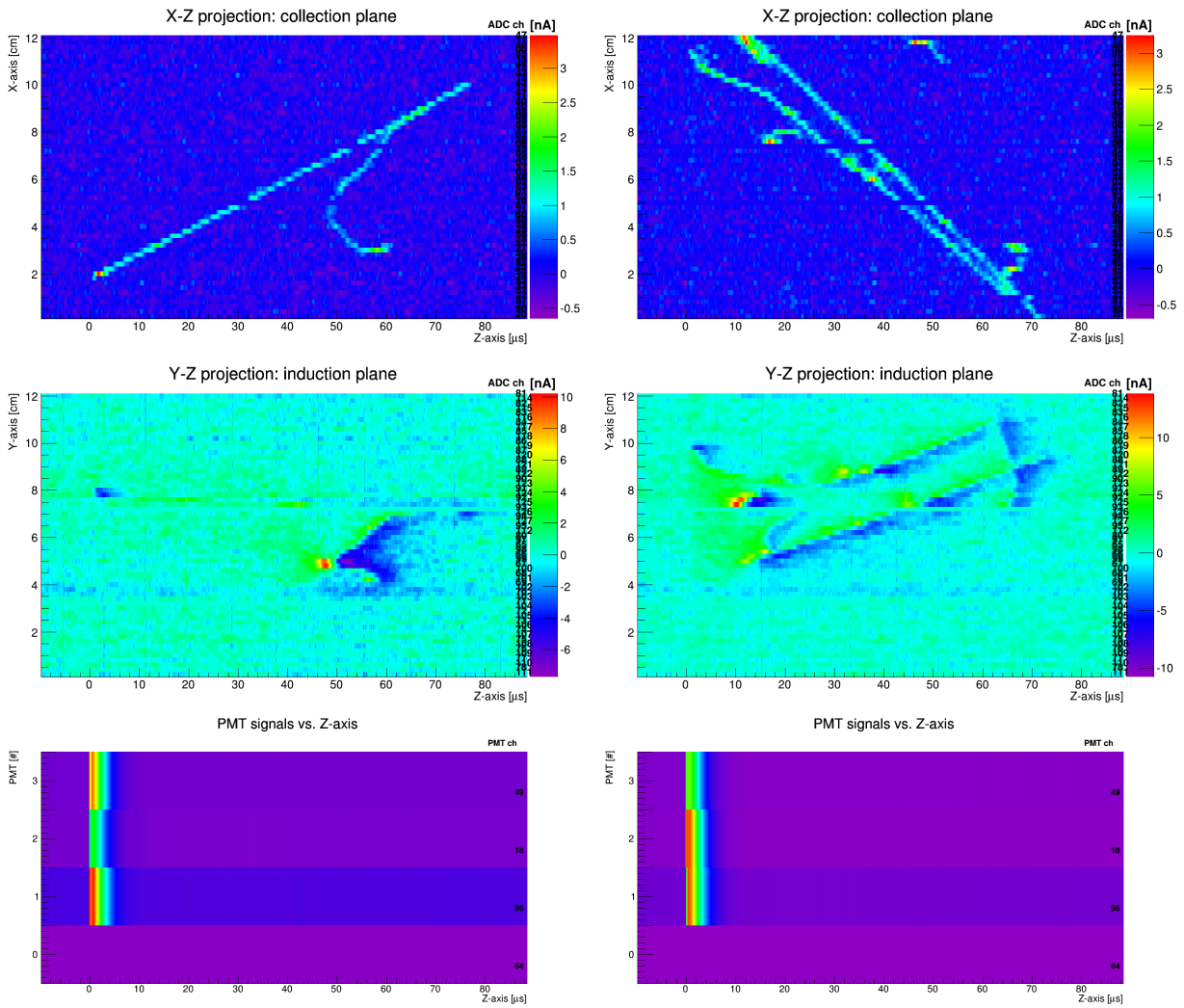


Figure F.2: Plots of events recorded with EXO-100. Left, a muon that produced a δ ray. Right, multiple tracks originating from muon interaction.

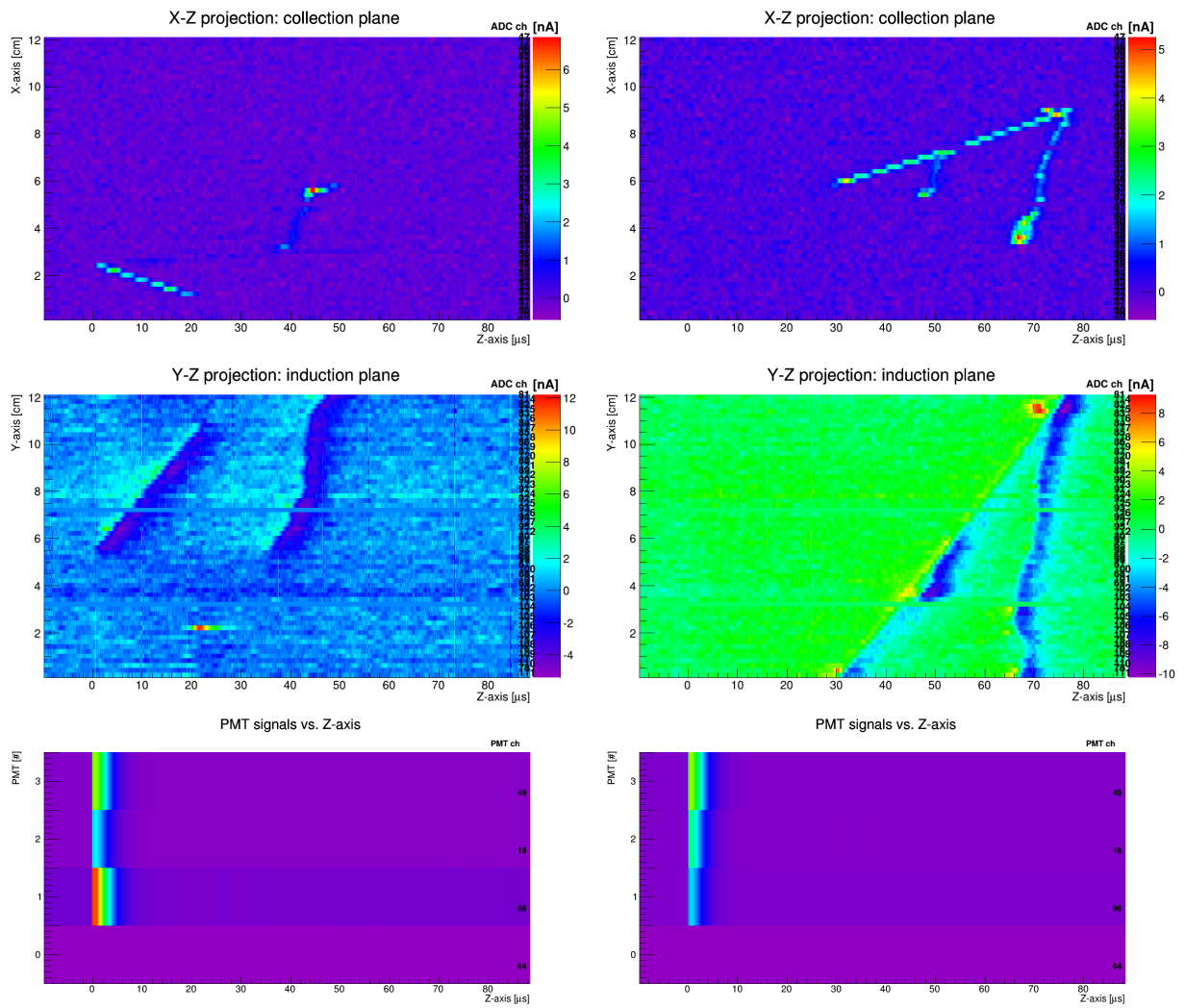


Figure F.3: Plots of events recorded with EXO-100. Left, a muon that passed parts of the detector and a secondary particle. Right, a muon hitting the cathode and extracting a proton from it. Thereafter, it produced a δ ray.

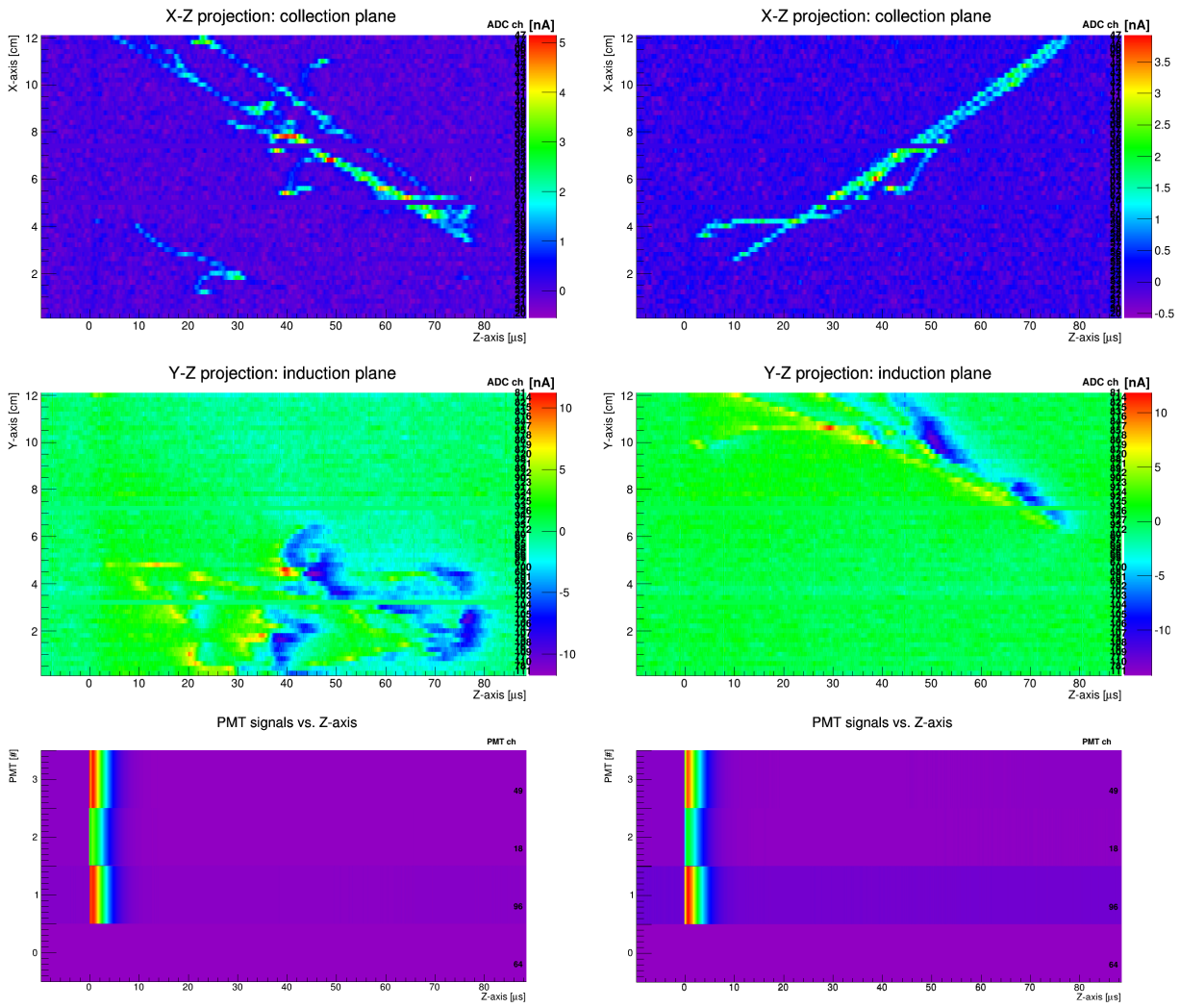


Figure F.4: Plots of events recorded with EXO-100. Two electro magnetic showers.

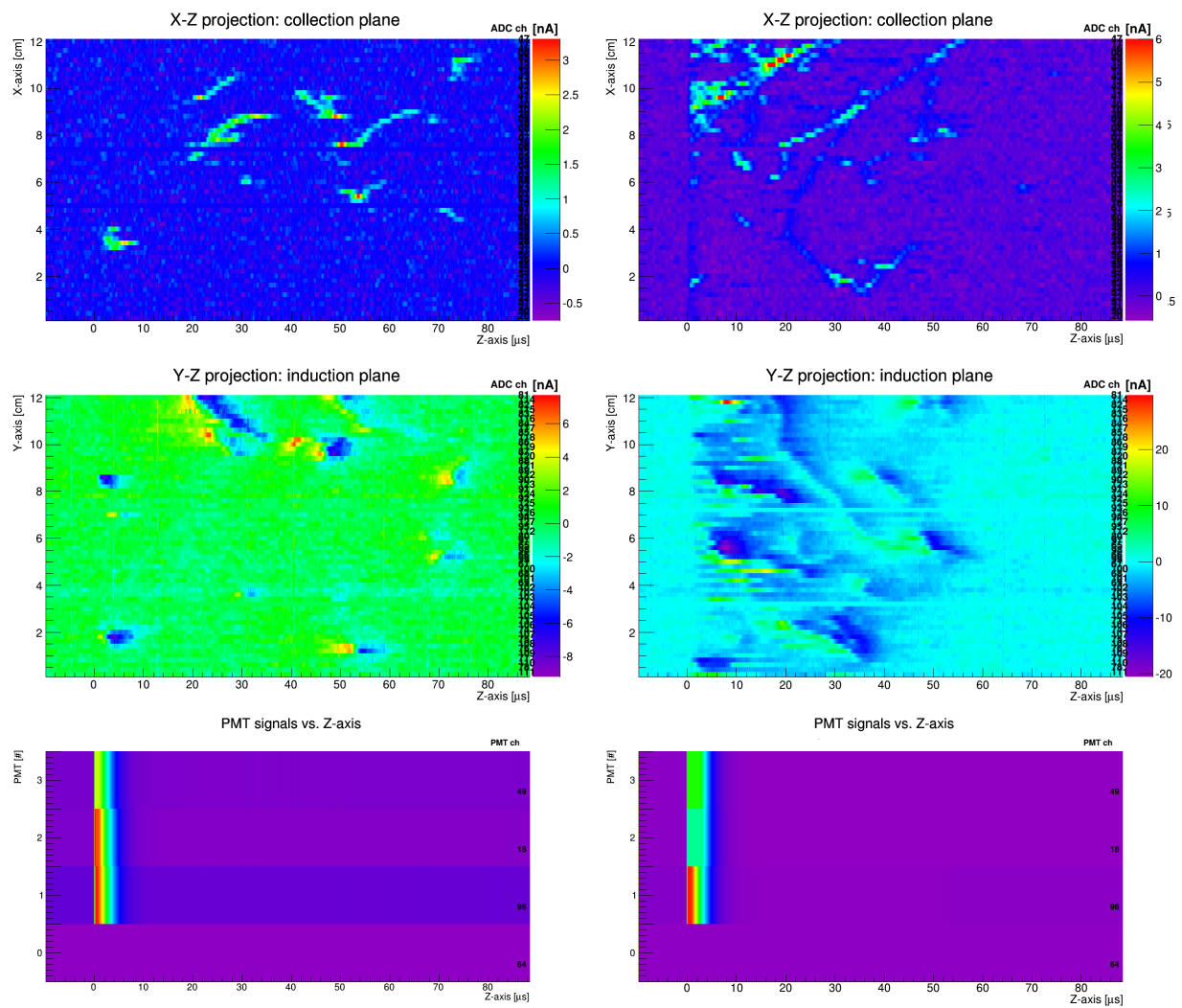


Figure F.5: Plots of events recorded with EXO-100. Two electro magnetic showers.

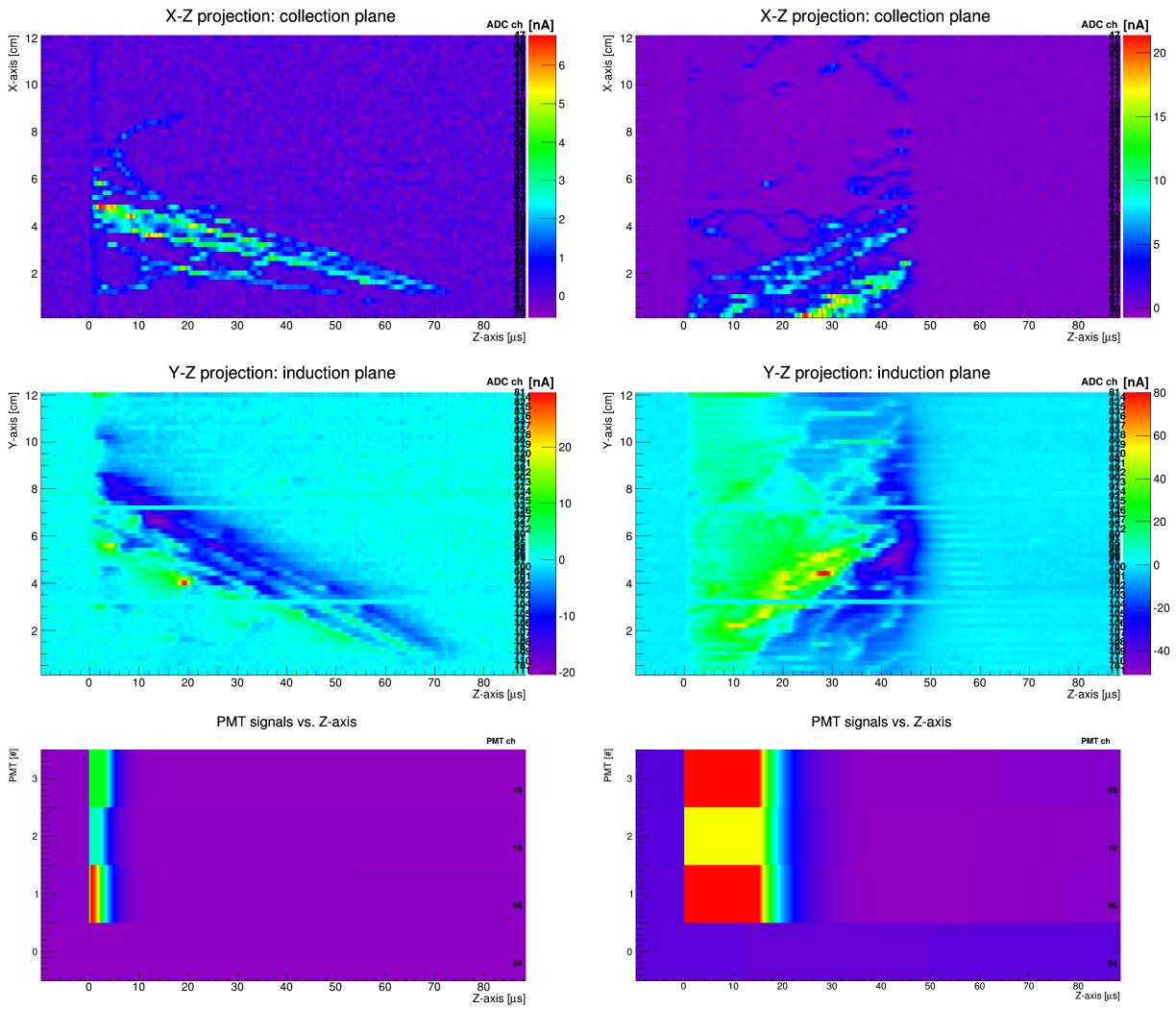


Figure F.6: Plots of events recorded with EXO-100. Two electro magnetic showers. The event on the right side was recorded at a field strength of 2 kV cm^{-1} . The length of the drift volume can be seen. All PMT's are saturated by this extreme event.

The multivariate normal distribution

In the data analysis presented in Chapter 7, the multivariate normal distribution plays a central role. To define the regions of the α 's in the charge light map, this distribution is used as a functional model. Moreover, it is used in the pairing algorithm to calculate the probability of a match. The multivariate normal distribution and its properties are described in details in [82]. The general form of it is

$$f(\mathbf{x}; \boldsymbol{\mu}, \boldsymbol{\Sigma}) = \frac{1}{\sqrt{(2\pi)^n \det(\boldsymbol{\Sigma})}} \exp\left(-\frac{1}{2}(\mathbf{x} - \boldsymbol{\mu})^T \boldsymbol{\Sigma}^{-1}(\mathbf{x} - \boldsymbol{\mu})\right) \quad (\text{G.1})$$

where n is the dimension of the distribution,

$$\boldsymbol{\mu} = \begin{pmatrix} \mu_1 \\ \mu_2 \\ \vdots \\ \mu_n \end{pmatrix} \quad (\text{G.2})$$

is a vector with the mean values, and

$$\boldsymbol{\Sigma} = \begin{pmatrix} \sigma_{11} & \sigma_{12} & \cdots & \sigma_{1n} \\ \sigma_{21} & \sigma_{22} & \cdots & \sigma_{2n} \\ & & \cdots & \\ \sigma_{n1} & \sigma_{n2} & \cdots & \sigma_{nn} \end{pmatrix} \quad (\text{G.3})$$

is the covariance matrix. If the distributions in all dimensions are independent

$$\Sigma_{ij} = 0; i \neq j, \quad (\text{G.4})$$

the covariance matrix becomes diagonal. In this case, the multivariate normal distribution satisfies

$$f(\mathbf{x}; \boldsymbol{\mu}, \boldsymbol{\Sigma}) = f_1(x_1; \mu_1, \Sigma_{11})f_2(x_2; \mu_2, \Sigma_{22}) \cdots f_n(x_n; \mu_n, \Sigma_{nn}), \quad (\text{G.5})$$

and becomes the product of n normal distributions. Thus, the multivariate normal distribution can be written in a simplified form

$$f(\mathbf{x}; \boldsymbol{\mu}, \boldsymbol{\Sigma}) = \frac{1}{\sqrt{(2\pi)^n \prod_{i=1}^n \sigma_{ii}}} \exp\left(-\frac{1}{2} \sum_{i=1}^n \left(\frac{(x_i - \mu_i)^2}{\sigma_{ii}^2}\right)\right). \quad (\text{G.6})$$

Bibliography

- [1] Albert, J. B. et al. (the EXO Collaboration), *Improved measurement of the $2\nu\beta\beta$ half-life of ^{136}Xe with EXO-200*, *Phys. Rev. C* **89**, 015502 (2014); [arXiv:1306.6106](#).
- [2] Albert, J. B. et al. (the EXO Collaboration), *Search for Majorana neutrinos with the first two years of EXO-200 data*, *Nature (London)* **510**, 299–234 (2014); [arXiv:1402.6956](#).
- [3] Delaquis, S. C. et al., *Development of a camera casing suited for cryogenic and vacuum applications*, *J. Instrum.* **8**, T12001 (2013); [arXiv:1310.6601](#).
- [4] Albert, J. B. et al. (the EXO Collaboration), *Measurements of the ion fraction and mobility of alpha and beta decay products in liquid xenon using EXO-200*, [arXiv:1506.00317](#) (2015).
- [5] Aad, G. et al. (the ATLAS Collaboration), *Observation of a new particle in the search for the Standard Model Higgs boson with the ATLAS detector at the LHC*, *Phys. Lett. B* **716**, 1–29 (2012); [arXiv:1207.7214](#).
- [6] Adam, W. et al. (the CMS Collaboration), *Observation of a new boson at a mass of 125 GeV with the CMS experiment at the LHC*, *Phys. Lett. B* **716**, 30–61 (2014); [arXiv:1207.7235](#).
- [7] Furry, W. H., *On Transition Probabilities in Double Beta-Disintegration*, *Phys. Rev.* **56**, 1184–1193 (1939).
- [8] Perkins, D. H. *Introduction to High Energy Physics*, 4th ed., Cambridge University Press, Cambridge 2000.
- [9] Aefsky, S. et al., *Fundamental Physics at the Intensity Frontier*, [arXiv:1205.2671](#) (2012).
- [10] Kayser, B., Gibrat-Debu, F. & Perrier, F. *The Physics of Massive Neutrinos*, World Scientific, Singapore 1989.
- [11] Boehm, F. & Vogel, P. *Physics of Massive Neutrinos*, 2nd ed., Cambridge University Press, Cambridge 1992.
- [12] Mohapatra, R. N. & Pal, P. B. *Massive Neutrinos in Physics and Astrophysics*, 3rd ed., World Scientific, Singapore 2004.
- [13] Akhmedov, E. K., *Neutrino oscillations: theory and phenomenology*, [arXiv:0610064](#) (2006).

- [14] Giuliani, A. & Poves, A., *Neutrinoless Double-Beta Decay*, *Adv. High Energy Phys.* **2012**, 857016 (2012).
- [15] Elliott, S. R. & Vogel, P., *Double Beta Decay*, *Annu. Rev. Nucl. Part. Sci.* **52**, 115–151 (2002); arXiv:0202264.
- [16] Ellis, C. D. & Wooster, W. A., *Continuous Spectrum of β -Rays*, *Nature (London)* **119**, 563–564 (1927).
- [17] Reines, F. & Cowan C. L., *The Neutrino*, *Nature (London)* **178**, 446–449 (1956).
- [18] Purcell, A. *Go on a particle quest at the first CERN webfest*. CERN Bulletin, <https://cds.cern.ch/journal/CERNBulletin/2012/35/News%20Articles/1473657>, accessed 14th of May 2015.
- [19] Wu, C. S., Ambler, E., Hayward, R. W., Hoppes, D. D., & Hudson P. P., *Experimental Test of Parity Conservation in Beta Decay*, *Phys. Rev.* **105**, 1413 (1957).
- [20] Lee, T. D., & Yang, C. N., *Question of Parity Conservation in Weak Interactions*, *Phys. Rev.* **104**, 254 (1956).
- [21] McKeowan, R. D. & Vogel, P., *Neutrino masses and oscillations: triumphs and challenges*, *Phys. Rep.* **394**, 315–356 (2004); arXiv:0402025.
- [22] Davis, R., Jr., Harmer, D. S. & Hoffman, K. C., *Search for Neutrinos from the Sun*, *Phys. Rev. Lett.* **20**, 1205–1209 (1968).
- [23] Hampel, W. et al. (the GALLEX Collaboration), *Final results of the ^{51}Cr neutrino source experiments in GALLEX*, *Phys. Lett. B* **420**, 114–126 (1998).
- [24] Abdurashitov, J. N. et al. (the SAGE Collaboration), *Measurement of the solar neutrino capture rate with gallium metal. III. Results for the 2002 – 2007 data-taking period*, *Phys. Rev. C* **80**, 015807 (2009); arXiv:0901.2200.
- [25] Fukuda, Y. et al. (Super-Kamiokande Collaboration), *Evidence for Oscillation of Atmospheric Neutrinos*, *Phys. Rev. Lett.* **81**, 1562 (1998).
- [26] Fukuda, Y. et al. (Super-Kamiokande Collaboration), *Constraints on Neutrino Oscillation Parameters from the Measurement of Day-Night Solar Neutrino Fluxes at Super-Kamiokande*, *Phys. Rev. Lett.* **82**, 1810 (1999).
- [27] Ahmed, Q. R. et al. (the SNO Collaboration), *Measurement of the Rate of $\nu_e + d \rightarrow p + p + e^-$ Interactions Produced by ^8B Solar Neutrinos at the Sudbury Neutrino Observatory*, *Phys. Rev. Lett.* **87**, 071301 (2001); arXiv:0106015.
- [28] Forero, D. V., Tortola, M. & Valle, J. W. F., *Global status of neutrino oscillation parameters after Neutrino-2012*, *Phys. Rev. D* **86**, 073012 (2012); arXiv:1205.4018.
- [29] Plaszczynski, S., *Neutrino matter with PLANCK*, arXiv:1012.2215 (2010).

- [30] Palanque-Delabrouille, N. et al., *Constraint on neutrino masses from SDSS-II/BOSS Ly α forest and other cosmological probes*, *J. Cosmol. Astropart. Phys.* **2015**, JCAP02(2015)045 (2012); [arXiv:1410.7244](#).
- [31] Ade, P. A. R. et al. (the PLANCK Collaboration), *Planck 2013 results. XVI. Cosmological parameters*, *Astron. Astrophys.* **571**, A16 (2014); [arXiv:1303.5076](#).
- [32] Drexlin, G. et al., *Current Direct Neutrino Mass Experiments*, *Adv. High Energy Phys.* **2013**, 293986 (2012); [arXiv:1307.0101](#).
- [33] Abbott, L. F., De Rújula, A. & Walker, T. P., *Constraints on the electron-neutrino mass from the supernova data A systematic analysis*, *Nucl. Phys. B* **299**, 734–756 (1988).
- [34] Osipowicz, A. et al. (the KATRIN Collaboration), *KATRIN: A next generation tritium beta decay experiment with sub-eV sensitivity for the electron neutrino mass*, [arXiv:0109033](#) (2001).
- [35] Aseev, V. N. et al., *Measurement of the electron antineutrino mass in tritium beta decay in the Troitsk nu-mass experiment*, *Phys. Atom. Nucl.* **75**, 464–478 (2012).
- [36] Weinheimer, Ch. et al., *High precision measurement of the tritium β spectrum near its endpoint and upper limit on the neutrino mass*, *Phys. Lett. B* **460**, 219–226 (1999).
- [37] Barabash, A. S., *Review of double beta decay experiments*, [arXiv:1403.2870](#) (2014).
- [38] Goeppert-Mayer, M., *Double Beta-Disintegration*, *Phys. Rev.* **48**, 512 (1935).
- [39] Weber, M. D., *Background Studies and Search for Neutrinoless Double Beta Decay in ^{136}Xe with the EXO-200 detector*, dissertation (2012).
- [40] Klapdor-Kleingrothaus H. V. & Krivosheina, I. V., *THE EVIDENCE FOR THE OBSERVATION OF $0\nu\beta\beta$ DECAY: THE IDENTIFICATION OF $0\nu\beta\beta$ EVENTS FROM THE FULL SPECTRA*, *Mod. Phys. Lett. A* **21**, 1547–1566 (2006).
- [41] Leo, W. R. *Techniques for Nuclear and Particle Physics Experiments*, 2nd ed., Springer-Verlag, Berlin 1987.
- [42] Leonard, D. S. et al. (the EXO Collaboration), *Systematic study of trace radioactive impurities in candidate construction materials for EXO-200*, *Nucl. Instrum. Meth. A* **591**, 490–509 (2008); [arXiv:0709.4524](#).
- [43] Auger, M. et al. (the EXO Collaboration), *The EXO-200 detector, part I: detector design and construction*, *J. Instrum.* **7**, P05010 (2012); [arXiv:1202.2192](#).
- [44] U.S. Department of Energy Office of Environmental Management, *Accident Investigation of the February 5, 2014, Underground Salt Haul Truck Fire at the Waste Isolation Pilot Plant, Carlsbad NM*, <http://energy.gov/ehss/downloads/accident-investigation-february-5-2014-underground-salt-haul-truck-fire-waste> (March 2014), accessed 9th of June 2015.

- [45] U.S. Department of Energy Office of Environmental Management, *Radio-logical Release Accident Investigation Report - Phase 1 Radiation Report*, <http://energy.gov/em/downloads/radiological-release-accident-investigation-report-phase-1-radiation-report>, (April 2014), accessed 9th of June 2015.
- [46] Ackerman, N. et al. (the EXO Collaboration), *Observation of Two-Neutrino Double-Beta Decay in ^{136}Xe with the EXO-200 Detector*, *Phys. Rev. Lett.* **107**, 212501 (2011); [arXiv:1108.4193](https://arxiv.org/abs/1108.4193).
- [47] SNOLAB. *User's Handbook*, 2nd revision, 26 June 2006.
- [48] Danilov, M. et al. (the EXO Collaboration), *Detection of very small neutrino masses in double-beta decay using laser tagging*, *Phys. Lett. B* **480**, 12–18 (2000); [arXiv:0002003](https://arxiv.org/abs/0002003).
- [49] Moe, M. K., *New approach to the detection of neutrinoless double-beta decay*, *Phys. Rev. C* **44**, R931(R) (1991).
- [50] Sinclair, D. et al. (the EXO Collaboration), *Prospects for Barium Tagging in Gaseous Xenon*, *J. Phys: Conf. Ser.* **309**, 012005 (2011).
- [51] Dolinski, M. J., *The Enriched Xenon Observatory: EXO-200 and Ba^+ tagging*, *Nucl. Phys. B (Proc. Suppl.)* **229–232**, 124–127 (2012).
- [52] Neuhauser, W. et al., *Localized visible Ba^+ mono-ion oscillator*, *Phys. Rev. A* **22**, 1137–1141 (1980).
- [53] Green, M. et al. (the EXO Collaboration), *Observation of single collisionally cooled trapped ions in a buffer gas*, *Phys. Rev. A* **76**, 02304 (2007); [arXiv:physics/0702122](https://arxiv.org/abs/physics/0702122).
- [54] Flatt, B. et al. (the EXO Collaboration), *A linear RFQ ion trap for the Enriched Xenon Observatory*, *Nucl. Instrum. Meth. A* **578**, 399–408 (2007); [arXiv:physics/0702122](https://arxiv.org/abs/physics/0702122).
- [55] Mong, B. et al. (the EXO Collaboration), *Spectroscopy of Ba and Ba^+ deposits in solid xenon for barium tagging in nEXO*, *Phys. Rev. A* **91**, 022505 (2015); [arXiv:1410.2624](https://arxiv.org/abs/1410.2624).
- [56] Twelker, K. et al. (the EXO Collaboration), *An apparatus to manipulate and identify individual Ba ions from bulk liquid Xe*, *Rev. Sci. Instrum.* **85**, 095114 (2014); [arXiv:1407.0618](https://arxiv.org/abs/1407.0618).
- [57] Brunner, T. et al. (the EXO Collaboration), *An RF-only ion-funnel for extraction from high-pressure gases*, *Int. J. of Mass Spectrom.* **379**, 110–120 (2015); [arXiv:1412.1144](https://arxiv.org/abs/1412.1144).
- [58] Jeng, S., Fairbank, W., & Miyajima, M., *Measurements of the mobility of alkaline earth ions in liquid xenon*, *J. Phys. D* **42**, 035302 (2009).
- [59] Walters, A. J. & Mitchell, L. W., *Mobility and lifetime of ^{208}Tl ions in liquid xenon*, *J. Phys. D* **36**, 1323 (2003).
- [60] Wamba, K. et al. (the EXO Collaboration), *Mobility of thorium ions in liquid xenon*, *Nucl. Instrum. Meth. A* **555**, 205–210 (2005); [arXiv:0503560](https://arxiv.org/abs/0503560).
- [61] Yves Martin, Jean-Michel Martin, and Luc Espic from la Haute Ecole d'Ingénierie et de Gestion du Canton de Vaude (HEIG-VD) in Switzerland, (personal communications, 2005–2013).

- [62] Bartels, J., Ten Bruggencate, P., Hausen, H., Hellwege, K. H., Schäfer, & Schmidt, E., *Landolt-Börnstein; Zahlenwerte und Funktionen*, 6. Auflage, II. Band, 2. Teil, Springer-Verlag, Berlin 1960.
- [63] Degarmo, E. P., Black, J. T., Kohser, R. A., *Materials and Processes in Manufacturing*, 9th ed., John Wiley & Sons, Singapore 2003.
- [64] Smith, W. F., Hashemi, J., *Foundations of Materials Science and Engineering*, 4th ed., McGraw-Hill, New York 2006.
- [65] Strauss, T. et al., *A steerable UV laser system for the calibration of liquid argon time projection chambers*, *J. Instrum.* **9**, T11007 (2014); [arXiv:1406.6400](#).
- [66] Silva, C. et al., *Reflection of the xenon scintillation light from Polytetrafluoroethylene (PTFE)*, *IEEE Nucl. Sci. Symp. Conf. Rec.* **2008**, 1253–1258 (2008); [arXiv:0910.1056](#).
- [67] Gehman, V. M. et al., *Fluorescence efficiency and visible re-emission spectrum of tetraphenyl butadiene films at extreme ultraviolet wavelengths*, *Nucl. Instrum. Meth. A* **654**, 116–121 (2011); [arXiv:1104.3259](#).
- [68] Borer, K. et al., *First results with the ORPHEUS dark matter detector*, *Astropart. Phys.* **22**, 199–210 (2004); [arXiv:astro-ph/0404311](#).
- [69] A. Roth, *Vacuum Sealing Techniques*, American Institute of Physics, New York 1994.
- [70] Robert C. Richardson and Eric N. Smith, *Experimental Techniques in Condensed Matter Physics at Low Temperatures*, Addison-Wesley Publishing Company, Inc., Redwood City, California 1988.
- [71] Seddon, J. R. T., Thurlow, M. S., Lees, M. J. & Lucas, P. G. J., *Optical flow visualization system for the cryogenic environment*, *Rev. Sci. Instrum.* **76**, 063903 (2005).
- [72] Rebel, B. et al., *High voltage in noble liquids for high energy physics*, *J. Instrum.* **9**, T08004 (2014); [arXiv:1403.3613](#).
- [73] Prof. Dr. Lutz Dümbgen from the Institute of Mathematical Statistics and Actuarial Science at the University of Bern, (personal communication, 2nd of June 2014).
- [74] Pfeiffer Vacuum, *The Vacuum Technology Book*, Volume II.
- [75] Herbert Wittel, Dieter Muhs, Dieter Jannasch und Joachim Vošiek, *Roloff/Matek Maschinenelemente*, 21. Auflage, Springer Vieweg, Wiesbaden, 2013.
- [76] Paul Horowitz and Winfield Hill, (1989). *The Art of Electronics* (2nd ed.). New York, NY: Cambridge University Press.
- [77] Slade, P. G., *An Investigation Into the Factors Contributing to Welding of Contact Electrodes in High Vacuum*, *IEEE Trans. Parts, Mater., Packag.* (1965–1971) **7**, 23–33 (1971).
- [78] Boccone, V. et al. (the ArDM Collaboration), *Development of wavelength shifter coated reflectors for the ArDM argon dark matter detector*, *J. Instrum.* **4**, P06001 (2009); [arXiv:0904.0246](#).

- [79] Giroux, G. et al., *A light readout system for gas TPCs*, *J. Instrum.* **9**, P01005 (2014); [arXiv:1311.4511](#).
- [80] Kuang, P. et al., *Improved Surface Wettability of Polyurethane Films by Ultraviolet Ozone Treatment*, *J. Appl. Polym. Sci.* **118**, 3024–3033 (2010).
- [81] Jánossy, L., *Rate of n -fold Accidental Coincidences*, *Nature (London)* **153**, 165–165 (1944).
- [82] Tong, Y. L., *The Multivariate Normal Distribution*, Springer-Verlag New York Inc., New York, 1990.

Acknowledgement

I would like to thank my supervisor **Razvan Gornea** for giving me the opportunity to work with the EXO collaboration and complete my PhD program. It has been exciting and great fun to work with you! Gratefully, I look back to countless days in the lab and many passionate discussions. Thank you very much!

I express deep and sincere gratitude to **Jean-Luc Vuilleumier**. In particular, your support during the last phase of my thesis was extraordinary! Your guidance, encouragement, suggestion, and very constructive criticism have contributed immensely to this thesis. Merci mille fois!!

I am very thankful to **Tamer Tolba** for his support and kindness. In times of trouble, related to work as well as not, you have always been around to encourage me. Danke vielmals!

Furthermore, I would like to thank the rest of the EXO-Bern group: **Domenico Franco, Guillaume Giroux, Manuel Weber, and Martin Auger**. It has been a great time with you guys!

I am very thankful to **Peter Rowson** for accepting to be the external referee of my thesis and for his useful comments and corrections. Furthermore I am grateful to the time we spent together in the lab during your visit for the high voltage tests with miniEXO.

I would like to thank **Nicolas Thomas** for chairing my doctoral defence!

My deep gratitude goes to **Jacques Farin** for his help in constructing the gas handling system and for his support during the last weeks of EXO Bern. Your visits have enriched my time in Bern, merci beaucoup!

I acknowledge with thanks the members of the alpha ion data analysis group: **William Fairbank, Razvan Gornea, Tessa Johnson, Brian Mong, and Erica Smith**.

I would like to express my gratitude to the LHEP workshops: **Jan Christen, Roger Hänni, Roger Liechti, Pascal Lutz, Lorenzo Meier, Fritz Nydegger, Gregor Pfäffli, and Camilla Tognina**. It is your enduring support which made this project possible in the first place! It has always been a great pleasure to work with you, merci viumau!

I appreciated the support of the LHEP over all these years. In particular I am thankful to: **Martin Auger, Lukas Bütikofer, Damian Göldi, Marcel Häberli, Sabine Joos, Igor Kreslo, Mathias Lüthi, Martti Nirkko, Christoph Rudolf von Rohr, and Marcel Zeller**.

It had been inspiring and great fun to conduct research with you — not exclusively fundamental but always experimental...

Stefan Janos, you showed us the stunning Meißner-Ochsenfeld effect, you demonstrated the miraculous persistent mode of a super conducting magnet immersed in liquid helium, and you tasted marvellously grown solid argon with me. Thankfully I look back to your lasting participation, mnohokrát vám ďakujem!

Furthermore I am grateful to **Marcella Esposito**, **Beat Hiltbrunner**, **Irene Neeser**, **Palmira Sciarra**, **Ursula Witschi**, and **Daniela Zürcher**.

I would like to thank **Simon Milligan** for language editing the abstract, introduction, and conclusion.

I am thankful to my fellow students for the time we spent during the entire physics studies. We have experienced a lot of fun times! I am convinced this friendship will lead us to new adventures.

My dear **Bänz Bessire**! Many times, we've been out drinking. Many times we've shared our thoughts. Well I hope that someday buddy, we will be travelling again! Thank you for your countless visits in the cryo-lab, for patiently and understandingly listening to my worries, and moreover, for shearing your credit card with me in times of need. Muchas gracias!

I wish to express my deepest gratitude to my friends: **Gäbu**, **Hännu**, **Gil**, **Katia**, **Luca**, **Chregu**, **Anna**, **Demi**, **Löni**, **Milon**, **Eli**, **Ännu**, and **Michu**. You have supported and encouraged me ever since I can remember!

In particular I would like to thank my dear flatmate **Fabienne**. Thank you for tolerating me over the past couple of months and letting me vegetate day and night in *our* living room!

Most of all I would like to thank my parents **Fränze** and **Gäse** for their love, patience, and never ending support.

This work was supported by the Swiss National Science Foundation.

Declaration of consent

on the basis of Article 28 para. 2 of the RSL05 phil.-nat.

Name/First Name: Delaquis / Sébastien Claude

Matriculation Number: 04-107-421

Study program: Physics

Bachelor

Master

Dissertation

Title of the thesis: Construction and operation of the EXO-100
cryogenic facility for R&D in liquid xenon:
advances in barium ion tagging

Supervisor: Prof. R. Gornea

I declare herewith that this thesis is my own work and that I have not used any sources other than those stated. I have indicated the adoption of quotations as well as thoughts taken from other authors as such in the thesis. I am aware that the Senate pursuant to Article 36 para. 1 lit. r of the University Act of 5 September, 1996 is authorised to revoke the title awarded on the basis of this thesis. I allow herewith inspection in this thesis.

Bern, 5th of October 2015

Place/Date



Signature

Curriculum vitae

Name:	Sébastien Claude Delaquis
Date of birth:	23rd of January, 1983
Place of origin:	Rechthalten FR, Switzerland
Citizenship:	Swiss
October 2015	Defence of doctoral dissertation.
2011 – 2015	Ph.D. student under the supervision of Prof. Dr. Razvan Gornea at the Physikalischen Institut at the Albert Einstein Center for Fundamental Physics at the Laboratory for High Energy Physics of the University of Bern, Switzerland.
December 2010	Awarded with the degree of <i>Master of Science in Physics</i> .
2008 – 2010	Master student under the supervision of Prof. Dr. Antonio Ereditato and Dr. Igor Kreslo at the Physikalischen Institut at the Albert Einstein Center for Fundamental Physics at the Laboratory for High Energy Physics of the University of Bern, Switzerland.
November 2009	Awarded with the degree of <i>Bachelor of Science in Physics</i> .
2004 – 2009	Bachelor studies of physics, mathematics, and astronomy at the University of Bern, Switzerland.
June 2003	Passed the <i>Matura Exam</i> .
2001 – 2003	Gymnasium Hofwil Münchenbuchsee BE, Switzerland.
1989 – 2001	Waldorf school of Bern and Ittigen, Switzerland.

List of publications

During the time of this PhD thesis, the candidate has co-authored a number of publications in different scientific journals. A list in chronological order is presented in the following:

- Auger, M. et al. (the EXO Collaboration), *Search for Neutrinoless Double-Beta Decay in ^{136}Xe with EXO-200*, *Phys. Rev. Lett.* **109**, 032505 (2012); [arXiv:1205.5608](#).
- Albert, J. B. et al. (the EXO Collaboration), *Improved measurement of the $2\nu\beta\beta$ half-life of ^{136}Xe with EXO-200*, *Phys. Rev. C* **89**, 015502 (2014); [arXiv:1306.6106](#).
- Delaquis, S. C. et al., *Development of a camera casing suited for cryogenic and vacuum applications*, *J. Instrum.* **8**, T12001 (2013); [arXiv:1310.6601](#).
- Giroux, G. et al., *A light readout system for gas TPCs*, *J. Instrum.* **9**, P01005 (2014); [arXiv:1311.4511](#).
- Albert, J. B. et al. (the EXO Collaboration), *Search for Majorana neutrinos with the first two years of EXO-200 data*, *Nature (London)* **510**, 299–234 (2014); [arXiv:1402.6956](#).
- Twelker, K. et al. (the EXO Collaboration), *An apparatus to manipulate and identify individual Ba ions from bulk liquid Xe*, *Rev. Sci. Instrum.* **85**, 095114 (2014); [arXiv:1407.0618](#).
- Albert, J. B. et al. (the EXO Collaboration), *Search for Majoron-emitting modes of double-beta decay of ^{136}Xe with EXO-200*, *Phys. Rev. D* **90**, 092004 (2014); [arXiv:1409.6829](#).
- Albert, J. B. et al. (the EXO Collaboration), *Investigation of radioactivity-induced backgrounds in EXO-200*, *Phys. Rev. C* **92**, 015503 (2015); [arXiv:1503.06241](#).
- Albert, J. B. et al. (the EXO Collaboration), *Measurements of the ion fraction and mobility of alpha and beta decay products in liquid xenon using EXO-200*, [arXiv:1506.00317](#).

